NONLINEAR DYNAMICS OF SHELLS AND PLATES SUBJECTED TO PULSATILE FLOW

By

Eleonora Tubaldi

Department of Mechanical Engineering
McGill University
Montreal, Quebec, Canada

11th July 2017

A thesis submitted to McGill University

in partial fulfillment of the requirements of the degree of Doctor of Philosophy

Abstract

Flow-induced vibrations due to unsteady flow often occur in many engineering areas. A specific type of unsteady flow is represented by oscillatory and pulsatile flows, which are prevalent in industrial and biological systems; applications include pump and valve operations in pipeline systems as well as blood circulation. Associated to pulsatility, wave propagation in elastic tubes is recognised as the fundamental principle of the pressure pulse in arteries. This propagation phenomenon is due to the fluid-structure interaction and not to fluid compressibility. The pulse wave velocity is related to the underlying vessel wall stiffness. In biomechanics and vascular surgery, thin-walled shell theory can be applied to model the mechanics of veins, arteries, pulmonary passages, and artificial blood vessels.

This thesis focuses on the development of a new theoretical framework able to reproduce the nonlinear dynamic response of shells and plates to axial pulsatile flow. The flow is set in motion by a pulsatile pressure gradient. Coupled fluid-structure Lagrange equations of motion for a non-material volume subject to pulsatile flow and pressure with and without wave propagation are obtained and presented for the first time in the literature. The studied systems are represented by a plate periodically supported and a circular cylindrical shell with flexible boundary conditions. The fluid model is based on the potential flow theory. Numerical bifurcation analysis and time integration methods are employed to investigate the stability of the systems described using a refined reduced order model.

The plate is modeled based on the von Kármán nonlinear plate theory and it is assumed to be periodically simply supported in both in-plane directions with immovable edges. The flow channel is bounded by a rigid wall. The effects on the dynamics of the plate of different system parameters such as flow velocity, pulsation amplitude, pulsation frequency, and channel pressurization are fully discussed.

In vascular surgery, artificial blood vessels used for repairing and replacing damaged thoracic aorta in cases of aneurysm, dissection or coarctation can be modeled as thin-walled shells conveying pulsating flow. For this purpose, in this study, isotropic and orthotropic circular cylindrical shells with mechanical properties of woven Dacron thoracic prostheses are modeled using the nonlinear Novozhilov shell theory. A pulsatile time-dependent blood flow model is considered by applying physiological waveforms of velocity and pressure during the heart beating period. The fluid is assumed to be Newtonian and the pulsatile flow is formulated using a hybrid model that contains the unsteady effects obtained from the linear potential flow theory and the pulsatile viscous effects obtained from the unsteady time-averaged Navier-Stokes equations. Geometrically nonlinear vibrations displaying interesting and intricate nonlinear dynamics (chaos, amplitude modulation and period-doubling bifurcation) are presented via frequency-response curves, time histories, bifurcation diagrams, and Poincaré maps.

This study provides an efficient fluid-structure interaction model that can reveal important aspects on the nonlinear dynamics and stability of systems conveying pulsatile flow. It also addresses a crucial but still unexplored issue in cardiovascular surgery related to the dynamics of Dacron vascular grafts subject to physiological pulsatile blood flow. An innovative formulation of the three-dimensional quasi-linear viscoelasticity is presented and applied to fit original experimental data of relaxation in axial and circumferential directions of a woven Dacron aortic graft. Experimental dynamic tests have been conducted on a Dacron prosthesis pressurized with a blood analog fluid. Modal damping values and natural frequencies have been estimated by experimental modal analysis. Numerical simulations and comparisons with experimental results are reported.

Sommaire

Les vibrations induites par un écoulement à vitesse variable se manifestent souvent dans plusieurs domaines en ingénierie. Un type spécifique d'écoulement est celui pulsé, qui se produit dans des systèmes biologiques et industriels; des exemples sont les pompes et valves des pipelines et par le système circulatoire. Associée à la pulsatilité, la propagation des ondes dans des tuyaux élastiques est considérée le principe fondamental du pouls de pression dans les artères. Ce phénomène de propagation est une conséquence de l'interaction fluide-structure et non de la compressibilité du fluide. La vitesse de propagation des ondes est associée à la rigidité des parois des vaisseaux. En biomécanique et chirurgie vasculaire, la théorie des coques minces peut être utilisée pour décrire la mécanique des veines, artères, passages pulmonaires et prothèses vasculaires synthétiques.

Cette thèse a comme objectif le développement d'une méthode théorique qui vise à reproduire la dynamique non-linéaire de coques et piastres soumises à un écoulement pulsé. Un gradient de pression pulsé cause le mouvement du fluide. Les équations de Lagrange qui considèrent l'interaction fluide-structure sur une structure flexible soumise à un écoulement et une pression pulsé avec et sans la propagation des ondes sont obtenues pour la première fois en littérature. Les systèmes étudiés sont une piastre périodiquement supportée et une coque circulaire cylindrique avec des conditions aux rives flexibles. Le modèle du fluide se base sur la théorie à potentiel. L'analyse numérique de bifurcation et l'intégration dans le temps sont utilisées pour étudier la stabilité du system représenté par un modèle d'ordre réduit.

La piastre est modelée en appliquant la théorie non-linéaire des piastres de von Kármán et elle est supposée d'être périodiquement supportée dans les deux directions dans le plan avec des supports immobiles. De l'autre côté par rapport à la piastre, l'écoulement du fluide est en contact avec une surface rigide. L'effet sur la dynamique de la piastre des différents paramètres - comme la vitesse de l'écoulement, l'amplitude de la pulsation, la fréquence de la pulsation, et la pressurisation du canal - est analysé en détail.

En chirurgie vasculaire, les prothèses synthétiques utilisées pour réparer et remplacer les parties de l'aorte thoracique endommagées par un aneurisme ou une dissection peuvent être modelées comme des coques minces qui transportent un écoulement pulsé. Dans ce but, des coques circulaires cylindriques isotropes et orthotropes avec les mêmes propriétés mécaniques des prothèses vasculaires en Dacron sont modelées en utilisant la théorie non-linéaire de Novozhilov. L'écoulement du sang est considéré pulsé et il reproduit la forme d'onde de vitesse et pression pendant le cycle cardiaque. Le fluide est considéré newtonien et l'écoulement pulsé est formulé en utilisant un modèle hybride qui considère les effets instationnaires de la théorie à potentiel et les effets visqueux pulsés obtenus grâce aux équations de Navier-Stokes moyennées dans le temps. Les vibrations non-linéaires du system sont caractérisées par un comportement dynamique intéressant et complexe (chaos, modulation en amplitude, bifurcation double-période) qui est présenté grâce aux courbes de réponse en fréquence, dans le temps, digrammes des bifurcations et mappes de Poincaré.

Cette étude fournit une méthode efficace d'interaction fluide-structure qui révèle des aspects importants sur la dynamique non-linéaire et la stabilité des systèmes qui transportent un écoulement pulsé. Une attention particulière est dédiée à un problème inexploré malgré crucial en chirurgie vasculaire associé à la dynamique des prothèses vasculaire en Dacron soumises à l'écoulement pulsé du sang. Une formulation innovative de la viscoélasticité quasi-linéaire tri-dimensionnelle est présentée et appliqueé aux données expérimentales de relaxation en direction circonférentielle et axiale d'une prothese aortic en Dacron. Une analyse modale experimentale a été performée sur une prothèse en Dacron pressurizée par un fluide alogue au sang. Les valeurs du taux d'ammortissement modale et les fréquences naturelles ont été estimés grâce à l'analyse modale lineare. Des simulations numériques et des comparaisons avec les données experimentales sont reportées dans cette thèse.

Acknowledgments

First and foremost I want to thank my advisor Prof. Marco Amabili, who has been a tremendous mentor for me. I would like to express my gratitude to him for encouraging me in my research and for allowing me to grow as a researcher as well as a person. I couldn't have asked for a more worthwhile and fulfilling graduate experience.

A special acknowledgement goes to my co-supervisor Prof. Michael P. Païdoussis. It has been an honour to be his Ph.D. student. His advice on both research and *joie de vivre* has been priceless. You once jokingly asked me to write a full chapter of my thesis in verse, to honour the fact that I am from the town of poetry Recanati. It is with great regret that I announce to you that I have not fulfilled your request. I felt a simple quote from Leopardi would explain why I didn't venture to do it: "everything since Homer has improved, except poetry". I hope you will enjoy the thesis nonetheless.

Thanks to Dr. Farbod Alijani for having helped and taught me immensely during my first year at McGill University.

I gratefully acknowledge the funding sources MEDA (McGill University) and FQRNT Fonds de Recherche Nature et Technologie (Quebec Minister of Education) that made my Ph.D. work possible.

My time at McGill was enjoyable in large part due to the many friends that became part of my life. I am grateful for the time spent in the laboratory with Giovanni Ferrari and my *socia* Margherita Capriotti. I would like to thank Giovanni for being my loyal colleague and my reference point at McGill, always ready to listen to my "existential doubts" throughout these years. Margherita, thank you for all the dinners we prepared together and for the sleepless nights spent studying and chatting.

Thanks to Prabakaran Balasubramanian for being always willing to help in the lab and for being a great cricket coach. I also thank Ivan Breslavskyi for our fruitful conversations on biomechanics.

My time at McGill was also enriched during lunch and coffee breaks by friends in other research groups at McGill University: Albert Peiret and Eleonora Botta above all. Both of you have enormously supported me during the ups and the downs of my research.

I would like to acknowledge Evelina Nikolaidou, Dea van Lierop, and Eleonora Botta for the countless pleasant moments we shared. Our first meeting at the MEDA event was just a forerunner of all the amazing dinners, adventures, and trips that were (and are) still to come. Thank you for shaping my years at McGill with profound conversations and lots of calories!

I am grateful for the time spent with roommates and friends from the swing dance community, for my theater troupe and our memorable performances, and for many other people and memories from École Polytechnique de Montreal.

A special thanks to my family. Words cannot express how grateful I am to my parents who raised me with a love of science and literature and supported me in all my pursuits. Your encouraging words sustained me thus far. Thank you for having instilled in me the gift of curiosity that drives me as a researcher and as a young woman. I am extremely grateful to my brother and his sense of humour that always know how to make me smile. Marco, thank you for being a big part of my foundation and my first supporter.

I would also like to thank all of my friends in Europe who incented me to strive towards my goals: Piera, Elsa, Nancy, Andrea S., Andrea R., our calls and chats made me feel close to you despite the ocean. My childhood friends Ludovica R., Ludovica U., Michela, Laura, Silvia, Irene, and Lorenzo, thank you for your true friendships. I cherish every moment we spent together as teenagers as well as in our adult lives.

At the end, I would like to express my deep appreciation to Liam for all the dances in the kitchen, for the dinners you prepared while I was working, for our road trips. Most of all, I want to thank you for your patience and unconditional support throughout these challenging years synthetized in the sentence: “You can do it Ele”.

List of publications

Journal Papers

1. M. Amabili, G. Ferrari, P. Balasubramanian, E. Tubaldi, Application of three-dimensional quasi-linear viscoelasticity to relaxation of an aortic woven Dacron graft, *submitted in an international journal*.

2. E. Tubaldi, M. Amabili, M.P. Païdoussis, Nonlinear dynamics of Dacron aortic prostheses conveying pulsatile flow, *submitted in an international journal.*

3. E. Tubaldi, M. Amabili, M.P. Païdoussis, Nonlinear dynamics of shells conveying pulsatile flow with pulse-wave propagation. Theory and numerical results for a single harmonic pulsation, Journal of Sound and Vibration, 369 (2017) 217-245.

4. E. Tubaldi, M. Amabili, M.P. Païdoussis, Fluid–structure interaction for nonlinear response of shells conveying pulsatile flow, Journal of Sound and Vibration, 371 (2016) 252-276.

5. E. Tubaldi, M. Amabili, F. Alijani, Nonlinear vibrations of plates in axial pulsating flow. Journal of Fluids and Structures, 56 (2015) 33-55.

Proceedings

1. E. Tubaldi, M.Amabili, M.P. Païdoussis, Nonlinear vibrations of woven Dacron prostheses conveying pulsatile flow, ASME International Mechanical Engineering Congress and Expositions, 3-9 November, 2017, Tampa, Florida, USA. *Accepted paper.*

2. M. Amabili, P. Balasubramanian, G. Ferrari, E. Tubaldi, Experimental investigation on the viscoelastic and dynamic behaviour of an aortic Dacron graft, ASME International Mechanical Engineering Congress and Expositions, 3-9 November, 2017, Tampa, Florida, USA. *Accepted paper.*

3. M. Amabili, E. Tubaldi, M.P. Païdoussis, Fluid-Structure Interaction of Dacron aortic prostheses conveying pulsatile flow, 14th U.S. National Congress on Computational Mechanics, 17-20 July, 2017, Montreal, Quebec, Canada. *Accepted paper.*

4. E. Tubaldi, M.A mabili, M.P. Païdoussis, Nonlinear response of shells conveying pulsatile flow with pulse-wave propagation, ASME International Mechanical Engineering Congress and Expositions, 11-17 November, 2016, Phoenix, Arizona, USA.

5. E. Tubaldi, M. Amabili, M.P. Païdoussis, Nonlinear response of shells conveying pulsatile flow, XXIV ICTAM, 21-26 August, 2016, Montreal, Quebec, Canada.

6. E. Tubaldi, M. Amabili, M. Païdoussis, Fluid-Structure Interaction for nonlinear response of aorta replacement. ASME International Mechanical Engineering Congress and Expositions, November 13–19, 2015, Houston, Texas, USA.

7. E. Tubaldi, M. Amabili, F. Alijani, Nonlinear vibrations of plates in axial pulsating flow. ASME 2014 International Mechanical Engineering Congress and Expositions, November 14-20, 2014, Montreal, Quebec, Canada.

Preface

Thin-walled structures in contact with axial fluid flow can be found in many engineering and biomechanical systems and their dynamics are inevitably influenced by flow-induced inertia and forces. Making the thickness as small as possible is one of the main design requirements of structural elements in order to reduce spare material and to lighten the structure. However, in particular when subject to flow-induced vibration, structures can undergo large displacements and instability that must be analyzed using nonlinear elasticity in order to prevent their failure. Several important aspects of the structural response can only be predicted by nonlinear theory such as the transition from one dynamical state to the next one and the exploration of nonstandard dynamics (*i.e.* quasiperiodic and chaos regimes).

Thin plates immersed in flowing fluid are widely used in many floating and submarine structures (ships, submarines, torpedoes) excited by an unsteady flow, and water retaining structures (dams, storage vessels) subject to earthquake loading. Under these conditions, the plate dynamic response to different sorts of excitations, such as harmonic fluid excitations, becomes of considerable interest. Moreover, the local resonant vibration behavior of plates has always represented a great concern to shipbuilding companies and operators. While extensive literature exists on the nonlinear dynamics of plates in a light medium (usually air), the literature related to nonlinear studies of plates coupled to flowing dense (heavy) fluid is scarce.

In this thesis, nonlinear coupled fluid-structure interaction Lagrange equations of motion for plates in axial pulsatile flow are developed. The effect of different system parameters such as flow velocity, pulsation amplitude, pulsation frequency, and channel pressurization on the stability of the plate and its geometrically nonlinear response to pulsating flow are fully discussed. The results show that the presence of positive transmural uniform pressure and small pulsation frequency would destroy the pitchfork bifurcation (divergence) that flat plates exhibit when subjected to uniform flow. Moreover, in the case of zero uniform transmural pressure, numerical results show a hardening type behavior for the entire flow velocity range when the pulsation frequency is spanned in the neighbourhood of the plate's fundamental frequency. On the contrary, a softening type behavior is presented when a uniform transmural pressure is introduced.

Shells are curved light-weight structures made of shell elements and are very stiff for both in-plane and bending loads because of the curvature of their middle surface. For this reason they are widely used in many engineering fields where structures with the minimum amount of material are needed to meet the design requirements. In these applications (i.e. aeronautics, automotive engineering, space industry), the shells have a small thickness compared to the other dimensions and are referred to as thin-shells. Studying their stability with nonlinear theories is particularly interesting since they can easily present large displacements associated to small strains before collapse. When subjected to dynamic loads with moderate and large amplitudes, radial displacements larger than the shell thickness occur. In this case, nonlinear shell theories should be applied to study the dynamic behavior of these systems that can present complex dynamics.

In biomechanics, thin-walled shells can be used to model the mechanics of vein, arteries and pulmonary passages. The peculiar characteristic of the cardiovascular system is the pulse generated by the heart. The highly pulsatile nature of the blood flow combined with the compliance of the arteries make the vessel walls locally deform and recover with corresponding recoil. A wave motion is consequently generated in the arterial tree where pressure and the flow waves propagate downstream in the form of progressive waves at the same wave speed. How efficient1y the pressure pulse transmits depends on the propagation and reflection characteristics through different arteries and vascular branching junctions. The arterial pulse wave velocity (PWV) has been shown to be related to the underlying vascular stiffness because of its dependence on the geometric and elastic properties of the local arterial wall. With differing vascular impedances, wave reflections arise, because of the mismatching in impedances.

In vascular surgery, Dacron and ePTFE (expanded polytetrafluoroethylene) represent the standard materials for large-diameter (12-30 mm) vascular grafts. These implants are widely used in various circumstances of vascular maladies requiring replacements of components of the cardiovascular tree, such as vessel patches for aneurysms, however, it is well known that they have distinctly different mechanical properties than the host arteries. The energy loss due to reflection and propagation of the pulse wave as it encounters the graft is considered to be the most significant mechanism to graft failure because of compliance mismatch. Their low compliance also compromises the efficiency of the whole human cardiovascular system. Wide knowledge about the distinctly different mechanical properties of the Dacron implants with respect to the native aorta is available in literature while very little is known about the dynamic behavior of these prostheses.

To the author's knowledge, this is the first study to address the dynamic response of a woven Dacron graft currently used in thoracic aortic replacements to pulsatile physiological blood flow and pressure. Nonlinear vibrations of the shell conveying pulsatile flow and subjected to pulsatile pressure are investigated taking into account the effects of the pulse-wave propagation. For the first time in literature, coupled fluid-structure Lagrange equations of motion for a non-material volume with wave propagation in case of pulsatile flow are developed. Physiological waveforms of blood pressure and flow velocity are approximated with the corresponding Fourier series. To investigate the effect of the pulse wave propagation, only the first harmonic of the Fourier expansion is considered to describe the pulsatile pressure and flow. A parametrical study is performed for different values of modal damping coefficients and pulsatile wave speeds. For different combinations of these parameters, out of the physiological frequency range, interesting and intricate nonlinear dynamics, such as chaos and amplitude modulations, are detected in the vicinity of the fundamental natural frequency of the vessel. Several superharmonic resonance peaks appear in the physiological frequency range by including higher harmonics in the Fourier expansion of the physiological waveforms of pressure and velocity.

Finally, in the limit case of low modal damping values, it is found that the prosthesis presents asymmetric vibration with deformation of the cross-section. In this deformed condition, high stress localized regions appear in the inner wall and flow separation or turbulence can develop eventually causing the failure of the prosthesis. Experimental results based on the damping identification and modal analysis tests of a woven Dacron graft are reported. The numerical natural frequencies are compared with the experimental results showing to be in very good agreement.

This thesis' main contribution to knowledge is the creation of an efficient fluid-structure interaction model that can be utilized to study the dynamic response of flexible plates and shells in axial pulsatile flow. In particular, because of its relevant application in the field of cardiovascular surgery, its conclusions can be used to improve the understanding of the crucial issue of vascular grafts patency. Its potential is to reveal important aspects of vascular mechanics, physiology, and pathology by comparing the dynamic behaviors of native and artificial blood vessels.

Informing surgeons of the effects in the differences between dynamical behaviors of prostheses with respect to the human arteries can aid in surgical decision making. Eventually, this could also lead to inspiring the design and creation of new materials or techniques for the fabrication of next generation prostheses.

The fluid-structure interaction model presented can also be applied to study the possibility of buckling with cross-section deformation of a straight thoracic aortic segment for critical physiological pressure and flow conditions. In the case of collapsed arteries, the identification of regions of large mechanical stresses on the artery surface can indicate possible ways for aortic dissection to be initiated. This could be of crucial importance in human health since aortic dissection is considered one of the most undiagnosed serious cardiovascular pathologies.

Experimental activities have been conducted to characterize the mechanical and dynamic properties of woven Dacron aortic replacements.

Uniaxial extension and relaxation tests have been performed on strips of a woven Dacron aortic prosthesis. An innovative quasi-linear viscoelastic model has been introduced to experimentally investigate, for the first time, the direction-dependent relaxation of the aortic graft by using a bi-dimensional material model. This model implies a relevant simplification in case of direction-dependent viscoelasticity typical of aortic prostheses.

Normal modes, natural frequencies and viscous damping ratios of a woven Dacron prosthesis with internal pressurized fluid have been obtained by means of a modal analysis. Numerical simulations based on a structural model with surface waves in the longitudinal direction of the prosthesis (crimped structure) have been performed. Comparisons with the experimental results are reported and discussed in depth.

The present thesis is article-based. Among the five papers reported here, three are published and the two most recent ones have been submitted in peer-reviewed international journals.

The author is the primary author of the first four papers presented. Her contribution to the conception, design, and realization of such papers is primary, covering the mathematical modelling, the implementation of the numerical solution and corresponding results, and the writing of the manuscripts. The co-authors of these papers are the author's supervisors who contributed in advising and supporting roles throughout this doctoral research project. Dr. Farbod Alijani, co-author of the first paper presented here, has also collaborated with the author in the initial phase of her Ph.D. studies by providing technical support with the use of the software AUTO.

The fifth and final paper presented in this thesis is the result of the collaboration of Prof.Amabili with Dr.Giovanni Ferrari, Mr. Prabakaran Balasubramanian and the author. In particular, the author has participated to the realization of the tensile and relaxation tests reported in this manuscript.

The experimental activities on a woven Dacron prosthesis presented in Chapter 7 have been performed by Dr. Giovanni Ferrari and Mr. Prabakaran Balasubramanian. The author has assisted these experiments by providing guidance with technical notes on the clinical practice of prostheses installation in the attempt to better reproduce physiological conditions in the experimental setup.

Contents

Thesis Outline

The thesis is structured by articles showing the several steps leading to the development of the proposed fluid-structure interaction model for plates and shells in axial pulsatile flow.

Chapter 1 introduces some concepts and methods used throughout the thesis for both nonlinear dynamics and fluid-structure interactions. A detailed literature review on nonlinear vibrations of plates and shells in axial steady and pulsatile flow is presented in the same chapter. Due to the relevant application of the present work in cardiovascular surgery and biomechanics, the most significant studies on Dacron prostheses and pulsatile flow in blood vessels are included in the literature review. In the Introduction, the motivation and the objectives of the present work are clearly stated.

Chapter 2 deals with the stability and the nonlinear vibrations of plates in axial pulsatile flow. The paper "Nonlinear vibrations of plates in axial pulsating flow" published in the Journal of Fluids and Structures [1] is presented in this chapter. Lagrange equations of motion are derived for the case of unsteady flow velocity. The effects of the oscillatory component of the velocity and the transmural uniform pressure on the stability of the plates in axial flow are discussed.

Chapter 3 treats the dynamic behavior of shells subjected to pulsatile pressure and axial flowing fluid without wave propagation phenomenon. It is assumed that the oscillatory pressure variations occurred simultaneously at every point of shell, making the fluid oscillate in bulk. The paper “Fluid-Structure Interaction for nonlinear response of shells conveying pulsatile flow” published in the Journal of Sound and Vibration [2] is reported. The isotropic shell taken into account is assumed to roughly approximate the Dacron vascular prostheses used for replacing damaged thoracic aorta in cases of dissection or aneurysm. The pulsatile flow and pressure reproduce the physiological time-dependent velocity and pressure waveforms in the thoracic aorta.

Chapter 4 presents the extension of the fluid-structure interaction model for flexible shells conveying pulsatile flow and pressure (Chapter 3) with the addition of the effect of pulse-wave propagation. The corresponding paper “Nonlinear dynamics of shells conveying pulsatile flow with pulse-wave propagation. Theory and numerical results for a single harmonic pulsation” published in the Journal of Sound and Vibration [3] is presented. A pulsatile blood flow model is considered by applying the first harmonic of the physiological waveforms of velocity and pressure during the heart beating period. The woven Dacron aortic prosthesis is modelled as an orthotropic circular cylindrical shell.

In Chapter 5, the fluid-structure interaction method illustrated in Chapter 4 is applied to the same woven Dacron graft subjected to physiological pulsatile blood flow and pressure. The manuscript “Nonlinear dynamics of Dacron aortic prostheses conveying pulsatile flow” recently submitted in a peer-reviewed international journal is reported. Interesting results on the dynamic behavior of the prosthesis for different values of heart rate are discussed in depth.

Chapter 6 presents results of uniaxial extension and relaxation tests on strips of a woven Dacron prosthesis. An innovative quasi-linear viscoelastic formulation is introduced to consider direction-dependent viscoelasticity of the prosthetic fabric. The manuscript “Application of three-dimensional quasi-linear viscoelasticity to relaxation of an aortic woven Dacron Graft" presented in this chapter has been recently submitted to a peer-reviewed international journal.

In Chapter 7, natural frequencies and modal damping values estimated via experimental modal analysis of a woven Dacron graft are reported. Numerical natural frequencies are compared with the experimental results.

Chapter 8 represents the concluding chapter of the thesis. It summarizes the objectives previously stated highlighting the significant findings of the present work. Discussions on ongoing related research as well suggestions for future works are explored.

Chapter 1

Introduction and Literature Review

1.1 Introduction

In a very fundamental sense, the effect of the pulsation constitutes a central problem in the field of fluid-body interactions. Understanding the impact of oscillating flows of heavy fluids in flexible channels is of crucial interest for many biological and industrial processes. The pulsatile nature of blood flow dictates numerous aspects of circulatory physiology and pathology. Pulsatile flow is also observed in engines and hydraulic systems, as a result of rotating mechanisms pumping the fluid.

The objective of this study is to reveal new nonlinear phenomena in these systems and to advance theoretical understanding resulting from the development of a new theoretical framework that fully captures the mutual coupling of fluids and flexible solids. The physical and mathematical modeling of pulse wave propagation, based on general fluid dynamical principles, is integrated, for the first time, with the study of the nonlinear dynamics of thin-walled structures subjected to dynamic loads. The intrinsic interdisciplinary aspects of this research clearly show the relevance of the proposed innovative modeling tool. Potential applications in cardiovascular research and clinical practice are presented. From an engineering perspective, artificial and native blood vessels can be considered cylindrical structures subject to combined loads due to surrounding tissues and to blood flow and pressure. Any compliant vessel may buckle under these loads and deform from their originally straight cylindrical configuration. Moreover, the dynamic response analysis can reveal if sudden changes in diameter appears for certain heart rates provoking fluctuations in the shear stress and disturbed blood flow. This in turn may cause significant material damage, weakening transverse wall stiffness, leading to the initiation of a permanent wall dilatation or dissection. The stability and the dynamic behavior of these systems is an important issue for vasculature even if it has not been extensively studied so far.

As a consequence of this lack in literature, a mathematically exact solution, within the hypotheses of potential flow and the series solution, has been developed in this thesis and the corresponding numerical results are presented. This theoretical approach is adapted to both plates and shells' elastic bodies. This model can be utilized when the flow exciting the thin-walled structure contains harmonic components. Residual stresses because of pulsatile pressurization are evaluated and included in the model.

Experimental results on the charactirization of mechanical and dynamic properties of woven Dacron aortic prostheses are included in this dissertation. The objective is to justify the values of some parameters (such as modal viscous damping and natural frequencies) considered in the numerical simulations of the fluid-structure interaction model applied to the aortic grafts made of Dacron.

1.2 Literature Review

Flow-induced vibrations of plates and shells are a major problem in many engineering applications including aerospace, aeronautics, automotive, nuclear, and naval industries. Plates are structural elements with a flat surface with given thickness and they can be found in wing skin, tail fins, flaps, and control surfaces of aircrafts and submarines.

Shells are light-weight structures made of shell elements, typically curved, and assembled to form large structures such as aircraft fuselage, spacecraft, rockets, cars, and storage tanks. Shell structures also appear in the form of membranes in many biological systems such as arteries, veins, pulmonary, and urinary passages. In order to accurately predict the nonlinear response of the structure, it is necessary to consider numerical models that take into account (i) nonlinear effects such as large structural deflections, and (ii) fluid-structure interactions. Both theoretical and experimental aspects of nonlinear vibrations and stability of shells and plates with and without fluid structure interaction have been addressed by Amabili in his book [4]. All important aspects of fluid-structure interactions in slender structures in axial flow have been covered and synthesized by Païdoussis in his monograph [5]. Extensive literature reviews on the topic of nonlinear dynamics of shells *in vacuo*, filled with or surrounded by quiescent and flowing fluids can be found in [6, 7]. These reviews point to the fact that there remains much to be learned about nonlinear vibrations of shells and plates.

The present literature review focuses on linear and geometrically nonlinear vibrations of plates and shells with fluid-structure interaction with industrial and biomedical applications. This review is structured as follows: after presenting the most significant studies of the very rich literature on the vibrations of shells and plates in axial flow, particular attention is devoted to the venerable subject of pulsatile flow. The dynamics of pipes, plates and shells subject to pulsatile flow is profoundly reviewed. In physiological systems, pulsatility is manifested in pressure and flow waves propagating throughout the whole circulatory tree. Understanding the physical principles of blood circulation has been the objective of hemodynamicists for centuries. For this reason, this literature review covers only the studies that are considered the standard reference sources in hemodynamics. The problem of stability (divergence and flutter) of pliable shells coupled to flowing fluid is also reviewed. Finally, the most significant studies on Dacron prostheses used for thoracic aortic replacements and the assessed effects of their insertion in the cardiovascular system are presented.

1.2.1 Plates in axial steady flowing fluid

The literature related to linear vibrations of plates coupled to fluid is quite extensive (see Lamb [8], Kwak and Kim [9], Kwak [10], Fu and Price [11], Amabili and Kwak [12]). The majority of the approximate analytical methods that are used to study flow-induced vibrations are based on the assumption attributed to Lamb [8]; that the vibration modes of the structure in contact with still fluid (wet modes) are the same as those *in vacuo* (dry modes). Amabili and Kwak [12] removed the simplified assumption of identical wet and dry modes and obtained the mode shapes of the coupled system via the Rayleigh-Ritz approach. Experiments on large amplitude vibrations of a circular plate at the bottom of a water-filled container were presented by Chiba [13]. In the case of flowing fluid, and in addition to the inertia effect of the fluid, the stiffness of the coupled plate-flow system decreases with the flow speed, eventually leading to instability. Moreover, the presence of gyroscopic terms in the equations of motion gives rise to complex modes and therefore different points of the plate do longer oscillate in-phase. Guo and Paidoussis [14] used the Galerkin approach to study the hydroelastic instabilities of parallel assemblies of rectangular plates coupled to flow. They found that divergence and coupled mode flutter may occur for plates with any type of end supports, while single-mode flutter only arises for non-symmetrically supported plates. Kerboua *et al.* [15] used a different approach based on the combination of Finite Element Method (FEM) and Sander's shell theory to determine the natural frequencies of rectangular plates in contact with flowing fluid. In their study, the velocity potential and Bernoulli's equation were used to express the fluid pressure acting on the structure. A general aerodynamic case of a single elastic plate embedded in a rigid surface ("baffle") has been treated in Dowell [16]. Dowell also discussed the case of both finite and infinite plates on periodic supports for high supersonic flow [17]. As the number of bays becomes larger, he found that the flow velocity at which flutter occurs decreases. In supersonic flow, the elastic plate deflections increase from one bay to the next bay and this must be considered. For a finite square panel, Dowell [18] found that at high Mach number the flutter frequency is between the first and the second panel natural modal frequencies, while over the subsonic range of Mach number the flutter frequency rapidly falls to zero and the panel diverges rather than flutters.

The literature related to nonlinear studies of plates coupled to flowing fluid is scarce. Nonlinear flutter of rectangular plates was investigated by Dowell [19, 20]. Ellen [21] studied the asymptotic nonlinear stability of simply supported rectangular plates subjected to incompressible flow (on one side only) considering both structural and fluid-dynamic non linearities. The analysis performed by [21] was based on single-mode Galerkin approach and it was shown that fluid-flow nonlinearities introduce a subcritical instability while the stabilizing structural nonlinearities have a dominant effect in controlling the overall nonlinear behavior. Lucey *et al*. [22] examined the dynamics of a finite length plate, mainly in post-divergence regime where coupled-mode flutter may arise. The flow was considered to be inviscid, and the solution of the coupled problem was obtained by boundary-element and finite-difference method.

1.2.2 Shells conveying steady flowing fluid

The effects of internal flow on the stability of circular cylindrical shells have been extensively investigated both theoretically and experimentally by Paidoussis and Denise [23], Weaver and Unny [24] and Paidoussis *et al.* [25, 26]. Chen [27] wrote a comprehensive review on flow-induced of circular cylindrical shells with emphasis on nuclear reactor system components.

Matsuzaki and Fung [28] derived an exact analytic expression for the unsteady fluid pressure acting on the internal walls of a simply-supported circular cylindrical tube of finite length carrying flow. The results were applied to the buckling of a cylinder influenced by an internal flow and to the flutter of a cylinder with such a flow. They also examined the effect of viscous damping. One of their main findings is associated to the fact that buckling load of a cylinder subjected to axial and/or circumferential compression is always decreased by a subsonic internal flow.

Lakis *et al.* [29] presented a hybrid approach combining the finite element method (FEM) and Sanders' shell theory, in order to study the dynamic problem of anisotropic fluid-filled conical shells. In this method, an exact displacement function, derived from Sanders' shell theory, was considered. In a successive study [30], this method was extended by including the influence of flowing fluid on the vibrations of an open cylindrical shell in the absence of fluid pressures and initial tensions. The effects of the presence of internal and/or external fluid on the free vibrations of the shell were investigated. Zhang *et al.* [31] developed a finite element model for studying the vibration of pre-stressed thin cylindrical shells conveying fluid. The method they proposed was based on Sanders' nonlinear theory of thin shells and classical potential flow theory. They found that the frequencies increase as initial axial tensions, internal pressures, and radius-thickness ratios increase, and as flow velocities and length-radius ratios decrease. Their model has been compared with published experimental results proving to be reliable for the dynamic problem of prestressed thin cylindrical shells conveying fluid.

By neglecting the effect of fluid viscosity and considering the potential flow model, nonlinear forced vibrations and stability of shells interacting with fluid flow were investigated by Koval'chuk [32]. He used Donnell's nonlinear theory together with the Galerkin approach and the Krylov-Bogolyubov-Mitropol'skii averaging technique to study the nonlinear vibrations of the shell, neglecting the effect of axisymmetric modes.

Theory and experiments for the dynamic stability of circular cylindrical shells subjected to incompressible subsonic liquid and air flow have been reported by Karagiozis *et al.* [33-36].

The effect of imperfections on the nonlinear stability of shells containing fluid flow has been investigated by Amabili *et al.* [37] by using a refined model. A Lagrangian approach based on (i) Donnell's theory retaining in-plane inertia and (ii) Sanders-Koiter theory was utilized and differently from previous works, the effect of fluid viscosity considered by using the time averaged Navier–Stokes equations. It was shown that asymmetric geometric imperfections with the same number of circumferential waves as the mode associated with instability play a significant role, transforming the pitchfork bifurcation at divergence to a folding (saddle-node) bifurcation. Good agreement was shown with the available experimental results for divergence of aluminium shells conveying water.

The combined effect of geometric imperfections and fluid flow on the nonlinear vibrations and stability of shells has been investigated by del Prado *et al.* [38]. The behavior of the thin-walled shell was modeled by Donnell's nonlinear shallow-shell theory and the shell was assumed to be subjected to a static uniform compressive axial pre-load plus a harmonic axial load. A low-dimensional model was obtained by using the Galerkin method and the numerical solutions were found by using a Runge-Kutta scheme. It was shown that the parametric instability regions, bifurcations and basins of attraction are affected by the initial geometric imperfection and the flow velocity.

1.2.3 Dynamics of pipes, plates and shells under pulsatile flow

A specific type of unsteady flows includes oscillatory and pulsatile flows which occur in many engineering areas, such as the flow in hydraulic and pneumatic and pumping systems or applications of heat transfer. Oscillatory and pulsating flows in branching pipes have been extensively studied by investigators interested in biology. Additionally, a significant number of works can be found in literature concerning oscillatory or pulsatile flows in straight pipes (see for example, Uchida [39], Gerrard and Hughes [40], Hino *et al.* [41], Muto and Nakane [42], Shemer *et al.* [43]).

Chen [44] was the first to have examined the stability of simply supported pipes with a flow velocity with a time dependent harmonic component superimposed on the steady velocity. Since the fluid acceleration associated to the imposed velocity perturbations is neglected in Chen's equation of motion, Paidoussis and Issid [45] re-derived the equation of motion considering the neglected term. The longitudinal acceleration of the fluid was included making this model suitable for studying flow containing harmonic components. Ginsberg [46] derived the general equations of motion for small transverse displacement of a pipe conveying fluid based on the transverse force exerted by the flowing fluid. For the case of a simply supported pipe, the Galerkin method was utilized to obtain the solution. The dynamic instability regions were evaluated and it was shown that they increase with increased amplitude of fluctuation. Paidoussis [47] presented a theoretical analysis of the dynamical behaviour of slender flexible cylinders in axial flow, the velocity of which was perturbed harmonically in time. He found that parametric instabilities are possible for certain ranges of frequencies and amplitudes of the perturbations. These instabilities occur over specific ranges of flow velocities and, in the case of cantilevered cylinders, are associated with only some of the modes of the system. They found that the major instability region starts at a pulsating frequency which is equal to twice the natural frequency of the shell with quiescent water. Bohn and Herrmann [48] investigated the dynamic behavior of articulated pipes conveying fluid with small periodic disturbances. They showed the influence of the magnitude of low rate oscillation on the appearance of parametric and combination resonances. Moreover, they defined an algebraic criterion base on the minimum flow rate amplitude in order to avoid parametric resonance.

Ariaratnam and Namachchivaya [49] performed dynamic stability studies on cylindrical pipes obtaining explicit stability conditions for perturbations of small intensity by using the method of averaging. For large harmonic perturbation they proposed a numerical method based on Floquet theory due to Bolotin to obtain stability boundaries. The effects of flow velocity, dissipative forces, boundary conditions, and virtual mass on the extent of the parametric instability regions were discussed. Lee *et al.* [50] derived more realistic pipe dynamic equations (equations of axial, radial, and transverse vibrations, and equations of fluid momentum and continuity) which described fully coupled fluid-structure interaction mechanisms. They used Newton's Law of motion to derive the equation to address the vibration of pipelines and used the deformable moving control volume concept to derive fluid equations. Their model can be used to solve practical problems encountered in valve and pump operations.

Gorman *et al.* [51] derived the non-linear equation of motion of a flexible pipe conveying unsteady flowing fluid from the continuity and momentum equations of unsteady flow. These equations are fully coupled through equilibrium of contact forces, the normal compatibility of velocity at the fluid pipe interfaces, the conservation of mass, as well as the Poisson and friction coupling. A combination of the finite difference method and the method of characteristics is employed to extract displacements, hydrodynamic pressure, and flow velocities from the equations. A numerical example of a pipeline conveying fluid with a pulsating flow has been illustrated.

For non-steady flow in rectangular conduits, there is a decisive lack of information in the literature. Landau and Lifshits [52] reported the results of a purely harmonic flow giving the periodic solution of oscillating flow between two parallel plates in complex form. Fan and Chao [53] conducted a study on parallel, viscous, incompressible flow through long rectangular ducts when the axial pressure gradient is an arbitrary function of time. They found that under a harmonically oscillating pressure gradient for fast oscillation, there is a flattening of the velocity profile in the core region and the maximum velocity does not occur on the axis but near the wall. Similar characteristics had been experimentally observed by Richardson and Tyler [54] and theoretically investigated by Sexl [55] for flow through circular pipes and Uchida [39] for periodic motion.

The literature on the aspects of dynamic instabilities of shells conveying pulsating fluid is scarce. Kadoli and Ganesan [56] studied the parametric instabilities in composite cylindrical shells containing the flow of a pulsating hot fluid. A coupled fluid structure interaction problem for a pulsating flow of hot water was used along with the time independent geometric stiffness matrix formulated based on the initial stresses due to flow of hot fluid through the composite cylindrical shell.

Kubenko *et al.* [57] studied one-frequency nonlinear oscillations of a shell interacting with flowing fluid and subjected to the action of external periodic loads. The velocity of fluid in the shell could be either constant or contain pulsating terms of small amplitude. He extended the previous works of Koval'chuk [32] and Koval'chuk and Kruk [58], by using the mathematical procedure for the Krylov-Bogolyubov-Mitropol’skii method in studying multi-mode nonlinear free, forced, and parametrically excited vibrations of shells in contact with flowing fluid. Koval’chuk1 and Kruk [59] also studied the postcritical nonlinear vibrations of thin cylindrical orthotropic shells conveying a pulsating fluid. Kubenko *et al.* [60] investigated the vibrations of cylindrical shells interacting with a fluid flow and subjected to external periodic pressure with slowly varying frequency.

1.2.4 Pulsatile flow in blood vessels

The most obvious feature about blood flow in arteries is that it is pulsatile. Morgan and Kiely [61] and Womersley [62] were the first to study the blood flow in arteries based upon the differential equations of liquid flow in a thin-walled elastic tube. Their classical solution of the problem of oscillatory flow in an elastic tube has been successively expanded by Atabek [63], Cox [64], and Ling [65]. Womersley compared theory with experiments [66], considering tethering, branching, and longitudinal variation of the cross-sectional area, and giving particular attention to the computational method. Womersley [67] also developed the equations describing the arterial flow treating the whole arterial tree as being in a steady state oscillation.

The monograph by McDonald [68], whose first edition appeared in 1960, introduced a new approach to study arterial hemodynamics concentrated on pulsatile phenomena. Based on this new approach, any pulse waveform has been considered to have a mean value and fluctuations around this mean expressed as a series of harmonic components. Pressure/flow relationships have been considered to be near linear so that any harmonic component of a pressure wave could be related only to the same harmonic of pressure and flow wave recorded simultaneously.

In the ten years that have elapsed since the publication of McDonald's monograph, there have been very rapid advances in the understanding of the physical performance of the mammalian cardiovascular system based on experiments and mathematical development of the theory as shown in Bergel's monograph [69]. Theoretical consideration of the relationship between pulsatile pressure and flow, vessel wall properties, arterial impedance, reflections, and wave propagation are very deeply covered by McDonald in the second edition of his monograph [70]. Nichols and O'Rourke, both protégés of McDonald, wrote the third, fourth and fifth edition [71] of McDonald's monograph endorsing the same approach on theoretical, physiological, and clinical principles on arterial pulsation resulting from ventricular ejection.

Another remarkable monograph on the mechanics of circulation was written by Pedley [72] who included the prediction of flow patterns and wall shear stresses in arteries, both significant in the genesis of arterial diseases. Another major area of research that he addressed concerns flow in vessels, such as veins, when they undergo collapse (as discussed in Section 1.2.5). The physics of blood flow and the coupling of fluids and solids in the heart, arteries, veins, microcirculation are presented in precise terms of mechanics by Fung in his monograph [73].

In arteries, the pulsating blood flow causes wave propagation in the vessel walls. It is the propagation of the pulse that determines the pressure gradient during the flow at every location of the arterial tree. The interaction between the fluid and the vessel walls depends mostly on the physical-mechanical properties of the arterial tissues and the blood. In particular, the propagation velocity of pulse waves through the arteries is a means of diagnosing atherosclerotic arterial damage and determining the arterial tonus. The arterial pulse wave velocity (PWV) has been shown to be related to the underlying wall stiffness through the Moens-Korteweg [74] equation and has been used in a variety of applications for non-invasive estimation of arterial stiffness [75]. Taylor [76] showed that the presence of reflected waves causes the measured transmission velocity of a harmonic wave to vary greatly with frequency. Using the technique of measuring wave front velocities with a delay line (McDonald [77]), Nichols and McDonald [78] made an extensive study of the wave velocity in the ascending aorta of dogs, showing that phase velocity values, averaged over the first ten harmonics, were in close agreement with the velocity of the wave front. Their results also demonstrated that an increase in mean arterial pressure increases the pulse wave velocity. Recently, pulsatile flow characteristics and wave propagation through elastic tubes have been extensively studied on the macroscale by Zamir [79].

1.2.5 Stability of blood vessels

Any compliant structure runs the danger of collapsing. The dynamics of pliable shells is of direct interest to haemodynamics. Notably, veins and pulmonary passages are considered collapsible tubes [80] meaning that they can exhibit large area changes in response to small changes in transmural pressure [81]. The configuration of the tube and the tract affects the flow, and vice versa. When critical conditions are reached, the flow and the channel wall begin to exhibit self-excited oscillations (flutter). In the last decades, an enormous amount of theoretical and experimental work has been done on the statics and dynamics of pliable shells conveying fluid [82]. Conrad [83] and Katz *et al.* [84] were the first to demonstrate limit-cycle oscillations by using thin rubber tubes in experiments. Since then, great attention has been given to such oscillations because the combination of the flexible channel with the internal flow provides an unexpectedly rich nonlinear system [85]. A physiological example of self-excited oscillations of venae cavae during heart surgery using extracorporeal circulation has been presented by Matsuzaki [86].

Vessel collapse is most readily observed in the veins, but the arteries also collapse when subjected to high external pressure [87], even if they are traditionally considered capable of withstanding large deformations without adverse effects [88]. Recently, Amabili *et al.* [89] investigated the phenomenon of aortic dissection using a shell model. They identified for the first time the nonlinear buckling (collapse) of the aorta as a possible reason for the appearance of high stress regions at the inner layer of the aorta wall that may be responsible for the initiation of dissection. Aortic dissection is a catastrophic cardiovascular disease that occurs with a sudden rupture of the internal layer (tunica intima) of the aortic wall [90, 91]. A geometrically nonlinear model has been used to examine the possibility of buckling with cross-section deformation (i.e. shell-like buckling) of a straight thoracic aortic segment under specific pressure and flow conditions. The most critical combinations of pressure and flow during a heart beating period were considered as possible causes of triggering the buckling phenomenon. Preliminary results indicate that for specific pressure and quasi-steady flow, the collapse of the aorta occurs with considerable deformation. This collapse lasts for a short period of time because the pressure upstream forces the aortic wall back to its original shape.

1.2.6 Vascular surgery: Dacron grafts

In vascular surgery, artificial blood vessels can be modeled as thin-walled shells conveying pulsating flow. Implants are used in various circumstances of vascular maladies requiring replacements of components of the cardiovascular system such as vessel patches for aneurysms. Surgeons perform vascular prosthesis implantation to exclude the compromised arterial portion (afflicted with aneurysm or dissection for instance) from luminal pulsatile blood flow. This may be carried out by providing an artificial blood flow passage via a synthetic conduit. In particular, two techniques - open surgical repair (OSR) and endovascular aneurysm repair (EVAR) - are employed to repair the vessel avoiding rupture. Open surgical repair is a traditional and standard treatment modality based on a well-established procedure to treat patients with a high risk of rupture [92, 93]. In an open repair the surgeon will open the abdominal cavity, clamp the aorta just above and below the aneurysm and then sew a fabric tube or graft made of polyethylene terephthalate (Dacron® or PET) or expanded polytetrafluoroethylene (ePTFE) inside the aneurysm. Both the proximal and distal segments are stitched to healthy tissue.

Large diameter (12-30 mm) vessel replacements with Dacron are the accepted clinical practice [94]. In particular, tightly woven, crimped, and non-supported Dacron fabric prostheses are currently used to replace thoracic and abdominal aorta with high rates of success [95]. Dacron vascular grafts were first implanted by Julian in 1957 and DeBakey 1958 [96]. Early clinical evidence showed that Dacron was the most promising material among the porous woven fabrics tested as arterial prostheses [97]. Abbott [98], in his report addressed to vascular surgeons regarding the evaluation of safety, efficacy, and expected performance of arterial prostheses, identified their most desirable characteristics such as biocompatibility, durability, and porosity. Biomechanical properties, even if not absolutely necessary, are highly desirable. Indeed, prostheses should match the viscoelastic properties of the arteries to which they are to be anastomosed. This property of the central blood vessels, known as compliance, is responsible for the efficient propagation of the pressure pulse to the peripheral vessels. With pulsatile blood flow, the compliant aorta acts as an elastic reservoir, absorbing energy during systole and releasing it during diastole. When a pressure wave encounters a discontinuity in geometry or elastic properties, for example at an anastomosis between a graft and an artery, it will be partially reflected with a reduction in the energy transmitted along the vessel. As current synthetic grafts are significantly stiffer than host vessels, substantial energy losses may occur through the graft [99].

Currently available textile vascular implants are not significantly different from those introduced six decades ago. Their structural geometry is analogous to traditional textile structures rather than to that of an arterial vessel. This difference is highlighted when late clinical complications arising from behavioural mismatch at the artery-implant anastomosis [100]. Indeed, arteries behave as distensible cylindrical conduits whilst the non-compliant nature of Dacron grafts increases the risk of thrombosis and is known to reduce graft patency [101]. Very little is known about the dynamic behavior of vascular prostheses that can cause unwanted hemodynamic effects leading to their failure.

1.3 Theoretical Background

In this section some of the basics of the dynamics of structures, fluids, and coupled systems are briefly reviewed. The Lagrange equations of motions used for studying the dynamical behavior of fluid-structure interaction systems are presented. The fundamentals of nonlinear dynamics, stability, bifurcation analysis, and modern computational tools are also introduced. Finally, key concepts used throughout the thesis are defined here.

1.3.1 Periodic nonlinear vibrations: softening and hardening systems

One main feature in non-linear systems is the resonant frequency dependence on the vibration amplitude. For very small amplitudes, the resonance peak coincides with the natural frequency of the linear approximation. However, for larger amplitudes, the resonance frequency decreases with amplitude for softening systems and increases with amplitude for hardening systems [102].

An equation that exhibits an enormous range of well-known nonlinear behaviours and that is commonly used as an archetype in nonlinear dynamics is the Duffing equation [103]. This equation is a nonlinear second order differential equation that represents forced mass-spring systems with viscous damping, where the restoring force of the spring is nonlinear and it is given by

$$m\ddot{x}+c\dot{x}+k_1x+k_2x^2+k_3x^3=f(t), \tag{1.1}$$

where m is the mass, c is the viscous damping coefficient, k_1 is the linear spring stiffness, k_2 is the quadratic, k_3 is the cubic stiffness, x is the vibration amplitude and $f(t)$ is the time-dependent force excitation. Eq. (1.1) can be rewritten in the form

$$\ddot{x}+2\zeta\omega\dot{x}+\omega^2x+\left(k_2/m\right)x^2+\left(k_3/m\right)x^3=f(t)/m, \tag{1.2}$$

where ζ is the modal damping ratio and ω is the natural circular frequency of the linearized system.

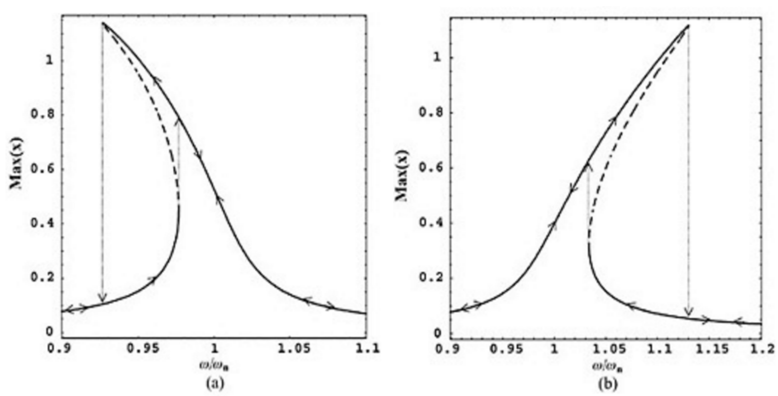

Fig. 1.1. Frequency-response curve of forced damped Duffing equation (a) softening, (b) hardening nonlinear response; stable solution (continuous line), unstable solution (dashed line), ↑ or ↓ jumps (Amabili [4]).

The response of such a system to harmonic excitation with a forcing frequency Ω in the neighbourhood of its linear resonance ω is shown in the frequency-response curves Fig. 1.1(a-b). The softening behavior of the system Fig. 1.1(a) is given by (i) the quadratic nonlinearity, (ii) the cubic nonlinearity with negative sign of k_3, (iii) the combination of quadratic and cubic nonlinearities. The hardening nonlinear behavior is given by the prevalence of the cubic nonlinearities with positive sign of k_3 on the quadratic one. A hysteretic effect arises for increasing and decreasing the excitation frequency and a limit point with vertical tangent is identified in both curves. A jump phenomenon is detected in correspondence to that point causing a switch from one branch to another of the stable solution.

The nonlinear behavior of plates usually presents a hardening response while shells experience a softening type response for small amplitude vibrations and a hardening type for large amplitude vibrations (Fig. 1.2).

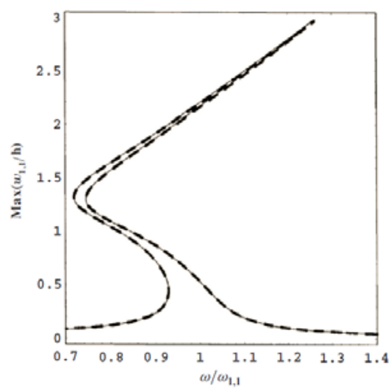

Fig. 1.2. Amplitude of the response of a spherical shell versus the excitation frequency (Amabili [4]).

In nonlinear systems, other periodic solutions can be detected, such as subharmonic and superharmonic vibrations. In the case of sub-harmonic resonance, the driving force with frequency Ω produces a response at frequencies Ω/N, where N is an integer, and thus the resonance occurs at integer multiples of the fundamental frequency ω. Similarly, there will be resonance responses at low frequencies ω/N. This is the so-called super-harmonic resonance.

1.3.2 Numerical integration of Lagrange equations of motion

Partial differential equations governing systems dynamics can be discretized into an N second-order ordinary differential equations in the following form

$$\ddot{x}_j + 2\zeta_j\omega_j\dot{x}_j + \sum_{i=1}^{N} z_{j,i}x_i + \sum_{i=1}^{N}\sum_{k=1}^{N} z_{j,i,k}x_i x_k + \sum_{i=1}^{N}\sum_{k=1}^{N}\sum_{l=1}^{N} z_{j,i,k,l}x_i x_k x_l = f_i\cos(\Omega t) \qquad for \;\; j = 1,\ldots,N \tag{1.3}$$

where N is an integer representing the number of degrees of freedom used to discretize the original partial differential equations, $z_{j,i}$ are the coefficients associated to the linear stiffness terms, $z_{j,i,k}$ and $z_{j,i,k,l}$ are the coefficients associated with the quadratic and cubic stiffness terms, respectively. The two most common methods used to obtain the discretized equation (Eq. (1.3)) of continuous systems are the Galerkin method and an energy approach leading to the Lagrange equations of motion. In both cases, the displacements are expanded using a sum of trial functions that satisfy the geometrical boundary conditions. However, while the Galerkin method discretizes the partial differential equations, the Lagrangian equations of motion are directly obtained minimizing the energy of the system. For a system of N degrees of freedom and generalized coordinates q_j, the Lagrange equations are

$$\frac{\mathrm{d}}{\mathrm{d}t}\left(\frac{\partial T}{\partial \dot{q}_j}\right)-\frac{\partial T}{\partial q_j}+\frac{\partial U}{\partial q_j}=Q_j \qquad j=1...N, \tag{1.4}$$

where T is the kinetic energy of the system, U is the potential energy of the system. The generalized forces Q are given by

$$Q_j=-\frac{\partial F}{\partial \dot{q}_j}+\frac{\partial W}{\partial q_j}, \tag{1.5}$$

Where F represents the Rayleigh's dissipation function that takes into account nonconservative damping forces proportional to generalized velocities and W is the virtual work done by external forces.

The generic j-th equation of motion can be recast into the following two first-order equations

$$\begin{cases} \dot{x}_j = y_j \\ \dot{y}_j=-2\zeta_j\omega_j y_j-\sum_{i=1}^{N} z_{j,i}x_i-\sum_{i=1}^{N}\sum_{k=1}^{N} z_{j,i,k}x_i x_k-\sum_{i=1}^{N}\sum_{k=1}^{N}\sum_{l=1}^{N} z_{j,i,k,l}x_i x_k x_l+f_j\cos(\omega t) \end{cases} \tag{1.6}$$

for $j = 1,..,N$. The resulting ordinary differential equation (ODE) system can be studied via two numerical schemes: direct numerical integration or continuation and bifurcation analysis.

Direct numerical integration of the equations of motion by using Gear's backward differentiation-formula (BDF), such as DIVPAG routine of the IMSL library [104], is suitable for dynamical systems with relatively high dimensions that exhibit different timescales in the response.

In nonlinear vibrations, turning and bifurcation points may exist, leading to region with multiple solutions. Continuation methods [105] are able to pass turning points, to discover bifurcation points, and to follow secondary branches. Once a fixed point is found (e.g. trivial undeformed configuration of the unloaded system) a parameter can be varied (such as pressure, flow velocity and forcing frequency) until a bifurcation occurs, representing the instability point. A specific algorithm for branch switching must be used at the bifurcation point to investigate the post-critical behavior.

A well-known software for continuation and bifurcation analysis of nonlinear ODE is AUTO [106]. This software is also capable of branch switching by using the pseudo-arclength continuation and collocation methods. Continuation methods allow following the solution path, with the advantage that unstable solutions can also be obtained.

1.3.3 Nonlinear and internal resonances

The resonant solutions of nonlinear systems under harmonic excitation can be expected near the excitation circular frequencies Ω satisfying the following relations [107]

$$k\,\Omega = \sum_{j=1}^{N} m_j \omega_{n,j} \qquad j = 1,..,N \qquad k = 1, 2,.. \quad m_j = 0, \pm 1, \pm 2,.. \tag{1.7}$$

where ω is the circular frequency of the harmonic excitation and ω_j, j=1,..,N are the natural circular frequencies of the discretized system. Specific cases of equation (1.7) are

- Subharmonic resonance $\Omega = n_j \omega_j$ with $n_j = 2, 3, \ldots$;
- Superharmonic resonance $\Omega = \omega_j / k$ with $k = 2, 3, \ldots$;
- Sub-superharmonic resonance $\Omega = m_j \omega_j / k$ with $m_j / k \neq 1, 2, \ldots$ and $k / m_j \neq 1, 2, \ldots$.

In nonlinear systems, the commensurability of natural frequencies results in coupling of the normal modes and may cause their strong interaction. As a result, energy is interchanged between these modes, and multi-frequency, multi-modal response occurs. This phenomenon is known as internal resonance. As a consequence, complex responses with additional resonance peaks are observed for nonlinear systems in the presence of internal resonances. When the ratio of two or several natural frequencies is close to the ratio of small integers

$$\omega_i / \omega_j = n \qquad n = 1, 2, .., \quad i, j = 1, ..., N \tag{1.8}$$

Internal resonances are detected. Typical cases are:

- one-to-one (1:1) internal resonance characteristic of doubly symmetric systems which have pairs of modes with the same natural frequency (e.g. circular shells, circular and square plates);
- one-to-two (1:2) internal resonance $\omega_i \approx 2\, \omega_j$;
- multiple internal resonances involving more than two modes.

Internal resonances can also give additional branches in the solution through bifurcations when the excitation circular frequency Ω approaches ω_i. This typically happens in axial-symmetric systems (e.g. circular cylindrical shells and circular plates) where two orthogonal modes exist with the same frequency (1:1 internal resonance). These modes are called companion modes and they are angularly described by $\sin(n\theta)$ and $\cos(n\theta)$, respectively, n being the circumferential wavenumber. Even if an external excitation drives only one of these two modes, close to the resonance a pitchfork bifurcation of the periodic solution arises, and a traveling wave periodic solution appears, given by a combination of both the two modes with a specific phase shift. Even if the companion mode is not directly excited, an energy transfer appears in correspondence to this bifurcated branch between the driven and the companion mode because of the internal resonance.

1.3.4 Bifurcations theory

Varying one or more parameters in a nonlinear system can affect the type of long-time dynamical motion and bifurcations can arise. The study of these changes in nonlinear dynamics due to the variation of control parameters μ is referred to as bifurcation theory. The value of the parameters giving a qualitative or topological change in the nature of motion or equilibrium is called critical μ_{cri} or bifurcation value [4]. For certain values of μ, even a slight change might set off drastic changes in behavior, for example: (i) the number and/or stability or singular points could change, (ii) a periodic orbit could appear/disappear or gain/loose stability, and (iii) a chaotic attractor could appear/disappear or change character. A general dynamic system described by a set of n autonomous first-order differential equations can be written as

$$\dot{x} = F\left(x,\mu\right); \quad x = x(t) \in R^n, \ \mu \in R^k, \tag{1.9}$$

where F is an n-vector of generally nonlinear functions, x is an n-vector of state variables, and μ is a k-vector of control or bifurcation parameters. An equilibrium point x_0 has to satisfy the fixed point condition $F(x_0,\mu)=0$. By definition, a singular point x_0 is hyperbolic if the Jacobian at that point $J\left(x_0,\mu\right) = \left.\frac{\partial F}{\partial x}\right|_{x=x_0}$ has no eigenvalues with zero real part. However, if there is at least one eigenvalue with zero real part, the equilibrium point is called a nonhyperbolic or degenerate fixed point and stability is determined by the nonlinear terms. The nature of motion about the equilibrium point (stability of the solution) is determined by the sign of the real part of the eigenvalues of the Jacobian matrix. The motion about the equilibrium point is unstable if one eigenvalue has a positive real part. The linear stability analysis can be performed in order to determine the bifurcation value μ_{cri} for which the fixed points become nonhyperbolic [108]. If at the stationary state x_0 the bifurcation parameter is μ_{cri}, then (x_0, μ_{cri}) is a bifurcation point.

Bifurcations are classified into continuous, discontinuous and catastrophic, depending on how the state of the system varies when the control parameter is gradually varied through its critical value. A dangerous bifurcation, when the response jumps to a remote chaotic attractor, is also known as "blue sky catastrophe". Usually reversing the control parameter, a bounded response remains on the path of the new attractor resulting in hysteresis.

Bifurcations of autonomous systems can be static, when solution branches are constituted by fixed point, or dynamic. A particular type of static bifurcation where the system transitions from one fixed point to three fixed points is called pitchfork bifurcation. Based on the stability of the branches, the pitchfork bifurcation can be supercritical or subcritical: in the first case a stable solution turns unstable, and two stable branches emerge on each side of the unstable solution (Fig. 1.3). In the case of a subcritical bifurcation, an unstable solution gains stability and two branches of unstable solution emerge. An example of dynamic bifurcation is the Hopf bifurcation where a branch of fixed points meets a branch of periodic solutions.

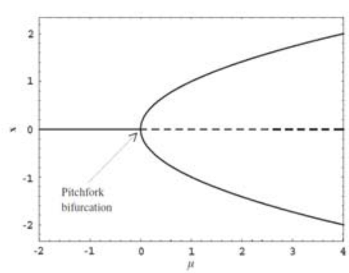

Fig. 1.3. Supercritical pitchfork bifurcation (Amabili [4]).

The stability of periodic solutions can be studied using the Floquet theory that represents the analysis of linear systems of differential equations with periodic coefficients. Floquet multipliers are analogous to the eigenvalues of Jacobian matrices of equilibrium points. A set of linear, homogeneous, time periodic differential equations is given by [109]

$$\frac{\mathrm{d}x}{\mathrm{d}t} = A(t)x\,, \tag{1.10}$$

where $A(t)$ is an $n\times n$ matrix with minimal period T. The general solution of Eq. (1.10) can be written as the sum of n periodic functions multiplied by exponential terms

$$x(t) = \sum_{i}^{n} c_i\, e^{\beta_i t} p_i\left(t\right), \tag{1.11}$$

where c_i are constant values that depend on the initial conditions, $p_i(t)$ are n-vector functions periodic with period T, and β_i are the Floquet exponents. Floquet multipliers λ_i are associated to Floquet exponents by the relationship $\lambda_i = e^{\beta_i T}$. The Floquet exponents determine the long term behavior of the system. The periodic solution is stable if all Floquet exponents have negative real parts or, equivalently, all Floquet multipliers $|\lambda_i| < 1$ for $i = 1, .., N$. If any Floquet multiplier has modulus greater than one, the periodic solution is unstable.

When a Floquet multiplier becomes equal to -1, a period-doubling bifurcation appears. This bifurcation refers to periodic vibrations in which the period doubles. The periodic solution that existed before the bifurcation value μ_{cri} with oscillation frequency Ω, continues as an unstable solution. In the case of supercritical bifurcation, a new stable branch is created at the bifurcation with oscillation frequency $\Omega/2$ (double period). In the case of a subcritical bifurcation, a branch of unstable period-doubled solution is destroyed at the bifurcation point and the bifurcation is considered catastrophic since the behavior of the system for $\mu > \mu_{cri}$ can be dangerous or explosive [110]. This scenario represents one of the routes to chaos.

When two complex conjugate Floquet multipliers reach unit modulus, a so-called Neimark-Sacker bifurcation appears. It is also named secondary Hopf since it is the Hopf bifurcation of a periodic solution. In case of a supercritical bifurcation, a new branch of stable quasiperiodic solution appears. In case of a subcritical bifurcation, a branch of unstable quasi-periodic solution is destroyed causing a catastrophic bifurcation. Circular cylindrical shells in nonlinear vibrations regime can experience supercritical Neimark-Sacker bifurcations [4].

1.3.5 Chaotic vibrations

Chaos is the *random-like* behavior of a deterministic system; in other words, the system is deterministic, nevertheless it behaves as if it were random but with a most significant difference. Indeed, while random systems are not restrained to specific state-space regions, the chaotic ones are. It is a type of motion that is sensitive to changes in initial conditions. In particular, the slightest change in the initial conditions results in trajectories that diverge exponentially at any given time sufficiently long afterwards.

Only nonlinear system - with a number of dimensions equal or bigger than three - can exhibit chaos. An excellent engineering treatment of the theory of chaos is given by Moon [111] which clearly defines the peculiar characteristics of chaotic vibrations:

- high sensitivity to small changes in the initial conditions;
- broad frequency spectrum of vibration even if the excitation is simply harmonic;
- fractal nature of the oscillation in the phase space, denoting a strange attractor that can be observed in the Poincaré maps;
- the existence of a particular route to chaos showing an increasing complexity of regular motion (e.g. period doubling bifurcations);

- the possibility of transient chaotic motion when the motion looks chaotic during a finite time and it appears to move on the strange attractor, but eventually settles into a periodic or quasiperiodic motion.

1.3.6 Poincaré maps

A Poincaré map is a collection of points obtained by collecting and storing a single point of the trajectory of the system in phase space for each cycle of motion, with consistent timing [111].

For a periodically forced, second-order nonlinear oscillator, a Poincaré map can be obtained by stroboscopically observing the position $x(t)$ and velocity $\dot{x}(t)$ at a particular phase of the forcing function (H. Poincaré, 1854-1912). A Poincaré section converts a continuous time evolution into a discrete time mapping. The motion will appear as a sequence of dots in the phase plane $(x(t), \dot{x}(t))$. A two-dimensional map is given by the plot of time-sampled sequence of data $x_n = x(t_n)$ and $y_n = \dot{x}(t_n)$ in the phase-plane and it is represented by the following difference equations

$$x_{n+1} = f\left(x_n, y_n\right), \qquad y_{n+1} = g\left(x_n, y_n\right). \tag{1.12}$$

When there is a driving motion of period T and the sampling rule is taken as $t_n = nT + t_0$, with n an integer, the two-dimensional map is called a Poincaré map [111]. Thus, if the motion is periodic (period-1), the Poincaré map consists of a single point in a $(x, \dot{x})$-plot; it consists of two points for period-2 motion. In general, being the excitation frequency Ω, the plot of a subharmonic motion with circular frequency $\Omega t / n$ consists of n points in the Poincaré map.

If the vibration motion consists of two or more incommensurate frequencies (quasi-periodic motion), the points on the corresponding Poincaré section will densely fill up a closed smooth curve [112].

A cloud of points in some defined pattern would suggest chaotic motion. In this case, a fractal nature phase space plots is often revealed, whereby a small such region, when blown up, displays a similar character at a more microscopic scale. The appearance of fractal-like patterns in Poincaré maps is a strong indicator of chaotic motion [111].

1.3.7 Fluid-Structure Interaction

In many fluid-structure interaction problems, the flow velocity vector is characterized by a dominant steady flow-velocity component while all the others are perturbations induced by structural motion. Thus,

$$\mathbf{V} = U\mathbf{i} + \mathbf{v}, \tag{1.13}$$

where $\mathbf{V}$ is the flow velocity vector, U is the undisturbed flow velocity in the x-direction, $\mathbf{i}$ is the unitary vector in the x-direction and $\|\mathbf{v}\| \ll U$. These flows are defined as linearized flows since, under these hypotheses, the Navier-Stokes equations can be linearized and simplified considerably. Uniform flows approaching a body can often be treated as irrotational and isentropic and the fluid can be considered inviscid. In these cases, the flow field may be expressed as

$$\mathbf{V} = \nabla\Psi = U\mathbf{i} + \nabla\Phi, \tag{1.14}$$

where Ψ is a scalar potential function made of two components: one due to the mean flow, and one to the velocity potential Φ associated with the flow perturbations caused by the presence of the body. This unsteady perturbation potential Φ satisfies the Laplace equation

$$\nabla^2\Phi = 0. \tag{1.15}$$

Hence, Euler's equations simplify to the well-known unsteady Bernoulli equation

$$\frac{\partial\Phi}{\partial t} + \frac{1}{2}V^2 + \frac{P}{\rho_F} = 0, \tag{1.16}$$

where $V^2 = \nabla\Psi \cdot \nabla\Psi$, ρ_F is the fluid density. The pressure P is measured relative to the stagnation pressure of the free stream and it is defined by

$$P = P_0 + p, \tag{1.17}$$

where P_0 corresponds to the steady potential flow and p is the perturbation component. It is assumed that the disturbances causing the deformations for the structures are sufficiently small for their squares and higher-order terms to be ignored [5].

The fluid domain is assumed to be a cylinder of infinite extent, inside a periodically supported shell of infinite length as shown in Fig. 1.4. Thus, the velocity potential can be obtained using the method of separation of variables [4]. The distance between the periodical supports is L and R is the radius of the shell. As a result, the shell radial displacement, the velocity potential and the perturbation pressure are periodic functions with main period $2L$.

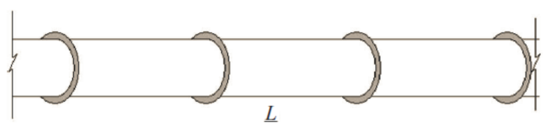

Fig. 1.4. Infinite circular cylindrical shell periodically supported at distance L (Karagiozis *et al.* [36]).

A cylindrical coordinate system x, r, θ is introduced with the origin at one shell end. The radial displacement of the shell middle surface is indicated with w taken positive outward. The condition of impermeability of the surface of the shell may be expressed mathematically as

$$\left.\frac{\partial \Phi}{\partial r}\right|_{r=R} = \left(\frac{\partial w}{\partial t} + U \frac{\partial w}{\partial x} \right), \tag{1.18}$$

that must be satisfied at any point of the contact surface between the shell and the fluid if no cavitation occurs. By using the method of separation of variables, Φ has the following form

$$\Phi(x,r,\theta,t) = \sum_{m=1}^{M} \sum_{n=0}^{N} \phi_m(x)\, \psi_{m,n}(r) \cos(n\theta)\, f_{m,n}(t). \tag{1.19}$$

Substituting Eq. (1.19) in Eq. (1.15) and applying the condition that the velocity potential must be regular at $r = 0$, it is found that

$$\phi_m(x) = \sin(m\pi x/L) \quad \text{and} \quad \psi_{m,n}(r) = \mathrm{I}_n(m\pi x/L), \tag{1.20}$$

where I_n is the modified Bessel functions of the order n of the first kind. Eq. (1.18) is satisfied by assuming

$$\Phi = \sum_{m=1}^{M}\sum_{n=0}^{N} \frac{L}{m\pi} \frac{\mathrm{I}_n(m\,\pi\,r/L)}{\mathrm{I}_n^{'}(m\,\pi\,R/L)} \left(\frac{\partial w_{m,n}}{\partial t} + U\frac{\partial w_{m,n}}{\partial x} \right), \tag{1.21}$$

where $\mathrm{I}_n^{'}$ is the derivative of I_n with respect to the argument.

By linearizing equation (1.16), it may be shown that the perturbation pressure p can be written as

$$p = -\rho_F \left(\frac{\partial \Phi}{\partial t} + U\frac{\partial \Phi}{\partial x} \right)\bigg|_{r=R}. \tag{1.22}$$

Hence, the perturbation pressure at the shell wall, using Eq. (1.21) and Eq. (1.22), is given by

$$p = -\rho_F \sum_{m=1}^{M}\sum_{n=0}^{N} \frac{L}{m\pi} \frac{\mathrm{I}_n(m\,\pi\,R/L)}{\mathrm{I}_n^{'}(m\,\pi\,R/L)} \left(\frac{\partial}{\partial t} + U\frac{\partial}{\partial x} \right)^2 w_{m,n}. \tag{1.23}$$

Neglecting the effect of the fluid weight on the structure, Green's theorem is used to obtain the total energy E_{TF} associated to the flow as follows [4]

$$E_{TF} = \frac{1}{2}\rho_F \iiint_{\Gamma} \mathbf{v}\cdot\mathbf{v}\,\mathrm{d}\Gamma = \frac{1}{2}\rho_F \iiint_{\Gamma} \nabla\Psi\cdot\nabla\Psi\,\mathrm{d}\Gamma = \frac{1}{2}\rho_F \iint_{S} \left(\Psi\frac{\partial \Psi}{\partial n} \right)\bigg|_{S} \mathrm{d}S, \tag{1.24}$$

where Γ and S are the cylindrical fluid volume inside the shell (delimited by the length L) and the boundary surface of this volume, respectively, and n is the coordinate along the normal to the boundary, taken positive outward. The mean flow potential Ux does not give any time-varying contribution to the energy of the flowing fluid, so it does not affect the shell dynamics. The total energy of the fluid can be reduced to

$$E_F = T_F + E_G - V_F, \tag{1.25}$$

where T_F represents the kinetic energy of the fluid, E_G is the so-called gyroscopic energy and V_F is the potential energy of the fluid.

The kinetic energy T_F of the fluid associated to the perturbation potential is given by

$$T_F = \frac{1}{2}\rho_F \sum_{m=1}^{M}\sum_{n=0}^{N}\int_0^{2\pi}\int_0^{L}\frac{L}{m\pi}\frac{\mathrm{I}_n(m\,\pi\,R/L)}{\mathrm{I}_n^{'}(m\,\pi\,R/L)}\dot{w}_{m,n}^2\;\mathrm{d}x\,R\,\mathrm{d}\vartheta. \tag{1.26}$$

The potential-like energy V_F can be expressed as

$$V_F = -\frac{1}{2}\rho_F \sum_{m=1}^{M}\sum_{n=0}^{N}\int_0^{2\pi}\int_0^{L}\frac{L}{m\pi}\frac{\mathrm{I}_n(m\,\pi\,R/L)}{\mathrm{I}_n^{'}(m\,\pi\,R/L)}U^2\left(\frac{\partial w_{m,n}}{\partial x}\right)^2\mathrm{d}x\,R\,\mathrm{d}\vartheta, \tag{1.27}$$

where V_F is negative meaning that the stiffness of the system decreases with U.

The gyroscopic energy E_G associated with the perturbation potential is

$$E_G = \frac{1}{2}\rho_F \sum_{m=1}^{M}\sum_{n=0}^{N}\sum_{l=1}^{M}\sum_{k=0}^{N}\int_0^{2\pi}\int_0^{L}\frac{U\,L}{m\,\pi}\frac{\mathrm{I}_n(m\,\pi\,R/L)}{\mathrm{I}_n^{'}(m\,\pi\,R/L)}\left(\dot{w}_{m,n}\frac{\partial w_{l,k}}{\partial x}+\dot{w}_{l,k}\frac{\partial w_{m,n}}{\partial x}\right)\mathrm{d}\,x\,R\,\mathrm{d}\,\theta. \tag{1.28}$$

In the case of harmonic vibrations, the gyroscopic energy E_G is globally zero proving that the system is conservative and no energy is dissipated. Indeed, the fluid was assumed inviscid. The gyroscopic energy represents the energy transferred among modes associated with the gyroscopic effect and it is related to the inertial Coriolis force. It is characteristic of systems with mass transport, called gyroscopic systems.

The Lagrange equations of motion (Eq. (1.4)) for fluid-structure interaction systems are written as

$$\frac{d}{dt}\left[\frac{\partial\left(T_S+T_F+E_G\right)}{\partial \dot{q}_j}\right]-\frac{\partial\left(T_S+T_F+E_G\right)}{\partial q_j}+\frac{\partial\left(U_S+V_F\right)}{\partial q_j}=Q_j, \quad j=1...N, \tag{1.29}$$

where T_S and U_S represent the kinetic and potential energy of the structure, respectively. In the present case, $\partial T_S/\partial q_j = \partial T_F/\partial q_j = 0$. The gyroscopic energy E_G can be written in the following vectorial form

$$E_G = \frac{1}{2}\mathbf{q}^{\mathrm{T}}\mathbf{G}\,\dot{\mathbf{q}}, \tag{1.30}$$

where the gyroscopic matrix $\mathbf{G}$ is an antisymmetric matrix with zeros on the diagonal. Applying this antisymmetric characteristic, the following expression is obtained

$$\frac{d}{dt}\left(\frac{\partial E_G}{\partial \dot{q}_j}\right) = -\frac{\partial E_G}{\partial q_j}. \tag{1.31}$$

Thus, the final expression of the Lagrange equations of motion can be written as

$$\frac{d}{dt}\left[\frac{\partial\left(T_S+T_F\right)}{\partial\dot{q}_j}\right]-2\frac{\partial E_G}{\partial q_j}+\frac{\partial\left(U_S+V_F\right)}{\partial q_j}=Q_j,\quad j=1...N. \tag{1.32}$$

Chapter 2

Plates in axial pulsatile flow

In this chapter, the stability and nonlinear vibrations of plates in axial confined pulsatile flow are studied. The system investigated consists of an infinitely wide and infinitely long thin plate periodically supported made of isotropic homogeneous material subjected to an inviscid axial pulsatile flow on its upper surface. The mathematical model has been developed by the author and it is outlined here. The fluid is set in motion by an oscillatory pressure gradient. The nonlinear Lagrange equations of motion of the coupled system are obtained and solved by using a code based on the pseudo-arc-length continuation and collocation scheme. Different system parameters, such as flow velocity, pulsation amplitude, pulsation frequency, and channel pressurization are investigated and corresponding findings are compared to the case with steady flow. The paper "Nonlinear vibrations of plates in axial pulsating flow" published in the Journal of Fluids and Structures [1] is presented in this chapter.

NONLINEAR VIBRATIONS OF PLATES IN AXIAL PULSATING FLOW

E. Tubaldi, M. Amabili, F. Alijani

Department of Mechanical Engineering, McGill University

Abstract

A theoretical approach is presented to study nonlinear vibrations of thin infinitely long and wide rectangular plates subjected to pulsatile axial inviscid flow. The flow is set in motion by a pulsating pressure gradient. The case of plates in axial uniform flow under the action of constant transmural pressure is also addressed for different flow velocities. The plate is assumed to be periodically simply supported in both in-plane directions with immovable edges and the flow channel is bounded by a rigid wall. In this way the system under study is a finite rectangular plate with conditions on the fluid and the plate boundaries coming from the periodicity of the infinite system. The equations of motion are obtained based on the von Kármán nonlinear plate theory retaining in-plane inertia via Lagrangian approach. The fluid model is based on the potential flow theory. The resulting Lagrange equations of motion of the coupled system contain quadratic and cubic nonlinear terms and are studied by using a code based on the pseudo-arc-length continuation and collocation scheme. The effect of different system parameters such as flow velocity, pulsation amplitude, pulsation frequency and channel pressurization on the stability of the plate and its geometrically nonlinear response to pulsating flow are fully discussed. It has been found that the presence of positive transmural uniform pressure and small pulsation frequency would destroy the pitchfork bifurcation (divergence) that flat plates exhibit when subjected to uniform flow. Moreover, in case of zero uniform transmural pressure numerical results show a

hardening type behavior for the entire flow velocity range when the pulsation frequency is spanned in the neighbourhood of the plate's fundamental frequency. On the contrary, a softening type behavior is presented when a uniform transmural pressure is introduced.

2.1 Introduction

Thin plates immersed in flowing fluids are widely used in many engineering applications where small plate thickness is required to minimize the weight, improve thermal exchange and to reduce costs. Under these conditions, the plate dynamic response to different sorts of excitations, such as fluid excitations, becomes of great interest.

The dynamic interaction between an elastic plate and a surrounding fluid medium has been deeply investigated in literature. In particular, the literature related to linear vibrations of plates coupled to fluid is quite extensive (see e.g. Lamb [8], Kwak [9], Kwak and Kim [10], Fu and Price [11], Amabili and Kwak [12]). The majority of the older approximate analytical methods that are used to study flow-induced vibrations are based on the assumption attributed to Lamb [8] that the vibration modes of the structure in contact with still fluid (wet modes) are the same as those *in vacuo* (dry modes). In fact, it is based on this assumption that the so-called non-dimensional added virtual mass incremental factors (NAVMI) can be used to estimate the natural frequencies of the plate in still fluid from the natural frequencies *in vacuo* as shown by Kwak and Kim [9], and Kwak [10]. Amabili and Kwak [12] removed the simplified assumption of identical wet and dry modes and obtained the mode shapes of the coupled system via Rayleigh-Ritz approach. Theoretical analysis and experimental studies have been carried out on the nonlinear hydroelastic vibrations of a cylindrical shell with an elastic bottom by Chiba (see [13], [113] and [114]). Guo and Paidoussis [14] used Galerkin approach to study the hydroelastic instabilities of parallel assemblies of rectangular plates coupled to flow. They found that divergence and coupled mode flutter may occur for plates with any type of end supports, while single-mode flutter only arises for non-symmetrically supported plates. Tubaldi and Amabili [115] derived the eigenfrequencies and complex modes of an infinite plate periodically supported and coupled to flowing fluid using the Rayleigh-Ritz method. They found that for sufficiently high flow velocities the system becomes statically unstable. Implicit in the authors' analysis was the assumption that the plate deflection was the same between any two successive supports in the flow direction, aside from a phase change (change in sign) between two successive supports and the next set of supports, i.e. from one “bay” to the next. Indeed, for the low speed case treated by the authors, the instability is divergence at low speeds (rather than flutter which occurs at supersonic speeds) and the divergence instability is dominated by a single structural mode. In a successive study, Tubaldi *et al.* [116] studied the nonlinear vibrations of such system. They found that in the case of flat plates, bifurcation diagrams with respect to the flow velocity present a static loss of stability due to a pitchfork bifurcation. When geometric imperfections are taken into account, the pitchfork bifurcation disappears and the system presents a continuous post-buckling configuration. A hardening type nonlinearity was found for the entire flow velocity range explored in the case of flat plate. Conversely, an initial softening behavior turning to strong hardening for large vibration amplitudes was obtained for imperfect plates.

The literature related to nonlinear studies of plates coupled to flowing fluid is scarce. Nonlinear flutter of rectangular plates was investigated by Dowell [19, 20]. Ellen [21] studied the asymptotic nonlinear stability of simply supported rectangular plates subjected to incompressible flow (on one side only) considering both structural and fluid-dynamic nonlinearities. The analysis was based on single-mode Galerkin approach and it was shown that fluid-flow nonlinearities introduce a subcritical instability while the stabilizing structural nonlinearities have a dominant effect in controlling the overall nonlinear behavior. Lucey *et al.* [22] examined the dynamics of a finite length plate, mainly in post-divergence regime where coupled-mode flutter may arise. The flow was considered to be inviscid and the solution of the coupled problem was obtained by boundary-element and finite-difference method.

The unsteady interaction between a simple elastic plate and a mean flow has a number of interesting features such as the existence of negative-energy waves (NEWs). Indeed by introducing the concept of modal wave energy, Landahl [117] and Benjamin [118, 119] showed that over a range of frequencies, neutral modes with negative wave energy exist (also named class A waves by Benjamin). In particular, Landahl [117] explained the seemingly paradoxical result that damping destabilizes class A waves by studying the flutter of an infinite panel in incompressible potential flow. It was shown that these waves are associated with a decrease of the total kinetic and elastic energy of the fluid and the wall, so that any dissipation of energy in the wall will only increase the wave. It was also found that the Kelvin-Helmholtz type of instability will occur when the effective stiffness of the panel is too low to withstand the pressure forces induced on the wall. Using the same concept of modal wave energy, Peake [120] studied the nonlinear stability of plates for heavy fluid loading considering both plate and fluid nonlinearities analytically. Also in this case it was found that the instability may arise if the destabilizing force due to the fluid loading exceeds the restoring stiffness of the plate.

Unsteady flow-induced vibrations often occur in many engineering areas, for example, the flow in hydraulic and pneumatic and pumping systems or applications of heat transfer as well as biological systems. A specific type of unsteady flows includes oscillatory and pulsatile flows, which are prevalent in many biological, industrial and natural systems (due to pump and valve operations in pipeline systems and even in human circulation). Oscillatory and pulsating flows in branching pipes have been extensively studied by investigators concerned especially in biology. Additionally, a number of work have been reported in the literature concerning oscillatory or pulsatile flows in straight pipes (see for example Uchida [39], Gerrard and Hughes [40], Hino *et al.* [41], Muto and Nakane [42], Shemer *et al.* [43], Kerczek and Davis [121], Schneck and Ostrach [122], Elad *et al.* [123]).

Pioneering studies related to dynamic instability of pipes conveying fluctuating fluid were from Chen [27] followed by Ginsberg [46], Paidoussis [47] and Paidoussis and Issid [45]. Ginseberg [46] derived the general equations of motion for small transverse displacement of a pipe conveying fluid based on the transverse force exerted by the flowing fluid. For the case of a simply supported pipe, the Galerkin method was utilized to obtain the solution. The dynamic instability regions were evaluated and it was shown that the region of dynamic instability increases with increased amplitude of fluctuations. Paidoussis [47] presented a theoretical analysis of the dynamical behaviour of flexible cylinders in axial flow, the velocity of which is perturbed harmonically in time. He found that parametric instabilities are possible for certain ranges of frequencies and amplitudes of the perturbations. These instabilities occur over specific ranges of flow velocities, and in the case of cantilevered cylinders are associated with only some of the modes of the system. Paidoussis and Issid [45] derived the equation of motion of a flexible pipe conveying fluid by taking into account the effects of external pressurization, external tension and the longitudinal acceleration of the fluid. Their numerical model could be utilized when flow contains harmonic components. Unsteady flow characteristics and wave propagation through elastic tubes have also been studied on the macroscale by Womersley [62] and Zamir [124]. Womersley [62] was one of the first to experimentally study pulsatile flow and performed his studies on the femoral artery of a dog. In these studies, the velocity profiles, viscous drag, and Reynolds number were calculated from the pressure gradient. It was the pressure gradient that was used to determine the flow characteristics indirectly. Since then, much work has been performed on the flow stability and transition to turbulence of oscillatory and pulsatile flow both experimentally and numerically (see [125-129]). Numerous experimental investigations were focused on fundamental studies of fully developed periodic pipe flows with sinousoidally varying pressure gradients (or flow rates). Low speed (laminar) pulsating flows were studied in order to analyze the flows through small pipes or in the blood circulation systems. Berguer *et al.* [130] developed a numerical model to analyze both laminar and turbulent pulsatile flows in aortic aneurysm models using physiological resting and exercise waveforms. They also compared hemodynamic stresses for non-Newtonian and Newtonian flows. The decreased stresses generated as a sequence of non-Newtonian effect were significant in realistic flow conditions. Recently, Khanafer *et al.* [131] numerically analyzed pulsatile turbulent flow, using simulated physiological rest and exercise waveforms, in axisymmetric-rigid aortic aneurism models. Khanafer *et al*. [132] also represented the first computational study to analyze turbulent pulsatile flow within compliant walls of an aneurysm and to determine realistic aneurysm wall stress values. The literature on the aspects of dynamic instabilities of composite shells conveying pulsating fluid is very much scarce. Kadoli and Ganesan [56] studied the parametric instabilities in composite cylindrical shells containing a pulsating hot fluid flow. A coupled fluid-structure interaction problem for a pulsating flow of hot water was used along with the time independent geometric stiffness matrix formulated based on the initial stresses due to flow of hot fluid through the composite cylindrical shell. They found that the major instability region starts at a pulsating frequency which is equal to twice the natural frequency of the shell with quiescent water.

The present study aims to extend the recent work of Tubaldi *et al.* [116] by studying nonlinear vibrations and stability of thin rectangular plates with immovable edges coupled to axial pulsatile flow. The case of plates in axial uniform flow under the action of constant transmural pressure is also addressed for different flow velocities. Lagrange equations of motion are derived for the case of unsteady flow velocity. The effect of different system parameters such as flow velocity, pulsation amplitude, pulsation frequency, and channel pressurization on the stability of the plate and its geometrically nonlinear response to pulsating flow are fully discussed. The frequency-amplitude responses presented here show a hardening type behavior in case of zero uniform transmural pressure. On the other hand, in the presence of uniform transmural pressure a softening type behavior is found.

2.2 Mathematical formulation

The system under investigation, shown in Fig. 2.1 consists of an infinitely wide and infinitely long thin plate made of isotropic homogeneous material subjected to an inviscid axial pulsatile flow on its upper surface. The plate is taken in the proximity of a rigid wall as shown in the Fig. 2.1. A right-handed rectangular Cartesian reference system $(O;x,y,z)$ is considered with the x,y plane coinciding with the middle surface of the plate in its initial undeformed configuration and the z axis normal to it. The distance between the plate and the rigid wall is denoted by H and U is the undisturbed flow velocity of the axial pulsatile flow.

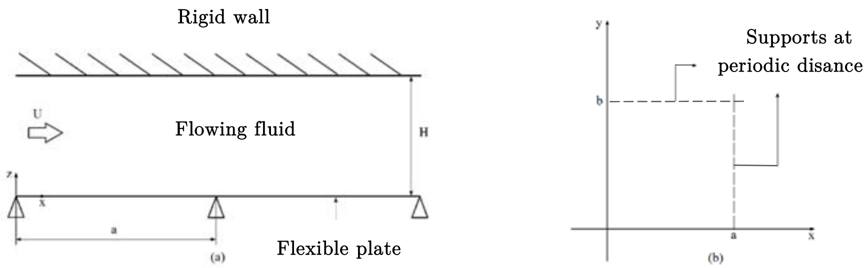

Fig. 2.1. Schematic of the plate in axial flow with rigid wall.

The plate is assumed to be simply supported with immovable edges and therefore the following boundary conditions should be satisfied at each edge (see [4])

$$u = v = w = 0 \text{ and } M_x = 0 \text{ at } x = 0, a, \tag{2.1a-d}$$

$$u = v = w = 0 \text{ and } M_y = 0 \text{ at } y = 0, b. \tag{2.2a-d}$$

where M_x and M_y are the bending moments of the plate per unit length and can be obtained as follows:

$$M_x = -\frac{Eh^3}{12(1-\nu^2)}\left(\frac{\partial^2 w}{\partial x^2} + \nu\frac{\partial^2 w}{\partial y^2}\right), \tag{2.3a}$$

$$M_y = -\frac{Eh^3}{12(1-\nu^2)}\left(\frac{\partial^2 w}{\partial y^2} + \nu\frac{\partial^2 w}{\partial x^2}\right), \tag{2.3b}$$

and u, v, w are the displacements of a point on the middle surface of the plate in x, y and z directions, respectively. The discretization of the system can be obtained by using the Rayleigh-Ritz method. A base of plate displacements satisfying the geometric boundary conditions must be chosen to discretize the system. For this purpose, the following expressions are considered as expansions of the displacements u, v and w

$$u(x, y, t) = \sum_{r=1}^{R}\sum_{s=1}^{S} u_{rs}(t)\sin\left(\frac{r\pi x}{a}\right)\sin\left(\frac{s\pi y}{b}\right), \tag{2.4a}$$

$$v(x, y, t) = \sum_{c=1}^{C}\sum_{d=1}^{D} v_{c,2d}(t)\sin\left(\frac{c\pi x}{a}\right)\sin\left(\frac{2d\pi y}{b}\right), \tag{2.4b}$$

$$w(x, y, t) = \sum_{m=1}^{M}\sum_{n=1}^{N} w_{mn}(t)\sin\left(\frac{m\pi x}{a}\right)\sin\left(\frac{n\pi y}{b}\right), \tag{2.4c}$$

where m and n are the numbers of half-waves in x and y directions, respectively. The generalized coordinates $u_{rs}(t), v_{c,2d}(t), w_{mn}(t)$ are unknown time-depending functions. M and N indicate the number of terms in the expansion of w and are usually smaller than the number of terms in the expansions of u (denoted by r and s) and v (denoted by c and d). It should be noted that the expansion of the displacement v includes only even number of half-waves in y-direction due to the symmetry of the system and since the fluid flow is just in x-direction. It can be noticed that the bending moment (Eq. (2.3a-b)) at the edges of a periodically simply supported plate is zero if the supports are equally spaced. Indeed, applying the expansion of the transversal displacement w (Eq. (2.4c)) to the expression of the bending moments (Eq. (2.3a-b)) in x- and y-direction, the sinus terms of the expansion vanish on the edges as shown in the boundary conditions in Eq. (2.1d) and Eq. (2.2d).

2.2.1 Elastic strain energy and kinetic energy of the plate

The elastic strain energy U_p, assuming plane stress hypothesis, i.e. neglecting shear deformation, is given by

$$U_p = \frac{1}{2}\int_0^a\int_0^b\int_{-h/2}^{h/2}\left(\sigma_{xx}\varepsilon_{xx} + \sigma_{yy}\varepsilon_{yy} + \tau_{xy}\gamma_{xy}\right)\mathrm{d}x\,\mathrm{d}y\,\mathrm{d}z \tag{2.5}$$

where h is the plate thickness; a, b are the in-plane dimensions in x and y directions, respectively and $\sigma_{xx}, \sigma_{yy}, \tau_{xy}$ are the Kirchhoff stresses for homogeneous isotropic materials. Moreover, $\varepsilon_{xx}, \varepsilon_{yy}, \gamma_{xy}$ are the Green's strains that can be written as follows

$$\varepsilon_{xx} = \varepsilon_{x,0} - z\frac{\partial^2 w}{\partial x^2}\ , \qquad \varepsilon_{yy} = \varepsilon_{y,0} - z\frac{\partial^2 w}{\partial y^2}\ , \qquad \gamma_{xy} = \gamma_{xy,0} - 2z\frac{\partial^2 w}{\partial x \partial y}\ , \tag{2.6a-c}$$

where $\varepsilon_{x,0}, \varepsilon_{y,0}, \gamma_{xy,0}$ are the middle surface strains and they have the following expressions according to the von Kármán nonlinear plate theory

$$\varepsilon_{x,0} = \frac{\partial u}{\partial x} + \frac{1}{2}\left(\frac{\partial w}{\partial x}\right)^2, \quad \varepsilon_{y,0} = \frac{\partial v}{\partial y} + \frac{1}{2}\left(\frac{\partial w}{\partial y}\right)^2, \quad \gamma_{xy,0} = \frac{\partial u}{\partial y} + \frac{\partial v}{\partial x} + \frac{\partial w}{\partial x}\frac{\partial w}{\partial y}. \tag{2.7a-c}$$

The kinetic energy T_p of the plate, neglecting rotary inertia, is given by

$$T_p = \frac{1}{2}\rho_s h \int_0^a \int_0^b \left(\dot{u}^2 + \dot{v}^2 + \dot{w}^2\right) \mathrm{d}x\, \mathrm{d}y \ , \tag{2.8}$$

where ρ_s is the mass density of the plate.

2.2.2 Plate-flow interaction

The fluid is assumed to be inviscid and incompressible, and the flow to be irrotational. Hence, the fluid-structure interaction can be described by the linear potential flow theory. By introducing the scalar potential function Ψ, the velocity vector of the fluid $\mathbf{V}$ may be written as

$$\mathbf{V} = \nabla\Psi. \tag{2.9}$$

The potential Ψ is expressed as:

$$\Psi = Ux + \Phi, \tag{2.10}$$

where the first component is due to the mean flow associated with the undisturbed flow velocity U and the second one is the unsteady perturbation potential Φ associated with the plate motion.

The potential of the perturbation velocity satisfies the Laplace equation:

$$\nabla^2\Phi = 0. \tag{2.11}$$

The boundary conditions representing impermeability condition and no cavitation at the plate and at the wall are:

$$\left.\frac{\partial\Phi}{\partial z}\right|_{z=0} = \dot{w} + U\frac{\partial w}{\partial x}, \tag{2.12a}$$

$$\left.\frac{\partial\Phi}{\partial z}\right|_{z=H} = 0. \tag{2.12b}$$

Performing the Galerkin technique [115] showed that the perturbation potential can be obtained as follows:

$$\Phi(x,y,z,t) = \sum_{r=1}^{\tilde{R}}\sum_{s=1}^{\tilde{S}}\left[\sin\left(\frac{r\pi x}{a}\right)\sin\left(\frac{s\pi y}{b}\right)m_{rs}(z)k_{rs}(t)\right], \tag{2.13}$$

where the coefficient k_{rs} is defined as

$$k_{rs}(t)=\left[\dot{w}_{rs}(t)+\frac{2U\pi}{a}\sum_{p=1}^{M}\left(\beta_{pr}\,p w_{ps}(t)\right)\right], \tag{2.14}$$

in which

$$\beta_{pr}=\begin{cases}0 & \text{if } p=r \text{ or if both } p \text{ and } r \text{ are even or odd}\\ \dfrac{-2r+(p+r)(-1)^{r-p}-(p-r)^{r+p}}{2\pi(p^2-r^2)} & \text{otherwise}\end{cases} \tag{2.15}$$

$$m_{rs}(z)=\frac{e^{\alpha_{rs}z}+e^{\alpha_{rs}(2H-z)}}{(1-e^{2\alpha_{rs}H})\alpha_{rs}},\qquad \alpha_{rs}=\sqrt{\left(\frac{r\pi}{a}\right)^2+\left(\frac{s\pi}{b}\right)^2}. \tag{2.16a-b}$$

2.2.3 Flow energy

Neglecting gravity, the total energy E_{tf} associated with the inviscid and incompressible flow can be obtained as follows:

$$E_{tf}=\frac{1}{2}\rho_f\int_{\tilde{V}}\nabla\Psi\cdot\nabla\Psi\,\mathrm{d}V, \tag{2.17}$$

where $\tilde{V}$ is the fluid volume.

Tubaldi and Amabili [115] found that the total energy of the fluid can be reduced to

$$E_f=-\frac{1}{2}\rho_f\int_0^a\int_0^b\left(\dot{w}+U\frac{\partial w}{\partial x}\right)\Phi(x,y,0,t)\,\mathrm{d}x\,\mathrm{d}y, \tag{2.18}$$

where E_f is the energy associated with the perturbation potential and it has the following form

$$\begin{aligned}E_f=-\frac{1}{2}\rho_f\Bigg\{&\frac{ab}{4}\sum_{m=1}^{M}\sum_{n=1}^{N}\dot{w}_{mn}^2 m_{mn}(0)+\frac{b\pi U}{2}\sum_{m=1}^{M}\sum_{n=1}^{N}\sum_{p=1}^{M}\dot{w}_{mn}w_{pn}m_{mn}(0)p\beta_{pm}\\&+\frac{b\pi U}{2}\sum_{m=1}^{M}\sum_{n=1}^{N}\sum_{r=1}^{M}\dot{w}_{rn}w_{mn}m_{mn}(0)m\beta_{mr}+\frac{b\pi^2U^2}{a}\sum_{m=1}^{M}\sum_{n=1}^{N}\sum_{r=1}^{M}\sum_{p=1}^{M}w_{rn}w_{pn}m_{mn}(0)rp\beta_{rm}\beta_{pm}\Bigg\}.\end{aligned} \tag{2.19}$$

Indeed, the energy E_f can conveniently be divided into three terms

$$E_f=T_f+E_g-V_f, \tag{2.20}$$

where T_f, V_f and E_g are the reference kinetic energy, the potential energy and the gyroscopic energy of the fluid, respectively and they have the following expressions

$$T_f = -\frac{1}{2}\rho_f \frac{ab}{4}\sum_{m=1}^{M}\sum_{n=1}^{N}\dot{w}_{mn}^2 m_{mn}(0), \tag{2.21a}$$

$$E_g = -\frac{1}{2}\rho_f \left\{ \frac{b\pi U}{2}\sum_{m=1}^{M}\sum_{n=1}^{N}\sum_{p=1}^{M}\dot{w}_{mn} w_{pn} m_{mn}(0) p\beta_{pm} + \frac{b\pi U}{2}\sum_{m=1}^{M}\sum_{n=1}^{N}\sum_{r=1}^{M}\dot{w}_{rn} w_{mn} m_{mn}(0) m\beta_{mr} \right\}, \tag{2.21b}$$

$$V_f = \frac{1}{2}\rho_f \frac{b\pi^2 U^2}{a}\sum_{m=1}^{M}\sum_{n=1}^{N}\sum_{r=1}^{M}\sum_{p=1}^{M} w_{rn} w_{pn} m_{mn}(0) rp\beta_{rm}\beta_{pm}. \tag{2.21c}$$

The gyroscopic energy, Eq. (2.21b), represents the energy transferred among modes associated with the gyroscopic effect and it is related to the inertial Coriolis force. When increasing the flow velocity, the modes are changed from the well-known “in-phase” (i.e. with all points of the plate moving in-phase or anti-phase and fixed nodal lines) mode shapes of simply supported plates to complex mode shapes where points are moving with phase differences and nodal lines are no more fixed. For small flow velocities, the real part of the mode, which has the same shape of the natural mode of the plate for zero flow velocity, is predominant. On the contrary for large flow velocities, the imaginary part, which usually has the shape of two longitudinal half-waves for the first mode, becomes more significant as a consequence of the gyroscopic effect of the flowing fluid.

Eq. (2.21a-c) are associated with the perturbation potential and can also be written in the following form

$$2T_f = \dot{\mathbf{w}}^{\mathbf{T}}\mathbf{M_f}\dot{\mathbf{w}}, \tag{2.22a}$$

$$2E_g = \dot{\mathbf{w}}^{\mathbf{T}}\mathbf{C_f}\mathbf{w}, \tag{2.22b}$$

$$2V_f = \mathbf{w}^{\mathbf{T}}\mathbf{K_f}\mathbf{w}, \tag{2.22c}$$

where the vector $\mathbf{w}$ is defined as $\mathbf{w} = \left[w_{11}(t),...w_{1N}(t), w_{21}(t),...w_{2N}(t),...w_{MN}(t)\right]$.

2.2.4 Pulsatile flow

By assuming unsteady inviscid flow in a long duct of arbitrary cross-section, the constant property 1D unsteady Euler equation of the conservation of momentum reduces to

$$\frac{\mathrm{d}p}{\mathrm{d}x} = -\rho_f \frac{\mathrm{d}U}{\mathrm{d}t}, \tag{2.23}$$

where p is the undisturbed pressure field. It is assumed that the flow disturbance due to the plate motion diminishes far from the plate. The change in cross-section is not included in the continuity equation since in the present study it is negligible compared to the channel height H ($w << H$). Hence, the pressure gradient that drives the fluid is expressed by

$$\nabla p = -(\rho_f \dot{U}, 0, 0). \tag{2.24}$$

We write the pressure and flow velocity in Eq. (2.23) as superposition of steady and unsteady (pulsatile in our case) components, using

$$p(x,t) = p_s + \tilde{p}(x,t), \tag{2.25a}$$

$$U(t) = U_s + \tilde{U}(t), \tag{2.25b}$$

where p_s and U_s represent the steady component of the pressure field and the mean flow velocity, respectively. For a parallel flow the unsteady parts become

$$\frac{\mathrm{d}\tilde{p}}{\mathrm{d}x} = -\rho_f \frac{\mathrm{d}\tilde{U}}{\mathrm{d}t}. \tag{2.26}$$

In particular, a flow having a harmonic component superposed on the mean flow velocity U_s is considered flowing through the channel. Hence, the flow velocity $U(t)$ can be written as

$$U(t) = U_s\left(1 + \chi \sin\left(\Omega t\right)\right), \tag{2.27}$$

thus the flow acceleration is

$$\dot{U}(t) = U_s\ \chi\ \Omega \cos\left(\Omega t\right), \tag{2.28}$$

where χ is the ratio between the pulsation amplitude and the steady velocity and Ω is the pulsation frequency.

Substituting Eq. (2.28) in Eq. (2.23) we obtain

$$\frac{\mathrm{d}p}{\mathrm{d}x} = \frac{\mathrm{d}\tilde{p}}{\mathrm{d}x} = -\rho_f \chi U_s\, \Omega \cos(\Omega t). \tag{2.29}$$

Hence, the pressure gradient that drives the fluid is expressed by a harmonic function, as it has to be, because the fluid acceleration is pulsating along the channel.

The pulsatile flow discussed here is ideal since it is assumed that at the same time instant, the flow velocity is the same for all points of the control volume. Indeed, since it is impossible to experimentally reproduce a pulsatile flow without introducing phase lag in the flow velocity in the axial direction, our ideal study is a good approximation of a real case when the phase lag in the velocity between the inlet (*x=0*) and outlet (*x=L*) surface can be considered small.

2.2.5 Lagrange Equations of Motion

As shown in Appendix A, the Lagrange equations of motion for the plate coupled to flowing fluid, knowing that $\partial T_p / \partial q_j = \partial T_f / \partial q_j = 0$, are

$$\frac{\mathrm{d}}{\mathrm{d}t}\left[\frac{\partial\left(T_p + T_f + E_g\right)}{\partial \dot{q}_j}\right] - \frac{\partial E_g}{\partial q_j} + \frac{\partial\left(U_p + V_f\right)}{\partial q_j} = Q_j, \quad j = 1...dof\ , \tag{2.30}$$

where $dof = R \cdot S + M \cdot N + C \cdot D$ is the number of degrees of freedom and $\mathbf{q} = \left[q_1, ..., q_{dof}\right]^T = \left[u_{rs}, v_{c,2d}, w_{mn}\right]^T$, for $r = 1..R$, $s = 1..S$, $m = 1..M$, $n = 1..N$, $c = 1..C$, $d = 1..D$.

It should be noted that the energy of the flowing fluid gives no contribution to the equations related to in-plane displacements.

Under the hypothesis of unsteady flow the gyroscopic term $\frac{\mathrm{d}}{\mathrm{d}t}\left[\frac{\partial E_g}{\partial \dot{w}_{mn}}\right]$ becomes

$$\frac{\mathrm{d}}{\mathrm{d}t}\left[\frac{\partial E_g}{\partial \dot{w}_{mn}}\right] = -\frac{b\dot{U}\pi\rho_f}{4}\sum_{p=1}^{M} w_{pn}\left(m_{pn}(0) + m_{mn}(0)\right) p\beta_{pm} - \frac{\partial E_g}{\partial w_{mn}}, \tag{2.31}$$

hence the Lagrangian equations Eq. (2.30) related to out-of-plane displacement can be rewritten as

$$\frac{\mathrm{d}}{\mathrm{d}t}\left[\frac{\partial\left(T_p + T_f\right)}{\partial \dot{w}_{m,n}}\right] - \frac{b\dot{U}\pi\rho_f}{4}\sum_{p=1}^{M} w_{pn}\left(m_{pn}(0) + m_{mn}(0)\right) p\beta_{pm} - 2\frac{\partial E_g}{\partial w_{mn}} + \frac{\partial\left(U_p + V_f\right)}{\partial w_{mn}} = Q_{mn}\ , \tag{2.32}$$

for $m = 1...M$, $n = 1...N$. The term depending on the flow acceleration $\dot{U}$ did not appear in the formulation of [115] where a steady flow was considered. The generalized forces Q_j can be obtained as follows

$$Q_j = \frac{\partial W}{\partial q_j}, \tag{2.33}$$

where W is the virtual work done by the external forces. In the present study, the virtual work is given by pressure field $p = p_s + \tilde{p}(t)$ and it has the following expression

$$W = -\int_0^a \int_0^b w(x, y, t)\, p(x, t)\, \mathrm{d}x\, \mathrm{d}y = W_I + W_{II}, \tag{2.34}$$

where

$$W_I = -\int_0^a \int_0^b w(x, y, t)\, p_s\, \mathrm{d}x\, \mathrm{d}y, \tag{2.35a}$$

$$W_{II} = -\int_0^a \int_0^b w(x, y, t)\, \tilde{p}(x, t)\, \mathrm{d}x\, \mathrm{d}y. \tag{2.35b}$$

Equation (2.34) is exact for infinitesimal deflection w of the plate, since in the Lagrangian description the pressure changes direction for large deformations in order to be always normal to the plate surface. However, for moderate deflections of thin plates equation (2.34) can be considered a good approximation.

Subsituting Eq. (2.4c) into Eq. (2.35a), the virtual work W_I can be rewritten as

$$W_I = -p_s \frac{4ab}{\pi^2} \sum_{\substack{m=1 \\ m\ \text{odd}}}^{M} \sum_{\substack{n=1 \\ n\ \text{odd}}}^{N} \frac{w_{mn}}{m\, n}. \tag{2.36}$$

Similarly, the virtual work W_{II} can be obtained as

$$W_{II} = -\rho_f\, \dot{U}\, \frac{2a^2 b}{\pi^2} \sum_{m=1}^{M} \sum_{\substack{n=1 \\ n\ \text{odd}}}^{N} \frac{(-1)^m\, w_{mn}}{m\, n}. \tag{2.37}$$

Eq. (2.32) and Eq. (2.33) can be written in the following matrix form:

$$\mathbf{M}\ddot{\mathbf{q}} + (\mathbf{C} + \mathbf{C_f})\dot{\mathbf{q}} + \left[\mathbf{K_p} + \mathbf{K_f} + \mathbf{N_2}(\mathbf{q}) + \mathbf{N_3}(\mathbf{q}, \mathbf{q})\right]\mathbf{q} = \mathbf{f}, \tag{2.38}$$

where $\mathbf{M} = \mathbf{M_p} + \mathbf{M_f}$, $\mathbf{M_p}$ being the mass matrix of the plate and $\mathbf{C}$ the damping matrix which is added to the equations of motion to simulate dissipation. Moreover, $\mathbf{K_p}$ is the linear stiffness matrix of the plate, $\mathbf{N_2}$ gives the quadratic nonlinear stiffness terms, $\mathbf{N_3}$ denotes the cubic nonlinear terms and $\mathbf{f}$ is the vector representing external forces obtained using Eq. (2.33), Eq. (2.36) and Eq. (2.37). The nonlinear terms in such a model are only associated with the structure; however, by changing the inertia of the system, its nonlinear properties consequently change. In order to obtain the equations of motion in a suitable form for numerical implementation, the system (2.38) is multiplied by the inverse of the mass matrix and then is written in the state-space form as follows

$$\begin{cases} \dot{\mathbf{q}} = \mathbf{y} \\ \dot{\mathbf{y}} = -\mathbf{M}^{-1}\left(\mathbf{C} + \mathbf{C_f}\right)\dot{\mathbf{q}} - \left[\mathbf{M}^{-1}\left(\mathbf{K_p} + \mathbf{K_f}\right) + \mathbf{M}^{-1}\mathbf{N}_2(\mathbf{q}) + \mathbf{M}^{-1}\mathbf{N}_3(\mathbf{q},\mathbf{q})\right]\mathbf{q} + \mathbf{M}^{-1}\mathbf{f} \end{cases} \tag{2.39}$$

where $\mathbf{y}$ is the vector of the generalized velocities and the dissipation term $\mathbf{M}^{-1}\mathbf{C}$ is given by

$$\mathbf{M}^{-1}\mathbf{C} = \begin{bmatrix} 2\omega_1\xi_1 & \cdots & 0 \\ 0 & \ddots & 0 \\ 0 & \cdots & 2\omega_j\xi_j \end{bmatrix} \tag{2.40}$$

which is related to the modal damping ratio of each generalized coordinate ξ_j. Matrix (2.40) is assumed to be diagonal in order to use modal damping.

An alternative approach to discuss the fluid-structure interaction between the plate and the fluid flow is presented in Appendix B by applying the Bernoulli's theorem to obtain the relationship between the perturbation pressure p^* and the perturbation potential Φ.

2.3 Numerical results

The equations of motion have been obtained by using the *Mathematica* software by [133] in order to perform analytical surface integrals of trigonometric functions. A non-dimensionalization of variables is performed for computational convenience: the frequencies are divided by the natural radian frequency ω_{11} of the fundamental mode, and the vibration amplitudes are divided by the plate thickness h. The set of nonlinear ordinary differential equations (2.39) has been solved by using the software AUTO by [106] that is capable of continuation of the solution, bifurcation analysis and branch switching by using the pseudo-arclength continuation and collocation method. In particular, the plate response under harmonic excitations has been studied in three steps as follows:

- The bifurcation analysis begins at zero velocity where the initial solution is the trivial undisturbed configuration of the plate by considering the uniform transmural pressure p_s as the first continuation parameter at fixed excitation frequency far from the resonance frequency of the plate, i.e. far away from ω_{mn};
- After reaching the desired uniform transmural pressure p_s amplitude and having the configuration of the plate due to pressurization, the steady flow velocity U_s is used as the bifurcation parameter and it is incremented to reach a desired steady flow velocity (since the χ ratio is kept constant, the pulsation amplitude varies with U_s). In particular, in the case of pulsatile flow, increasing the flow velocity the corresponding oscillatory pressure increases as well;
- Once the desired steady flow velocity U_s is reached, the bifurcation continues by considering the pulsation frequency Ω as the continuation parameter to obtain the frequency-amplitude response of the plate.

The case analyzed here is an infinite plate with continuous simply supported constraints periodically repeated in x and y directions at distance a and b, respectively, and subjected to an inviscid axial pulsatile flow on its upper side. The characteristics of the system are: $a = b = 1$ m, h = 0.002 m, $H = 0.5$ m, Young's modulus $E = 206 \cdot 10^9$ Pa, Poisson ratio $\nu = 0.3$, $\rho_s = 7850$ kg/m^3, and $\rho_f = 10^3$ kg/m^3.

Results have been obtained by using a model with 29 *dof* with the following terms in Eq.(4a-c):

$w_{11}, w_{12}, w_{13}, w_{21}, w_{22}, w_{23}, w_{31}, w_{32}, w_{33}, u_{21}, u_{22}, u_{23}, u_{24}, u_{41}, u_{42}, u_{43}, u_{44}, u_{61}, u_{81}, v_{12}, v_{14}, v_{16}, v_{18}, v_{22}, v_{24}, v_{32}, v_{34}, v_{42}, v_{44}$.

The validity and the accuracy of a model with 29 *dof* has been already discussed in the convergence analysis previously performed in the paper [116] in the case of uniform flow as shown in Appendix C (Fig. C1).

2.3.1 Nonlinear stability analysis

The complete scenario of the static solutions of the plate for different uniform transmural pressures p versus the dimensional uniform flow velocity U $(\chi = 0)$ for the fundamental generalized coordinate w_{11} is presented in Fig. 2.2 obtained via AUTO software by [106]. It can be observed that for $p = 0$ as the flow velocity increases, the plate remains undeformed $(w_{11} = 0)$ until a supercritical pitchfork bifurcation appears at $U = 7.15$ m/s and the system loses stability by static divergence. It is evident that after the pitchfork bifurcation, by increasing further the flow velocity, the amplitude of the response increases continuously. In presence of uniform transmural pressure there is no unstable branch since the pitchfork bifurcation is destroyed and a continuous post-buckling configuration is obtained by increasing the flow velocity. In particular, the pitchfork bifurcation is destroyed by the loss of symmetry of the configuration caused by the presence of the pressure. In general, any term of the equations of motion causing an initial transversal displacement different from zero (such as geometric imperfections or pressurization) destroys the pitchfork bifurcation and this is analogous to the continuous buckling of Euler-Bernoulli straight beams under eccentric axial loads or curved beams.

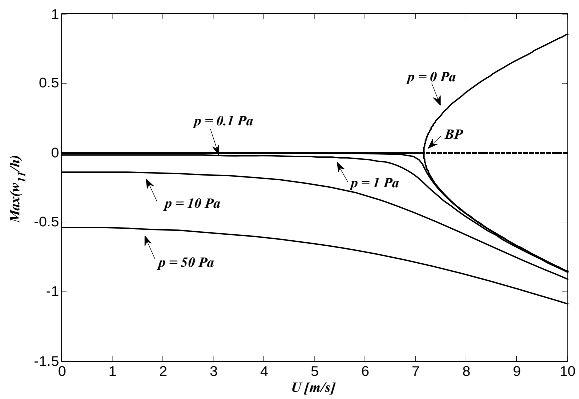

Fig. 2.2. Bifurcation diagram of the non-dimensional amplitude of the maximum of w_{11} versus the dimensional uniform flow velocity $(\chi = 0)$ for the perfect plate for different uniform transmural pressures p; stable solution (continuous line) and unstable solution (dashed line). *BP* stands for pitchfork bifurcation.

The effect of increasing the uniform flow velocity U $(\chi = 0)$ is to deform the plate further in the direction already determined by the transmural pressure static displacement. Moreover, by increasing the uniform transmural pressure p $(\chi = 0)$ the amplitude of the post-buckling solution increases. In order to validate the code, the effect of uniform transmural pressure on the transversal displacement of the plate in quiescent fluid ($U = 0$) is compared to the commercial finite element ABAQUS solution in Fig. 2.3. In particular, the ABAQUS nonlinear analysis takes into account the change in the area of the plate due to the transverse deflection; even though our solution neglects this higher order effect, the two curves presented in Fig. 2.3 show a good agreement in the results. This clarifies that the surface and direction change of the distributed load has a secondary effect in the present case since the deflection is not very large.

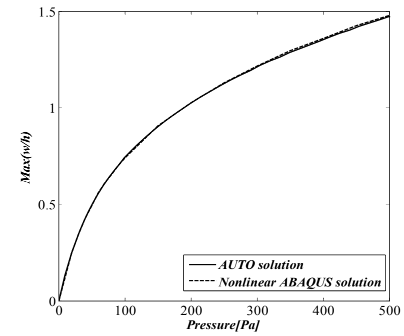

Fig. 2.3. Non-dimensional amplitude of the maximum of displacement w versus the dimensional uniform transmural pressure for the plate in quiescent flow $(U = 0)$; AUTO solution (continuous line) and Nonlinear ABAQUS solution (dashed line).

The effect of the pulsation amplitude of the flow velocity on the sum of the static plus dynamic deflection is shown in Fig. 2.4 where the fundamental generalized coordinate w_{11} is presented by varying the steady velocity U_s for different χ ratios (non-dimensional pulsating frequency).

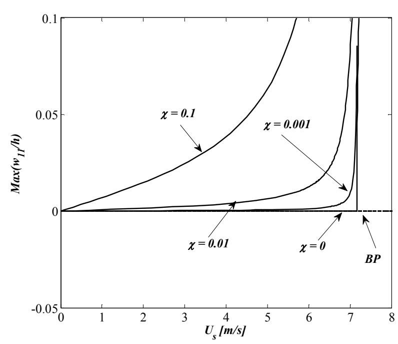

Fig. 2.4. Non-dimensional amplitude of the maximum of w_{11} versus the dimensional pulsatile flow velocity (non-dimensional pulsating frequency $\Omega/\omega_{11} = 0.01$) for the perfect plate for different pulsating amplitude ratios χ at zero transmural uniform pressure $(p_s = 0 \text{ Pa})$; stable solution (continuous line) and unstable solution (dashed line).

Also in the case of pulsatile flow, the pitchfork bifurcation is destroyed in favour of a continuous response (static plus dynamic) because of the oscillatory pressure gradient that drives the flow. Indeed, the symmetry of the system is broken by the presence of a time dependent transmural pressure linearly varying in the axial direction due to pulsation.

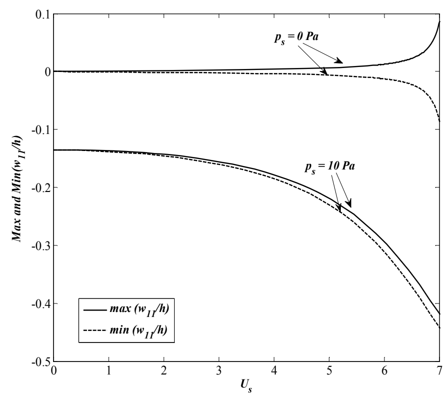

Fig. 2.5. Non-dimensional amplitude of the maximum and minimum of w_{11} versus the dimensional pulsatile flow velocity (non-dimensional pulsating frequency $\Omega/\omega_{11} = 0.01$, pulsation amplitude ratio $\chi = 0.01$) for the perfect plate with and without uniform transmural pressure. Please note that in this figure the ordinate does not start from zero.

As shown in Fig. 2.5, the effect of the uniform transmural pressure $(p_s = 10$ Pa$)$ prevails on the oscillatory pressure $\tilde{p}(t)$ driving a pulsatile flow with the non-dimensional pulsating frequency $\Omega/\omega_{11} = 0.01$ and an amplitude pulsatile ratio $\chi = 0.01$; in fact, the pulsatile ratio is quite small. Indeed, in this case the difference between the minimum and maximum amplitude of the generalized coordinate w_{11} due to pulsation is drastically reduced if compared to the case without transmural uniform pressure $(p_s = 0$ Pa$)$ for large flow velocities. In such a case $(p_s = 10$ Pa$)$, by increasing the amplitude pulsatile ratio χ , the amplitude of the dynamic system response to be added to the static deflection increases as shown in Fig. 2.6.

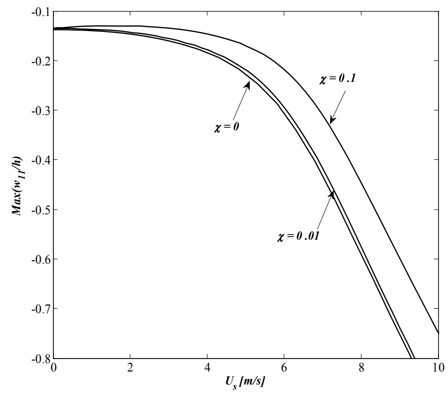

Fig. 2.6. Non-dimensional amplitude of the maximum of w_{11} versus the dimensional pulsatile flow velocity (non-dimensional pulsating frequency $\Omega/\omega_{11} = 0.01$) for the perfect plate for different pulsating amplitude ratios χ for transmural pressure $p_s = 10\,\mathrm{Pa}$. Please note that in this figure the ordinate does not start from zero.

2.3.2 Frequency-amplitude response

The next results represent the frequency-amplitude response of the same rectangular plate in axial pulsatile flow with and without uniform transmural pressure.

The frequency response curves are obtained in the frequency neighborhood of the fundamental complex mode and the pulsatile frequency Ω has been non-dimensionalized by the frequency ω_{11} of the fundamental mode of the plate at zero flow speed and zero transmural pressure.

Fig. 2.7 and Fig. 2.8 show the response of the same plate for different steady flow velocities U_s keeping constant the amplitude pulsatile ratio $\chi = 0.01$ and $\chi = 0.03$, respectively (the modal damping ratio is assumed to be $\xi = 0.05$ for all generalized coordinates; here the harmonic excitation is given just by the flow pulsation non being applied any external force); the maximum amplitude of the generalized coordinate w_{11} for different flow velocities is presented for zero transmural pressure $(p_s = 0\ \mathrm{Pa})$.

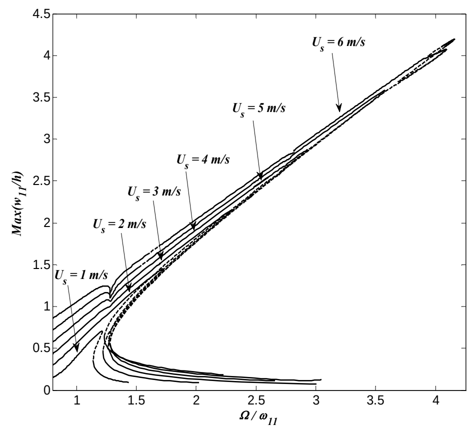

Fig. 2.7. Frequency-response curves for the fundamental generalized coordinate at different flow velocities; $p_s = 0$ Pa , $\chi = 0.01$ and $\xi = 0.05$ for all generalized coordinates; stable solution (continuous line) and unstable solution (dashed line).

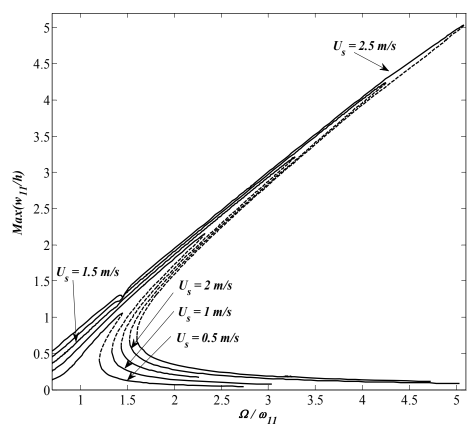

Fig. 2.8. Frequency-response curves for the fundamental generalized coordinate at different flow velocities; $p_s = 0$ Pa , $\chi = 0.03$ and $\xi = 0.05$ for all generalized coordinates; stable solution (continuous line) and unstable solution (dashed line).

It can be seen that the nonlinear behavior of the plate is hardening for the entire flow velocity range explored since the peak of the response moves towards right with respect to the natural frequency ω_{11}. It is shown that the maximum of the response increases by increasing the axial steady flow velocity U_s, which is logical because the pulsating velocity, which is the excitation, is also linearly increasing with U_s. In particular, for U_s = 2 m/s considering an amplitude pulsatile ratio $\chi = 0.03$, the maximum amplitude of the generalized coordinate w_{11} is twice the corresponding amplitude for $\chi = 0.01$. Hence, the effect of increasing the amplitude pulsatile ratio is to increase the amplitude and the nonlinear response of the fundamental generalized coordinate as shown in Fig. 2.9.

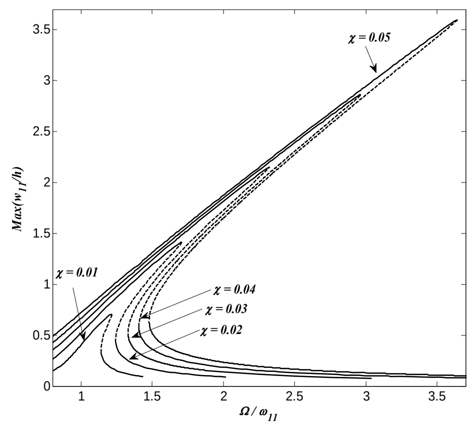

Fig. 2.9. Frequency-response curves for the fundamental generalized coordinate at different flow velocities; $p_s = 0$ Pa, $U_s = 1$ m/s and $\xi = 0.05$ for all generalized coordinates; stable solution (continuous line) and unstable solution (dashed line).

In Fig. 2.7 a sudden drop in the amplitude response is detected around $\Omega / \omega_1 \simeq 1.2$ and it is accentuated by increasing the flow velocity. Looking at the frequency response curves of the other generalized coordinates, we can identify the activation of nonlinear interactions with other modes in this frequency range. The frequency-amplitude response of the generalized coordinates $w_{11}, w_{21}, w_{31}, w_{23}, w_{33}$ (3D representations of the corresponding mode shapes are inserted inside the figures) of the plate for $U_s = 3$ m/s and $U_s = 5$ m/s are shown with an indication of stability in Fig. 2.10. They all present additional peaks and they participate in the response of the plate interacting with the fluid proportionally to their frequency-response amplitudes. Even though the nonlinear behavior presented here is particularly intricate only limit points (folding) and no other types of bifurcations are detected by AUTO. In particular, for $U_s = 5$ m/s the mode w_{21} gives an important quantitative contribution in the plate response around $\Omega / \omega_{11} \simeq 1.2$ and around $\Omega / \omega_{11} \simeq 3.8$ where also the mode w_{23} becomes significant, whereas the participation of modes w_{31} and w_{33} is less important. In nonlinear systems, the commensurability of natural frequencies results in coupling of the normal modes and may cause their strong interaction. As a result, energy is interchanged between these modes, and multifrequency, multi-modal response occurs.

This phenomenon is known as internal resonance. For thin plates, theoretical and experimental studies about internal resonance have been conducted by Yamaki and Chiba [134] and Yamaki *et al.* [135]. Modal interactions due to the nonlinearity may cause large-amplitude response of modes which linear analysis predicts to remain unexcited. In addition, complex responses with additional resonance peaks are often observed for nonlinear systems in the presence of internal resonances.

Internal resonances are detected when the ratio of two or several natural frequencies is closed to the ratio of small integers (see [4]). Modal interactions between modes w_{11}, w_{21}, w_{31} and w_{23} for $U_s = 5$ m/s, at different frequency ranges can be observed.

In order to better investigate the response of the plate in the neighborhood of the modal interaction regions, the time response and the phase space diagrams of the most significant generalized coordinates for the plate at $U_s = 5$ m/s are depicted in Fig. 2.11-Fig. 2.14.

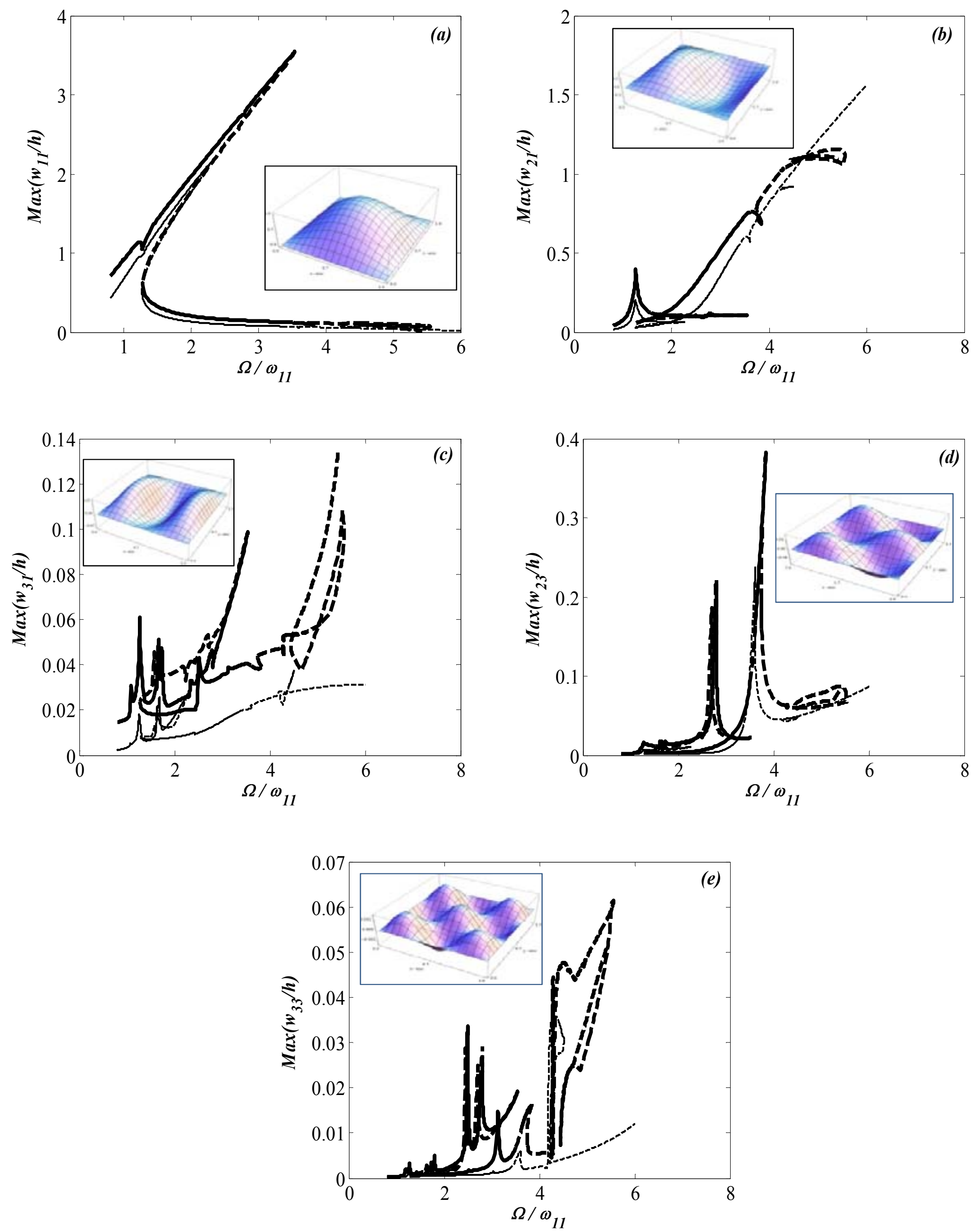

Fig. 2.10. Frequency-response curves and 3D plots of mode shapes; $U_s = 5\,\mathrm{m/s}$ (thick line), $U_s = 3\,\mathrm{m/s}$ (thin line), $p_s = 0\mathrm{Pa}$, $\chi = 0.01$ and $\xi = 0.05$ for all generalized coordinates; *(a)* maximum w_{11}/h, *(b)* maximum w_{21}/h, *(c)* maximum w_{23}/h, *(d)* maximum w_{31}/h, *(e)* maximum w_{33}/h; stable solution (continuous line) and unstable solution (dashed line).

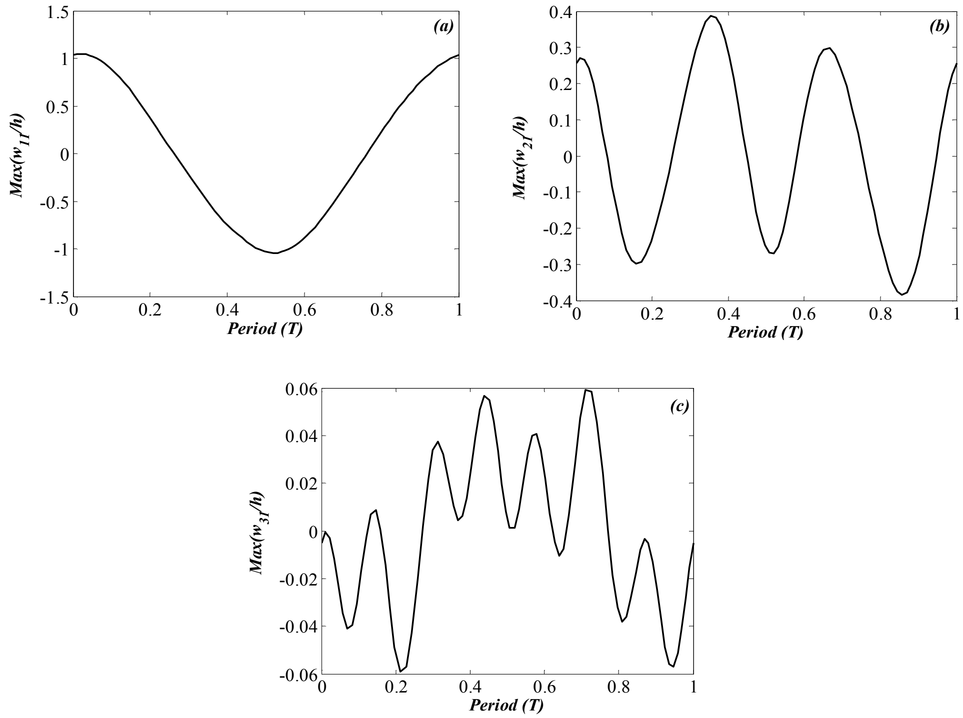

Fig. 2.11. Time response for $\Omega = 1.27\omega_{11}$, $U_s = 5\,\mathrm{m/s}$, $p_s = 0\,\mathrm{Pa}$, $\chi = 0.01$ and $\xi = 0.05$ for the most significant generalized coordinates; *(a)* maximum w_{11}/h, *(b)* maximum w_{21}/h, *(c)* maximum w_{31}/h. Please note that in these figures the ordinate does not start from zero.

In particular, Fig. 2.11 shows the time response at $\Omega/\omega_{11} = 1.27$ and Fig. 2.13 shows the response at $\Omega/\omega_{11} = 3.82$. The corresponding phase-plane diagrams of these generalized coordinates are reported in Fig. 2.12 and Fig. 2.14, respectively.

The loops in the phase plane diagrams are related to higher harmonics. For $\Omega/\omega_{11} = 1.27$, the phase-plane diagram of w_{21} in Fig. 2.12(b) shows three loops (third harmonic) and the phase plane diagram w_{31} shows seven loops (seventh harmonic) in Fig. 2.12(c). Indeed, for $\Omega/\omega_{11} \simeq 1.2$, a 3:1 and 7:1 internal resonance are detected between modes w_{11} and w_{21}, w_{11} and w_{31}, respectively.

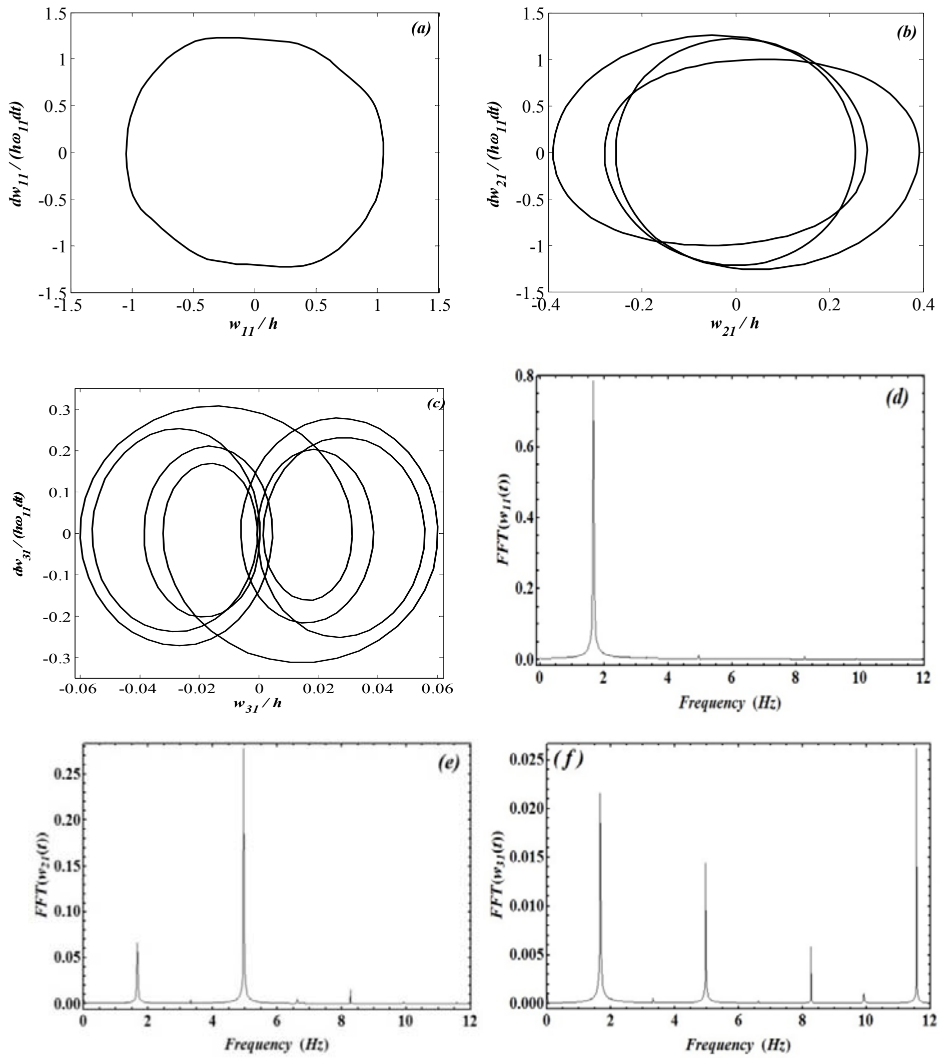

Fig. 2.12. Phase-plane diagrams for $\Omega = 1.27\omega_{11}$, $U_s = 5$ m/s, $p_s = 0$ Pa, $\chi = 0.01$ and $\xi = 0.05$ for the most significant generalized coordinates; *(a)* phase-plane diagram of w_{11}, *(b)* phase-plane diagram of w_{21}, *(c)* phase-plane diagram of w_{31}, *(d)* frequency spectrum of w_{11}, *(e)* frequency spectrum of w_{21}, *(f)* frequency spectrum of w_{31}. Please note that in the phase plane figures the ordinate does not start from zero.

The corresponding frequency spectrum of the most significant generalized coordinates is depicted in Fig. 2.12(d-f). The multiple peaks in Fig. 2.12(d-f) prove the presence of higher order harmonics in the response of modes w_{11}, w_{21} and w_{31}, respectively.

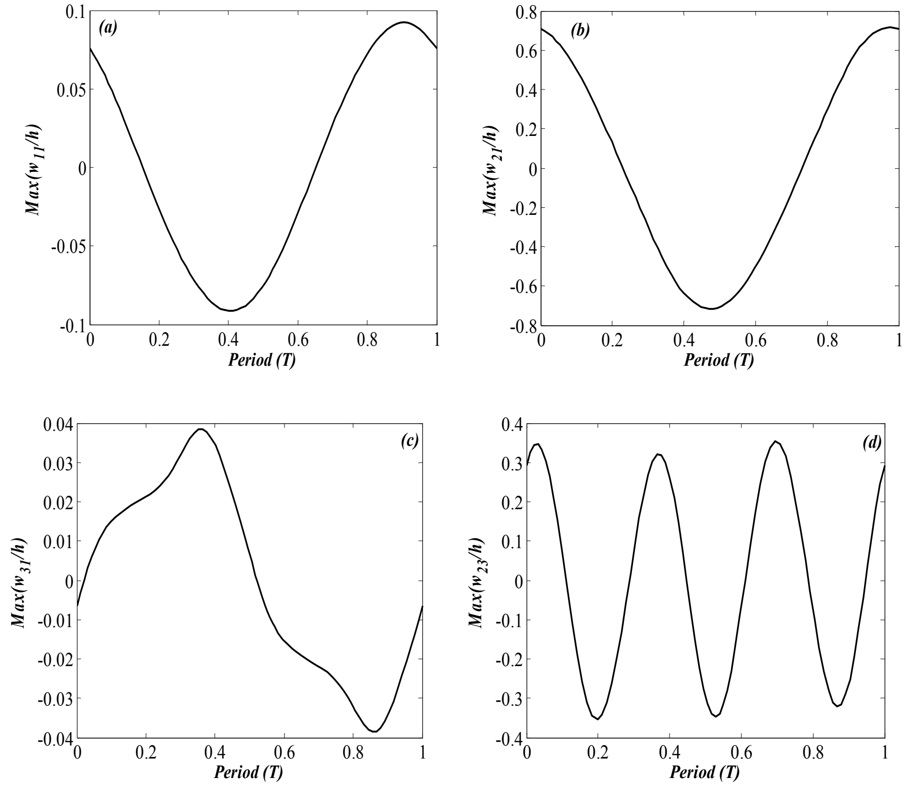

Fig. 2.13. Time response for $\Omega = 3.82\omega_{11}, U_s = 5$ m/s, $p_s = 0$ Pa, $\chi = 0.01$ and $\xi = 0.05$ for the most significant generalized coordinates; *(a)* maximum w_{11}/h, *(b)* maximum w_{21}/h, *(c)* maximum w_{31}/h, *(d)* maximum w_{23}/h. Please note that in these figures the ordinate does not start from zero.

Since the analysis performed here has as unique limit the number of modes used for discretizing the system, a higher order internal resonance can be detected regardless of the original equation of motion with accuracy of only third order; indeed, we are not dealing with a perturbation analysis and the nonlinearities in the stress-strain equations are exact. On the contrary, nonlinear normal modes analysis (especially with perturbation approach) can give inaccurate results for large amplitude vibrations as shown by Amabili and Touzé [136].

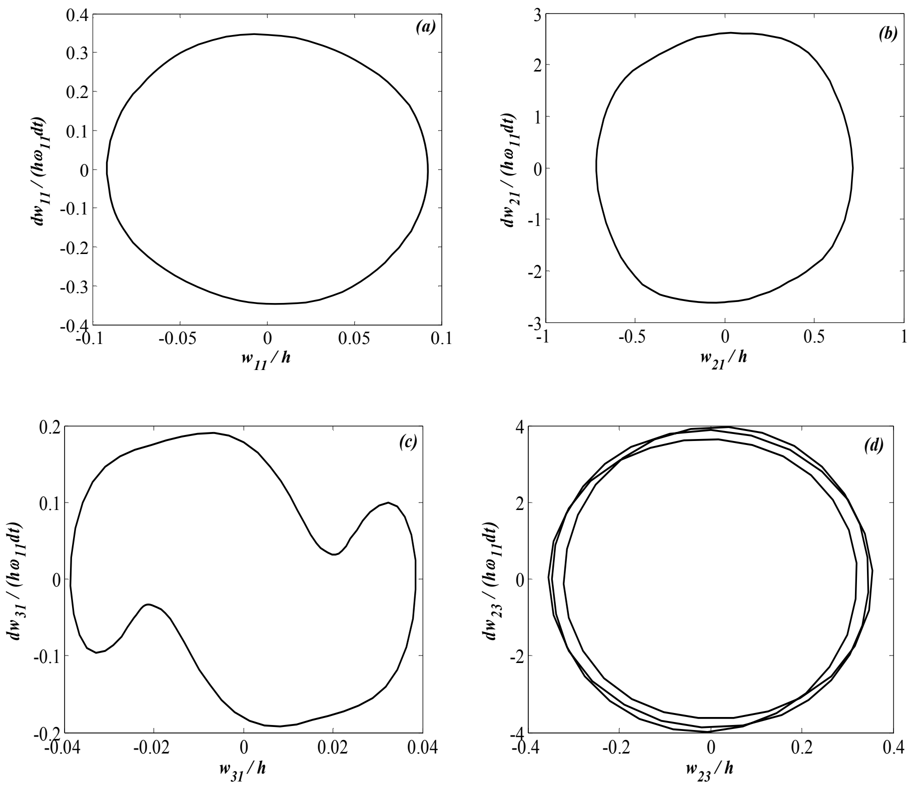

Fig. 2.14. Phase-plane diagrams for $\Omega = 3.82\omega_{11}$, $U_s = 5$ m/s, $p_s = 0$Pa, $\chi = 0.01$ and $\xi = 0.05$ for the most significant generalized coordinates; *(a)* phase-plane diagram of w_{11}, *(b)* phase-plane diagram of w_{21}, *(c)* phase-plane diagram of w_{31}, (*d)* phase-plane diagram of w_{23}. Please note that in these figures the ordinate does not start from zero.

For $\Omega/\omega_{11} = 3.82$, the mode w_{21} participates with the first harmonic (Fig. 2.14(b)), the mode w_{31} (Fig. 2.14(c)) contributes mainly with the second harmonic and the mode w_{23} (Fig. 2.14(d)) with the third harmonic. At $\Omega/\omega_{11} \simeq 3.8$, a 1:1, 2:1, 3:1 internal resonances are found between modes w_{11} and w_{21}, w_{11} and w_{31}, w_{11} and w_{23}, respectively.

The presence of uniform transmural pressure p_s affects the frequency-response relationship of the plate coupled to pulsatile flow. Fig. 2.15 shows linear (i.e. for small vibration amplitude, but calculated from nonlinear equations) frequency-response curves for the plate for different uniform transmural pressure when $\chi = 0.01$, $U_s = 5$ m/s and $\xi = 0.01$.

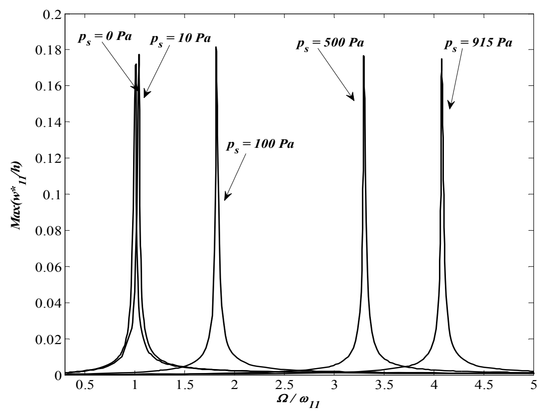

Fig. 2.15. Linear frequency-response curves for the plate for different transmural pressures when $\chi = 0.01$, $U_s = 0.05$ m/s, $\xi = 0.01$. The static displacement due to transmural pressure has been removed from the graph so that only the oscillatory component is presented.

It must be observed that the amplitude w^*_{11}/h presented in Fig. 2.15 is the non-dimensional amplitude of the first generalized coordinate after removing from it the static displacement due to the uniform transmural pressure p_s for zero flow velocity; in this way only the dynamic component of w_{11} is presented. It is shown that for small vibration amplitudes, the resonance frequency of the plate increases with the transmural pressure. In particular, according to Fig. 2.15, the response of the plate for $p_s = 915$ Pa (which gives a static displacement equal to twice the thickness) is about four times the fundamental frequency comparing to the case with zero transmural pressure. Note that in Fig. 2.15 the pulsating frequency is made dimensionless with respect to the fundamental frequency of the plate without uniform transmural pressure.

Fig. 2.16-2.18 present the effect of uniform transmural pressure $p_s = 915\,\mathrm{Pa}$ on the nonlinear response of the fundamental mode for several steady flow velocities U_s keeping constant the amplitude pulsatile ratio $\chi = 0.01$ (Fig. 2.16 and Fig. 2.17) and $\chi = 0.03$ (Fig. 2.18). In both cases, the response of the system has a softening-type behavior since the peak response moves to the left with respect to ω_{11}.

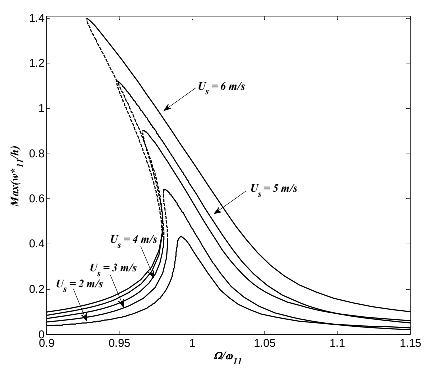

Fig. 2.16. Frequency-response curves for the fundamental generalized coordinate at different flow velocities; $p_s = 915\,\mathrm{Pa}$, $\chi = 0.01$ and $\xi = 0.01$ for all generalized coordinates; stable solution (continuous line) and unstable solution (dashed line).

It is well known that shells usually experience a softening type behavior for small amplitude vibrations and a hardening type behavior for large-amplitude while the nonlinear behavior of plates presents usually a hardening response. In the case discussed here, because of initial pressurization, the plate has become a shallow shell and consequently the nonlinear behavior of the structure has turned from a hardening type to a softening type. By increasing the steady flow velocity U_s, the softening behavior of the system is increased for both amplitude pulsatile ratios investigated here. Also in this case, by increasing the pulsation amplitude of the flow velocity, the amplitude of the response of the fundamental generalized coordinate considerably increases.

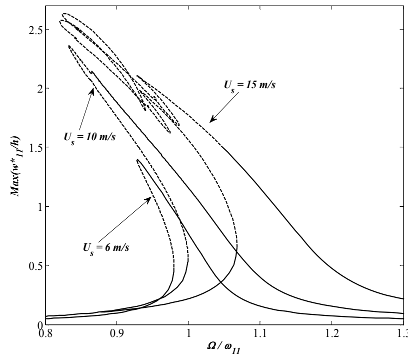

Fig. 2.17. Frequency-response curves for the fundamental generalized coordinate at different flow velocities; $p_s = 915$ Pa, $\chi = 0.01$ and $\xi = 0.01$ for all generalized coordinates; stable solution (continuous line) and unstable solution (dashed line).

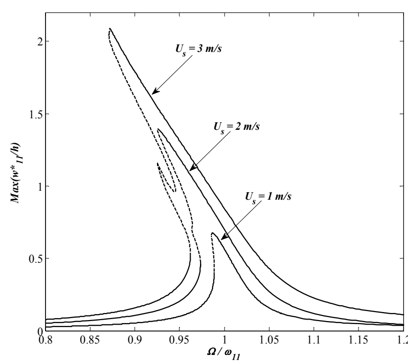

Fig. 2.18. Frequency-response curves for the fundamental generalized coordinate at different flow velocities; $p_s = 915$ Pa, $\chi = 0.03$ and $\xi = 0.01$ for all generalized coordinates; stable solution (continuous line) and unstable solution (dashed line).

2.4 Conclusions

The nonlinear vibrations and stability of thin rectangular plates with immovable edges coupled to axial pulsatile flow are discussed here. In addition, the case of plates in axial uniform flow under the action of constant transmural pressure is also addressed. Lagrange equations of motion are derived for the case of unsteady flow velocity. It has been found that the presence of positive transmural uniform pressure and small pulsation frequency destroys the pitchfork bifurcation (divergence) that flat plates exhibit when subjected to uniform flow. The effect of different system parameters such as flow velocity, pulsation amplitude, pulsation frequency, and channel pressurization on the stability of the plate and its geometrically nonlinear response to pulsating flow are fully discussed. The frequency-amplitude responses presented here show a hardening type behavior in case of zero uniform transmural pressure. The vibration amplitude is accentuated by increasing the steady component of the pulsatile flow velocity (keeping the pulsatile amplitude ratio constant) and by increasing the pulsation amplitude as well. On the other hand, in the presence of uniform transmural pressure a softening type behavior is detected. Moreover, internal resonances in the response of the fundamental mode with other modes are observed for certain frequency ranges.

Acknowledgments

The authors would like to thank NSERC Discovery Grant Program, Qatar Foundation, first author Fonds de recherche du Québec – Nature et technologies (FRQNT), and the second author Canada Research Chair, for their financial support.

Chapter 3

Shells conveying pulsatile flow

This chapter addresses the study of isotropic circular cylindrical shells with flexible boundary conditions conveying pulsatile flow and subjected to pulsatile pressure using the same model presented in Chapter 2. The interest on this subject is motivated by the functioning of the vascular tree where the blood flow is driven by the pulsating pressure gradient produced by the heart that is acting as a pump. The shell studied here aims to roughly represent the woven Dacron prostheses used nowadays in clinical practice for thoracic aortic replacement. The pulsatile time-dependent blood flow model is considered by applying physiological waveforms of velocity and pressure during the heart beating period. However, the way the pulsatile flow is modeled is ideal since it is assumed that, for a given time instant, the pulsatile pressure and flow velocity are the same for all points of the control volume. Consequently, the oscillatory pressure variations occurred simultaneously at every point of shell, making the fluid oscillate in bulk. Hence, the wave motion of local movements of the fluid caused by pressure changes in a deformable shell is not included. Since the pulse wave speed increases by reducing the elasticity of the shell, this approximation is adequate when the shell presents a low elasticity allowing the wave speed to be much higher than the maximum flow velocity. The paper "Fluid-Structure Interaction for nonlinear response of shells conveying pulsatile flow" published in the Journal of Sound and Vibration [2] is reported.

FLUID-STRUCTURE INTERACTION FOR NONLINEAR RESPONSE OF SHELLS CONVEYING PULSATILE FLOW

Eleonora Tubaldi, Marco Amabili, Michael P. Païdoussis

Department of Mechanical Engineering, McGill University

Abstract

Circular cylindrical shells with flexible boundary conditions conveying pulsatile flow and subjected to pulsatile pressure are investigated. The equations of motion are obtained based on the nonlinear Novozhilov shell theory via Lagrangian approach. The flow is set in motion by a pulsatile pressure gradient. The fluid is modeled as a Newtonian pulsatile flow and it is formulated using a hybrid model that contains the unsteady effects obtained from the linear potential flow theory and the pulsatile viscous effects obtained from the unsteady time-averaged Navier-Stokes equations. A numerical bifurcation analysis employs a refined reduced order model to investigate the dynamic behavior. The case of shells containing quiescent fluid subjected to the action of a pulsatile transmural pressure is also addressed. Geometrically nonlinear vibration response to pulsatile flow and transmural pressure are presented here via frequency-response curves and time histories. The vibrations involving both a driven mode and a companion mode, which appear due to the axial symmetry, are also investigated. This theoretical framework represents a pioneering study that could be of great interest for biomedical applications. In particular, in the future, a more refined model of the one presented here will possibly be applied to reproduce the dynamic behavior of vascular prostheses used for repairing and replacing damaged and diseased thoracic aorta in cases of aneurysm, dissection or coarctation. For this purpose, a pulsatile time-dependent blood flow model is considered here by applying physiological waveforms of velocity and

pressure during the heart beating period. This study provides, for the first time in literature, a fully coupled fluid-structure interaction model with deep insights in the nonlinear vibrations of circular cylindrical shells subjected to pulsatile pressure and pulsatile flow.

3.1 Introduction

Shell-like structural components used for aerospace and biomechanical applications are particularly challenging as they undergo significant deformations and stresses, involve fluid-structure interactions and are made of materials whose properties are not fully known.

Systematic research on the nonlinear dynamics of shells conveying fluid has been conducted by Païdoussis and it is synthesized in his monograph [5]. The effects of internal flow on the stability of circular cylindrical shells have been studied by Païdoussis and Denise [23], Weaver and Unny [24] and Païdoussis *et al.* [25, 26].

Theory for the dynamic stability of circular cylindrical shells subjected to incompressible subsonic liquid and air flow have been reported by Amabili et al. [137-140] and experiments by Karagiozis *et al.*[33, 34]. In the theoretical part of these studies, the shell was assumed to be in contact with inviscid fluid, and the fluid-structure interaction was described by the potential flow theory. Experiments on nonlinear dynamics of clamped shells subjected to axial flow were described in [33] and its visual experimental evidence was provided in [34]. A subcritical nonlinear softening behavior was reported for shells subjected to internal and external flow for the first time by Amabili [137]. It was found that, the interaction between the shell and the fully developed flow gives rise to instabilities in the form of static or dynamic divergence at sufficiently high flow velocities. The effect of imperfections on the nonlinear stability of shells containing fluid flow has been investigated by Amabili *et al.* [141] by using the most refined model at present; fluid viscosity has also been considered. Good agreement was shown with the available experimental results for divergence of aluminum shells conveying water.

Additional work can be found in the literature. The combined effect of geometric imperfections and fluid flow on the nonlinear vibrations and stability of shells has been investigated by del Prado *et al.* [38]. The behavior of the thin-walled shell was modeled by Donnell's nonlinear shallow-shell theory and the shell was assumed to be subjected to a static uniform compressive axial pre-load plus a harmonic axial load. A low-dimensional model was obtained by using the Galerkin method and the numerical solutions were found by using a Runge-Kutta scheme. It was shown that the parametric instability regions, bifurcations and basins of attraction are affected by the initial geometric imperfection and the flow velocity. The effect of fluid viscosity was also retained by Karagiozis *et al.* [142] in studying the nonlinear vibrations of harmonically excited circular cylindrical shells conveying water flow. Periodic, quasi-periodic, sub-harmonic and chaotic responses were detected, depending on the flow velocity, and amplitude of the harmonic excitation. It was found that, the softening behavior is enhanced by increasing the flow velocity.

By neglecting the effect of fluid viscosity and considering the potential flow model, nonlinear forced vibrations and stability of shells interacting with fluid flow were investigated in [32, 57, 58, 60]. Koval'chuk [32] used Donnell's nonlinear theory together with Galerkin approach and Krylov- Bogolyubov–Mitropol'skii averaging technique to study the nonlinear vibrations of the shell, neglecting the effect of axisymmetric modes. The same theory and solution methodology was used by Koval'chuk and Kruk [58]. However, in their analysis, the numerical model had six degrees of freedom that included four asymmetric modes plus two axisymmetric modes. The axisymmetric modes were described as quartic sine terms. Kubenko *et al.* [57] extended the previous works of [32, 58] by showing the mathematical procedure for the Krylov- Bogolyubov–Mitropol'skii method in studying multi-mode nonlinear free, forced and parametrically excited vibrations of shells in contact with flowing fluid. Kubenko *et al.* [60] have also studied the vibrations of cylindrical shells interacting with a fluid flow and subjected to external periodic pressure with slowly varying frequency. Nonlinear dynamics of cantilevered circular cylindrical shells subjected to flowing fluid has been investigated by Paak *et al.* [143], but the contribution of axisymmetric modes has been neglected. The nonlinear model of the shell was based on Flügge theory retaining nolinear terms due to mid-surface stretching, and the fluid model was based on the potential flow theory. The unsteady interaction and asymptotic dynamics of a viscous fluid with an elastic shell has also been examined by Chueshov and Ryzhkova [144] using the linearized Navier-Stokes equations and Donnell's nonlinear shallow shell theory.

A specific type of unsteady flows includes oscillatory and pulsatile flows which occur in biological systems, such as human respiratory and vascular systems, as well as in many engineering areas, for example, the flow in hydraulic and pneumatic and pumping systems or applications of heat transfer. Oscillatory and pulsating flows in branching pipes have been extensively studied by investigators concerned especially in biology. Additionally, a number of work have been reported in literature concerning oscillatory or pulsatile flows in straight pipes (see for example, Uchida [39], Gerrard and Hughes [40], Kerczek and Davis [121], Schneck and Ostrach [122], Hino *et al.* [41], Muto and Nakane [42], Shemer *et al.* [43], Elad *et al.* [123]). Pioneering studies related to dynamic instability of pipes conveying fluctuating fluid were from Chen [27] followed by Ginsberg [46], Païdoussis [47] and Païdoussis and Issid [45]. Ginsberg [46] derived the general equations of motion for small transverse displacement of a pipe conveying fluid based on the transverse force exerted by the flowing fluid. For the case of a simply supported pipe Galerkin method was utilized to obtain the solution. The dynamic instability regions were evaluated and it was shown that the region of dynamic instability increases with increased amplitude of fluctuation. Païdoussis [47] presented a theoretical analysis of the dynamical behaviour of flexible cylinders in axial flow, the velocity of which was perturbed harmonically in time. He found that parametric instabilities are possible for certain ranges of frequencies and amplitudes of the perturbations. These instabilities occur over specific ranges of flow velocities, and in the case of cantilevered cylinders are associated with only some of the modes of the system. Païdoussis and Issid [45] derived the equation of motion for a flexible pipe conveying fluid; effects of external pressurization and external tension were included, the longitudinal acceleration of the fluid was taken into account, hence this model can be applied to problems when the flow contains harmonic components.

In biomechanics, thin-walled shells can be used to model the mechanics of veins, arteries and pulmonary passages. Kamm [82] investigated the flutter phenomenon of veins and its associated collapse, while Païdoussis [5] investigated the fluid-structure interaction between the blood flow and the veins. The mechanisms leading to static collapse and flutter of biological systems have been explained but there remain questions regarding the causes that may lead to it because of the large deformations the system experiences. Thus, the dynamics of arteries should be easier to explain since arteries are traditionally considered capable of withstanding large deformations without adverse effects. In addition, arterial walls are structurally inhomogeneous, anisotropic and viscoelastic. In [145, 146], material nonlinearities (i.e. nonlinear stress-strain relations) based on hyperelastic and viscoelastic models have been used for modeling arteries in addition to geometrical nonlinearities (i.e. nonlinear strain-displacement relations). Material anisotropy, hyperelasticity, residual stresses have been accounted for in numerical models of the aortic wall in [147-149]. Unsteady flow characteristics and wave propagation through elastic tubes (like large arteries) have also been studied on the macroscale by Wormersly [62] and McDonald [70]. Womersley [62] was one of the first to experimentally study pulsatile flow and performed his studies on the femoral artery of a dog. In these studies, the velocity profiles, viscous drag, and Reynolds number were calculated from the pressure gradient. It was the pressure gradient that was used to determine the flow characteristics indirectly. Since then, many works have been developed on the flow stability and transition to turbulence of oscillatory and pulsatile flow both experimentally and numerically [41, 125-129]. Numerous experimental investigations were focused on fundamental studies of fully developed periodic pipe flows with sinusoidally varying pressure gradients (or flow rates). Low speed (laminar) pulsating flows were studied in order to analyze the flows through small pipes or in the blood circulation systems. Berguer *et al.* [130] developed a numerical model to analyze both laminar and turbulent pulsatile flows in aortic aneurysm models using physiological resting and exercise waveforms. They also compared hemodynamic stresses for non-Newtonian and Newtonian behavior and the non-Newtonian effects are demonstrated to be significant in realistic flow situations. Khanafer *et al.* [131] numerically analyzed pulsatile turbulent flow, using simulated physiological rest and exercise waveforms, in axisymmetric-rigid aortic aneurysm (AA) models. Khanafer *et al.* [132] also represented the first computational study to analyze turbulent pulsatile flow within compliant walls of an aneurysm and to determine realistic aneurysm wall stress values. Recently, Amabili *et al.* [89] have discussed the phenomenon of aortic dissection using a shell model. They identified for the first time the nonlinear buckling (collapse) of the aorta as a possible reason behind the appearance of high stress regions at the inner layer of the aortic wall that may be responsible for the initiation of dissection.

Furthermore, in vascular surgery, artificial blood vessels can be modeled as thin-walled shell in axial pulsating flow. Indeed, implants have been used in various circumstances of vascular maladies requiring replacements of components of the cardiovascular system such as vessel patches for aneurysms. Surgeons perform vascular prosthesis implantation to exclude the compromised arterial portion (afflicted with aneurysm or dissection for instance) from luminal pulsatile blood flow. This may be carried out by providing with an artificial blood flow passage via a synthetic conduit. In particular, two techniques - open surgical repair (OSR) and endovascular aneurysm repair (EVAR) - are employed to repair the vessel avoiding its rupture. Open surgical repair is a traditional and standard treatment modality based on a well-established procedure to treat patients with a high risk of rupture [92, 93]. In an open repair the surgeon will open the abdominal cavity, clamp the aorta just above and below the aneurysm and then sew a fabric tube or graft made of polyethylene terephthalate (Dacron® or PET) or polytetrafluoroethylene (PTFE) inside the aneurysm. Both the proximal and distal segments are stitched to healthy tissue. Large diameter (12-30 mm) vessel replacements with Dacron are the accepted clinical practice [94]. In particular, tightly woven, crimped and non-supported Dacron fabric prostheses are currently used to replace thoracic and abdominal aorta with high rates of success [95]. Indeed, Dacron is easy to use, durable, and have manageable resistance to thrombosis formation when used in large caliber vessels; however, it has also distinctly different mechanical properties than the native aorta [150]. The arteries of the body behave as distensible cylindrical conduits whilst non-compliant nature of Dacron grafts increases the risk of thrombosis and is known to reduce graft patency [101]. Very little is known about the dynamic behavior of vascular prostheses that can cause unwanted hemodynamic effects leading to their failure.

In this study, a shell with the mechanical properties of the Dacron aortic replacement is modelled as an isotropic cylindrical shell by means of nonlinear Novozhilov shell theory. A numerical bifurcation analysis employs a refined reduced order model to investigate the dynamic behavior of a pressurized shell conveying blood flow. A pulsatile time-dependent blood flow model is considered in order to study the effect of pressurization by applying physiological waveforms of velocity and pressure during the heart beating period. The fluid is modeled as a Newtonian pulsatile flow and it is formulated using a hybrid model that contains the unsteady effects obtained from the linear potential flow theory and the pulsatile viscous effects obtained from the unsteady time-averaged Navier-Stokes equations. Geometrically nonlinear vibration response to pulsatile flow is presented here via frequency-response curves and time histories. For high frequencies (out of the physiological range), the frequency response curves of the system present a sequence of period doubling and pitchfork bifurcations showing the existence of complex nonlinear dynamics for the circular cylindrical shell under consideration subject to high frequency harmonic excitation.

3.2 Governing equations and assumptions

In this study the nonlinear Novozhilov shell theory (Appendix D) is applied to model as isotropic linearly elastic shells the vascular prostheses currently used in aortic replacement surgery. The system under consideration is shown in Fig. 3.1 where $O(x, \theta, r)$ is the origin of coordinate system, R is the mean radius, h is the shell thickness, L is the shell length, u is the shell displacement in the x-direction, v is the shell displacement in the θ-direction and w is the shell displacement in the r-direction (taken positive outward).

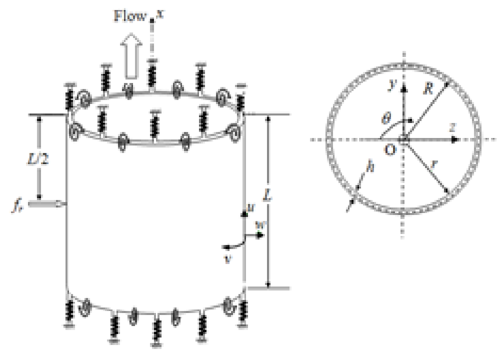

Fig. 3.1. Schematic of the shell in axial flow with boundary conditions at the shell ends.

The following boundary conditions, with flexible constraints to simulate connection with the remaining tissue, are applied at the shell ends $(x = 0, L)$,

$$v = w = 0, \quad N_x = -k_a u, \quad M_x = -k_r\left(\frac{\partial w}{\partial x}\right), \tag{3.1a-d}$$

where N_x is the axial stress per unit length, M_x is the bending moment per unit length and k_a is the distributed axial springs' stiffness for asymmetric modes and k_r is the rotational springs' stiffness applied at the shell edges. The flexible boundary conditions at the shell ends are assumed to simulate the connection with connective tissue and the resected aorta (i.e. axial and rotational constraints) [151]. In this study, as in the previous one conducted by Amabili *et al.* [89], the spring constraints are set to $k_a = 10^3\,\mathrm{N/m^2}$ and $k_r = 10^2\,\mathrm{N/rad}$.

3.2.1 Elastic strain energy and kinetic energy of the shell

A variational approach is employed to obtain the equations of motion for the aortic prosthesis segment. Specifically, the total kinetic energy of the shell is given by

$$T_s = \frac{1}{2}\rho_s h \int_0^{2\pi}\int_0^L \left\{\dot{u}^2 + \dot{v}^2 + \dot{w}^2\right\} \mathrm{d}x\, R\, \mathrm{d}\theta, \tag{3.2}$$

where ρ_S is the mass density of the shell and the overdot denotes a time derivative. In equation (3.2) the rotary inertia is neglected since the shell is assumed to be thin, according to Novozhilov nonlinear shell theory. The potential energy of the aortic wall U_S is made up of two contributions:

$$U_S = U_{shell} + U_{spring}. \tag{3.3}$$

The elastic strain energy U_{shell} (Appendix E) of an isotropic circular cylindrical shell is given by

$$U_{shell} = \frac{1}{2}\rho_S \int_0^L \int_0^{2\pi} \int_0^h \left(\sigma_x \varepsilon_x + \sigma_\theta \varepsilon_\theta + \tau_{x\theta}\gamma_{x\theta}\right)\left(1 + z/R\right) \mathrm{d}x\, R\, \mathrm{d}\theta\, \mathrm{d}z. \tag{3.4}$$

The potential energy stored by the axial and rotational springs at the shell ends is given by

$$U_{spring} = \frac{1}{2}\int_0^{2\pi} \left\{ k_a \left[\left(u\right)_{x=0}\right]^2 + k_a \left[\left(u\right)_{x=0}\right]^2 + k_r \left[\left(\frac{\partial w}{\partial x}\right)_{x=0}\right]^2 + k_r \left[\left(\frac{\partial w}{\partial x}\right)_{x=L}\right]^2 \right\} R\, \mathrm{d}\theta. \tag{3.5}$$

The shell displacements are discretized by using trigonometric expansions that identically satisfy the geometric boundary conditions; these trigonometric functions are the eigenmodes of the linear problem in case of simply supported boundary conditions. In particular,

$$\begin{aligned}
u(x,\theta,t) &= \sum_{m=1}^{8}\left[u_{m,n,c}(t)\cos(n\theta) + u_{m,n,s}(t)\sin(n\theta)\right]\cos(\lambda_m x) + \sum_{m=1}^{3} u_{m,2n,c}(t)\cos(2n\theta)\cos(\lambda_m x) + \sum_{\substack{m=1 \\ m\ odd}}^{11} u_{m,0}(t)\cos(\lambda_m x) + \sum_{\substack{m=2 \\ m\ even}}^{6} u_{m,0}(t)\cos(\lambda_m x), \\
v(x,\theta,t) &= \sum_{m=1}^{8}\left[v_{m,n,s}(t)\sin(n\theta) + v_{m,n,c}(t)\cos(n\theta)\right]\sin(\lambda_m x) + \sum_{m=1}^{6} v_{m,2n,c}(t)\sin(2n\theta)\sin(\lambda_m x), \\
w(x,\theta,t) &= \sum_{m=1}^{8}\left[w_{m,n,c}(t)\cos(n\theta) + w_{m,n,s}(t)\sin(n\theta)\right]\sin(\lambda_m x) + \sum_{m=1}^{11} w_{m,0}(t)\sin(\lambda_m x) + \sum_{\substack{m=1 \\ m\ odd}}^{11} w_{m,0}(t)\sin(\lambda_m x) + \sum_{\substack{m=2 \\ m\ even}}^{6} w_{m,0}(t)\sin(\lambda_m x),
\end{aligned} \tag{3.6a-c}$$

where n is the number of circumferential waves, m is the number of longitudinal half-waves, $\lambda_m = m\pi/L$, and t is the time; $u_{m,n}(t)$, $v_{m,n}(t)$ and $w_{m,n}(t)$ are the generalized coordinates [4]. A nonlinear term $\hat{u}(t)$ is added to the expansion of u (Eq. (3.6a)) to satisfy exactly the boundary conditions Eq. (3.1c); this term is obtained as a function of the generalized coordinates [37]. Thanks to the discretization with the generalized coordinates, the dynamic behavior of the shell coupled to quiescent fluid under pulsatile pressure can be studied with a reduced-order model of 48 *dof* obtained by selecting terms with odd numbers of longitudinal half-waves m. Indeed, the terms with even m are activated in case of flowing fluid when complex modes arise. The inevitable effect of introducing a slight asymmetric stretch on the implant during the surgical suture, added to the manufacturing imperfections of the textile graft itself, makes always appear geometric imperfections on the walls of implanted vascular prostheses. In the present study it is assumed that geometric imperfections (deviations from the ideal circular cylindrical shape) are associated to zero initial stress, which is an acceptable hypothesis since the implant is thin. Hence, in presence of asymmetric geometric imperfections, the nonlinear vibrations of the shell coupled to pulsatile flow under pulsatile pressure, can be investigated with a reduced-order model of 51 *dof* obtained by selecting terms with both odd and even numbers of longitudinal half-waves m and neglecting the companion modes with last subscript s. In equation (3.6), modes with n=2 circumferential waves are used in addition to axisymmetric modes (n=0) and modes with 2n. The reason for the selection of $n = 2$ is that these are the low frequency modes for shells of the length studied in the present paper; also, $n = 2$ is the buckling shape observed in reference [45] for this shell dimensions.

3.2.2 Fluid-structure interaction model

The fluid is modeled as a Newtonian pulsatile flow. Although blood is a suspension of red blood cells, white blood cells, and platelets in plasma, its non-Newtonian nature due to the particular rheology is relevant in small arteries (arterioles) and capillaries where the diameter of the arteries becomes comparable to the size of the cells. On the other hand, it has been well accepted that in medium-to-large arteries blood can be modeled as a viscous and Newtonian fluid. In addition, it is well known [75, 151] that in the heart chambers and blood vessels, blood is incompressible. Finally, the change in elasticity at the union between a prosthesis and the compliant artery leads to an abrupt change in diameter which in turn produces a distortion of the local flow field [99, 152], causing eventually undesirable flow patterns such as flow separation, vortex formation and turbulence [153]; hence, in this analysis, the flow in the aortic prosthesis is assumed to be turbulent fully developed. The fluid-structure interaction model obtains the unsteady fluid motion by potential flow theory and the pulsatile viscous effects for turbulent flow by the unsteady time-averaged Navier-Stokes equations.

An unsteady perturbation potential Φ is introduced that satisfies the Laplace equation

$$\nabla^2\Phi = \frac{\partial^2\Phi}{\partial x^2} + \frac{\partial^2\Phi}{\partial r^2} + \frac{1}{r}\frac{\partial\Phi}{\partial r} + \frac{1}{r^2}\frac{\partial^2\Phi}{\partial\theta^2} = 0. \tag{3.7}$$

If no cavitation occurs at the fluid-shell interface, the boundary condition expressing the contact between the shell wall and the flow is given by

$$\left.\frac{\partial\Phi}{\partial x}\right|_{r=R} = \left(\frac{\partial w}{\partial t} + U\frac{\partial w}{\partial x}\right), \tag{3.8}$$

where U is the undisturbed (pulsatile) blood flow velocity, which is time dependent.

Equation (3.8) and the Laplace equations are satisfied if the solution for the velocity potential is given by [5]

$$\Phi = \sum_{m=1}^{M}\sum_{n=0}^{N} \frac{L}{m\pi}\frac{\mathrm{I}_n(m\,\pi\,r/L)}{\mathrm{I}_n^{'}(m\,\pi\,R/L)}\left(\frac{\partial w_{m,n}}{\partial t} + U\frac{\partial w_{m,n}}{\partial x}\right), \tag{3.9}$$

where I_n is the modified Bessel function of the first kind of order *n,* and I_n' is the derivative of I_n with respect to its argument. Therefore, the perturbation pressure p at the shell inner wall interface is found to be given by

$$p = -\rho_F \sum_{m=1}^{M}\sum_{n=0}^{N} \frac{L}{m\pi}\frac{\mathrm{I}_n(m\,\pi\,R/L)}{\mathrm{I}_n^{'}(m\,\pi\,R/L)}\left(\frac{\partial}{\partial t} + U\frac{\partial}{\partial x}\right)^2 w_{m,n}\,, \tag{3.10}$$

where ρ_F is the fluid density.

3.2.3 Potential Flow Energy

Green's theorem is used to obtain the total energy E_F [4] associated with the flow, which can be divided into three terms: kinetic energy, potential energy and gyroscopic energy, as given in the expression below

$$E_F = T_F + E_G - V_F, \tag{3.11}$$

where T_F, V_F and E_G are the reference kinetic energy, the potential energy and the gyroscopic energy of the fluid, respectively and they have the following expressions [4]

$$T_F = \frac{1}{2}\rho_F \sum_{m=1}^{M}\sum_{n=0}^{N}\int_0^{2\pi}\int_0^L \frac{L}{m\pi}\frac{\mathrm{I}_n(m\,\pi\,R/L)}{\mathrm{I}_n'(m\,\pi\,R/L)}\,\dot{w}_{m,n}^2\,\mathrm{d}x\,R\,\mathrm{d}\vartheta\,,$$

$$V_F = -\frac{1}{2}\rho_F \sum_{m=1}^{M}\sum_{n=0}^{N}\int_0^{2\pi}\int_0^L \frac{L}{m\pi}\frac{\mathrm{I}_n(m\,\pi\,R/L)}{\mathrm{I}_n'(m\,\pi\,R/L)}\,U^2\left(\frac{\partial w_{m,n}}{\partial x}\right)^2\mathrm{d}x\,R\,\mathrm{d}\vartheta\,, \tag{3.12a-c}$$

$$E_G = \frac{1}{2}\rho_F \sum_{m=1}^{M}\sum_{n=0}^{N}\sum_{l=1}^{M}\sum_{k=0}^{N}\int_0^{2\pi}\int_0^L \frac{UL}{m\pi}\frac{\mathrm{I}_n(m\,\pi\,R/L)}{\mathrm{I}_n'(m\,\pi\,R/L)}\left(\dot{w}_{m,n}\frac{\partial w_{l,k}}{\partial x}+\dot{w}_{l,k}\frac{\partial w_{m,n}}{\partial x}\right)\mathrm{d}x\,R\,\mathrm{d}\vartheta.$$

In case of unsteady flow velocity *U(t)*, the expressions of T_F, V_F and E_G will be time dependent and because of that, a new term will appear in the Lagrange equations of motions as shown in Section 3.2.6.

3.2.4 Viscous Effects for Pulsatile flow

The unsteady time-averaged Navier-Stokes equations are employed to calculate the pulsatile viscous effects assuming that the flow is turbulent and fully developed. The result is a variable mean transmural pressure ΔP_{tm} along the shell because the pressure drop and a frictional traction on the internal wall in the axial direction. A detailed description of the solution for the unsteady time-averaged Navier-Stokes equations used here is given in [26, 141]. This type of hybrid model is particularly efficient from the computational point of view. In particular, in case of unsteady flow, the fluid pressure *P* on the shell surface assumes the following expression

$$P(x,R) = -\rho_F\left(\frac{f}{4R}U^2 + \frac{dU}{dt}\right)x + P(0,R), \tag{3.13}$$

where the friction factor f can be calculated by using the empirical Colebrook equation. Therefore, the first effect of fluid viscosity and fluid acceleration is the appearance of an additional triangular pressure distribution along the shell. In the present study, it is assumed that $P(\frac{L}{2}, R) = 0$ so that P is directly added to the pulsatile uniform pressure differential p_m acting on the shell wall (defined as the difference between the internal and external pressures on the shell wall), assumed positive outward. Therefore, the expression of P is given by

$$P(x,R) = \rho_f \left(\frac{f}{4R} U^2 + \frac{dU}{dt} \right) \left(\frac{L}{2} - x \right). \tag{3.14}$$

The pressure drop $\Delta P_{0,L}$ in the shell is

$$\Delta P_{0,L} = P(0,R) - P(L,R) = \rho_f \left(\frac{f}{4R} U^2 + \frac{dU}{dt} \right) L. \tag{3.15}$$

Neglecting the contribution of the flow acceleration, the constant axial friction traction force per unit area, is

$$\tau_x = f \rho_f U^2 / 8. \tag{3.16}$$

The friction factor f in Eq. (3.16) has been calculated as discussed in Appendix F.

3.2.5 Representation of Pulsatile Velocity and Pulsatile Pressure

The physiological waveforms of velocity and pressure during the heart beating period [154] are expressed in terms of Fourier series as follows

$$U(t) = \bar{U} + \sum_{n=1}^{8} \left(a_{v,n} \cos\left(n\,\Omega\,t\right) + b_{v,n} \sin\left(n\,\Omega\,t\right) \right), \tag{3.17a}$$

$$p_m(t) = \bar{p}_m + \sum_{n=1}^{N} \left(a_{p,n} \cos\left(n\,\Omega\,t\right) + b_{p,n} \sin\left(n\,\Omega\,t\right) \right), \tag{3.17b}$$

where Ω is the heart rate, $\bar{p}_m$ and $\bar{U}$ represent the steady component of the pressure field and the pulsatile mean flow velocity, respectively, and N represents the number of terms in the series expansion. The coefficients a_n and b_n are the Fourier cosine and sine coefficients, respectively. Specifically, in case of thoracic aorta (that has Womersley number $\alpha \simeq 19$), the phase lag between the oscillating pressure and the flow generated

[66] is ninety degree, as shown in Fig. 3.2 where N=8 terms in the Fourier expansion are used. In addition, the rapidly varying part of the flow lies in the proximity of the aortic wall while the central mass of the fluid reciprocates almost like a solid core [155].

The pulsatile flow discussed here is ideal since it is assumed that at the same time instant, the flow velocity is the same for all points of the control volume. The validity of this assumption is discussed in Appendix G.

3.2.6 Lagrange Equations of Motion

The expressions for the potential and kinetic energies of the shell (Eq. (3.2) and Eq. (3.4)) and the fluid Eq. (3.12a-c) are coupled in the Lagrange equations of motion. As shown in Appendix H, the Lagrange equations of motion for open systems in the present case, knowing that $\partial T_S / \partial q_j = \partial T_F / \partial q_j = 0$, are written as follows:

$$\frac{d}{dt}\left[\frac{\partial\left(T_S + T_F + E_G\right)}{\partial \dot{q}_j}\right] - \frac{\partial E_G}{\partial q_j} + \frac{\partial\left(U_S + V_F\right)}{\partial q_j} = Q_j, \quad j = 1 \ldots N_T \tag{3.18}$$

where T_s and T_F are the kinetic energy of the shell and the fluid, respectively, U_s and V_F are the potential energy of the shell and the fluid, respectively, E_G is the gyroscopic energy associated with the flow, and Q_j are the generalized external forces, including the transmural pressure ΔP_{tm}, which is affected by the physiological pulsatile pressure p_m (Eq. (3.17b)) and the pressure drop $\Delta P_{0,L}$ (Eq. (3.15)), and the axial friction forces τ_x (Eq. (3.16)) as expressed in

$$Q_j = \frac{\partial W}{\partial q_j} - \frac{\partial F}{\partial \dot{q}_j}, \tag{3.19}$$

where

$$W = \int_0^{2\pi}\int_0^L \left(\Delta P_{tm} w + \tau_x u\right) dx\, R\, d\vartheta = \int_0^{2\pi}\int_0^L \left[\left(\Delta P_{0,L} + p_m\right) w + \tau_x u\right] \mathrm{d}x\, R\, \mathrm{d}\vartheta, \tag{3.20a}$$

$$F = \frac{1}{2} c \int_0^{2\pi}\int_0^L (\dot{u}^2 + \dot{v}^2 + \dot{w}^2)\, \mathrm{d}x\, R\, \mathrm{d}\vartheta, \tag{3.20b}$$

where F represents nonconservative damping forces assumed to be of viscous type and taken into account by using Rayleigh's dissipation function; c is the viscous damping coefficient. Here the generic generalized coordinate, which are $u_{m,n}(t), v_{m,n}(t), w_{m,n}(t)$, is indicated with q_j. The number of generalized coordinates (i.e. degrees of freedom of the system) is N_T.

Under the hypothesis of unsteady flow the time derivative of the gyroscopic term $\partial E_G / \partial \dot{w}_{m,n}$ of the Lagrangian equation becomes

$$\frac{\mathrm{d}}{\mathrm{d}t}\left[\frac{\partial E_G}{\partial \dot{q}_j}\right] = \frac{\dot{U}}{U}\frac{\partial E_G}{\partial \dot{q}_j} - \frac{\partial E_G}{\partial q_j}. \tag{3.21}$$

Hence, Eq. (3.18) can be rewritten as

$$\frac{\mathrm{d}}{\mathrm{d}t}\left[\frac{\partial\left(T_S + T_F\right)}{\partial \dot{q}_j}\right] + \frac{\dot{U}}{U}\frac{\partial E_G}{\partial \dot{q}_j} - 2\frac{\partial E_G}{\partial q_j} + \frac{\partial\left(U_S + V_F\right)}{\partial q_j} = Q_j\,. \tag{3.22}$$

The vector $\mathbf{q}$ of the generalized coordinates $u_{m,n}(t), v_{m,n}(t), w_{m,n}(t)$ is introduced and the final equations of motion for the aortic wall are given in matrix form in the following expression:

$$\mathbf{M\ddot{q}} + \left(\mathbf{C} + \mathbf{C_F}\right)\mathbf{\dot{q}} + \left[\mathbf{K_S} + \mathbf{K_F} + \mathbf{N_2(q)} + \mathbf{N_3(q,q)}\right]\mathbf{q} = \mathbf{Q}\,, \tag{3.23}$$

where $\mathbf{M} = \mathbf{M_S} + \mathbf{M_F}$, $\mathbf{M_S}$ being the mass matrix of the shell and $\mathbf{C}$ the damping matrix which is added to the equations of motion to model dissipation. Moreover, $\mathbf{K_S}$ is the linear stiffness matrix of the shell, $\mathbf{N_2}$ gives the quadratic nonlinear stiffness terms, $\mathbf{N_3}$ denotes the cubic nonlinear terms and $\mathbf{Q}$ is the vector representing external loads, which includes pressurization of the shell in the radial direction and axial friction forces.

In order to obtain the equations of motion in a suitable form for numerical implementation, the system (3.23) is multiplied by the inverse of the mass matrix and then is written in the state-space form as follows

$$\begin{cases} \mathbf{\dot{q}} = \mathbf{y} \\ \mathbf{\dot{y}} = -\mathbf{M}^{-1}\left(\mathbf{C} + \mathbf{C_F}\right)\mathbf{\dot{q}} - \left[\mathbf{M}^{-1}\left(\mathbf{K_S} + \mathbf{K_F}\right) + \mathbf{M}^{-1}\mathbf{N_2(q)} + \mathbf{M}^{-1}\mathbf{N_3(q,q)}\right]\mathbf{q} + \mathbf{M}^{-1}\mathbf{Q} \end{cases} \tag{3.24}$$

where $\mathbf{y}$ is the vector of the generalized velocities and the dissipation term $\mathbf{M}^{-1}\mathbf{C}$ is given by

$$\mathbf{M}^{-1}\mathbf{C} = \begin{bmatrix} 2\omega_1\xi_1 & \cdots & 0 \\ 0 & \ddots & 0 \\ 0 & \cdots & 2\omega_j\xi_j \end{bmatrix} \tag{3.25}$$

where ξ_j is the modal damping ratio of each generalized coordinate and it is related to the coefficient c in Eq. (3.20b) that has a different value for each term of the mode expansion [4]. Matrix (3.25) is assumed to be diagonal in order to use the modal damping. In this study, the same damping ratio $\xi = 0.12$ is assumed for all modes.

3.3 Numerical results

The equations of motion have been obtained by using *Mathematica 10* software [133] in order to perform analytical surface integrals of trigonometric functions.

A non-dimensionalization of variables is performed for computational convenience: the frequencies are divided by the natural radian frequency $\omega_{1,2}$ of the fundamental mode (m=1, n=2), and the vibration amplitudes are divided by the shell thickness h. The set of nonlinear ordinary differential equations (3.24) has been solved by using the software AUTO [106] that is capable of continuation of the solution, bifurcation analysis and branch switching by using the pseudo-arclength continuation and collocation method. Here, the nonlinear analysis of the shell coupled to pulsatile flow subjected to pulsatile pressure is divided in three steps. First, the pulsatile pressure is increased at zero flow velocity up to reach the desired value (Fig. 3.2(a)) giving the wall deformation and the initial stresses. In the second step, the pulsatile flow velocity is used as bifurcation parameter until it reaches the physiological conditions (Fig. 3.2(b)). Once the desired pulsatile flow velocity is reached, the bifurcation continues by considering the pulsation frequency Ω (heart pulse) as the continuation parameter to obtain the frequency-amplitude response of the shell (aortic prosthesis).

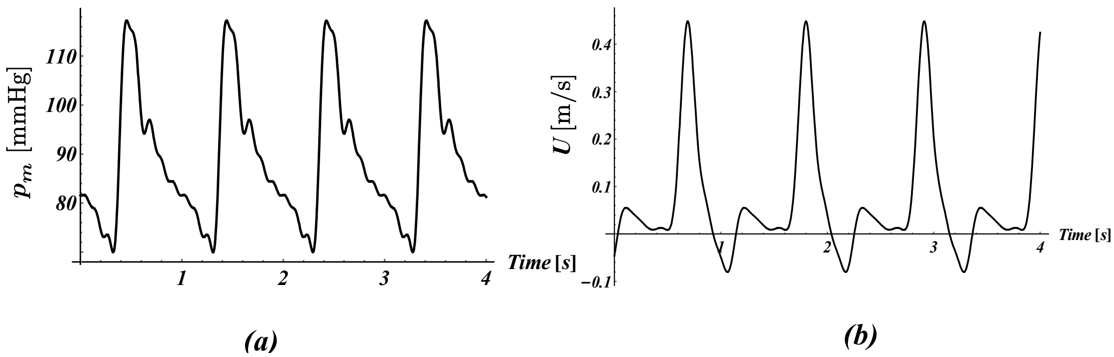

Fig. 3.2. Flow (a) and transmural pressure (b) values in the aortic segment with ninety degree phase lag (Fourier series N=8).

In order to investigate the behavior of shells containing quiescent fluid subjected to the action of a pulsatile transmural pressure, after the first step of the analysis, the bifurcation continues directly with the pulsation frequency Ω as continuation parameter at zero flow velocity.

The characteristics of the shell simulating a thoracic aortic replacement discussed here (Fig. 3.1) are: $L = 0.126$ m, $h = 0.361$ mm, $R = 0.01575$ m, $E = 10$ MPa, $\nu = 0.27$, $\rho_S = 1350\,\text{kg/m}^3$, $\rho_F = 1050\,\text{kg/m}^3$, where E and ν are the Young modulus and the Poisson ratio respectively, ρ_S is the density of the Dacron shell and ρ_F is the density of the blood. These elastic material properties have been chosen in agreement with previous studies [150, 156, 157] conducted on Dacron graft currently used in aortic replacements.

In this study, the dynamic behavior of the shell coupled to quiescent fluid under pulsatile pressure are studied with a reduced-order model of 48 *dof* obtained by selecting the terms with odd numbers of longitudinal half-waves m in Eq. (6a-c) since the terms with even m are only activated in case of flowing fluid when complex modes arise. For large-amplitude vibrations, the response of the shell near resonance is given by circumferentially traveling waves, which can appear in one direction or in the opposite angular direction. The traveling wave appears when a second standing wave (mode), the orientation of which is at $\pi/(2n)$ (where n is the number of nodal diameters) with respect to the previous one, is added to the driven mode. This second mode is called the *companion mode*. It has the same modal shape and frequency of the driven mode. These two modes with the same frequency (1:1 internal resonance) are angularly described by $cos(n\vartheta)$ and $sin(n\vartheta)$, respectively, with n being the circumferential wavenumber. In the present study n=2 is considered, since this is the fundamental mode of the shell. It is important to observe that the companion mode arises as a consequence of the symmetry of the system. Indeed, in presence of significant asymmetric imperfections, the nonlinear vibrations of the shell coupled to pulsatile flow under pulsatile pressure, can be investigated with a reduced-order model of 51 *dof* obtained neglecting the companion modes. Since the axial symmetry of the shell is broken by the imperfections, the traveling-wave response is largely modified, because natural frequencies of the driven and companion modes do not coincide anymore.

In the following section, both aforementioned models with 48 *dof* and 51 *dof* are applied to study the nonlinear response of shells subjected to pulsatile pressure with quiescent fluid and flowing pulsatile fluid, respectively. The physiological waveforms of velocity and pressure during the heart beating period [154] are expressed in terms of Fourier expansions Eq. (3.17a,b) considering N=8.

3.3.1 Time response to pulsatile transmural pressure and flow

The effects of physiological waveforms of velocity and pressure during the heart beating period (Fig. 3.2) on the aortic replacement are presented here through time responses of the shell for the angular coordinate $\vartheta = 0$ and for different values of the axial coordinate *x*. Under these conditions, the shell transversal sections will be circular at any point since only axisymmetric modes are activated.

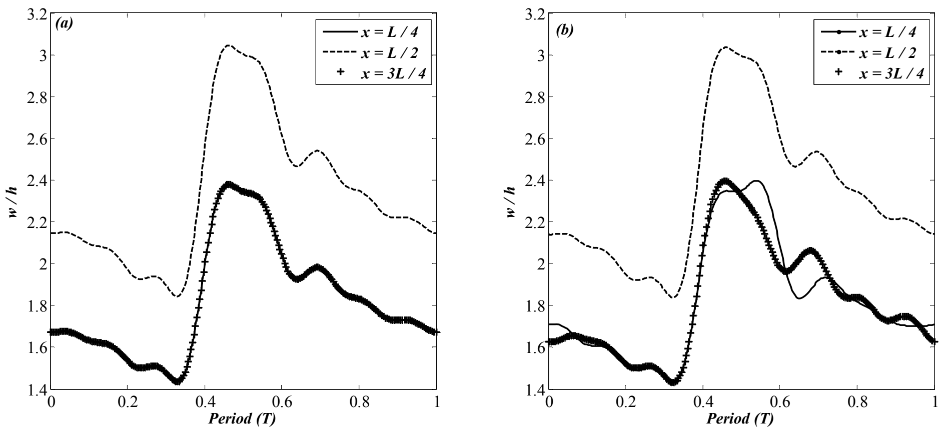

Fig. 3.3. Time response of the nondimensionalized radial displacement w/h under *(a)* pulsatile pressure (model 48 *dof*) and *(b)* pulsatile velocity and pressure (model 51 *dof*) with a pulsating frequency $\Omega = 5.65\ rad/s$ (around 54 beats per minute).

In particular, Fig. 3.3(a) shows the response of the shell with quiescent fluid under pulsatile pressure for $x = L/4, x = L/2$ and $x = 3L/4$, obtained with the model of 48 *dof*. As expected, the time responses reproduce the trend of the pulsating excitation and the maximum amplitude is reached at the pressure peak for $x=L/2$; in addition, the responses for $x= L/4$ and $x=3L/4$ are identical at any time of the time period. Fig. 3.3(b) shows the response of the shell under pulsatile pressure and velocity for $x=L/4$, $x=L/2$ and $x=3L/4$, obtained with the model of 51 *dof*. It can be noticed that, because of the gyroscopic effect of the blood flow, the time responses for $x= L/4$ and $x=3L/4$ are not identical anymore. Indeed, when the flow velocity is introduced, the mode shapes change from the classical ones of simply supported shells and complex mode shapes arise. The matrix $\mathbf{C_F}$ in Eq. (3.23) represents the energy transferred among modes associated with the gyroscopic effect and it is related to the Coriolis inertial force.

3.3.2 Frequency amplitude response to pulsatile transmural pressure in quiescent fluid

The next results represent the frequency-amplitude responses of the shell under the pulsatile transmural pressure given in Fig. 3.2(a) in quiescent fluid obtained with the 48 *dof* model. The presence of transmural pressure p_m affects the frequency response of the shell coupled to fluid and it is well known that for small vibration amplitudes, the resonance frequency of the shell increases [4]. For the shell under consideration, the resonance frequency at zero pressure is $\omega_{1,2} = 87.06\,\text{rad/s}$ associated to the mode $w_{1,2}$; when the shell is pressurized with the steady transmural pressure $\bar{p}_m = 11884\,\text{Pa}$ shown in Fig. 3.2(a), the frequency of the first asymmetric mode of the shell becomes $\omega^*_{1,2} = 5.05\omega_{1,2}$ and this value is used to non-dimensionalize the pulsating frequency Ω in the following figures. Fig. 3.4(a-d) shows the wide frequency spectrum of the maximum of the most significant axisymmetric modes $w_{1,0}/h$, $w_{3,0}/h$, $w_{5,0}/h$, $w_{7,0}/h$ (non-dimensionalized with respect to the thickness h of the shell) by increasing the pulsating forcing frequency Ω of the pulsatile pressure from the minimum heart rate of $5.65\,\text{rad/s}$ (around 54 beats per minute). The frequency range presented here is much wider the physiological regime.

In general, when the excitation frequency is small (see Fig. 3.4(a-d) for $\Omega/\omega^*_{1,2} < 0.2$), the shell vibrates axisymmetrically and the response is periodic. However, the existence of complex nonlinear dynamics is observed in Fig. 3.4(a-d) for the circular cylindrical shell subject to high frequency pulsation, i.e. $\Omega/\omega^*_{1,2} > 0.2$. Indeed, by increasing the frequency of the dynamic load, for certain ranges of the frequency spectrum, the axisymmetric modes become unstable in favor of the activation of the asymmetric modes through a series of period doubling (PD), pitchfork bifurcations (BP) and Neimark-Sacker bifurcations (TR).

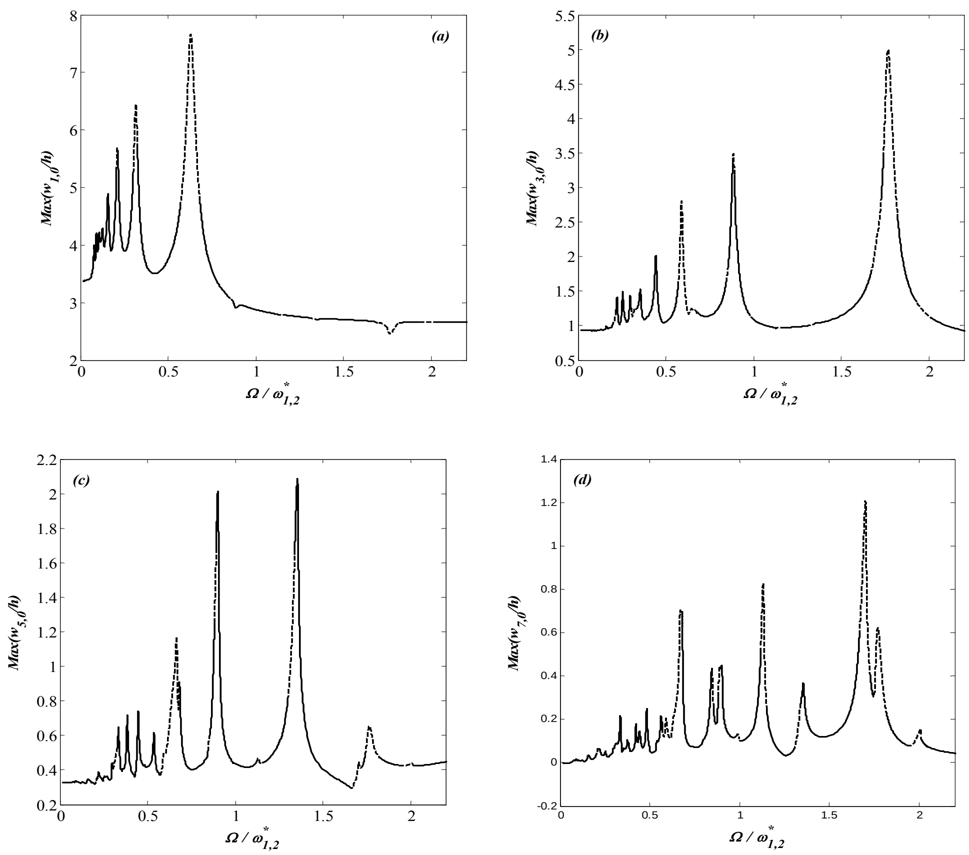

Fig. 3.4. Frequency response curve for the axisymmetric modes (*a*) $w_{1,0}$, (*b*) $w_{3,0}$, (*c*) $w_{5,0}$, (*d*) $w_{7,0}$ by varying the frequency Ω of the pulsatile pressure (model 48 *dof*); stable solution (continuous line), unstable solution (dashed line).

Specifically, a period doubling bifurcation is detected around $\Omega/\omega^*_{1,2} \simeq 0.2$ (Fig. 3.5) and a pitchfork bifurcation is found around $\Omega/\omega^*_{1,2} \simeq 0.3$ (Fig. 3.6). In these frequency ranges, both driven (with amplitude $w_{m,2,c}$) and companion (with amplitude $w_{m,2,s}$) modes are activated with several branches proving the complex dynamic behavior of the system as shown in Fig. 3.5(c-d) and Fig. 3.6(c-d). The amplitude of the companion modes detected is smaller compared to corresponding driven modes.

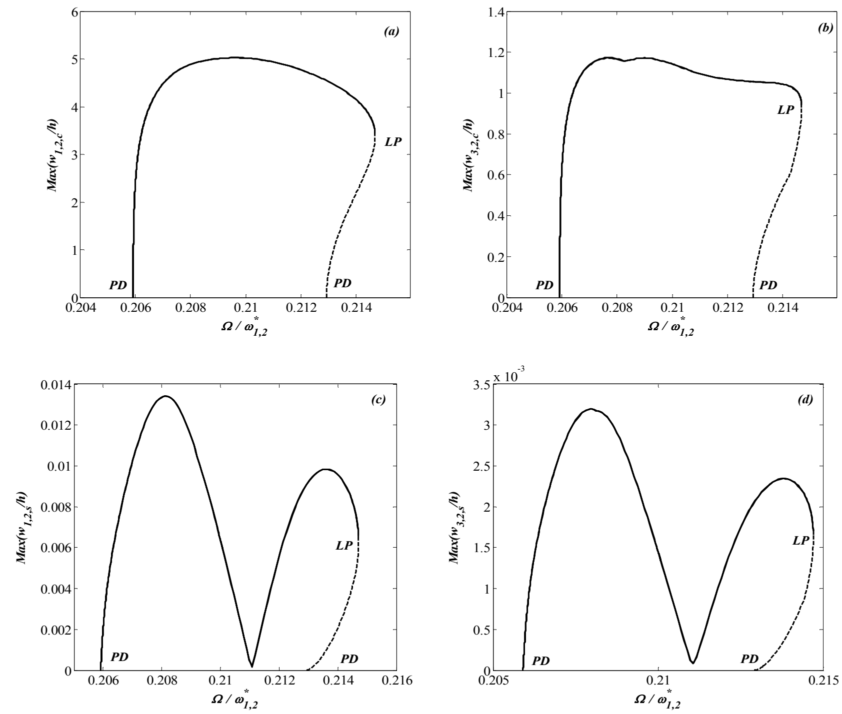

Fig. 3.5. Nondimensionalized amplitude of the asymmetric modes *(a)* $w_{1,2,c}$, *(b)* $w_{3,2,c}$, *(c)* $w_{1,2,s}$, *(d)* $w_{3,2,s}$ (model 48 *dof*) due to dynamic instability (PD, period doubling); stable solution (continuous line), unstable solution (dashed line); LP stands for limit point.

The companion mode has the same shape and natural frequency of the driven mode but rotated by $\pi/(2n)$, so it is orthogonal and presents an antinode in correspondence of the node of the driven mode. For reasons of symmetry, traveling waves can appear in one direction or in the opposite angular direction; both are solutions of the equations of motion. Indeed, it is important to observe that the companion mode arises as a consequence of the symmetry of the system. This phenomenon represents a fundamental difference with linear vibrations. Moreover, the presence of the companion mode in the shell response leads to the appearance of more complex phase relationships among the generalized coordinates.

In general, in circular shells under dynamic axial loads, period doubling bifurcations arise also for forcing frequencies close to twice the natural frequency of an asymmetric mode; this is usually referred as parametric instability [4]. Indeed, in this study, a period doubling bifurcation (dynamic instability) is detected around $\Omega/\omega^*_{1,2} \simeq 1.8$ (Fig. 3.7). Before the bifurcation, the system presents a stable periodic solution with frequency Ω while, after the bifurcation, a new solution is represented by the bifurcated branch with frequency $\Omega/2$ (double period).

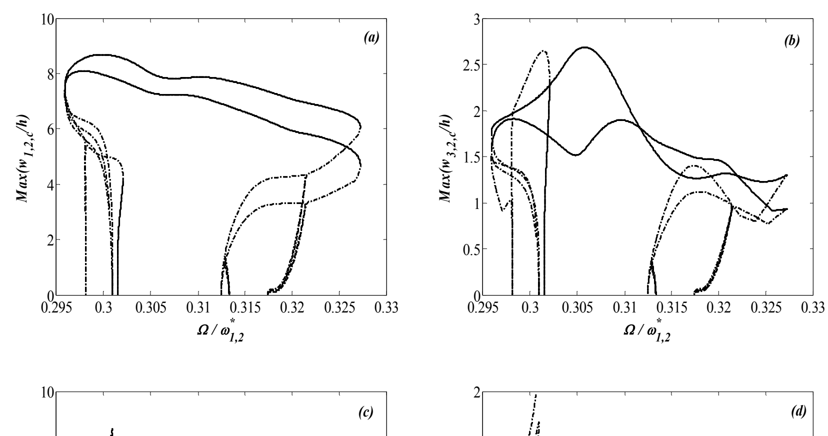

Fig. 3.6. Nondimensionalized amplitude of the asymmetric modes (*a*) $w_{1,2,c}$, (*b*) $w_{3,2,c}$, (*c*) $w_{1,2,s}$, (*d*) $w_{3,2,s}$ (model 48 *dof*) due to pitchfork bifurcation; stable solution (continuous line), unstable solution (dashed line).

As typical in nonlinear vibrations, multiple branches of solutions can be detected in the same frequency range (i.e. $\Omega/\omega_{1,2}^{*}\simeq 1.8$) as shown in Fig. 8 where only the companion modes are activated.

The fact that the frequency range $\Omega/\omega_{1,2}^{*}\simeq 1.8$ is slightly shifted with respect to $\Omega/\omega_{1,2}^{*}\simeq 2$ is due to the strong pulsatile component of the physiological pressure p_m that forces the natural frequency $\omega_{1,2}^{*}$ (associated here to its average value $\bar{p}_m$) to periodically change during the cycle. Moreover, modal interactions due to the nonlinearity may cause large-amplitude response of modes which linear analysis predicts to remain unexcited. In addition, complex responses with additional resonance peaks are often observed for nonlinear systems in the presence of internal resonances. Internal resonances are detected when the ratio of two or several natural frequencies is closed to the ratio of small integers (see Amabili [4]). Indeed in this study, since the ratio $\omega_{3,0}^{*}/\omega_{1,0}^{*}\simeq 3$, modal interactions between modes $w_{1,0}$ and $w_{3,0}$ can be observed as shown in Fig. 3.4(a-d) by calculating the frequency ratio between the peak of $w_{3,0}/h$ around $\Omega/\omega_{1,2}^{*}\simeq 1.8$ and the $w_{1,0}/h$ around $\Omega/\omega_{1,2}^{*}\simeq 0.6$.

Note here that $\Omega/\omega_{1,2}^{*}\simeq 0.6$ corresponds to $\Omega/\omega_{1,0}^{*}\simeq 1$ and therefore this is the main peak of the first axisymmetric mode ($n=0$). In fact, the frequency $\omega_{1,0}^{*}$ is equal to 273.46 rad/sec.

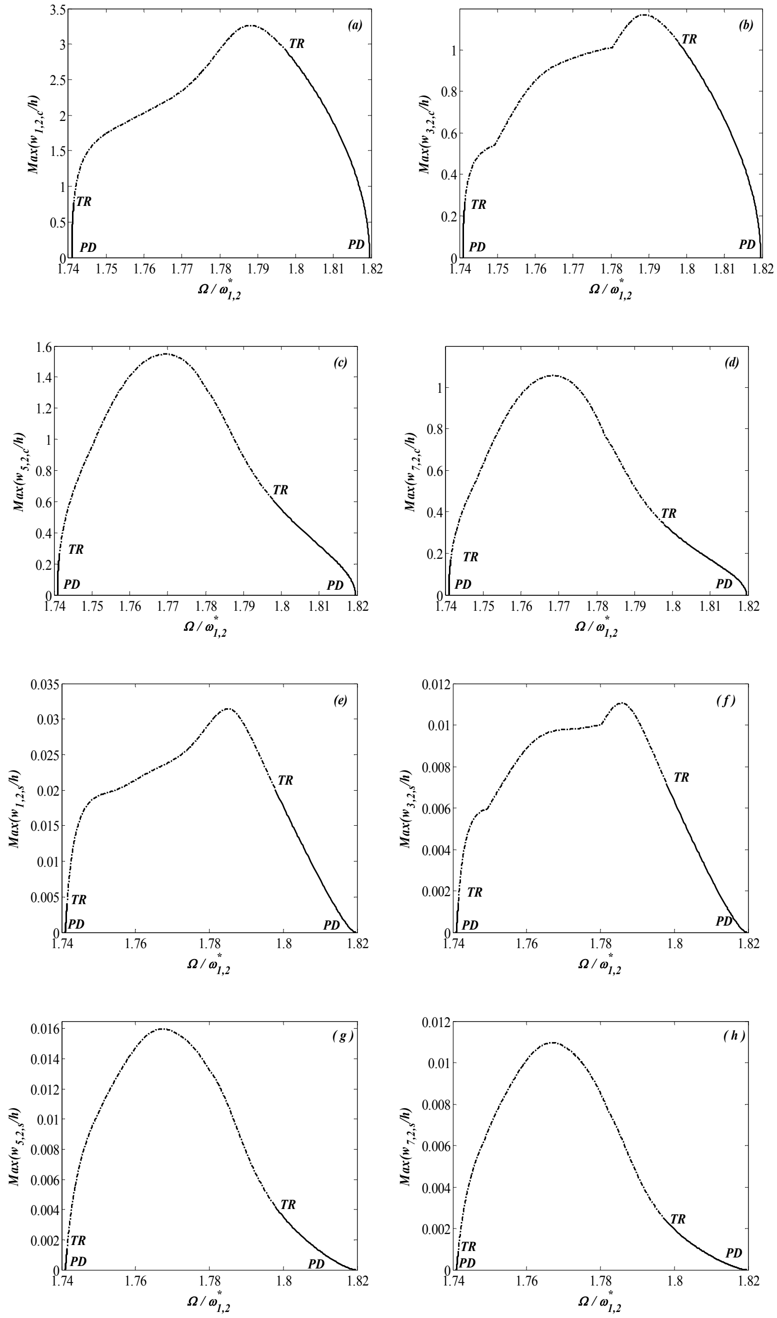

Fig. 3.7. Nondimensionalized amplitude of the asymmetric modes *(a)* $w_{1,2,c}$, *(b)* $w_{3,2,c}$, *(c)* $w_{5,2,c}$, *(d)* $w_{7,2,c}$, *(e)* $w_{1,2,s}$, *(f)* $w_{3,2,s}$, *(g)* $w_{5,2,s}$, *(h)* $w_{7,2,s}$ (model 48 *dof*) due to dynamic instability (PD, period doubling); stable solution (continuous line), unstable solution (dashed line). TR stands for Neimark-Sacker Bifurcation.

3.3.3 Frequency amplitude response to pulsatile transmural pressure in pulsatile flowing fluid

The next results represent the frequency-amplitude responses of the shell with asymmetric imperfections under the pulsatile transmural pressure given in Fig. 3.2(a) conveying the axial pulsatile flow in Fig. 3.2(b), obtained with the 51 *dof* model. As previously mentioned, in the following figures, the pulsating frequency Ω is made dimensionless with respect to the frequency of the first asymmetric mode of the shell $\omega_{1,2}^{*}$ under steady transmural pressure $\bar{p}_m$.

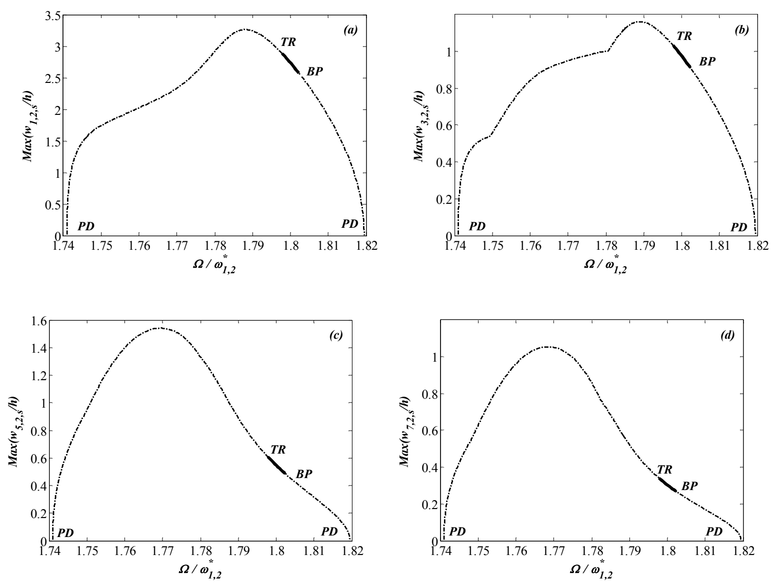

Fig. 3.8. Nondimensionalized amplitude of the asymmetric modes (*a*) $w_{1,2,s}$, (*b*) $w_{3,2,s}$, (*c*) $w_{5,2,s}$, (*d*) $w_{7,2,s}$ (model 48 *dof*) due to dynamic instability (PD, period doubling); stable solution (continuous line), unstable solution (dashed line). TR: Neimark-Sacker bifurcation; BP: pitchfork bifurcation.

In analogy with Fig. 3.4, Fig. 3.9 shows the wide frequency spectrum of the maximum of the axisymmetric modes $w_{1,0}/h$, $w_{3,0}/h, w_{5,0}/h, w_{7,0}/h$ (non-dimensionalized with respect to the thickness *h* of the shell) by increasing the pulsating forcing frequency Ω of the pulsatile pressure and pulsatile flow velocity from the minimum heart rate of 5.65 rad/s (around 54 beats per minute).

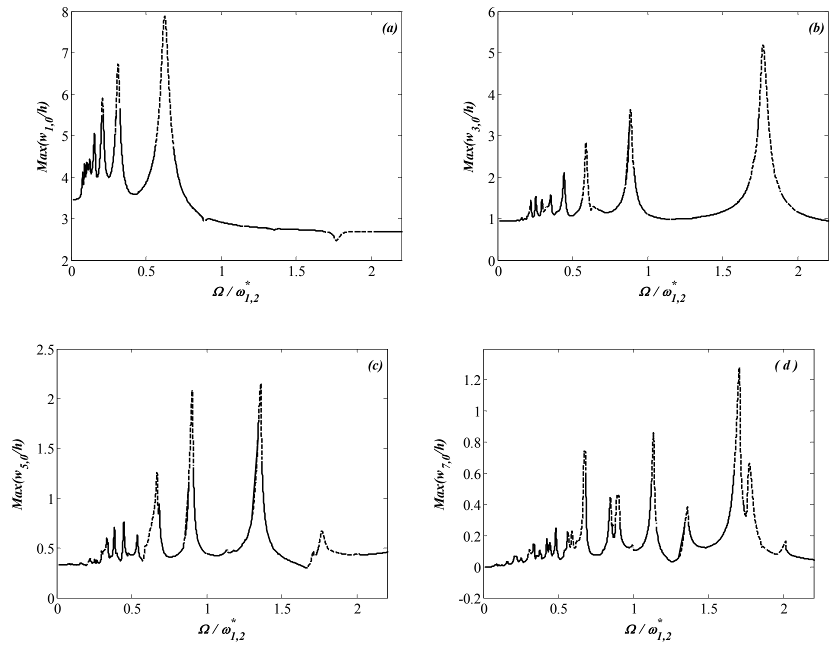

Fig. 3.9. Frequency response curve for the axisymmetric modes *(a)* $w_{1,0}$, *(b)* $w_{3,0}$, *(c)* $w_{5,0}$, *(d)* $w_{7,0}$ by varying the frequency Ω of the pulsatile pressure and flow (model 51 *dof*); stable solution (continuous line), unstable solution (dashed line).

As it can be seen by comparing Fig. 3.4 and Fig. 3.9, the general trend of the frequency response of the system subjected to pulsatile pressure in axial pulsatile flowing fluid accurately reproduces the one of the system subjected to the same pulsatile pressure in quiescent fluid. In the whole frequency spectrum, the amplitude of axisymmetric modes with an odd number of longitudinal half-waves $w_{1,0}$, $w_{3,0}$, $w_{5,0}$ is slightly bigger in the case of pulsatile flow. However, the main effect of the flowing fluid is to activate the axisymmetric modes with an even number of longitudinal half-waves $w_{2,0}$, $w_{4,0}$, $w_{6,0}$ as shown in Fig. 3.10.

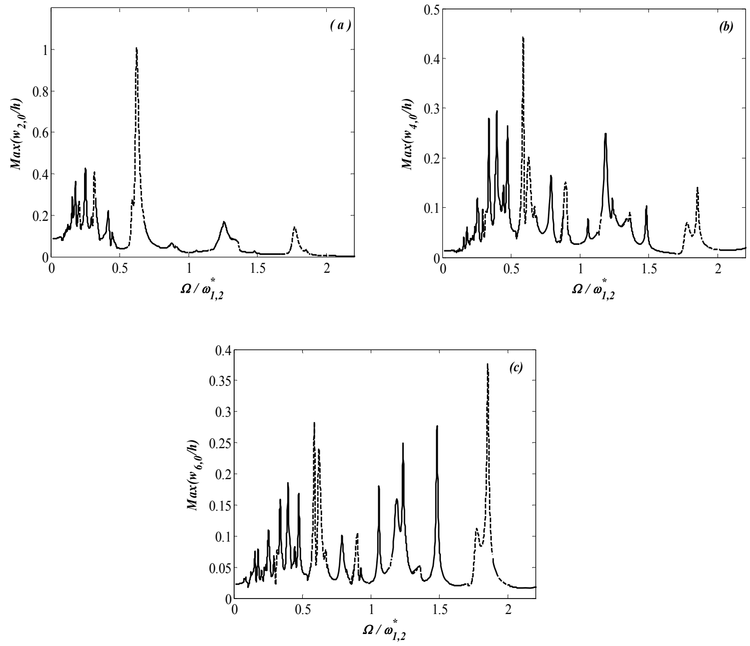

Fig. 3.10. Frequency response curve for the axisymmetric modes *(a)* $w_{2,0}$, *(b)* $w_{4,0}$, *(c)* $w_{6,0}$ by varying the frequency Ω of the pulsatile pressure and flow (model 51 *dof*); stable solution (continuous line), unstable solution (dashed line).

Also the bifurcations that activate the asymmetric modes are found in the same frequency ranges. In particular, a pitchfork bifurcation is found around $\Omega / \omega_{1,2}^{*} \simeq 0.3$ (Fig. 3.11) and two period doubling bifurcations are detected around $\Omega / \omega_{1,2}^{*} \simeq 0.2$ (Fig. 3.12) and $\Omega / \omega_{1,2}^{*} \simeq 1.8$ (Fig. 3.13), respectively. In all these regions of the frequency spectrum, the response of the system is not only axisymmetric, and both axisymmetric and asymmetric modes are excited.

An additional period doubling bifurcation (dynamic instability) is detected around $\Omega / \omega_{1,2}^{*} \simeq 2.28$ (Fig. 3.14). Before the bifurcation, the system presents a stable periodic solution with frequency Ω, while, after the bifurcation, the only stable solution is the bifurcated branch with frequency $\Omega/2$ (double period). This bifurcation exists only in presence of flow pulsation.

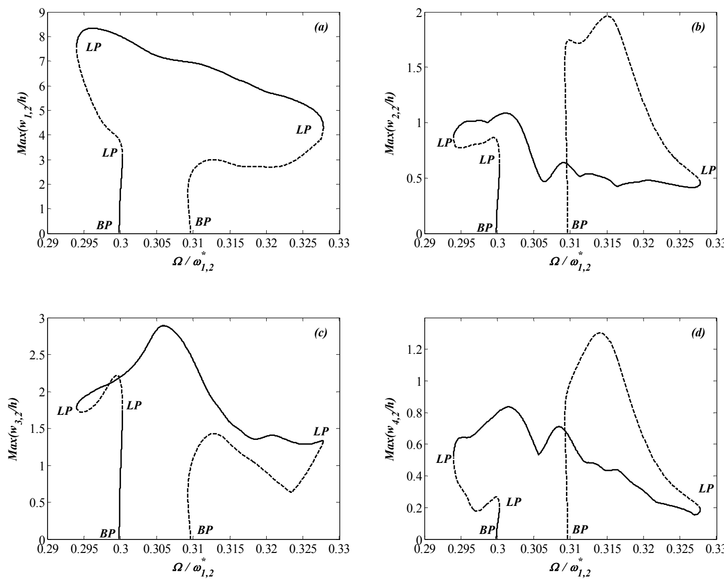

Fig. 3.11. Nondimensionalized amplitude of the asymmetric modes *(a)* $w_{1,2}$, *(b)* $w_{2,2}$, *(c)* $w_{3,2}$ and *(d)* $w_{4,2}$ due to a pitchfork bifurcation (BP) around $\Omega/\omega^*_{1,2} \simeq 0.3$; LP stands for limit point (model 51 *dof*).

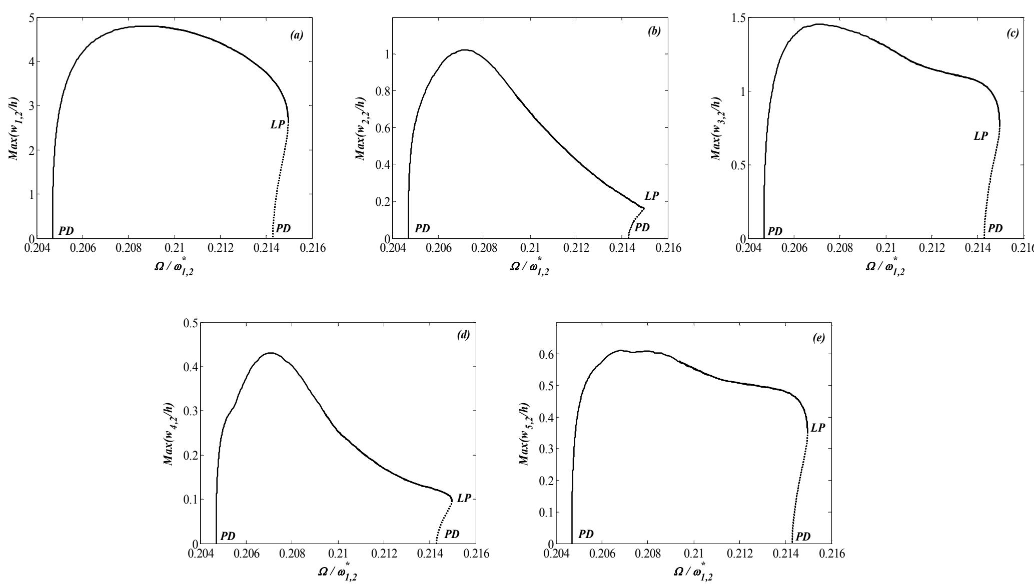

Fig. 3.12. Nondimensionalized amplitude of the asymmetric modes *(a)* $w_{1,2}$, *(b)* $w_{2,2}$, *(c)* $w_{3,2}$, *(d)* $w_{4,2}$ and *(e)* $w_{5,2}$ due to a dynamic instability (PD, period doubling) around $\Omega/\omega^*_{1,2} \simeq 0.2$; LP stands for limit point (model 51 *dof*).

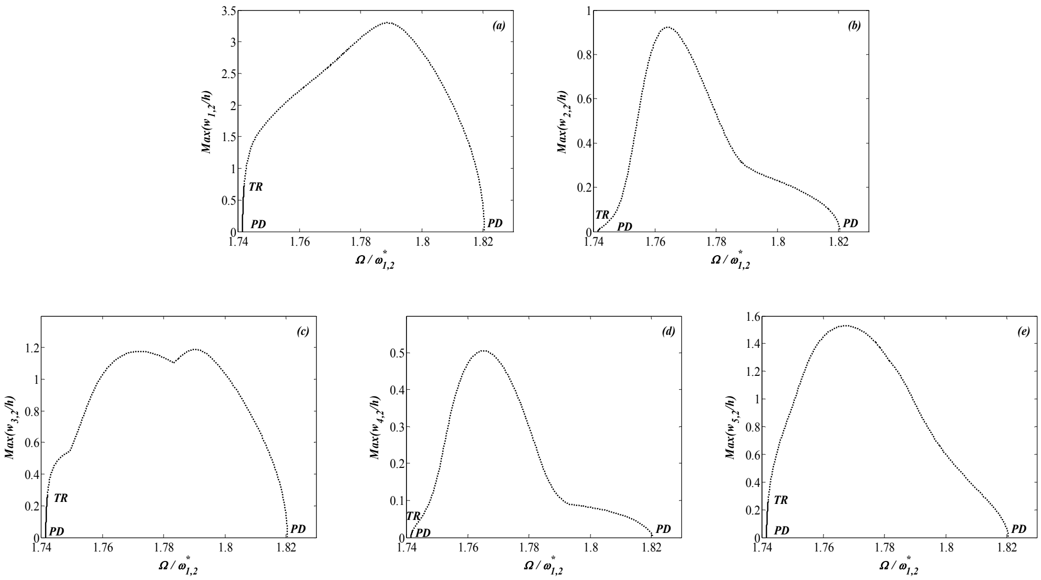

Fig. 3.13. Nondimensionalized amplitude of the asymmetric modes (*a*) $w_{1,2}$, (*b*) $w_{2,2}$, (*c*) $w_{3,2}$, (*d*) $w_{4,2}$, (*e*) $w_{5,2}$ due to dynamic instability (PD, period doubling) around $\Omega/\omega_{1,2}^{*} \simeq 1.78$ (model 51 *dof*).

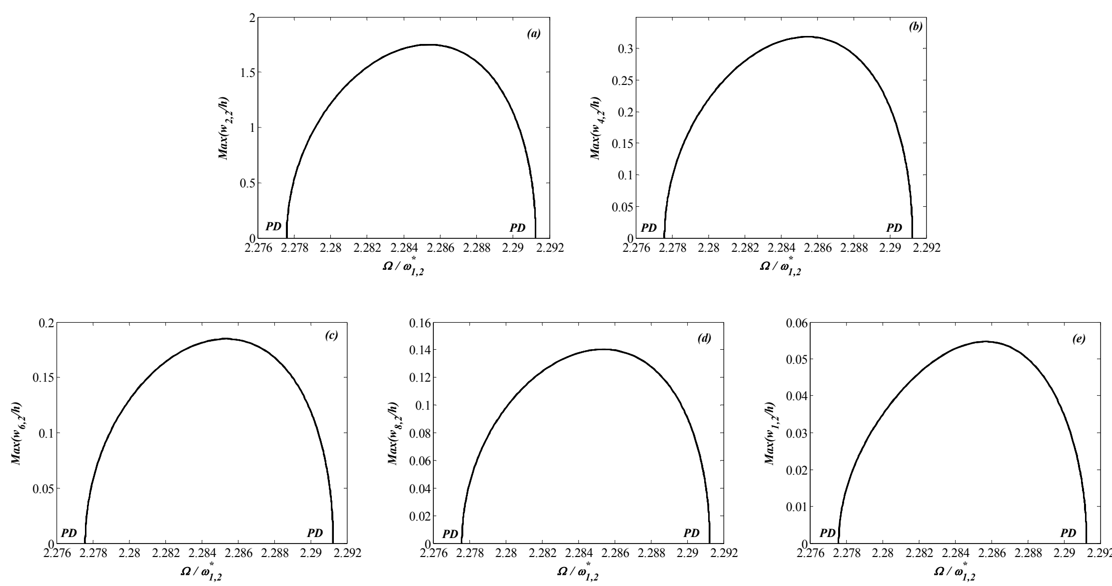

Fig. 3.14. Nondimensionalized amplitude of the asymmetric modes (*a*) $w_{2,2}$, (*b*) $w_{4,2}$, (*c*) $w_{6,2}$, (*d*) $w_{8,2}$, (*e*) $w_{1,2}$ due to dynamic instability (PD, period doubling) around $\Omega/\omega_{1,2}^{*} \simeq 2.28$ (model 51 *dof*).

3.4 Conclusions

In this study, a theoretical framework to model the dynamic behavior of a shell subjected to axial pulsatile pressure in quiescent and pulsatile flowing fluid is presented. The structural model has been developed by using the nonlinear Novozhilov shell theory for isotropic materials. A pulsatile time-dependent flow model based on the physiological waveforms of velocity and pressure during the heart beating period [154] has been taken into account. The fluid is modeled as a Newtonian pulsatile flow and it is formulated using a hybrid model that contains the unsteady effects obtained from the linear potential flow theory and the pulsatile viscous effects obtained from the unsteady time-averaged Navier-Stokes equations. The dynamic behavior of the shell studied here under pulsatile pressure and flow is presented via frequency-response curves and time histories.

In particular, the time responses reproduce the trend of the pulsating excitation; comparing the response for different values of the axial coordinate x, the gyroscopic effect associated to the presence of the axial flow can be noticed.

For low frequency periodic excitations, only axisymmetric modes with an odd number of longitudinal half waves are activated in case of shell subject to pulsatile pressure in quiescent fluid. However, in presence of pulsatile flowing fluid all the axisymmetric modes participate in the response. The frequency response curves of the system present a sequence of Neimark-Sacker, period doubling and pitchfork bifurcations showing the existence of complex nonlinear dynamics for circular cylindrical shells subject to high frequency periodic excitations.

The vibrations of shells containing quiescent fluid subjected to pulsatile transmural pressure are also studied involving driven and companion modes. Both families of modes are activated when bifurcations appear in the frequency spectrum of axisymmetric modes and both axisymmetric and asymmetric modes are excited in these frequency ranges.

The presence of companion modes in the shell response leads to the appearance of traveling waves around the shell. It has been found that the general trend of the frequency response of the axisymmetric modes of the system subjected to pulsatile pressure in axial pulsatile flowing fluid accurately reproduces the one in quiescent fluid with pulsatile pressure. The phenomenon of parametric resonance can be observed around $\Omega/\omega_{1,2}^{*} \simeq 1.8$; this instability takes place suddenly when a transition between stable to unstable regions occurs.

Concerning the limitations of the present work, a more accurate structural model should include the viscoelasticity and anisotropy of the graft material [150]. Nevertheless, this analysis represents the first study of nonlinear vibrations of shells with the mechanical properties of aortic replacements conducted with a global analysis tool (namely bifurcation analysis) capable of obtaining all stable and unstable solutions associated with aorta prosthesis under physiological and outside the physiological range of conditions of pulsatile transmural pressure and flow. In addition, this study provides, for the first time in literature, a fully coupled fluid-structure interaction model with deep insights in the nonlinear vibrations of circular cylindrical shells conveying pulsatile flow subjected to pulsatile pressure. Specifically, this study represents the first attempt to describe the nonlinear behavior of vascular prostheses whose dynamic response can cause unwanted hemodynamic effects leading to their failure. Since this type of analysis has never been performed for this type of biomechanical applications, a verification of the model can't be performed for now. However, future experimental activities have been planned by the authors in order to validate this preliminary study.

Acknowledgements

The authors would like to thank NSERC Discovery Grant Program, Qatar Foundation, first author Fonds de recherche du Québec – Nature et technologies (FRQNT), and the second author Canada Research Chair, for their financial support.

Chapter 4

Wave propagation phenomenon in shells conveying pulsatile flow

This chapter treats the introduction of the pulse-wave propagation phenomenon in the fluid-structure interaction model presented in Chapter 3. The circular cylindrical shell is made of an orthotropic material in order to closely represent the mechanical properties of the woven Dacron thoracic aortic prostheses. The theoretical framework and numerical results are presented for a single harmonic pulsation representing the first harmonic of the physiological waveforms of velocity and pressure during the heart beating period. The pressure gradient and the flow velocity are functions of both the axial coordinate and time. This implies a substantial complication in the formulation of the coupled Lagrange equations of motion. Indeed, considering a portion of the compliant vessel conveying pulsatile flow as a control volume, because of the wave propagation phenomenon within vessel, the net inflow of mass through the boundaries of the control volume is different from zero at any given time. In order to describe the appearance of travelling pressure and velocity waves in a confined incompressible flow, the deformable control volume has to accommodate the accumulation/subtraction of mass. This type of formulation is particularly interesting from a mathematical viewpoint, since even if the flow is governed by an elliptic equation (Laplace equation), the general behaviour of the fluid-structure interaction system is in many ways similar to that of a hyperbolic problem (wave equation). The paper "Nonlinear dynamics of shells conveying pulsatile flow with pulse-wave propagation. Theory and numerical results for a single harmonic pulsation" published in the Journal of Sound and Vibration [3] is presented.

NONLINEAR DYNAMICS OF SHELLS CONVEYING PULSATILE FLOW WITH PULSE-WAVE PROPAGATION

THEORY AND NUMERICAL RESULTS FOR A SINGLE HARMONIC PULSATION

Eleonora Tubaldi, Marco Amabili, Michael P. Païdoussis

Department of Mechanical Engineering, McGill University

Abstract

In deformable shells conveying pulsatile flow, oscillatory pressure changes cause local movements of the fluid and deformation of the shell wall, which propagate downstream in the form of a wave. In biomechanics, it is the propagation of the pulse that determines the pressure gradient during the flow at every location of the arterial tree. In this study, a woven Dacron aortic prosthesis is modelled as an orthotropic circular cylindrical shell described by means of the Novozhilov nonlinear shell theory. Flexible boundary conditions are considered to simulate connection with the remaining tissue. Nonlinear vibrations of the shell conveying pulsatile flow and subjected to pulsatile pressure are

investigated taking into account the effects of the pulse-wave propagation. For the first time in literature, coupled fluid-structure Lagrange equations of motion for a non-material volume with wave propagation in case of pulsatile flow are developed. The fluid is modeled as a Newtonian inviscid pulsatile flow and it is formulated using a hybrid model based on the linear potential flow theory and considering the unsteady viscous effects obtained from the unsteady time-averaged Navier-Stokes equations. Contributions of pressure and velocity propagation are also considered in the pressure drop along the shell and in the pulsatile frictional traction on the internal wall in the axial direction. A numerical bifurcation analysis employs a refined reduced order model to investigate the dynamic behavior of a pressurized Dacron aortic graft conveying blood flow. A pulsatile time-dependent blood flow model is considered by applying the first harmonic of the physiological waveforms of velocity and pressure during the heart beating period. Geometrically nonlinear vibration response to pulsatile flow and transmural pulsatile pressure, considering the propagation of pressure and velocity changes inside the shell, is presented here via frequency-response curves, time histories, bifurcation diagrams and Poincaré maps. It is shown that traveling waves of pressure and velocity cause a delay in the radial displacement of the shell at different values of the axial coordinate. The effect of different pulse wave velocities is also studied. Comparisons with the corresponding ideal case without wave propagation (i.e. with the same pulsatile velocity and pressure at any point of the shell) are discussed here. Bifurcation diagrams of Poincaré maps obtained from direct time integration have been used to study the system in the spectral neighborhood of the fundamental natural frequency. By increasing the forcing frequency, the response undergoes very complex nonlinear dynamics (chaos, amplitude modulation and period-doubling bifurcation), deeply investigated here.

4.1 Introduction

In deformable shells conveying pulsatile flow, pulsating pressure and flow propagate downstream in the form of progressive waves at the same wave speed. Lamb [158] considered for the first time in literature the problem of "the velocity of sound in a tube, as affected by the elasticity of the walls", thus involving both wave propagation and coupling between motions of the compressible fluid and the elastic tube wall. Lamb's work has been extended by numerous researchers dealing with the problem of wave-propagation in fluid-filled cylinders [159-161]. Unsteady flow characteristics and wave propagation through elastic tubes have also been studied more recently by Zamir [124].

In biomechanics, the pulsating flow of blood in the arteries causes wave propagation in the vessel walls and it is the propagation of the pulse that determines the pressure gradient during the flow at every location of the arterial tree. Womersley [62] was one of the first to experimentally study pulsatile flow performing his studies on the femoral artery of a dog. In these studies, it was the pressure gradient that was used to determine the flow characteristics indirectly. The interaction between the fluid and the vessel walls depends mostly on the physical-mechanical properties of the arterial tissues and the blood. In particular, the propagation velocity of pulse waves through the arteries is a means of diagnosing atherosclerotic arterial damage and determining the arterial tonus. The arterial pulse wave velocity (PWV) has been shown to be related to the underlying wall stiffness through the Moens-Korteweg [74] equation and has been used in a variety of applications for noninvasive estimation of arterial stiffness [75]. Taylor [76] showed that the presence of reflected waves causes the measured transmission velocity of a harmonic wave to vary greatly with frequency. Using the technique of measuring wave front velocities with a delay line (McDonald [77]), Nichols and McDonald [78] made an extensive study of the wave velocity in the ascending aorta of dogs, showing that phase velocity values, averaged over the first ten harmonics, were in close agreement with the velocity of the wave front. Their results also demonstrated that an increase in mean arterial pressure increases the pulse wave velocity.

Modeling three dimensional blood flow in compliant arteries is extremely challenging because of the complexity of solving the coupled blood flow/vessel deformation problem. For this reason in some studies (Taylor *et al.* [162] and Oshima *et al.*[163]), the rigid-wall approximation of the vessel is justified because the vessel diameter change during the cardiac cycle is observed to be approximately 5-10% in most of the major arteries; moreover, in diseased vessels, the arteries are even less compliant and, wall motion is further reduced. Perktold and Rappitsch [164] showed that in the case of carotid artery under normal conditions, wall deformability does not significantly alter the velocity field. They demonstrated the effect of wall distensibility on the flow and wall shear stress patterns by comparing with the results of a rigid wall model. In particular, they found that the rigid wall model agrees with the diastolic geometry at the end of the pulse period of the compliant model. Moreover, the flow rates at the common carotid inflow and at the external outflow were found to be equal in both cases. However, this holds true for arteries with small wall motion and may not be valid for arteries with larger wall deformation [165] (e.g. the thoracic aorta). In particular, assuming rigid vessel walls means neglecting the wave propagation phenomenon within the tube and consequently changing the character of the resultant solutions. For the analysis of flow in compliant vessels, Formaggia *et al.*[166] proposed an approach to couple three-dimensional domains of the original Navier-Stokes equations with a convenient one-dimensional domain used to describe wave propagation methods. In order to properly represent the propagation phenomenon due to the fluid-structure interaction and not to fluid compressibility, the 2D/3D fluid-structure problem has been coupled with a reduced one-dimensional model, which acts as an "absorbing" device for the waves exiting the computational domain. The appropriate framework for solving problems of computational modeling of blood flow in deforming vessels is the arbitrary Lagrangian-Eulerian (ALE) description of continuous media, in which the fluid and solid domains are allowed to move to follow the distensible vessels and the deforming fluid domain [162, 167]. The ALE approach has been employed, resulting in numerical models with a large number of degrees of freedom for developing realistic anatomic and physiologic models of the cardiovascular system. Figueroa *et al.* [165] developed a method for simulating blood flow in three-dimensional deformable models of arteries based on the coupling of the equations of the deformation of the vessel wall at the variational level as a boundary condition for the fluid domain, by using basic assumptions of a thin-walled structure. The computational effort in their method is comparable to that for rigid wall formulations while respecting the essential physics and enabling realistic simulation of wave-propagation phenomenon in the arterial system, as well as a linearized description of the wall deformation. Recently, Amabili *et al.* [89] investigated the stability of a straight aorta segment conveying blood flow using a numerical bifurcation analysis that employs a refined reduced-order model. In particular, they identified for the first time the nonlinear buckling (collapse) of the aorta as a possible reason behind the appearance of high stress regions at the inner layer of the aortic wall that may be responsible for the initiation of aortic dissection. A geometrically nonlinear shell theory that takes into account three anisotropic layers (intima, media and adventitia) and incompressible potential flow were used in the model. Virtually, the mechanics of all fluid-conveying conduits in mammals is of this type: arteries, veins, pulmonary and urinary passages. Such physiological systems have been and still are being studied intensively [5, 70, 82, 168]. The mechanisms leading to static collapse and flutter of collapsible tubes modelling blood flow in veins, pulmonary passages and the urethra have been deeply investigated [169-171] and they may be said to be well understood. Different numerical models have been used to simulate healthy aortic walls or aortas under pathological conditions [149, 172]. In recent models, material anisotropy, hyperelasticity of the aortic walls and residual stresses are considered in the analysis [173-175].

Artificial blood vessels can also be modeled as thin-walled shells conveying pulsatile flow. Theory for the dynamic stability of circular cylindrical shells subjected to incompressible subsonic liquid have been reported by Amabili *et al.* [137]. In vascular surgery, implants have been used in various circumstances of vascular maladies requiring replacements of components of the cardiovascular system, such as vessel patches for aneurysms. However, mismatching in mechanical properties of grafts and host arteries can cause unwanted hemodynamic effects leading to graft failure. In particular, the energy loss due to reflection and propagation of the pulse wave as it encounters the graft is considered to be the most significant mechanism leading to graft failure because of compliance mismatch [176, 177]. Large diameter (12-30 mm) vessel replacements with Dacron are the accepted clinical practice [94]: tightly woven, crimped and non-supported Dacron fabric prostheses are currently used to replace the thoracic and abdominal aorta with high rates of success [95]. Indeed, Dacron is easy to use, durable, and has manageable resistance to thrombosis formation when used in large caliber vessels; however, it has also distinctly different mechanical properties than the native aorta [150].

With respect to the interaction of the implant wall with the blood flow, Tubaldi *et al.* [2] studied the nonlinear vibrations of a shell with the mechanical properties of Dacron prostheses modeled as an isotropic cylindrical shell by means of the nonlinear Novozhilov shell theory under pulsatile pressure and flow. Specifically, physiological waveforms of velocity and pressure during the heart beating period were applied in order to investigate the effect of the dynamic loading conditions of the shell. Results displayed a complex nonlinear dynamics (sequence of period doubling and pitchfork bifurcations) for the circular cylindrical shell subjected to high frequency harmonic excitation (beyond of the physiological range). The pulsatile flow taken into account was ideal since it was assumed that, for a given time instant, the pulsatile pressure and flow velocity were the same for all points of the control volume. Consequently, the oscillatory pressure variations occurred simultaneously at every point of shell, making the fluid oscillate in bulk. Hence, the wave motion of local movements of the fluid caused by pressure changes in a deformable shell was not taken into account.

In this study, the effects of the pulse-wave propagation in the nonlinear vibrations of shells conveying pulsatile flow and subjected to pulsatile pressure are investigated. A circular cylindrical shell described by means of the nonlinear Novozhilov shell theory is used to model a Dacron thoracic aortic replacement. The material considered is orthotropic and the boundary conditions are flexible (distributed axial and rotational springs) to simulate the connection with the connective tissues. An input oscillatory pressure at the shell entrance is considered and it propagates down the shell causing a wave motion within the shell where, as a consequence, the pressure gradient and the flow velocity are functions of both the axial coordinate and time. Coupled fluid-structure Lagrange equations for a non-material volume with wave propagation in case of pulsatile flow are developed. The fluid is modeled as a Newtonian pulsatile flow, and pulsatile viscous effects are taken into account. Time responses of the radial displacement of the shell show the presence of a traveling wave propagating downstream. Frequency responses corresponding to two different pulse wave velocities are compared with the ideal case of pulsatile pressure and velocity without pulse wave propagation. Interesting and intricate nonlinear dynamics (such as chaos and amplitude modulations) are detected in the vicinity of the fundamental natural frequency, i.e. for a pulsation frequency larger than the physiological range. A two-to-one internal resonance is identified, giving rise to pitchfork bifurcations and leading to complex nonlinear dynamics.

This study provides an efficient fluid-structure interaction model that can be applied to simulate human aorta and aortic replacements, once coupled to a laminated anisotropic shell with hyperelastic material properties. In the present study, the numerical results are for a single harmonic pulsation spanning a frequency range much wider than the physiological range in order to investigate the nonlinear dynamics of the system.

4.2 Structural model

In this study, the nonlinear Novozhilov shell theory is applied to model the woven Dacron vascular prostheses currently used in aortic replacement surgery. The system under consideration is shown in Fig. 4.1 where $O(x, \theta, r)$ is the origin of the coordinate system, R is the mean radius, h is the shell thickness, L is the shell length, u is the shell displacement in the x-direction, v is the shell displacement in the θ-direction and w is the shell displacement in the r-direction (taken positive outward).

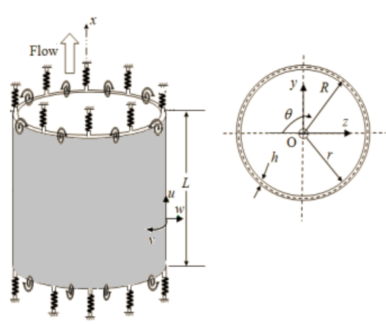

Fig. 4.1. Schematic of the shell conveying flow with boundary conditions at the shell ends.

The following boundary conditions, with flexible constraints to simulate connection with the remaining tissue, are applied at the shell ends $(x = 0, L)$,

$$v = w = 0, \quad N_x = -k_a\, u, \quad M_x = -k_r \left(\frac{\partial w}{\partial x}\right), \tag{4.1a-d}$$

where N_x is the axial stress per unit length, M_x is the bending moment per unit length and k_a is the stiffness of the distributed axial springs for asymmetric modes only since axisymmetric modes are not restrained axially and k_r is the stifness of the rotational springs applied at the shell edges for all modes. The flexible boundary conditions at the shell ends are assumed to simulate relatively stiff axial constraints for asymmetric deformations, enabling simulation of connective tissue stresses and remaining parts of the aorta, but allowing rotations [151] and axial axisymmetric motion.

4.2.1 Elastic strain energy and kinetic energy of the shell

A variational approach (already published by the authors in [2]) is employed to obtain the equations of motion for the aortic prosthesis segment. Specifically, the total kinetic energy of the shell is given by

$$T_s = \frac{1}{2}\rho_s\, h \int_0^{2\pi}\int_0^{L} \left\{\dot{u}^2 + \dot{v}^2 + \dot{w}^2\right\} \mathrm{d}\,x\, R\, \mathrm{d}\,\theta\,, \tag{4.2}$$

where ρ_s is the mass density of the shell and the overdot denotes the time derivative. The potential energy of the Dacron shell U_S is made up of two contributions:

$$U_S = U_{shell} + U_{spring}. \tag{4.3}$$

The elastic strain energy U_{shell} of the orthotropic circular cylindrical shell, assuming plane elastic stress, is given by

$$U_{shell} = \frac{1}{2}\int_0^{L}\int_0^{2\pi}\int_{-h/2}^{h/2} \left(\sigma_x\varepsilon_x + \sigma_\theta\varepsilon_\theta + \tau_{x\theta}\gamma_{x\theta}\right)\left(1 + z / R\right) \mathrm{d}\,x R\;\mathrm{d}\,\theta\;\mathrm{d}\,z\,, \tag{4.4}$$

where ε and γ are the strains, whose directions are indicated by the subscript, and σ and τ are the corresponding stresses. For orthotropic linearly elastic material, E_x and E_θ are the Young's moduli in x and θ direction, respectively, and $\nu_{\theta x}$ is the Poisson ratio; for the Possion ratios exist the expression $\nu_{\theta x} E_x = \nu_{x\theta} E_\theta$. The elastic strain energy can be written as

$$
\begin{aligned}
U_S = & \frac{1}{2}\frac{E_x h}{1-\nu_{\theta x}^2 E_x / E_\theta}\int_0^L\int_0^{2\pi}\left[\varepsilon_{x,0}^2+\frac{E_\theta}{E_x}\varepsilon_{\theta,0}^2+2\nu_{\theta x}\,\varepsilon_{x,0}\,\varepsilon_{\theta,0}+\frac{G_{x\theta}}{E_x}\left(1-\nu_{\theta x}^2 E_x/E_\theta\right)\gamma_{x\theta,0}^2\right]\mathrm{d}x\,R\,\mathrm{d}\theta \\
& +\frac{1}{2}\frac{E_x h^3}{12\left(1-\nu_{\theta x}^2 E_x / E_\theta\right)}\int_0^L\int_0^{2\pi}\left[k_x^2+\frac{E_\theta}{E_x}k_\theta^2+2\nu_{\theta x}\,k_x\,k_\theta+\frac{G_{x\theta}}{E_x}\left(1-\nu_{\theta x}^2 E_x/E_\theta\right)k_{x\theta}^2\right]\mathrm{d}x\,R\,\mathrm{d}\theta \\
& +\frac{1}{2}\frac{1}{R}\frac{E_x h^3}{6\left(1-\nu_{\theta x}^2 E_x / E_\theta\right)}\int_0^L\int_0^{2\pi}\left[\varepsilon_{x,0}\,k_x+\frac{E_\theta}{E_x}\varepsilon_{\theta,0}\,k_\theta+\nu_{\theta x}\,\varepsilon_{x,0}\,k_\theta+\nu_{\theta x}\,\varepsilon_{\theta,0}\,k_x\right. \\
& \left.+\frac{G_{x\theta}}{E_x}\left(1-\nu_{\theta x}^2 E_x/E_\theta\right)\gamma_{x\theta,0}\,k_{x\theta}\right]\mathrm{d}x\,R\,\mathrm{d}\theta,
\end{aligned}
\tag{4.5}
$$

where $\varepsilon_{i,0}$ and $\gamma_{i,0}$ are the strains referred to the middle surface of the shell, k_x and k_θ are the changes in curvature and $k_{x\theta}$ is the change in torsion of the shell middle surface. The strains of the middle surface and the changes in curvature and torsion can be written as nonlinear quadratic functions of the displacements u, v and w of points of the middle surface through strain-displacement relationships that are given in [38] for the nonlinear Novozhilov shell theory. The potential energy stored by the axial and rotational springs at the shell ends is given by

$$
U_{spring}=\frac{1}{2}\int_0^{2\pi}\left\{k_a\left[\left(u\right)_{x=0}\right]^2+k_a\left[\left(u\right)_{x=L}\right]^2+k_r\left[\left(\frac{\partial w}{\partial x}\right)_{x=0}\right]^2+k_r\left[\left(\frac{\partial w}{\partial x}\right)_{x=L}\right]^2\right\}R\,\mathrm{d}\theta. \tag{4.6}
$$

The shell displacements are discretized by using trigonometric expansions that identically satisfy the geometric boundary conditions; these trigonometric functions are the eigenmodes of the linear problem in case of simply supported boundary conditions. In particular,

$$
u(x,\theta,t)=\sum_{m=1}^{8}\left[u_{m,n,c}(t)\cos(n\theta)+u_{m,n,s}(t)\sin(n\theta)\right]\cos(\lambda_m x)+\sum_{m=1}^{3}u_{m,2n,c}(t)\cos(2n\theta)\cos(\lambda_m x)+\sum_{\substack{m=1\\ m\ odd}}^{11}u_{m,0}(t)\cos(\lambda_m x)+\sum_{\substack{m=2\\ m\ even}}^{6}u_{m,0}(t)\cos(\lambda_m x),
$$

$$v(x,\theta,t)=\sum_{m=1}^{8}\left[v_{m,n,s}(t)\sin(n\theta)+v_{m,n,c}(t)\cos(n\theta)\right]\sin(\lambda_m x)+\sum_{m=1}^{6}v_{m,2n,c}(t)\sin(2n\theta)\sin(\lambda_m x), \quad \text{(4.7a-c)}$$

$$w(x,\theta,t)=\sum_{m=1}^{8}\left[w_{m,n,c}(t)\cos(n\theta)+w_{m,n,s}(t)\sin(n\theta)\right]\sin(\lambda_m x)+\sum_{\substack{m=1\\ m\ odd}}^{11}w_{m,0}(t)\sin(\lambda_m x)+\sum_{\substack{m=2\\ m\ even}}^{6}w_{m,0}(t)\sin(\lambda_m x),$$

where n is the number of circumferential waves, m is the number of longitudinal half-waves, $\lambda_m = m\pi/L$, and t is the time; $u_{m,n}(t)$, $v_{m,n}(t)$ and $w_{m,n}(t)$ are the generalized coordinates [4]. A nonlinear term $\hat{u}(t)$ is added to the expansion of u (Eq.(4.7a)) to satisfy exactly the natural boundary condition Eq(4.1c); this term is obtained as a function of the generalized coordinates [37]. In case of geometric imperfections, which break the axial-symmetry of the system, it is possible to assume that, in addition to axisymmetric modes, only asymmetric modes with subscript c are activated. Thanks to the global discretization and in presence of imperfections, a reduced-order model can be considered by selecting terms with last subscript c yielding a model with 51 degrees of freedom (*dofs*).

4.3 Fluid-structure interaction model

The fluid is modeled as a Newtonian pulsatile flow. Although blood is a suspension of red blood cells, white blood cells, and platelets in plasma, it is well accepted that in medium-to-large arteries blood can be modeled as a viscous, incompressible Newtonian fluid. The proposed fluid-structure interaction model is used to obtain the unsteady fluid motion by potential flow theory and the pulsatile viscous effects for turbulent flow by the unsteady time-averaged Navier-Stokes equations. The high-frequency time dependence in the aortic flow, as well as the irrotational flow profiles at the ventricles, enable us to approximate the haemodynamics using the potential flow analysis [178].

The shell is considered to be conveying incompressible, isentropic and irrotational flow. The flow velocity vector $\mathbf{v_F}$ can be expressed as

$$\mathbf{v_F} = U(x,t)\mathbf{i} + \nabla\Phi, \tag{4.8}$$

where *U(x,t)* is the pulsatile axial flow velocity, which is periodic in time but is also function of the axial coordinate *x* as a consequence of the wave-propagation model assumed here, and Φ is the unsteady perturbation potential associated to the shell motion; **i** represents the unit vector in the *x*-direction. The unsteady perturbation potential Φ satisfies the Laplace equation

$$\nabla^2\Phi = \frac{\partial^2\Phi}{\partial x^2} + \frac{\partial^2\Phi}{\partial r^2} + \frac{1}{r}\frac{\partial\Phi}{\partial r} + \frac{1}{r^2}\frac{\partial^2\Phi}{\partial\theta^2} = 0. \tag{4.9}$$

In case of compliant vessels (i.e. time-dependent control volume), the Laplace equation (4.9) derives from an integral law of mass conservation by equating the rate of change of mass inside the control volume to the net inflow of mass (see Appendix I). If no cavitation occurs at the blood-aorta interface, the boundary condition expressing the contact between the shell wall and the flowing fluid is given by

$$\left(\frac{\partial\Phi}{\partial r}\right)_{r=R} = \left(\frac{\partial w}{\partial t} + U(x,t)\frac{\partial w}{\partial x}\right), \tag{4.10}$$

where *U(x,t)* is the pulsatile blood flow velocity distribution within the deformable shell. Eqs. (4.9) and (4.10) are satisfied if the solution for the velocity potential is given by [5]

$$\Phi = \sum_{m=1}^{M}\sum_{n=0}^{N}\frac{L}{m\pi}\frac{\mathrm{I}_n(m\,\pi\,r/L)}{\mathrm{I}_n'(m\,\pi\,R/L)}\left(\frac{\partial w_{m,n}}{\partial t} + U(x,t)\frac{\partial w_{m,n}}{\partial x}\right), \tag{4.11}$$

where I_n is the modified Bessel function of the first kind of order *n,* and I_n' is the derivative of I_n with respect to its argument.

The Dacron implant considered here is meant to be a replacement for the thoracic aorta. In this portion of the aorta, the Womersley number is very high ($\alpha \approx 15$) and for this reason the central mass of the fluid reciprocates almost like a solid core [155]. Indeed, the flow in the aorta and pulmonary trunk is similar to an entrance type flow that is not developed. Consequently, the validity of the assumption of the potential flow is justified by the fact that the core of the flow can be considered an inviscid region (potential core) that is surrounded by a thin developing boundary layer at the wall [179]. It is well known that in large arteries, because of the high value of the Womersley number and for Reynolds numbers sufficiently large, the boundary layer is very thin [75]. The roughness of the internal wall of the artery/implant influences the nature of the boundary layer. For this reason, pulsatile viscous effects are taken into account using the unsteady time-averaged Navier-Stokes equations. Finally, the vorticity in the aortic arch and the related effects as secondary flows (helices, vortices) typical of curved tubes, that can have a low impact on the flow in the thoracic aorta (straight tube) are neglected here. Frydrychowicz *et al*. [180] found that these secondary flow patterns predominantly depend on aortic diameter, shape (gothic, crook-shaped, cubic), angle, and age of the patients.

4.3.1 Fluid model: pulse-wave propagation of pulsatile velocity and pressure

In deformable shells conveying pulsatile flow, oscillatory pressure changes cause local movements of the fluid and deformation of the shell wall, which propagate downstream in the form of a wave. Hence, pressure and flow velocity distributions within the shell are oscillatory both in space and time and they can be represented by a Fourier series as follows:

$$U(x,t)=\bar{U}+\sum_{n=1}^{N}\left(a_{v,n}\cos\left(n\,\Omega\,(t-x/c_0)\right)+b_{v,n}\sin\left(n\,\Omega\,(t-x/c_0)\right)\right), \qquad (4.12a)$$

$$p_m(x,t)=\bar{p}_m+\sum_{n=1}^{N}\left(a_{p,n}\cos\left(n\,\Omega\,(t-x/c_0)\right)+b_{p,n}\sin\left(n\,\Omega\,(t-x/c_0)\right)\right), \qquad (4.12b)$$

where Ω is the heart rate, $\bar{p}_m$ and $\bar{U}$ represent the steady components of the pressure field and the pulsatile mean flow velocity, respectively, and N is the number of terms in the series expansion. The coefficients a_n and b_n are the Fourier cosine and sine coefficients, respectively, and are different for the velocity and pressure distributions; therefore they have a different second subscript. The wave speed c_0 is given approximately by the so called Moens-Korteweg formula, well-known in haemodynamics [74] ,

$$c_0 = \sqrt{\frac{E_\theta\ h}{2\ \rho_F\ R}}\ , \tag{4.13}$$

where E_θ is the circumferential Young's modulus of the shell and ρ_F is the constant fluid density.

The Moens-Korteweg formula has the limitation of neglecting the viscous effects of the flow. This hypothesis is acceptable for the case studied here, since for blood flow in large arteries the Reynolds and the Womersley numbers are much larger than one and consequently the inertial effects dominate over the viscous ones. Hence, neglecting the blood viscosity in the tube outside the boundary layer next to the wall is often acceptable for the wave propagation problem. Under these hypotheses, the pulse wave analysis of an ideal fluid flow provides a reasonable approximation [75]. However, in some studies, the effect of viscosity and the nonlinear convection terms in the Navier-Stokes equations have been included to represent the wave speed with more accuracy [181].

4.3.2 Energy of the Flow

Using Green's theorem, the total energy of the flowing fluid is given by

$$E_{TF} = \frac{1}{2}\rho_F \int_\Gamma \mathbf{v_F}\cdot\mathbf{v_F}\ \mathrm{d}\Gamma = \frac{1}{2}\rho_F \int_\Gamma \left(U+\nabla\Phi\right)\cdot\left(U+\nabla\Phi\right)\mathrm{d}\Gamma = \frac{1}{2}\rho_F\int_\Gamma U^2 \mathrm{d}\Gamma + \rho_F \int_\Gamma U\frac{\partial\Phi}{\partial x}\,\mathrm{d}\Gamma + \frac{1}{2}\rho_F\int_S \Phi\frac{\partial\Phi}{\partial n}\,\mathrm{d}S, \tag{4.14}$$

where Γ is the cylindrical fluid volume inside the shell (delimited by the length L); in the scalar product $\left(\mathbf{v_F}\cdot\mathbf{v_F}\right)$ the flow velocity vector $\mathbf{v_F}$ has been expressed as the sum of the pulsatile axial flow velocity $U(x,t)$, which is oscillatory both in space and time, and the unsteady perturbation potential $\Phi(x,t)$; S is the boundary surface of the volume Γ and n is the coordinate along the outer normal of the boundary. The integral associated with the term U^2 is neglected since it does not give any energy contribution that is function of the generalized coordinates, so it disappears in the equations of motion. The last integral on the right-hand side of Eq.(4.14) can be expressed as follows

$$\frac{1}{2}\rho_F \int_S \Phi \frac{\partial \Phi}{\partial n}\,\mathrm{d}S = \frac{1}{2}\rho_F \left[\int_{S_{in}} \Phi \frac{\partial \Phi}{\partial n}\,\mathrm{d}S_{in} + \int_{S_{out}} \Phi \frac{\partial \Phi}{\partial n}\,\mathrm{d}S_{out} + \int_{S_{shell}} \Phi \frac{\partial \Phi}{\partial n}\,\mathrm{d}S_{shell} \right], \tag{4.15}$$

where S_{in}, S_{out} and S_{shell} represent respectively the inlet, outlet and shell surface of the boundary surface S. Because of the phase delay due to the pulse wave propagation of pressure and velocity waves, it is found that

$$\int_{S_{in}} \Phi \frac{\partial \Phi}{\partial n}\,\mathrm{d}S_{in} \neq \int_{S_{out}} \Phi \frac{\partial \Phi}{\partial n}\,\mathrm{d}S_{out}. \tag{4.16}$$

As a consequence, these terms will appear in the modified gyroscopic and potential energy of the flow. The last integral of the right hand side of Eq. (4.15) can be divided into three terms: kinetic energy T_F , potential energy V_F and gyroscopic energy E_G , as given in the expression below

$$\frac{1}{2}\rho_F \int_{S_{shell}} \Phi \frac{\partial \Phi}{\partial n}\,\mathrm{d}S_{shell} = T_F + E_G - V_F, \tag{4.17}$$

where

$$T_F = \frac{1}{2}\rho_F \sum_{m=1}^{M}\sum_{n=0}^{N} \int_0^{2\pi}\int_0^L \frac{L}{m\pi}\frac{\mathrm{I}_n(m\pi R/L)}{\mathrm{I}_n^{'}(m\pi R/L)}\dot{w}_{m,n}^2\,\mathrm{d}x\,R\,\mathrm{d}\theta,$$

$$V_F = -\frac{1}{2}\rho_F \int_0^{2\pi}\int_0^L \sum_{m=1}^{M}\sum_{l=1}^{M}\sum_{n=0}^{N}\sum_{k=0}^{N} \frac{U(x,t)^2 L}{m\pi}\frac{\mathrm{I}_n(m\pi R/L)}{\mathrm{I}_n^{'}(m\pi R/L)}\frac{\partial w_{m,n}}{\partial x}\frac{\partial w_{l,k}}{\partial x}\,\mathrm{d}x\,R\,\mathrm{d}\theta, \tag{4.18a-c}$$

$$E_G = \frac{1}{2}\rho_F \int_0^{2\pi}\int_0^L \sum_{m=1}^{M}\sum_{n=0}^{N}\sum_{l=1}^{M}\sum_{k=0}^{N} \frac{U(x,t)\,L}{m\pi}\frac{\mathrm{I}_n(m\pi R/L)}{\mathrm{I}_n^{'}(m\pi R/L)}\left(\dot{w}_{m,n}\frac{\partial w_{l,k}}{\partial x} + \dot{w}_{l,k}\frac{\partial w_{m,n}}{\partial x}\right)\mathrm{d}x\,R\,\mathrm{d}\theta.$$

Since the velocity $U(x,t)$ is time and space dependent, new terms associated to V_F and E_G will appear in the Lagrange equations of motions; the subscript G stands for gyroscopic. Moreover, it is important to notice that in this case, the potential energy V_F cannot be simplified in the expression with two summations [4] used for the case without wave propagation, since *U(x,t)* depends on the axial coordinate.

4.3.3 Pulsatile viscous effects

The unsteady time-averaged Navier-Stokes equations [26, 37] are employed to calculate the pulsatile viscous effects. A variable mean transmural pressure ΔP_{tm}, representing the pressure drop along the shell, and an axial frictional traction force τ_x, acting on the internal wall, are introduced in the model. This type of hybrid model is particularly efficient from the computational point of view. In particular, in case of unsteady flow, the fluid pressure P on the shell surface takes on the following expression

$$P(x,R,t) = -\rho_F\left(\frac{f}{4R}U(x,t)^2 + \frac{\partial U(x,t)}{\partial t}\right)x + P(0,R,t), \tag{4.19}$$

where the friction factor f can be calculated by using the experimental Colebrook equation (assuming $f = 0.097$). It is assumed that $P(L/2,R)=0$, so that P is directly added to the pulsatile uniform pressure differential p_m acting on the shell wall (defined as the difference between the internal and external pressures on the shell wall), assumed positive outward. Therefore, the expression for P is given by

$$P(x,R,t) = \rho_F\left(\frac{f}{4R}U(x,t)^2 + \frac{\partial U(x,t)}{\partial t}\right)\left(\frac{L}{2} - x\right). \tag{4.20}$$

The pressure drop in the shell is

$$\Delta P_{0,L} = P(0,R,t) - P(L,R,t) = \rho_F\left(\frac{f}{4R}U(x,t)^2 + \frac{\partial U(x,t)}{\partial t}\right)L. \tag{4.21}$$

The pulsatile axial friction traction force per unit area [182] is

$$\tau_x(x,t,R) = -\rho_F\left(f\frac{U(x,t)^2}{8} + \frac{R}{2}\frac{\partial U(x,t)}{\partial t}\right). \tag{4.22}$$

4.3.4 Lagrange Equations of Motion for Open Systems

The potential and kinetic energies of the shell and of the fluid are coupled in the Lagrange equations of motion. The vector $\mathbf{q}$ that includes all the generalized coordinates $u_{m,j}(t), v_{m,j}(t), w_{m,j}(t)$ is introduced for sake of simplicity in the notation; the generic generalized coordinate is indicated by q_j. The Lagrange equations of motion for open systems [183], in case of pulsatile flow with pulse wave propagation, can be written as follows:

$$\begin{aligned}&\frac{d}{dt}\left[\frac{\partial\left(T_S+T_F+\bar{E}_G\right)}{\partial\dot{q}_j}\right]-\frac{\partial\bar{E}_G}{\partial q_j}+\frac{\partial\left(U_S+\bar{V}_F\right)}{\partial q_j}\\&+\frac{1}{2}\rho_F\int_S\frac{\partial}{\partial\dot{q}_j}\left(\mathbf{v_F}\cdot\mathbf{v_F}\right)\left(\mathbf{v_F}-\mathbf{v_S}\right)\cdot\mathbf{n}\,\mathrm{d}S-\frac{1}{2}\rho_F\int_S\left(\mathbf{v_F}\cdot\mathbf{v_F}\right)\left(\frac{\partial\mathbf{v_F}}{\partial\dot{q}_j}-\frac{\partial\mathbf{v_S}}{\partial\dot{q}_j}\right)\cdot\mathbf{n}\,\mathrm{d}S=Q_j,\quad j=1\ldots N_T,\end{aligned}\tag{4.23}$$

where T_S, T_F and U_S have been previously defined in Eq. (4.2), Eq. (4.18a) and Eq. (4.3), respectively. The modified potential energy $\bar{V}_F$ and the modified gyroscopic energy $\bar{E}_G$ of the flow are calculated not only at the shell wall, as given by Eq. (4.18b,c), but also at the inlet and outlet surfaces (see Appendix J). The vectors $\mathbf{v_F}$ and $\mathbf{v_S}$ are the velocity vectors of the fluid and of the structure at a generic point on the boundary surface S, respectively; N_T is the number of degrees of freedom. The surface integrals are evaluated at the boundary surface S of the volume Γ, and $\mathbf{n}$ denotes the outer normal unit vector at that surface. The last two terms on the left hand side of Eq. (4.23) represent the correction terms in the version of the Lagrange equations of motion for a non-material volume containing the flux of kinetic energy appearing to be transported through the surface of the control volume (see Appendix G).

The generalized external forces Q_j are represented by

$$Q_j=-\rho_F\left(\frac{\partial}{\partial q_j}\int_\Gamma U\frac{\partial\Phi}{\partial x}\,\mathrm{d}\Gamma+\frac{\partial}{\partial\dot{q}_j}\int_\Gamma U\frac{\partial\Phi}{\partial x}\,\mathrm{d}\Gamma\right)-\frac{\partial F}{\partial\dot{q}_j}+\frac{\partial W}{\partial q_j},\tag{4.24}$$

where the first two integrals on the right-hand side represent an effect of the pulse-wave propagation inside the shell and are included in Q_j since they do not depend on the generalized coordinates and their derivatives, being therefore equivalent to a load; and the last two terms are related to the viscous damping and the pulsatile viscous effects, being

$$F = \frac{1}{2} c \int_0^{2\pi} \int_0^L \left(\dot{u}^2 + \dot{v}^2 + \dot{w}^2 \right) \mathrm{d}\, x \, R \, \mathrm{d}\, \theta \, , \tag{4.25a}$$

$$W = \int_0^{2\pi} \int_0^L \left[\left(\Delta P_{0,L} + p_m \right) w + \tau_x u \right] \mathrm{d}\, x \, R \, \mathrm{d}\, \theta \, , \tag{4.25b}$$

where c is the viscous damping coefficient and the expression of the virtual work W done by the displacement independent pressure load is exact for infinitesimal deflection w of the shell and it can still be considered a good approximation for moderate deflections of thin shells. On the contrary, for large deformations, it is crucial to model the pressure as a displacement dependent load (see Appendix K).

The resulting equations of motion for the system are given in matrix form by the following expression

$$(\mathbf{M_S} + \mathbf{M_F})\ddot{\mathbf{q}} + \left(\mathbf{C} + \mathbf{C_F}\right)\dot{\mathbf{q}} + \left[\mathbf{K_S} + \mathbf{K_F} + \mathbf{N_2}(\mathbf{q}) + \mathbf{N_3}(\mathbf{q}, \mathbf{q})\right]\mathbf{q} = \mathbf{Q}, \tag{4.26}$$

where $\mathbf{M_S}$ and $\mathbf{M_F}$ are the mass matrices of the shell and the fluid, respectively, $\mathbf{C_F}$ is the gyroscopic matrix due to the flow, $\mathbf{K_F}$ is stiffness matrix due to the flow and $\mathbf{C}$ the damping matrix that is added to the equations of motion in order to simulate dissipation. Moreover, $\mathbf{K_S}$ is the linear stiffness matrix of the shell, $\mathbf{N_2}$ gives the quadratic nonlinear stiffness terms of the shell, $\mathbf{N_3}$ denotes the cubic nonlinear terms of the shell, and $\mathbf{Q}$ is the vector representing the external loads (including viscous effects and pulsatile effects). In order to obtain the equations of motion in a suitable form for numerical implementation, the system Eq. (4.26) is multiplied by the inverse of the mass matrix and is then written in state-space form as follows:

$$\begin{cases} \dot{\mathbf{q}} = \mathbf{y} \\ \dot{\mathbf{y}} = -\mathbf{M}^{-1}\left(\mathbf{C}+\mathbf{C_F}\right)\dot{\mathbf{q}} - \left[\mathbf{M}^{-1}\left(\mathbf{K_S}+\mathbf{K_F}\right)+\mathbf{M}^{-1}\mathbf{N_2(q)}+\mathbf{M}^{-1}\mathbf{N_3(q,q)}\right]\mathbf{q}+\mathbf{M}^{-1}\mathbf{Q}, \end{cases} \tag{4.27}$$

where $\mathbf{y}$ is the vector of the generalized velocities and $\mathbf{M}$ is the total mass matrix $\mathbf{M} = \mathbf{M_S} + \mathbf{M_F}$; the dissipation term $\mathbf{M}^{-1}\mathbf{C}$ is given by

$$\mathbf{M}^{-1}\,\mathbf{C} = \begin{bmatrix} 2\omega_1\varsigma_1 & \cdots & 0 \\ 0 & \ddots & 0 \\ 0 & \cdots & 2\omega_{N_T}\varsigma_{N_T} \end{bmatrix}, \tag{4.28}$$

and it is related to the modal damping ratio ς_j and the natural frequency ω_j (rad/s) of each generalized coordinate q_j. Matrix (4.28) is assumed to be diagonal in order to use modal damping. In general, experiments are necessary in order to determine the damping ratios. It must also be noticed that the damping ratios obtained for small amplitude vibrations are generally increasing in case of large amplitude vibrations, and this increase can be very large [184, 185].

4.4 Numerical results

The equations of motion have been obtained by using the *Mathematica* software [133] in order to perform analytical surface integrals of trigonometric functions. A non-dimensionalization of variables is performed for computational convenience: the frequencies are divided by the natural radian frequency ω_{12} of the fundamental mode, and the vibration amplitudes are divided by the shell thickness h. The set of nonlinear ordinary differential equations Eq. (4.27) has been solved by using the software AUTO [106] that is capable of continuation of the solution, bifurcation analysis and branch switching by using the pseudo-arclength continuation and collocation method. Here, the nonlinear analysis of the aortic prosthesis is divided into three steps. First, the pulsatile pressure is increased at zero flow velocity up to the desired value (Fig. 4.2(b)), giving the wall deformation and the initial stresses. In the second step, the pulsatile blood flow velocity is used as a bifurcation parameter until it reaches the physiological conditions (Fig. 4.2(a)).

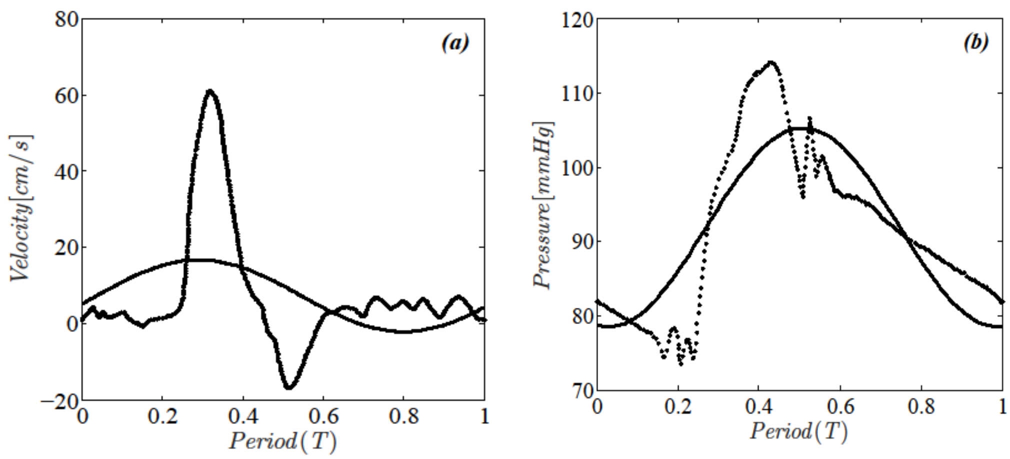

Fig. 4.2. *(a)* Flow velocity and *(b)* transmural pressure values in the aortic segment; dotted line: physiological data [186], continuous line: Fourier series N=1.

Once the desired pulsatile flow velocity is reached, the bifurcation continues by considering the pulsation frequency Ω (heart pulse) as the continuation parameter to obtain the frequency-amplitude response of the aortic prosthesis. However, the software AUTO, cannot follow quasi-periodic and chaotic solutions. Hence, a home-developed continuation code performing direct integration of the equations of motion by means of IMSL DIVPAG Fortran routine, which uses the Adams-Gear integration scheme, has been applied to investigate the nonlinear response of the system in those frequency ranges. In the direct integration method, at any increment of the bifurcation parameter, which is the excitation frequency, the solution is restarted by using the solution at the previous point, plus a small perturbation, as the initial condition. The Poincaré maps and the corresponding bifurcation diagrams obtained by this method allow studying very complex nonlinear dynamics.

In this study, the characteristics of the Dacron implant under consideration, referring to Fig. 4.1, are: L =0.18 m, h=0.361 mm, R=0.015 m, $\nu_{\theta x}$ =0.3, E_θ=12 MPa, E_x=0.87 MPa, ρ_S=1247 kg/m^3, ρ_F=1050 kg/m^3, k_a=10^3 N/m^2, k_r=10^2 N/rad. These material properties have been chosen in agreement with previous studies [150, 187, 188] conducted on Dacron grafts currently used in aortic replacements.

The physiological waveforms of velocity and pressure [186] in the thoracic aorta are considered for the Dacron replacement and they are expressed in terms of Fourier series. As a first approximation, only the first harmonic of the Fourier expansion is considered to describe the pulsatile pressure and flow, as shown in Fig. 4.2. The potential effect of the introduction of the replacement graft on the alteration of the physiological waveforms of pressure and velocity is neglected here. Indeed, this is a very interesting topic that unfortunately hasn't been deeply investigated in literature because of its complexity. In particular, both geometrical and material mismatch of the artificial vessel with respect to the native aorta play a role in this regard. To the knowledge of the authors, some studies [189, 190] that addressed this subject found that the effect of the insertion in a thoracic aortic replacement affects slightly the shape of the pressure and velocity waveforms without altering the general trend of the function (mean flow values and main peaks of the function). For this reason, it is assumed that the first harmonic of the Fourier series used to represent the pulsatile flow in this study, is not affected by this slight alteration.

Moreover, two different pulse wave velocities c_0 have been considered in order to study the effect of this parameter on the dynamic response of the vessel with wave propagation.

In particular, the mean aortic pulse wave velocity c_0 = 3.6 m/s [191] has been compared to the pulse wave velocity c_0 = 11.72 m/s obtained with the Moens-Korteweg formula (Eq. (4.13)) for the Dacron implant considered here.

4.4.1 Time responses for pulsatile transmural pressure and flow

The time response of the Dacron implant subjected to steady plus the first harmonic component of physiological waveforms of velocity and pressure during the heart beating period is presented in Fig. 4.3; in particular, the shell radial displacement w, non-dimensionalized with respect to the thickness h, is shown at the angular coordinate $\theta = 0$ versus time and at three different axial positions x=$L/4$, $L/2$, $3L/4$. The shell transverse sections are circular at any point since only axisymmetric modes are activated in this case.

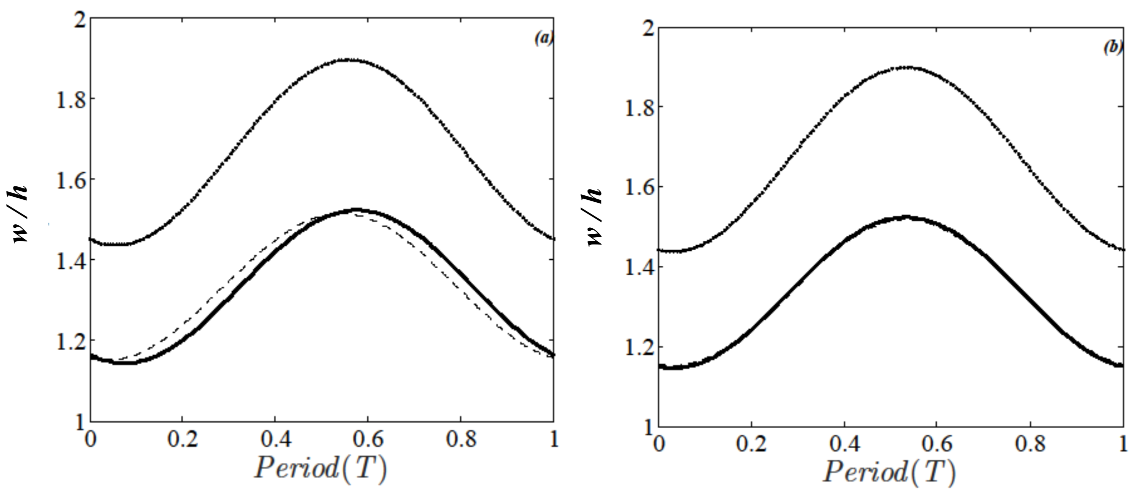

Fig. 4.3. Time response of the nondimensionalized radial displacement *w/h* under pulsatile pressure and velocity *(a)* with wave propagation with the mean aortic pulse wave velocity *(b)* without wave propagation; dashed line: $x = L/4$, dotted line: $x = L/2$, continuous line: $x = 3L/4$.

The dynamic response of deformable shells conveying pulsatile flow with wave propagation with the mean aortic pulse wave velocity obtained with the software AUTO is shown in Fig. 4.3(a) and can be compared to the response of the shell without wave propagation, i.e. with the same oscillatory pressure and velocity at all the points of the control volume simultaneously, which is presented in Fig. 4.3(b). The approximation implied in the case without wave propagation is acceptable only when the shell presents a low elasticity allowing the wave speed to be much higher than the maximum flow velocity. In Fig. 4.3(a), because of the phenomenon of pulse-wave propagation, the shell radial displacement for $x = 3L/4$ is clearly delayed with respect to the one for $x = L/4$, whereas in Fig. 4.3(b) the two corresponding curves are overlapped.

4.4.2 Frequency-amplitude response: wave propagation phenomenon with the mean aortic pulse wave velocity versus the non-propagation case

The effect of the wave motion with the mean aortic pulse wave velocity on the nonlinear vibrations of shells conveying pulsatile flow is discussed here by means of frequency-amplitude responses through the comparison with the case without wave propagation. When the shell is pressurized with the steady transmural pressure $\bar{p}_m = 12253\ \mathrm{Pa}$, which is the mean value obtained in Fig. 4.2(b), the frequency of the first axisymmetric mode becomes $\omega_{1,0}^* = 5.894\,\omega_{1,2} = 35.75\ \mathrm{Hz}$ (here $\omega_{1,2}$ is the natural frequency of the non-pressurized mode m=1, n=2) and this value is used to non-dimensionalize the pulsating frequency Ω in the following figures. The superscript * is used to indicate the natural frequency of the pressurized shell.

Fig. 4.4 presents the maximum amplitude of the response versus the non-dimensional pulsating frequency Ω for the most significant axisymmetric modes $w_{1,0}/h$ and $w_{2,0}/h$ (non-dimensionalized with respect to the thickness h of the shell) obtained by increasing the pulsating frequency. In particular, Fig. 4.4(a-b) shows the frequency-amplitude responses of the case with wave propagation and Fig. 4.4(c-d) refer to the case without wave propagation.

The frequency range presented here is much wider than the physiological one, which is limited to $\Omega/\omega^{*}_{1,0} \leq 0.0931$ with the assumption that no higher harmonics are introduced by the pulsation (which is not the case since higher harmonics are actually present, as shown in Fig. 4.2).

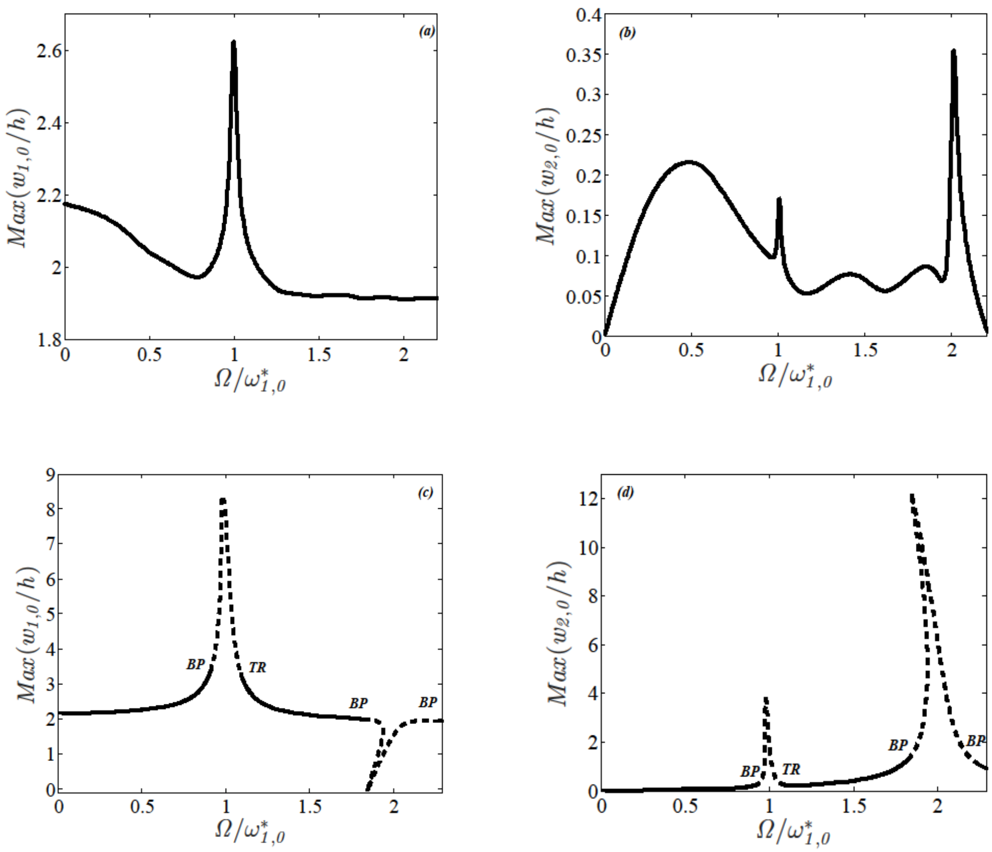

Fig. 4.4. Frequency response curves for the axisymmetric modes: *(a)* $w_{1,0}$, *(b)* $w_{2,0}$ with wave propagation with mean aortic pulse wave velocity; *(c)* $w_{1,0}$, *(d)* $w_{2,0}$ without wave propagation, obtained by varying the frequency Ω; stable solution (continuous line), unstable solution (dashed line), pitchfork bifurcation (BP) and Neimark-Sacker bifurcation (TR); $\zeta = 0.1$.

In both cases, the modal damping ratio $\zeta = 0.1$ is assumed for all the generalized coordinates. The shell subjected to wave propagation vibrates axisymmetrically and the response is periodic throughout the frequency range investigated.

On the other hand, the case without wave propagation presents two pitchfork bifurcations (BP) close to the linear resonance, *i.e.* $\Omega / \omega_{1,0}^{*} \approx 1$, and around $\Omega / \omega_{1,0}^{*} \approx 2$, that causes the activation of the asymmetric modes (specifically modes with n=2), as shown in Fig. 4.5 and Fig. 4.6, respectively.

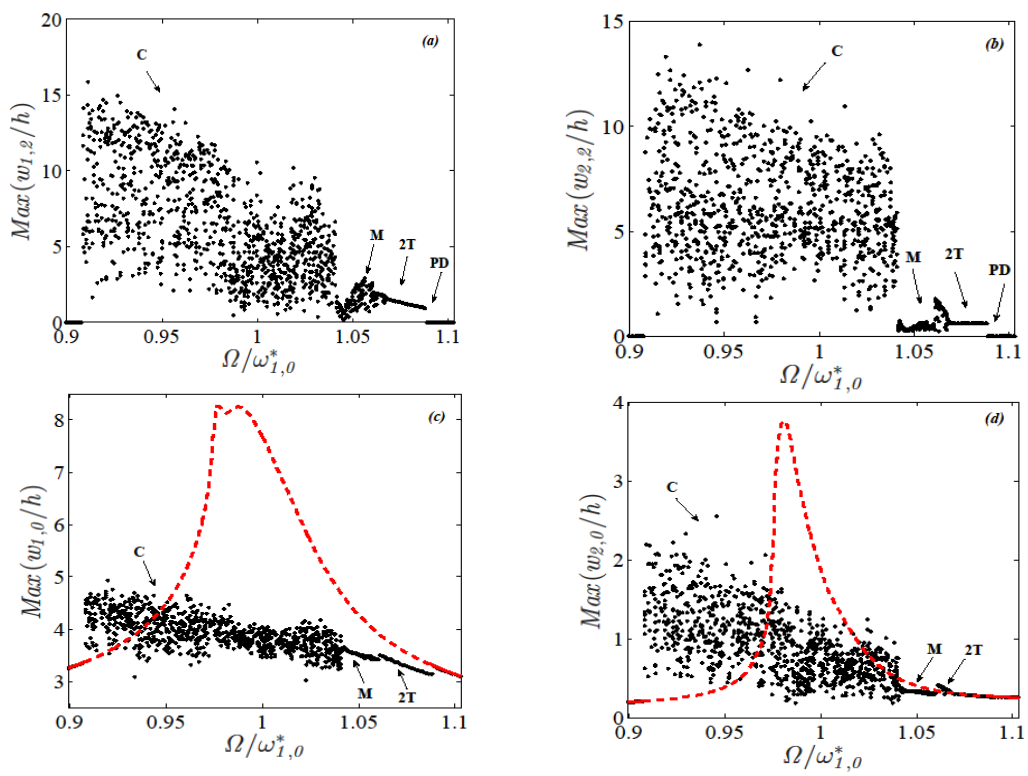

Fig. 4.5. Bifurcation diagrams for the asymmetric modes *(a)* $w_{1,2}$, *(b)* $w_{2,2}$ and axisymmetric modes *(c)* $w_{1,0}$, *(d)* $w_{2,0}$ without wave propagation for $\Omega / \omega_{1,0}^{*} \approx 1$; direct integration solution (black dotted line), unstable AUTO solution (red dashed line) ; $\zeta = 0.1$.

Results in Fig. 4.5 and Fig. 4.6 are the steady-state solutions and present the maximum of the generalized coordinates in a pulsation period. It is well known that complex responses with additional resonance peaks are often observed for nonlinear systems in the presence of internal resonances.

In particular, internal resonances can appear when the ratio of two or several natural frequencies is close to the ratio of small integers (see Amabili [4]). In this study, since the ratio $\omega^*_{2,0}/\omega^*_{1,0} \approx 2$, a 2:1 internal resonance between modes $w_{1,0}$ and $w_{2,0}$ is observed, as shown in Fig. 4.4(a-d).

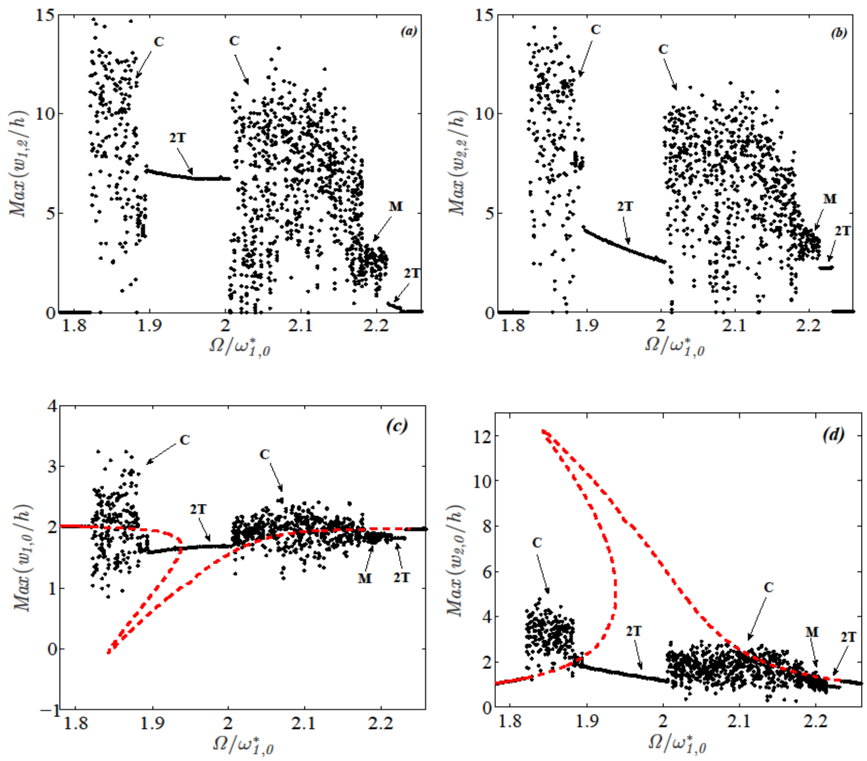

Fig. 4.6. Bifurcation diagrams for the asymmetric modes: *(a)* $w_{1,2}$, *(b)* $w_{2,2}$, and for the axisymmetric modes *(c)* $w_{1,0}$, *(d)* $w_{2,0}$ without wave propagation for $\Omega/\omega^*_{1,0} \approx 2$; direct integration solution (black dotted line), unstable AUTO solution (red dashed line); $\zeta = 0.1$.

Moreover, also the frequency ratio between the modes $w_{1,2}$ and $w_{1,0}$ is close to 2 (*i.e.* $\omega^*_{1,2}/\omega^*_{1,0} \approx 2$), causing a more complex nonlinear dynamics in this frequency range. Since in both ranges close to the linear resonance, *i.e.* $\Omega/\omega^*_{1,0} \approx 1$, and close to $\Omega/\omega^*_{1,0} \approx 2$, the software AUTO [106] could only determine an unstable solution in the case without wave propagation, the maximum vibration amplitudes shown in Fig. 4.5 and Fig. 4.6

are obtained by means of a self-developed continuation code based on direct integration of the equations of motion by using the IMSL DIVPAG package, which uses the Adams-Gear integration scheme. The tool used to investigate parametrically the response of the shell in these frequency ranges is the Poincaré map sections shown in Figs. 4.7 and 4.8 for $\Omega / \omega^*_{1,0} \approx 1$ and Figs. 4.9 and 4.10 for $\Omega / \omega^*_{1,0} \approx 2$, respectively.

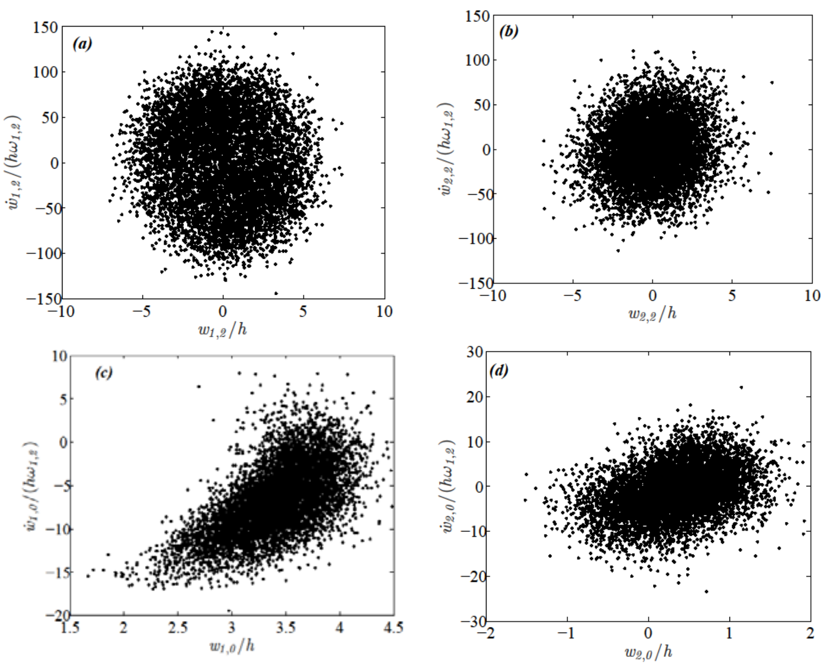

Fig. 4.7. Poincaré maps of the case without wave propagation: *(a)* $w_{1,2}$, *(b)* $w_{2,2}$, *(c)* $w_{1,0}$, *(d)* $w_{2,0}$ for $\Omega / \omega^*_{1,0} = 0.933$; $\zeta = 0.1$.

Simple periodic motion, a period-doubling bifurcation (PD), periodic response with twice the excitation period (2T), amplitude modulations (quasi-periodic motion, M) and chaotic response (C) have been detected in both frequency ranges. In particular, in the case without wave propagation the pitchfork bifurcation at $\Omega / \omega^*_{1,0} \approx 0.908$ (Fig. 4.4(c)) causes an explosive change in the response; the phenomenon observed is called "blue sky catastrophe" whereby the simply periodic solution is transformed into a chaotic region.

This chaotic response is obtained at the resonance of mode (1,0). In the Poincaré map sections for $\Omega/\omega^*_{1,0}=0.933$, shown in Fig. 4.7, the shape of the chaotic attractor is a kind of hypersphere and it is evident that the response is associated with hyperchaos. Quasi-periodic motion (amplitude-modulated response) is detected in the Poincaré map sections for $\Omega/\omega^*_{1,0}=1.052$ (Fig. 4.8) by an infinite number of points filling a closed curve.

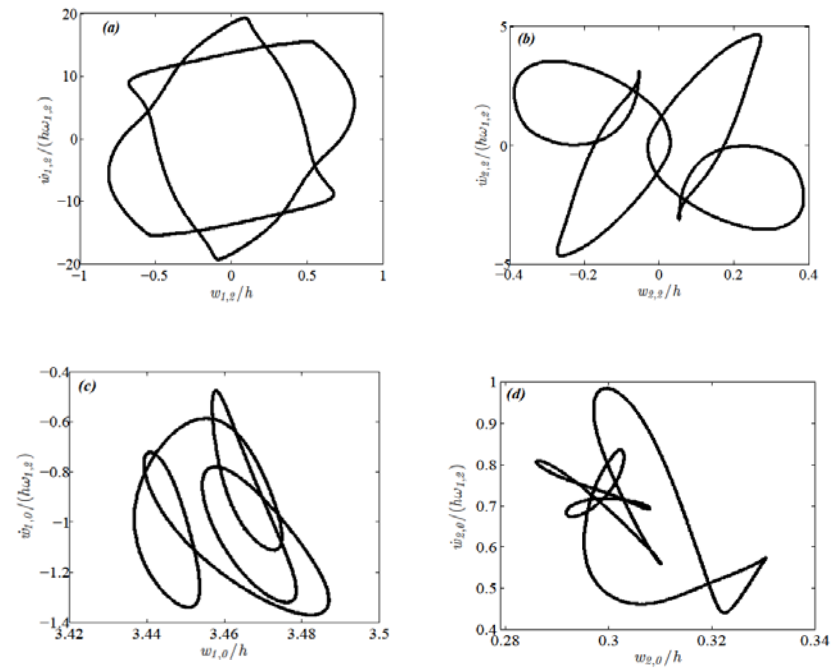

Fig. 4.8. Poincaré maps of the case without wave propagation: *(a)* $w_{1,2}$, *(b)* $w_{2,2}$, *(c)* $w_{1,0}$, *(d)* $w_{2,0}$ for $\Omega/\omega^*_{1,0}=1.052$; $\zeta = 0.1$.

It can be observed that the curves in Fig. 4.8(a-b), representing the Poincaré map sections of the asymmetric modes $w_{1,2}$ and $w_{2,2}$ respectively, are composed by two intersecting curves symmetric with respect to the origin.

Indeed, they have originated by the “movements” of the two points of the bifurcation diagrams of Poincaré maps in Figures 4.5(a-d) obtained for $1.068\le\Omega/\omega^*_{1,0}\le1.088$, i.e. in regime of a periodic response with two times the excitation period (2T) caused by a period doubling (PD). Therefore, reading Figure 4.5 from the right-hand side to the left, a period-doubling bifurcation is first detected, followed by quasi-periodic response and only then chaos appears.

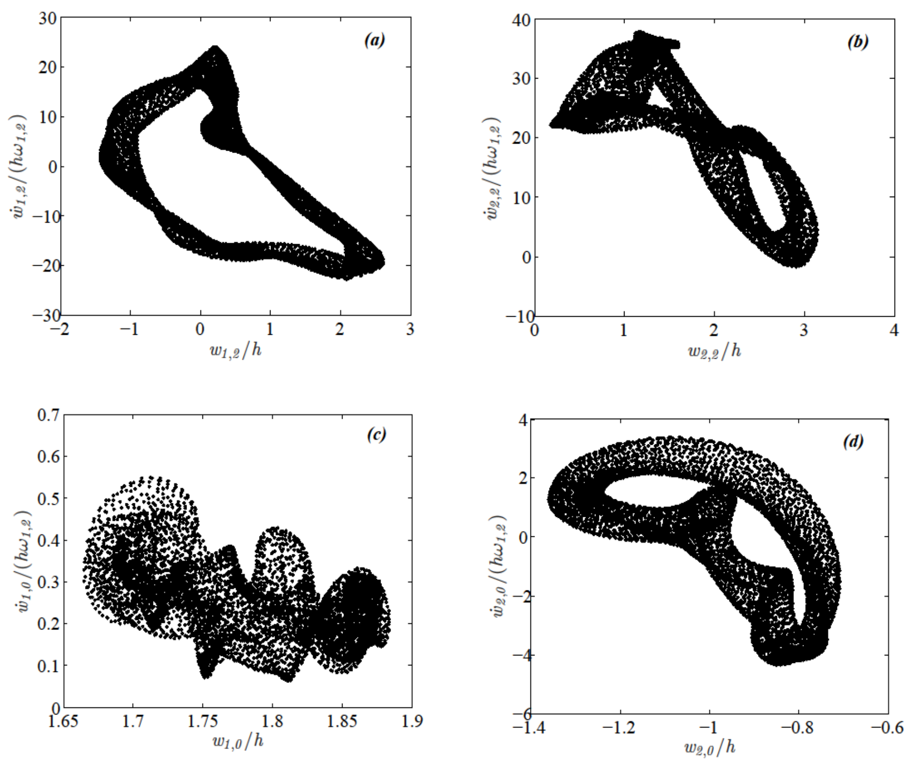

Fig. 4.9. Poincaré maps of the case without wave propagation: *(a)* $w_{1,2}$, *(b)* $w_{2,2}$, *(c)* $w_{1,0}$, *(d)* $w_{2,0}$ for $\Omega/\omega_{1,0}^{*}=2.2$; $\zeta = 0.1$.

Hence, the "blue sky catastrophe" phenomenon, detected by increasing the pulsating frequency, is instead interpreted as a more usual route to chaos when the frequency axis is read from the higher frequencies to the lower ones; this is usual for a softening type system, as the present one.

Similar complex nonlinear dynamics are observed in the case without wave propagation for $\Omega/\omega_{1,0}^{*}\approx 2$, as shown in Fig. 4.6. A "blue sky catastrophe" phenomenon is detected, whereby a sudden, explosive change in the response occurs for $\Omega / \omega^*_{1,0} \approx 1.822$ (hyperchaos).The system regains stability with a period-2 (i.e. (2-T) periodic) orbit for $\Omega / \omega^*_{1,0} \approx 1.896$.

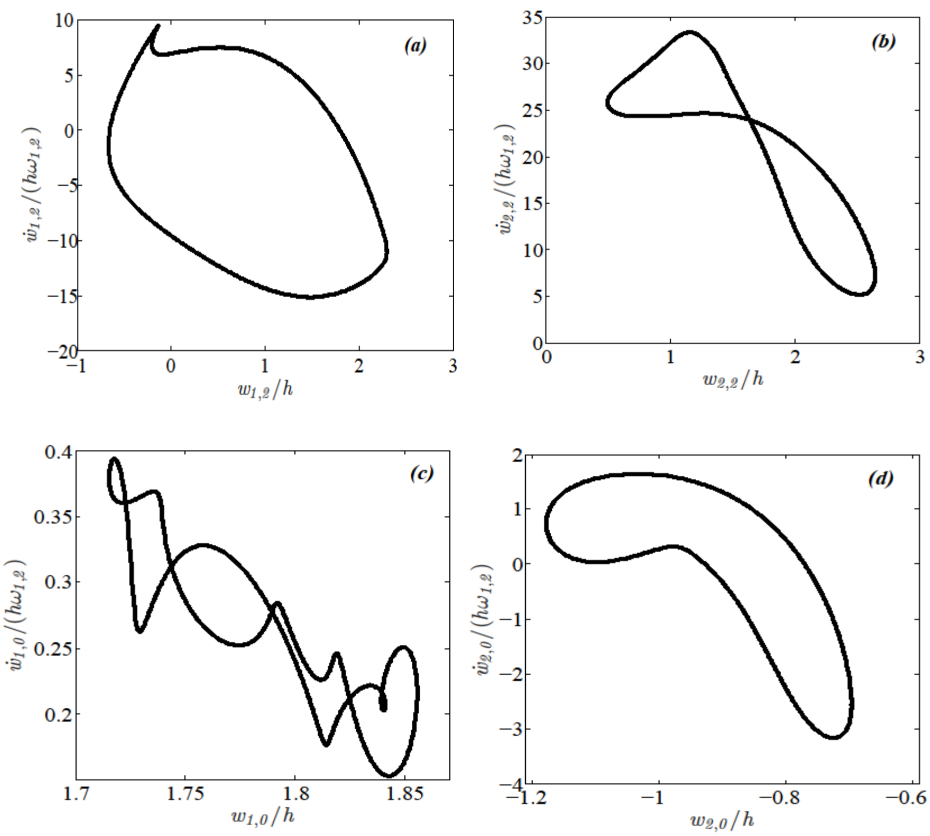

Fig. 4.10. Poincaré maps of the case without wave propagation: *(a)* $w_{1,2}$, *(b)* $w_{2,2}$, *(c)* $w_{1,0}$, *(d)* $w_{2,0}$ for $\Omega / \omega^*_{1,0} = 2.214$; $\zeta = 0.1$.

However, by increasing the forcing frequency Ω, the (2-T) periodic orbit loses stability at $\Omega / \omega^*_{1,0} \approx 2.01$ and this gives rise to another chaotic region of hyperchaos. Immediately after this region, Fig. 4.6 shows a region of lower vibration amplitude with alternated chaos and quasi-periodic solutions. Poincaré map sections for $\Omega / \omega^*_{1,0} \approx 2.2$ in Fig. 4.9 show that the system response is chaotic but subjected to a strange attractor. Indeed, the strange attractor is the quasi-periodic solution, whose Poincaré map sections for $\Omega / \omega^{*}_{1,0} \approx 2.214$, see Fig. 4.10, display a closed orbit.

Fig. 4.11 shows the effect of the modal damping ratio ζ on the nonlinear response of the system for the axisymmetric mode $w_{1,0}$ around the linear resonance. Comparison is presented between the case with wave propagation with the mean aortic pulse wave velocity and the case without wave propagation. In order to obtain the same maximum amplitude of vibration at the resonance peak with the two models, the damping ratio ζ used in the case without wave propagation must be about 10 times larger than the one for the corresponding case with wave propagation. In particular, in the case with wave propagation, pitchfork bifurcations appear in this frequency range only for values of $\zeta \leq$ 0.05.

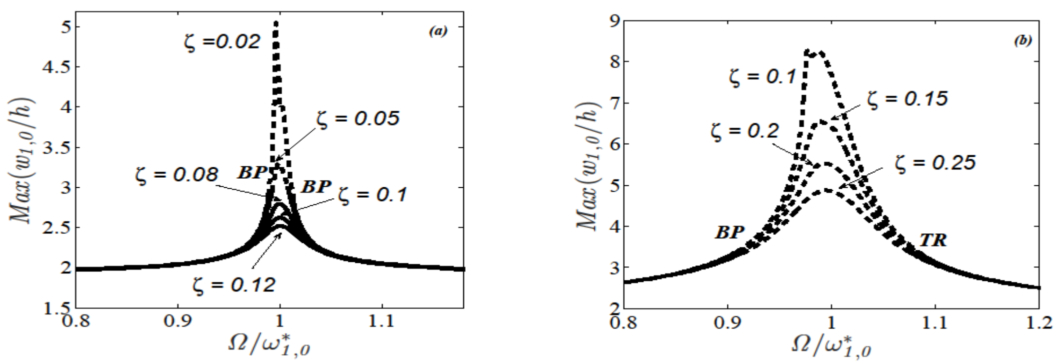

Fig. 4.11. Frequency response curves (AUTO solution) for the axisymmetric mode $w_{1,0}$ for different values of modal damping ζ: (*a*) with wave propagation with the mean aortic pulse wave velocity, (*b*) without wave propagation; stable solution (continuous line), unstable solution (dashed line), pitchfork bifurcation (BP) and Neimark-Sacker bifurcation (TR).

4.4.3 Chaotic vibrations of shells conveying pulsatile flow with the mean aortic pulse wave speed

As shown in the previous section, in order to observe interesting nonlinear dynamics in the case of shells conveying pulsatile flow with the mean aortic pulse wave velocity, the damping ratio ζ has to be relatively small (for the geometry considered here $\zeta \leq 0.05$). Fig. 4.12 shows the frequency-amplitude responses of the most significant axisymmetric modes, $w_{1,0}$, $w_{2,0}$, $w_{3,0}$, $w_{4,0}$, of the shell with wave propagation for a wide frequency range. As in the case without wave propagation, one main peak appears close to the linear resonance, *i.e.* $\Omega / \omega^*_{1,0} \approx 1$, and another one around $\Omega / \omega^*_{1,0} \approx 2$; both are associated with pitchfork bifurcations (BP) that cause the activation of the asymmetric modes, as shown in the bifurcation diagrams of Poincaré maps in Fig. 4.13. However, away from the peaks, the behavior of the two systems is very different. In particular, in the case with wave propagation, the amplitude of the first axisymmetric mode $w_{1,0}$ decreases for $\Omega / \omega^*_{1,0} < 1$, before reaching the peak corresponding to the linear resonance. The response of $w_{2,0}$ presents a rounded maximum around $\Omega / \omega^*_{1,0} = 0.5$, which is not present at all for the case without wave propagation.

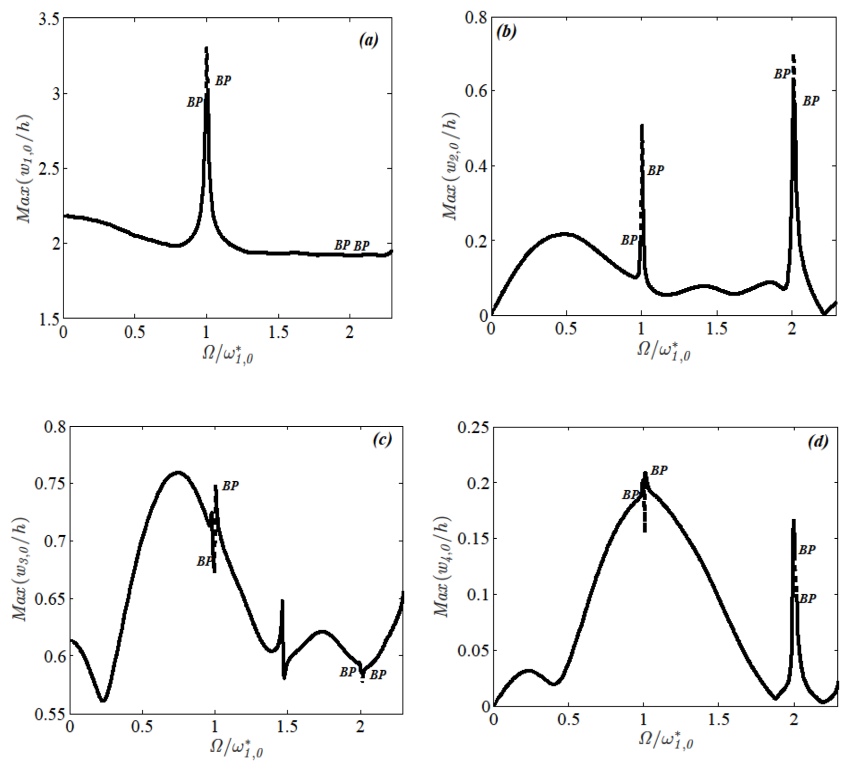

Fig. 4.12. Frequency response curves for the axisymmetric modes with wave propagation with the mean aortic pulse wave velocity: *(a)* $w_{1,0}$, *(b)* $w_{2,0}$, *(c)* $w_{3,0}$, *(d)* $w_{4,0}$ by varying the frequency Ω; stable solution (continuous line), unstable solution (dashed line), pitchfork bifurcation (BP); $\zeta = 0.05$.

In order to investigate the behavior of the system in the range close to the linear resonances, Poincaré maps have been computed by direct integration of the equations of motion. The bifurcation diagrams obtained by these Poincaré maps are shown in Fig. 4.13. A "blue sky catastrophe" is detected around $\Omega/\omega^*_{1,0}\approx 0.9918$ causing the activation of the asymmetric modes and leading the system to a chaotic regime as shown in the Poincaré map sections in Fig. 4.14 ($\Omega/\omega^*_{1,0}=0.995$) and Fig. 4.15 ($\Omega/\omega^*_{1,0}=1.002$), both characterized by clouds of points. However, the points are more sparse in Fig. 4.14 and more organized in Fig. 4.15. Amplitude modulations have been detected for $1.002<\Omega/\omega^*_{1,0}<1.008$ as shown in the Poincaré map sections in Fig. 4.16 for $\Omega/\omega^*_{1,0}=1.003$. The frequency-response relationship in the vicinity of $\Omega/\omega^*_{1,0}\approx 2$ is presented in Fig. 4.17. A pitchfork bifurcation is detected for $\Omega/\omega^*_{1,0}\approx 2.005$ where a new branch appears, showing the activation of the asymmetric modes. This new branch is characterized by simple periodic motion and not by chaotic response as in the previous case without wave propagation (Fig. 4.6).

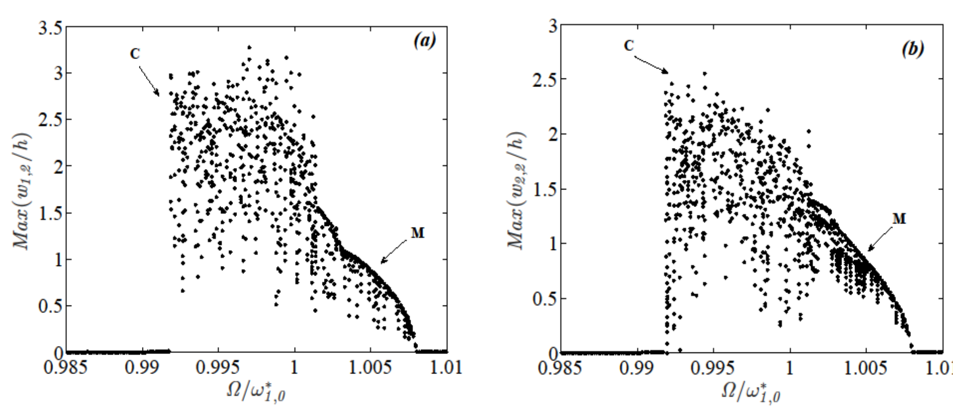

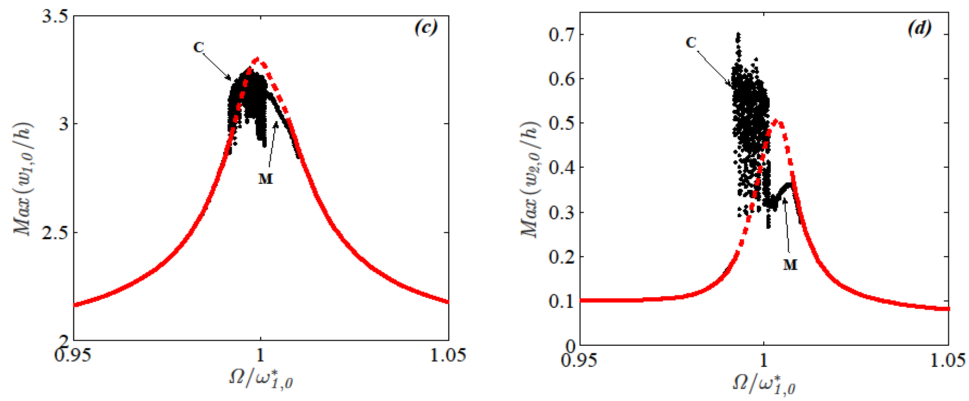

Fig. 4.13. Bifurcation diagrams for the asymmetric modes *(a)* $w_{1,2}$, *(b)* $w_{2,2}$, and for the axisymmetric modes *(c)* $w_{1,0}$, *(d)* $w_{2,0}$ with wave propagation with the mean aortic pulse wave velocity for $\Omega/\omega^*_{1,0} \approx 1$; direct integration solution (black dot line), unstable AUTO solution (red dashed line), stable AUTO solution (red continuous line) ; $\zeta = 0.05$.

4.4.4 Chaotic vibrations of shells conveying pulsatile flow with the Moens-Korteweg pulse wave velocity

The pulse wave velocity is an index of the stiffness and elasticity of the vessels. It is well known that an elevated pulse wave velocity is a marker of arterial stiffness in older adults [192]. Similarly, since textile prostheses have stiffer walls compared to the distensible arteries, their insertion has significant effects on blood pulse wave velocity [176, 193]. For the Dacron implant considered here, the corresponding pulse wave velocity given by the Moens-Korteweg formula is equal to c_0 = 11.72 m/s that is more than three times higher than the mean aortic pulse wave. This significant difference between the two values implies a substantial change in the dynamic behavior of the artificial vessel.

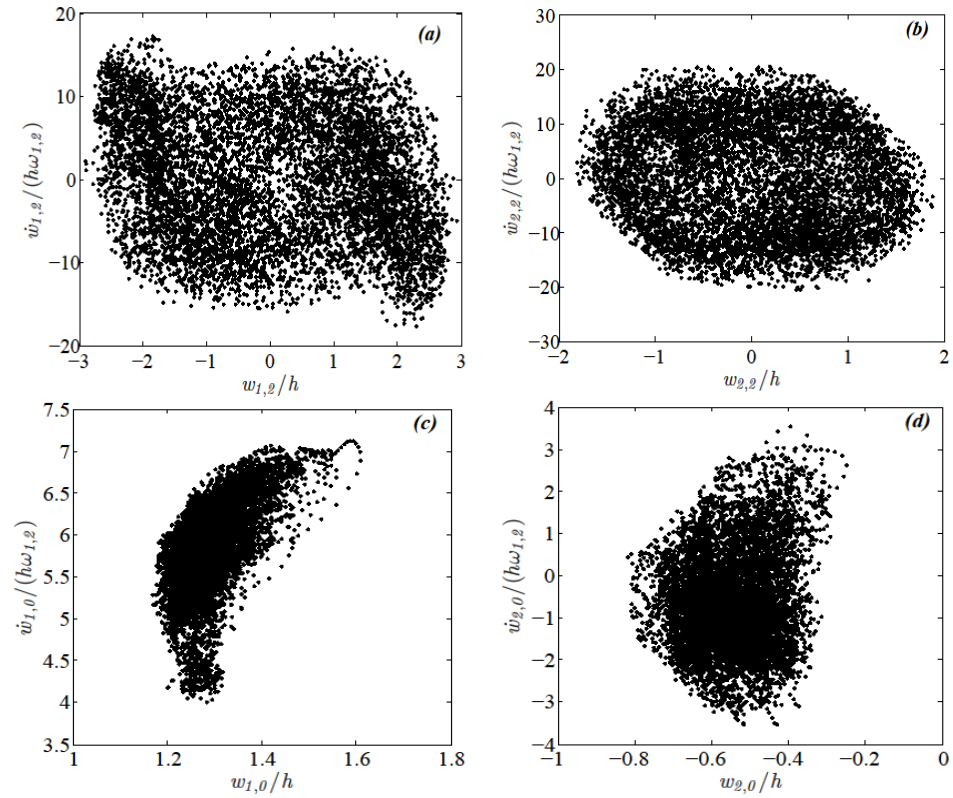

Fig. 4.14. Poincaré maps of the case with wave propagation with the mean aortic pulse wave velocity: *(a)* $w_{1,2}$, *(b)* $w_{2,2}$, *(c)* $w_{1,0}$, *(d)* $w_{2,0}$ for $\Omega/\omega_{1,0}^{*}=0.995$; $\zeta=0.05$.

Fig. 4.18 and Fig. 4.19 represent the bifurcation diagrams of the most significant axisymmetric and asymmetric modes, $w_{1,0}$, $w_{2,0}$, $w_{1,2}$, $w_{2,2}$, of the shell with wave propagation with c_0 = 11.72 m/s. As it can be observed comparing the bifurcation diagrams shown in Fig. 4.18 and Fig. 4.19 with Fig. 4.4(c-d), Fig. 4.5 and Fig. 4.6, the nonlinear dynamics of the shell conveying pulsatile flow with high wave velocity accurately reproduces the corresponding ideal case without wave propagation. Indeed, by increasing the pulse wave velocity, the behavior of the system with wave propagation is comparable to the limit case with the same oscillatory pressure and velocity at all the points of the control volume simultaneously. In both cases, complicated nonlinear dynamics like chaos, amplitude modulation and a period-doubling bifurcation are observed close to the linear resonance *i.e.* $\Omega / \omega_{1,0}^{*} \approx 1$, and around $\Omega / \omega_{1,0}^{*} \approx 2$, causing the activation of the asymmetric modes (specifically modes with n = 2) for a damping ratio ζ =0.1. To avoid redundancy in presenting the similar results, the corresponding Poincaré maps are not reported since they are analogous to Figs. 4.7-4.10.

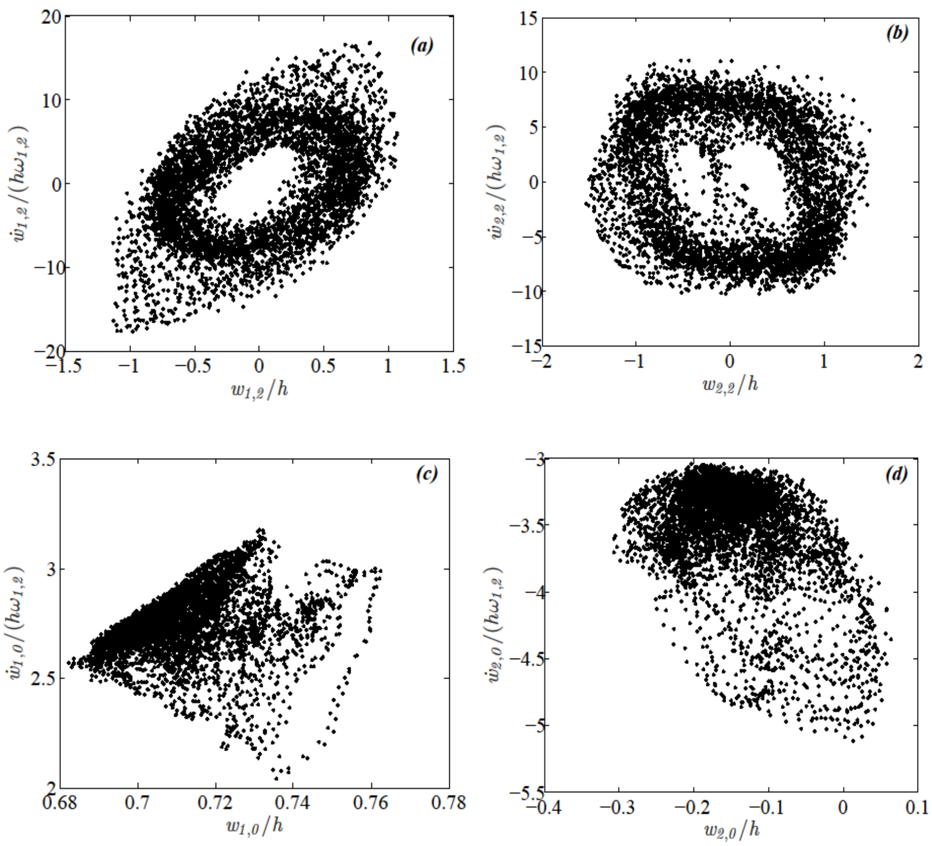

Fig. 4.15. Poincaré maps of the case with wave propagation with the mean aortic pulse wave velocity: (a) $w_{1,2}$, (b) $w_{2,2}$, (c) $w_{1,0}$, (d) $w_{2,0}$ for $\Omega / \omega_{1,0}^{*} = 1.002$; $\zeta = 0.05$.

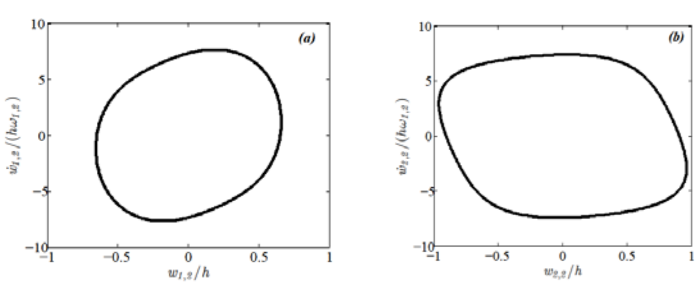

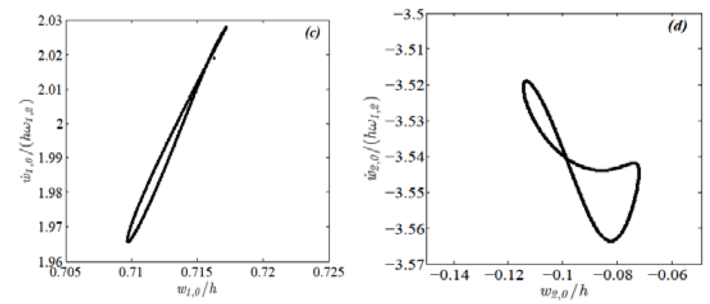

Fig. 4.16. Poincaré maps of the case with wave propagation with the mean aortic pulse wave velocity: (a) $w_{1,2}$, (b) $w_{2,2}$, (c) $w_{1,0}$, (d) $w_{2,0}$ for $\Omega/\omega^*_{1,0} = 1.003$; $\zeta = 0.05$.

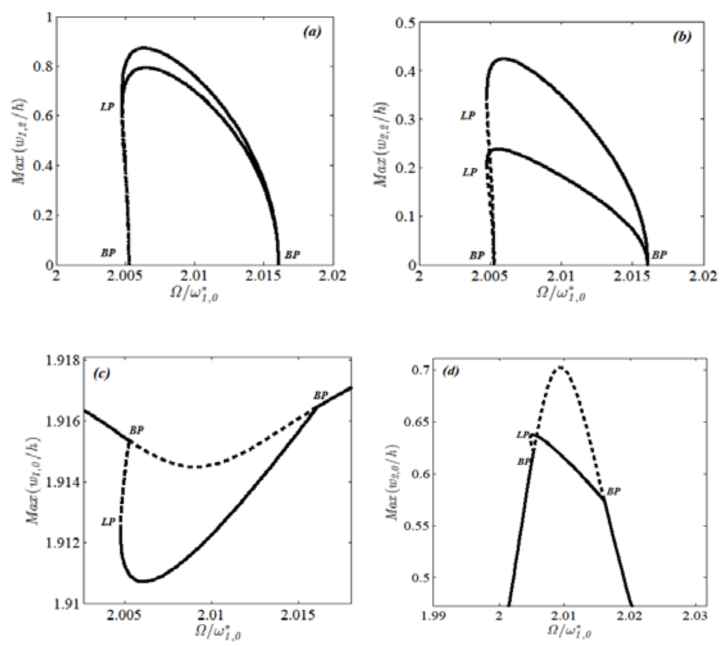

Fig. 4.17. Bifurcation diagrams for the asymmetric modes *(a)* $w_{1,2}$, *(b)* $w_{2,2}$ and for the axisymmetric modes *(c)* $w_{1,0}$, *(d)* $w_{2,0}$ with wave propagation with the mean aortic pulse wave velocity for $\Omega/\omega^*_{1,0} \approx 2$; unstable AUTO solution (dashed line), stable AUTO solution (continuous line) ; $\zeta = 0.05$.

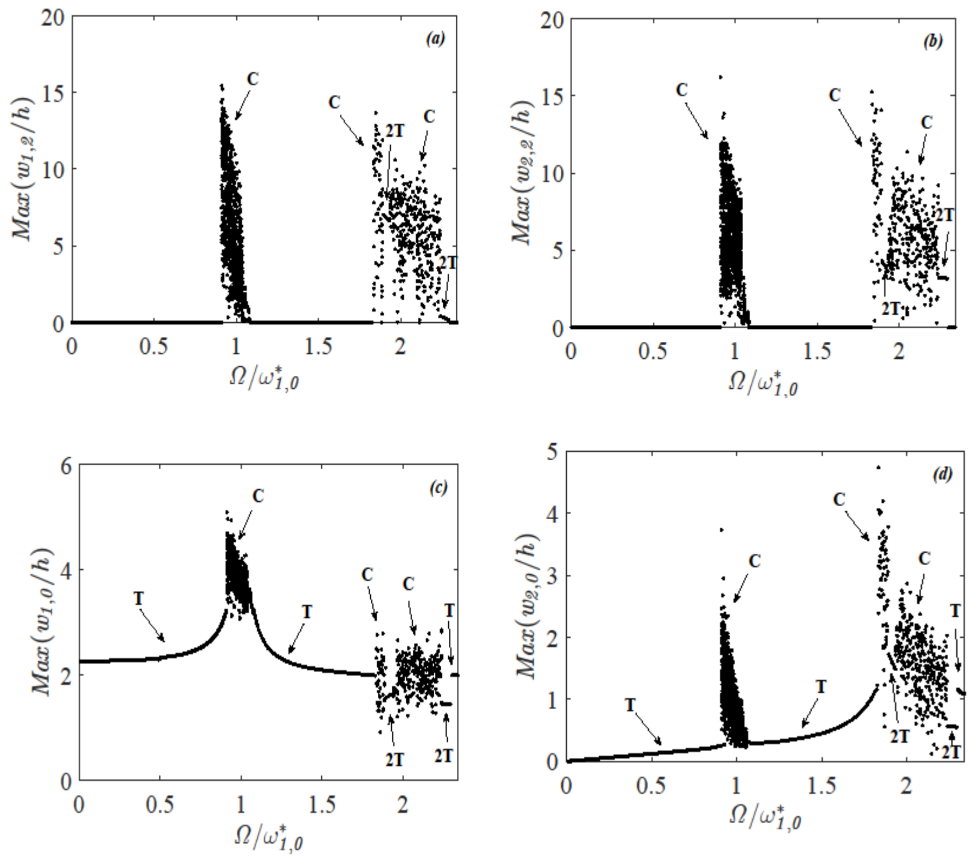

Fig. 4.18. Bifurcation diagrams for the asymmetric modes *(a)* $w_{1,2}$, *(b)* $w_{2,2}$ and axisymmetric modes *(c)* $w_{1,0}$, *(d)* $w_{2,0}$ with wave propagation with c_0 = 11.72 m/s (direct integration solution).

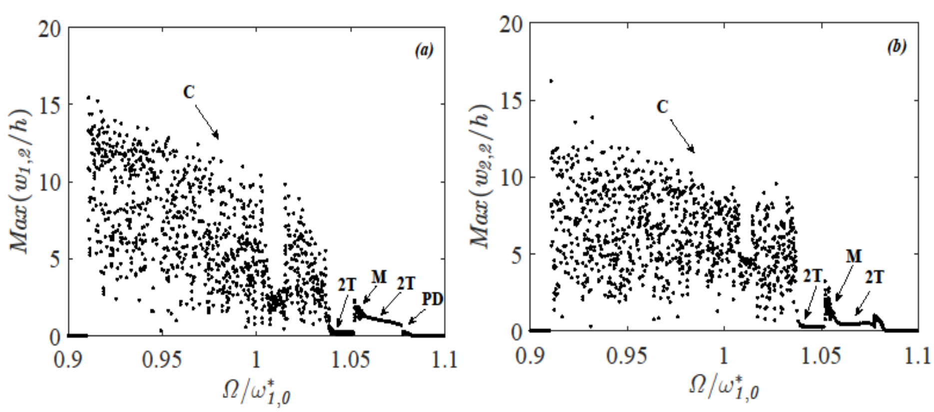

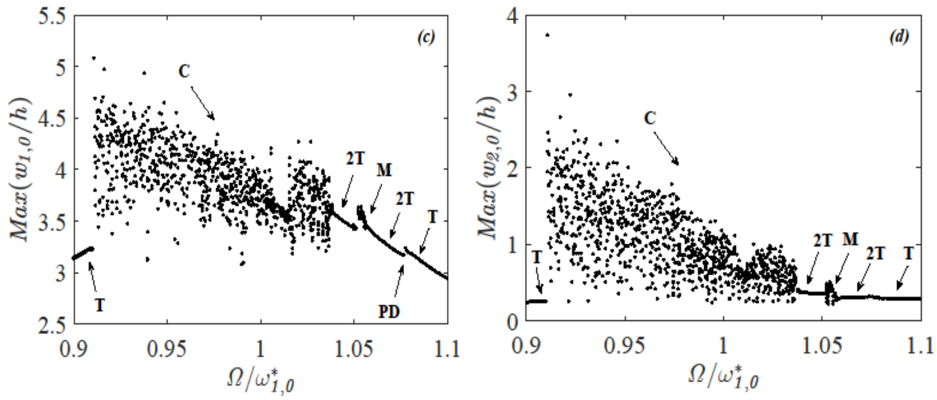

Fig. 4.19. Bifurcation diagrams for the asymmetric modes *(a)* $w_{1,2}$, *(b)* $w_{2,2}$ and axisymmetric modes *(c)* $w_{1,0}$, *(d)* $w_{2,0}$ with wave propagation with c_0 = 11.72 m/s for $\Omega/\omega^*_{1,0} \approx 1$ (direct integration solution).

4.5 Conclusions

This study addresses, for the first time in the literature, the effect of pulse wave propagation on nonlinear vibrations of shells excited by pulsatile pressure and flow. It is considered that an input oscillatory pressure at the shell entrance propagates down the shell causing a wave motion within the shell where the pressure gradient and the flow velocity are functions of both the axial coordinate and time.

Time responses of the shell radial displacement for different values of the axial coordinate clearly show the wave motion that propagates downstream inside the shell. The dynamic behavior of the shell under pulsatile pressure and flow has also been examined via bifurcation diagrams and Poincaré maps.

Two different pulse wave velocities have been considered in order to study the effect of this parameter on the dynamic response of the vessel with wave propagation. In particular, the mean aortic pulse wave velocity c_0 = 3.6 m/s [191] has been compared to the pulse wave velocity c_0 = 11.72 m/s obtained with the Moens-Korteweg formula for the Dacron implant considered here. These results have been compared with the case of shells conveying pulsatile pressure and velocity without considering the wave motion phenomenon (an adequate approximation for shells with low elasticity that allows the wave speed to be much higher than the maximum flow velocity). Indeed, for a modal damping ratio $\zeta = 0.1$ both cases without wave propagation and with the corresponding Moens-Korteweg pulse wave velocity present a complex response (chaos, amplitude modulation and a period-doubling bifurcation) close to the linear resonance with the activation of asymmetric modes, whereas the shell subjected to wave propagation with the mean aortic pulse wave velocity vibrates only axisymmetrically and the response is periodic throughout the frequency range investigated. Thus, it has been found that decreasing the pulse wave velocity stabilizes the system.

The effect of the modal structural damping ζ on the nonlinear response of the system of the axisymmetric mode $w_{1,0}$ around the linear resonance has been studied, in the case of wave propagation with the mean aortic pulse wave velocity. In order to obtain the same maximum amplitude vibration at the first resonance peak, the damping coefficient ζ used in the case with wave propagation should be reduced about 10 times with respect to the corresponding case without wave propagation. Chaotic vibrations and amplitude modulations in shells conveying pulsatile flow with wave propagation with the mean aortic pulse wave velocity have been detected in the vicinity of the linear resonance considering a damping ratio $\zeta = 0.05$.

With respect to the limitations of the present work, a more accurate structural model should include the viscoelasticity and possibly hyperelasticity of the graft material [150]. Moreover, for a proper representation of the physiological waveforms of pressure and velocity, more harmonics should be included in the Fourier expansion. In the second part of the present study, we expect that including higher harmonics in the Fourier expansion of the physiological waveforms of pressure and velocity will cause a shift towards lower frequencies of the first peak in the response. Consequently, this could eventually lead to the appearance of a peak in the response in the physiological frequency range, or closer to it. However, despite of limitations, this analysis represents the first study where nonlinear vibrations of aortic replacements are investigated and makes a substantial progress in order to simulate the dynamics of installed implants.

Acknowledgments

The authors would like to thank NSERC Discovery Grant program, Qatar Foundation grant NPRP 7-032-2-016 and the Canada Research Chair program for their financial support. The first author received a scholarship from the Fonds de recherche du Québec – Nature et technologies (FRQNT).

Chapter 5

Nonlinear dynamics of woven Dacron aortic prostheses

This chapter deals with the study of the dynamical behavior of a woven Dacron prosthesis conveying pulsatile blood flow. The mathematical fluid-structure interaction model considered is the one with the wave-propagation effect presented in Chapter 4. The pulse is of physiological shape. The objective is to detect possible vibration phenomena in the physiological frequency range originated by the fluid-structure interaction. It is well accepted that the long-term patency of the prosthesis depends on its ability to mimic the mechanical behavior of the host artery. However, if vibrations of the artificial vessel walls are activated for certain heart rates, the related high stress concentration combined with the fatigue cycles of the heart beats, could contribute to material deterioration. The final intent of this chapter is to expand the knowledge of the physiology and pathophysiology of Dacron arterial grafts, considering among the risks of possible complications, the large amplitude wall oscillations of the artificial vessels. The manuscript "Nonlinear dynamics of Dacron aortic prostheses conveying pulsatile flow" recently submitted in a peer-reviewed international journal is reported.

NONLINEAR DYNAMICS OF DACRON AORTIC PROSTHESES CONVEYING PULSATILE FLOW

Eleonora Tubaldi, Marco Amabili, Michael P. Païdoussis

Department of Mechanical Engineering, McGill University

Abstract

This study addresses the dynamic response to pulsatile physiological blood flow and pressure of a woven Dacron graft currently used in thoracic aortic replacements. The structural model of the prosthesis assumes a nonlinear cylindrical orthotropic shell described by means of nonlinear Novozhilov shell theory. The blood flow is modeled as Newtonian pulsatile flow, and unsteady viscous effects are included. Coupled fluid-structure Lagrange equations for open systems with wave propagation subject to pulsatile flow are applied. Physiological waveforms of blood pressure and velocity are approximated with the first eight harmonics of the corresponding Fourier series. Radial displacement time responses of the synthetic graft during exercise are compared to the ones at rest. Frequency-response curves in the physiological range show the geometrically nonlinear vibration response to pulsatile flow. During exercise, the bifurcation diagrams present several superharmonic resonance peaks. Different values of modal damping are considered. This study investigates a crucial issue in cardiovascular surgery and improves the understanding of vascular grafts patency through the analysis of their dynamic response to pulsatile flow.

5.1 Introduction

Dacron (polyethylene terephthalate) and ePTFE (expanded polytetrafluoroethylene) represent the standard materials for large-diameter (12-30 mm) vascular grafts used to replace components of the cardiovascular system in case of diseased arteries, such as vessel patches for aneurysms [194].

Dacron grafts are commonly used as aortic replacements since they function well in this high-flow, low resistance circuits with high long-term patency [94, 195]. The use of tightly woven, crimped Dacron fabric grafts is accepted in clinical practice to substitute the abdominal and thoracic aorta with high levels of success [95]. Dacron is durable, easy to use, and if used to replace large caliber vessels presents manageable resistance to thrombosis formation; however, the synthetic implant does not match the biomechanical behavior of that of the host artery [150].

Prostheses should match the viscoelastic properties of the arteries to which they are to be anastomosed. This property of the central blood vessels, known as compliance, is responsible of an efficient propagation of the pressure pulse to the peripheral vessels. With pulsatile blood flow, the compliant aorta acts as an elastic reservoir, absorbing energy during systole and releasing it during diastole. When a pressure wave encounters a discontinuity in geometry or elastic properties, for example at an anastomosis between a graft and an artery, it will be partially reflected, reducing the energy transmitted along the vessel. As current synthetic grafts are significantly stiffer than host vessels, substantial energy losses may occur through the graft [99].

The consequences of low compliant artificial vessels on aortic hemodynamics and the left ventricle have been investigated [196-198], but only few reports have quantified these effects on human cardiovascular system efficiency. Kim *et al.* [199] compared aortic input impedance characteristics between patients with aortic interposition Dacron grafts placed for traumatic aortic injury and normal age-matched control subjects. They found that at resting conditions, this compliance mismatch between the host aorta and the graft appears to be less important in the maintenance of distal blood flow during diastole. However, when high output is demanded, as during exercise, the compliance mismatch increases. This could explain the characteristic hemodynamic difference observed between the two groups including higher cardiac energetic cost to maintain a given flow due to a less compliant proximal aorta, and compromised decline in pressure pulse wave reflection. Matching the impedances would minimize wave reflection of the advancing pressure wave and it would restore the natural aortic Windkessel function [70, 200]. The compliance mismatch between arteries and grafts can also cause flow disruption, can contribute to false aneurysm formation [201] and it is known to reduce graft patency [101].

Extensive knowledge about the distinctly different mechanical properties of the Dacron implants with respect to the native aorta is available in literature [150, 156, 188], while very little is known about the dynamic behavior of these prostheses. Vascular grafts can be modeled as thin shells conveying pulsatile flow. A preliminary numerical study on the fluid-structure interaction between a thoracic aortic Dacron prosthesis and the blood flow was conducted by Tubaldi *et al.* [2]. Results show complex nonlinear dynamics (i.e. period doubling, pitchfork bifurcations) in case of high-frequency harmonic excitation (well beyond the physiological range). The pulsatile flow was considered “ideal”, meaning that for a given time instant, the pulsatile flow velocity and pressure were the same for all points of the control volume. Thus, the fluid was assumed to oscillate in bulk with simultaneous oscillatory pressure variations at every point of the shell. Theory for stability and dynamics of circular cylindrical shells conveying fluid has been developed by Amabili *et al.*[137, 140, 141] . The most important aspects of fluid-structure interactions in slender structures have been covered and synthesized by Païdoussis in the second volume of his monograph [5]. Veins, the urethra and pulmonary passages are physiological conduits that can be considered as pliable shells (collapsible tubes) [80], meaning that they can exhibit large area changes in response to small changes in transmural pressure [81, 169]. Indeed, even if they are surrounded by large masses and tissues and they are not necessarily straight or uniform along their length, their essential behavior can be represented by idealized models, the main one being the "Starling resistor" [202]. Vessel collapse is most readily observed in the veins (e.g. the jugular vein when standing erect, or the veins of the hand when an arm is raised), but the arteries also collapse when subjected to high external pressure [87], even if they are traditionally considered capable of withstanding large deformations without adverse effects. In deformable vessels conveying pulsatile flow, pulsating flow and pressure propagate downstream at the same wave speed in the form of travelling waves. The literature on wave propagation in compliant and collapsible tubes is truly vast [203, 204].

Blood pressure and flow waveforms depend on the physical properties of the cardiovascular system, such as the arterial geometry and distensibility [205]. Having a better understanding of the haemodynamics and pulse wave dynamics can be valuable for the diagnosis and treatment of most common arterial diseases. The pulse wave velocity (i.e. the propagation speed of pulse waves relative to the blood) through the arteries is an indirect measurement of arterial stiffness and tonus and it represents an important predictor of cardiovascular events such as atherosclerosis [206] and hypertension [207]. The pulse wave velocity (PWV) in arteries has been related to the underlying wall stiffness using the Moens-Korteweg [74] equation and it is considered a noninvasive estimation of arterial properties [75].

The highly pulsatile nature of the blood flow and the compliant nature of the blood vessels make the vascular system difficult to model. One-dimensional modelling is commonly applied to simulate in large arteries the changes in blood flow and cross-sectional averaged blood pressure and velocity in time and along the axial direction, with good accuracy and low computational cost [71, 72, 208, 209]. The difficulty of solving the coupled blood flow-vessel deformation problem makes modeling 3-D blood flow in flexible arteries extremely challenging. These models are usually applied when a detailed description of the 3-D flow field is required, for example at a specific part of the vascular system where fluid phenomena are complex and of physiological or pathological interest (e.g., near a bifurcation, within an aneurysm, or in the vicinity of a heart valve or a stenosis) [210]. 3D models require computational fluid dynamics (CFD) approaches and some of the most recent ones have been extended to fluid-structure interaction analysis between blood and the arterial wall [211]. Arbitrary Lagrangian-Eulerian (ALE) formulation is one of the most famous computational techniques used to solve problems of modeling of blood flow in complinat vessels. In this approach, the Navier-Stokes equations are written in a moving reference frame that follows the motion of the vascular structure interface [162, 167]. The evolution of the ALE formulation is a boundary-fitting technique, where the fluid-solid interface is accurately captured via continuous changes of the fluid grid. However, in situations in which the motion of the vascular structure is large, ALE formulations may result in time consuming computations [212]. Even though these accurate fluid-structure interaction models may provide detailed descriptions of deformation and flow phenomena, their computational intensity is such that they cannot be used to study wave-propagation phenomena in the entire arterial tree or major parts of it. The choice of model depends on the degree of detail required, and usually modelling of the fluid-structure interaction of blood flow in arteries requires the combination of different types of models each with their own spatial dimensions [166, 213, 214]. Pulse wave mechanics in systemic arteries can be described using mathematical and numerical tools based on lumped parameter models and 1-D wave propagation models [215, 216].

Arteries and veins *in vivo* are under significant mechanical stresses generated by blood pressure, lumen blood flow, surrounding tissue tethering, and body movement [75]. It is critical that arteries remain stable under these loads to maintain their physiological function.

While the mechanical properties of the arterial wall have been studied extensively [217, 218], articles related to the mechanical stability of arteries under physiological loads are rare. Han *et al.* [88] summarized in a literature review the state of the art studies regarding the stability of blood vessels reporting the common forms of buckling that occur, including cross-sectional collapse, longitudinal twist buckling, and bent buckling. Blood vessels, like water hoses or pipelines may also lose their stability under physiological loads due to fluid-structure interaction phenomena [171, 219]. Recently, Amabili *et al.* [89] investigated the stability of a shell roughly simulating a straight aorta segment conveying steady blood flow, using a numerical bifurcation analysis. The cross-sectional collapse (nonlinear buckling) of the vessel has been identified as being potentially responsible of the appearance of high-stress regions at the *intima* layer of the aortic wall. Thus, this phenomenon represents a possible reason behind the initiation of aortic dissection. It has been well documented that excessive mechanical stress represents a risk factor for the pathological development of vascular diseases such as atherosclerosis [220] and for aneurysm rupture and atherosclerotic plaque rupture [221, 222].

The present study is the first to address the dynamic response to pulsatile physiological blood flow and pressure of a woven Dacron graft interposition in the thoracic aorta. The effect of wall distensibility has been considered despite the limited elasticity of the woven Dacron prostheses in order to study the flow-induced wall oscillations of the implant. The structural model of the prosthesis assumes a nonlinear cylindrical orthotropic shell described by means of nonlinear Novozhilov shell theory. The blood flow is modeled as a Newtonian pulsatile flow, and unsteady viscous effects are included. Coupled fluid-structure Lagrange equations for open systems subject to pulsatile flow with wave propagation developed by Tubaldi *et al.*[3] are applied here. Physiological waveforms of blood pressure and flow velocity [186] are approximated with the first eight harmonics of the corresponding Fourier series. Time-responses of the radial displacement of the synthetic graft during exercise are compared to those at rest. Differences in the frequency content contributions are presented and discussed. Frequency-response curves in the physiological range display the geometrically nonlinear vibration response to pulsatile flow. During exercise (i.e. high pulsatile flow velocity and high heart rate) the dynamic response presents several superharmonic resonance peaks.

Modelling dissipation is particularly relevant. The effect of different values of modal damping on the dynamic behavior of the prosthesis is investigated. In the limit case of low modal damping values, the prosthesis displays more complicated nonlinear dynamics.

The growing understanding of the physiology and pathology of arterial grafts will ultimately produce practical therapeutic strategies for enhancing graft function and controlling currently common long-term adverse effects.

5.2 Methodology

In this study, woven Dacron artificial blood vessels currently used in aortic replacement surgery are modeled as thin-walled circular cylindrical shells. Because of their textile structure, Dacron prostheses are markedly anisotropic. A large difference exists in the modulus of elasticity between the circumferential and the axial directions.

Lee and Wilson [188] performed uniaxial tensile tests on woven Dacron implants and determined a typical stiffness ratio (circumferential/longitudinal) of about 15 for these materials. The strong anisotropy of the system is here taken into account by considering an orthotropic circular cylindrical shell. Moreover, the yarn structure and complex fabric design of the graft provide a nonlinear stress-strain behavior; however, the Dacron can be assumed to be linearly elastic around specific pressure values. In our analysis, the values of Young's modulus of the orthotropic material are obtained from the uniaxial tension tests given by [156, 188] linearized around the mean physiological pressure $\overline{p}_m = 100 \text{ mmHg}$. Hasegawa and Azuma [156] investigated experimentally stress relaxation patterns and the values of relaxation strength in Dacron synthetic grafts. Their results indicate that for these grafts stress relaxation is not prominent and they could be regarded approximately as perfectly elastic. Geometric nonlinearities in the strain-displacement relationships according to the classical Novozhilov nonlinear shell theory are retained in the model. The thin-walled circular cylindrical shell discussed here is shown in Fig. 5.1 with mean radius R, shell thickness h and shell length L. Because of the very thin nature of the shell under consideration (i.e. $h/R = 0.024$), rotary inertia and shear deformations can be neglected without compromising the accuracy of the model.

A cylindrical coordinate system $(O; x, r, \theta)$ is introduced with the origin O at the center of one end of the shell. The displacements of an arbitrary point of coordinates (x, θ) on the middle surface of the shell are denoted by u, v and w, in the axial, circumferential and radial directions, respectively; w is taken positive outwards.

The following flexible constraints are considered as boundary conditions in order to simulate connections with the host artery, and are applied at the shell ends $(x = 0, L)$:

$$v = w = 0, \quad N_x = -k_a\, u, \quad M_x = -k_r\left(\frac{\partial w}{\partial x}\right), \tag{5.1a-d}$$

where N_x and M_x are the axial stress and the bending moment per unit length, respectively.

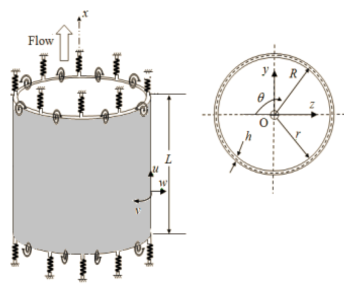

Fig. 5.1. Schematic of the shell in axial flow with boundary conditions at the shell ends.

The distributed axial k_a and rotational k_r stiffness of the springs represent flexible boundary conditions applied at the shell ends. They allow rotations [151] and axial axisymmetric motion while they also simulate relatively stiff axial constraints for asymmetric deformations, reproducing the connection with the remaining parts of the aorta.

5.2.1 Kinetic and Elastic Strain Energy of the Shell

An energy variational approach is used to obtain the equations of motion for the aortic prosthesis segment conveying pulsatile flow with wave propagation (already published by the authors [3]). The total kinetic energy of the shell is given by

$$T_s = \frac{1}{2}\rho_s\, h \int_0^{2\pi}\int_0^{L}\left\{\dot{u}^2 + \dot{v}^2 + \dot{w}^2\right\} \mathrm{d}\, x\, R\, \mathrm{d}\, \theta\,, \tag{5.2}$$

where ρ_s is the mass density of the structure and the overdot represents the time derivative. The potential energy of the Dacron prosthesis U_S is made of two contributions:

$$U_S = U_{shell} + U_{spring}. \tag{5.3}$$

For an orthotropic linearly elastic material, Young's moduli in the x and θ direction are denoted by E_x and E_θ, respectively, and the Poisson ratio is $\nu_{\theta x}$; for the Possion ratios the following expression holds true: $\nu_{\theta x} E_x = \nu_{x\theta} E_\theta$. Assuming plane elastic stress, the elastic strain energy can be written as

$$\begin{aligned} U_{shell} &= \frac{1}{2}\frac{E_x h}{1-\nu_{\theta x}^2 E_x / E_\theta}\int_0^L\int_0^{2\pi}\left[\varepsilon_{x,0}^2 + \frac{E_\theta}{E_x}\varepsilon_{\theta,0}^2 + 2\nu_{\theta x}\,\varepsilon_{x,0}\,\varepsilon_{\theta,0} + \frac{G_{x\theta}}{E_x}\left(1-\nu_{\theta x}^2\,E_x / E_\theta\right)\gamma_{x\theta,0}^2\right]\mathrm{d}\,x\,R\,\mathrm{d}\,\theta \\ &+\frac{1}{2}\frac{E_x h^3}{12\left(1-\nu_{\theta x}^2 E_x / E_\theta\right)}\int_0^L\int_0^{2\pi}\left[k_x^2 + \frac{E_\theta}{E_x}k_\theta^2 + 2\nu_{\theta x}\,k_x\,k_\theta + \frac{G_{x\theta}}{E_x}\left(1-\nu_{\theta x}^2\,E_x / E_\theta\right)k_{x\theta}^2\right]\mathrm{d}\,x\,R\,\mathrm{d}\,\theta \\ &+\frac{1}{2}\frac{1}{R}\frac{E_x h^3}{6\left(1-\nu_{\theta x}^2 E_x / E_\theta\right)}\int_0^L\int_0^{2\pi}\Bigg[\varepsilon_{x,0}\,k_x + \frac{E_\theta}{E_x}\varepsilon_{\theta,0}\,k_\theta + \nu_{\theta x}\,\varepsilon_{x,0}\,k_\theta + \nu_{\theta x}\,\varepsilon_{\theta,0}\,k_x \\ &+\frac{G_{x\theta}}{E_x}\left(1-\nu_{\theta x}^2\,E_x / E_\theta\right)\gamma_{x\theta,0}\,k_{x\theta}\Bigg]\mathrm{d}\,x\,R\,\mathrm{d}\,\theta, \end{aligned} \tag{5.4}$$

where $\varepsilon_{i,0}$ and $\gamma_{i,0}$ denote the strains referred to the middle surface of the shell, k_x and k_θ represent the changes in curvature and $k_{x\theta}$ defines the change in torsion of the shell middle surface. The changes in curvature and torsion and the strains of the middle surface can be expressed as nonlinear quadratic functions of the middle surface displacements u, v and w through strain-displacement relationships that can be found in [38] based on the nonlinear Novozhilov shell theory. The potential energy stored by the rotational and axial springs at the shell ends can be written as

$$U_{spring} = \frac{1}{2}\int_0^{2\pi}\left\{k_a\left[\left(u\right)_{x=0}\right]^2 + k_a\left[\left(u\right)_{x=L}\right]^2 + k_r\left[\left(\frac{\partial w}{\partial x}\right)_{x=0}\right]^2 + k_r\left[\left(\frac{\partial w}{\partial x}\right)_{x=L}\right]^2\right\}R\,\mathrm{d}\,\theta. \tag{5.5}$$

In order to discretize the system, the middle surface displacements u, v and w are expanded by using approximate trigonometric functions identically satisfying the geometric boundary conditions. A linear modal base consisting of the eigenmodes of the simply supported shell is used to discretize the system and build a reduced-order model. In order to reduce the number of degrees of freedom, it is important to use only the most significant modes. In particular,

$$u(x,\theta,t) = \sum_{m=1}^{8}\left[u_{m,n,c}(t)\cos(n\theta) + u_{m,n,s}(t)\sin(n\theta)\right]\cos(\lambda_m x) + \sum_{m=1}^{3}u_{m,2n,c}(t)\cos(2n\theta)\cos(\lambda_m x) + \sum_{\substack{m=1\\ m\ odd}}^{11}u_{m,0}(t)\cos(\lambda_m x) + \sum_{\substack{m=2\\ m\ even}}^{6}u_{m,0}(t)\cos(\lambda_m x),$$

$$v(x,\theta,t)=\sum_{m=1}^{8}\left[v_{m,n,s}(t)\sin(n\theta)+v_{m,n,c}(t)\cos(n\theta)\right]\sin(\lambda_m x)+\sum_{m=1}^{6}v_{m,2n,c}(t)\sin(2n\theta)\sin(\lambda_m x), \quad (5.6\text{a-c})$$

$$w(x,\theta,t)=\sum_{m=1}^{8}\left[w_{m,n,c}(t)\cos(n\theta)+w_{m,n,s}(t)\sin(n\theta)\right]\sin(\lambda_m x)+\sum_{\substack{m=1\\ m\,odd}}^{11}w_{m,0}(t)\sin(\lambda_m x)+\sum_{\substack{m=2\\ m\,even}}^{6}w_{m,0}(t)\sin(\lambda_m x),$$

where m represents the number of longitudinal half-waves, $\lambda_m=m\pi/L$, n denotes the number of circumferential waves, and t is the time; the generalized coordinates [4] are given by $u_{m,n}(t)$, $v_{m,n}(t)$ and $w_{m,n}(t)$. A nonlinear term $\hat{u}(t)$ is added to the expansion of u (Eq. (5.6a)) to satisfy the natural boundary condition Eq. (5.1.c); this term is given as a function of the generalized coordinates [37]. The presence of geometric imperfections on the prosthesis wall breaks the axial-symmetry of the system. Thus, it is assumed that only asymmetric modes with subscript c are activated in addition to axisymmetric modes. Applying a global discretization of the system in case of imperfections, a reduced-order model with 51 degrees of freedom (*dofs*) can be used selecting the terms with last subscript c in Eq. (5.6a-c).

5.2.2 Blood Flow Model in Large Arteries

The Dacron graft studied here is meant to be a thoracic aortic replacement. In this segment of the aorta, the Womersley number is very high ($\alpha \approx 15$) and consequently the central mass of the fluid behaves almost as a solid core [155]. Indeed, due to its high pulsatility, the blood flow in the aorta is similar to an entrance type flow, meaning that it does not have enough time to develop. Hence, potential flow theory can be used, since the core of the flow can be considered a potential core (i.e. inviscid region) surrounded by a thin developing boundary layer on the wall [179]. In addition, the high-frequency time-dependent blood flow in the aorta, as well as the irrotational flow at the ventricles, allow to approximate the hemodynamics via potential flow analysis [178]. It is commonly accepted that in large arteries for Reynolds numbers sufficiently large, the boundary layer is very thin [75]. In Section 5.2.5 the unsteady time-averaged Navier-Stokes equations are employed to calculate the pulsatile viscous effects on the internal wall.

The fluid is modeled as an incompressible Newtonian pulsatile flow. The assumption of Newtonian behavior of blood is acceptable for high shear rate flow, e.g. in the case of flow through large arteries, while the non-Newtonian character of blood is typical in small arteries and veins where the presence of the white blood cells, red blood cells, and platelets in plasma produces that specific behavior. The fluid-structure interaction model used here has been developed by Tubaldi *et al.* [3] and the fluid is modeled using a hybrid model that considers the unsteady fluid motion by potential flow theory and the unsteady viscous effects for turbulent flow by the unsteady time-averaged Navier-Stokes equations.

The shell is considered to be conveying isentropic, incompressible, and irrotational flow. Arteries and vascular prostheses are generally assumed to be tethered in the longitudinal direction, with their central axis fixed, and their wall to be allowed to deform only in the radial direction due to the internal pressure, which is considered to be constant over the luminal cross-section. This is consistent with the assumption that radial and azimuthal velocities are negligible compared to axial velocities [209, 223].

The flow velocity vector $\mathbf{v}_\mathbf{F}$ is given by

$$\mathbf{v}_\mathbf{F} = U(x,t)\mathbf{i} + \nabla\Phi, \tag{5.7}$$

where $\mathbf{i}$ represents the unit vector in the x-direction, $U(x,t)$ denotes the pulsatile axial flow velocity that is periodic in time but also, due to the wave-propagation phenomenon, it depends on the axial coordinate x. The unsteady perturbation potential Φ is associated with shell motion and it satisfies the Laplace equation [224]. Assuming that no cavitation occurs at the blood-prosthesis interface, the condition of impermeability of the surface of the vessel may be expressed mathematically as

$$\left.\frac{\partial \Phi}{\partial r}\right|_{r=R} = \left(\frac{\partial w}{\partial t} + U(x,t)\, \frac{\partial w}{\partial x} \right). \tag{5.8}$$

5.2.3 Pulse-Wave Propagation of Physiological Waveforms of Velocity and Pressure

In deformable vessels conveying pulsatile flow, the pulsating pressure and flow propagate downstream at the same wave speed in the form of travelling waves. Thus, a Fourier series can be used to represent pressure and flow velocity distributions, oscillatory both in space and time within the vessel, as follows:

$$U(x,t) = \bar{U} + \sum_{n=1}^{N} \left[a_{v,n} \cos\left(n\, \Omega\, (t - x / c_0)\right) + b_{v,n} \sin\left(n\, \Omega\, (t - x / c_0)\right) \right], \tag{5.9a}$$

$$p_m(x,t) = \bar{p}_m + \sum_{n=1}^{N} \left[a_{p,n} \cos\left(n\, \Omega\, (t - x / c_0)\right) + b_{p,n} \sin\left(n\, \Omega\, (t - x / c_0)\right) \right], \tag{5.9b}$$

where $\bar{p}_m$ and $\bar{U}$ denote the steady components of the pressure field and the mean flow velocity, respectively, Ω is the heart rate (HR), and N is the total number of terms in the Fourier series expansion. The coefficients b_n and a_n are the Fourier sine and cosine coefficients, respectively, and are different for the velocity and pressure distributions. The wave speed c_0 is approximately obtained by the Moens-Korteweg formula, widely used in haemodynamics [74] ,

$$c_0 = \sqrt{\frac{E_\theta\, h}{2\, \rho_F\, R}}\,, \tag{5.10}$$

where E_θ is the circumferential Young's modulus of the vessel and ρ_F is the constant blood density.

A limitation of the Moens-Korteweg formula is to neglect flow viscous effects. This hypothesis is adequate for the system studied here, since the Womersley and the Reynolds numbers are much larger than one for blood flow in large arteries and therefore inertial effects prevail over the viscous ones. Thus, for the wave propagation problem, neglecting the blood viscosity outside the boundary layer next to the inner wall is often acceptable. Under these hypotheses, pulse wave analysis of ideal flowing fluid provides a reasonable approximation [75]. However, in some studies, in order to define the wave speed with more accuracy [181], the nonlinear convection terms of the Navier-Stokes equations and the viscosity effect have been included.

5.2.4 Energy of the Flow

Green's theorem is used to obtain the total energy associated to the flow whose contribution on the shell surface can be divided into three terms: kinetic energy T_F, gyroscopic energy E_G, and potential energy V_F, where

$$T_F = \frac{1}{2}\rho_F \sum_{m=1}^{M}\sum_{n=0}^{N}\int_0^{2\pi}\int_0^L \frac{L}{m\pi}\frac{\mathrm{I}_n(m\pi R/L)}{\mathrm{I}_n'(m\pi R/L)}\dot{w}_{m,n}^2 \,\mathrm{d}x\, R\,\mathrm{d}\theta,$$

$$E_G = \frac{1}{2}\rho_F \int_0^{2\pi}\int_0^L \sum_{m=1}^{M}\sum_{n=0}^{N}\sum_{l=1}^{M}\sum_{k=0}^{N}\frac{U(x,t)\,L}{m\pi}\frac{\mathrm{I}_n(m\pi R/L)}{\mathrm{I}_n'(m\pi R/L)}\left(\dot{w}_{m,n}\frac{\partial w_{l,k}}{\partial x}+\dot{w}_{l,k}\frac{\partial w_{m,n}}{\partial x}\right)\mathrm{d}x\, R\,\mathrm{d}\theta. \quad (5.11\text{a-c})$$

$$V_F = -\frac{1}{2}\rho_F \int_0^{2\pi}\int_0^L \sum_{m=1}^{M}\sum_{l=1}^{M}\sum_{n=0}^{N}\sum_{k=0}^{N}\frac{U(x,t)^2 L}{m\pi}\frac{\mathrm{I}_n(m\pi R/L)}{\mathrm{I}_n'(m\pi R/L)}\frac{\partial w_{m,n}}{\partial x}\frac{\partial w_{l,k}}{\partial x}\,\mathrm{d}x\, R\,\mathrm{d}\theta,$$

Because of the phase delay associated to wave propagation of velocity and pressure waves, new terms will occur in the Lagrange equations of motion due to the energy of the flow in the inlet and outlet surface [3].

5.2.5 Pulsatile viscous effects

The nature of the boundary layer is influenced by the roughness of the inner wall of the prosthesis. For this reason, the unsteady time-averaged Navier-Stokes equations [26, 37] are used to take into account the pulsatile viscous effects. A variable mean transmural pressure $\Delta P_{0,L}$, representing the pressure drop along the shell, and an axial frictional traction force τ_x, acting on the internal wall, are introduced in the model. In case of unsteady flow, the fluid pressure P on the vessel surface is given by

$$P(x,R,t) = -\rho_F \left(\frac{f}{4R} U(x,t)^2 + \frac{\partial U(x,t)}{\partial t} \right) x + P(0,R,t), \tag{5.12}$$

where the friction factor f is calculated through the experimental Colebrook equation (assuming $f = 0.097$). Assuming that $P(L/2,R)=0$, it is possible to directly add the pressure P to the pulsatile uniform transmural pressure p_m acting on the vessel wall. The pressure drop along the vessel can be written as

$$\Delta P_{0,L} = P(0,R,t) - P(L,R,t) = \rho_F \left(\frac{f}{4R} U(x,t)^2 + \frac{\partial U(x,t)}{\partial t} \right) L. \tag{5.13}$$

The unsteady axial friction traction force per unit area [182] is

$$\tau_x(x,t,R) = -\rho_F \left(f \frac{U(x,t)^2}{8} + \frac{R}{2} \frac{\partial\, U(x,t)}{\partial\, t} \right). \tag{5.14}$$

5.2.6 Lagrange Equations of Motion

The Lagrange equations for a non-material volume, compared to the classical formulation for a material volume, involve a correction term given by the flux of kinetic energy transported through the surface of the control volume [183]. The vector $\mathbf{q}$ including all the generalized coordinates $u_{m,j}(t), v_{m,j}(t), w_{m,j}(t)$ is introduced for the sake of simplicity in the notation. The generic generalized coordinate is expressed by q_j. In case of pulsatile flow with pulse wave propagation, the Lagrange equations of motion for open systems can be written as [3]

$$\begin{aligned} &\frac{d}{dt}\left[\frac{\partial \left(T_S + T_F + \bar{E}_G \right)}{\partial \dot{q}_j} \right] - \frac{\partial \bar{E}_G}{\partial q_j} + \frac{\partial \left(U_S + \bar{V}_F \right)}{\partial q_j} \\ &+ \frac{1}{2} \rho_F \int_S \frac{\partial}{\partial \dot{q}_j} \left(\mathbf{v_F} \cdot \mathbf{v_F} \right) \left(\mathbf{v_F} - \mathbf{v_S} \right) \cdot \mathbf{n}\, \mathrm{d}S - \frac{1}{2} \rho_F \int_S \left(\mathbf{v_F} \cdot \mathbf{v_F} \right) \left(\frac{\partial \mathbf{v_F}}{\partial \dot{q}_j} - \frac{\partial \mathbf{v_S}}{\partial \dot{q}_j} \right) \cdot \mathbf{n}\, \mathrm{d}S = Q_j, \quad j = 1 \ldots N_T, \end{aligned} \tag{5.15}$$

where T_S, T_F and U_S have been previously defined in Eq. (5.2), Eq. (5.11a) and Eq. (5.3), respectively. The modified potential energy $\bar{V}_F$ and the modified gyroscopic energy $\bar{E}_G$ of the flow are calculated not only at the vessel wall, as given by Eq. (5.11b,c), but also at the inlet and outlet surfaces [3]. The vectors $\mathbf{v_F}$ and $\mathbf{v_S}$ are the velocity vector of the fluid and of the structure at a generic point on the boundary surface *S*, respectively; N_T is the number of degrees of freedom. The surface integrals are evaluated at the boundary surface *S* of the volume Γ, and **n** denotes the outer normal unit vector at that surface. The generalized external forces Q_j are given by

$$Q_j = -\rho_F \left(\frac{\partial}{\partial q_j} \int_\Gamma U \frac{\partial \Phi}{\partial x} \mathrm{d}\Gamma + \frac{\partial}{\partial \dot{q}_j} \int_\Gamma U \frac{\partial \Phi}{\partial x} \mathrm{d}\Gamma \right) + \frac{\partial W}{\partial q_j} - \frac{\partial F}{\partial \dot{q}_j}, \tag{5.16}$$

where the two integrals on the right-hand side represent an effect of the pulse-wave propagation inside the vessel and are included in Q_j since they are equivalent to a load not depending on the generalized coordinates or their derivatives. The last two terms are related to pulsatile viscous effects and viscous damping, as follows:

$$W = \int_0^{2\pi} \int_0^L \left[\left(\Delta P_{0,L} + p_m \right) w + \tau_x u \right] \mathrm{d}x \, R \, \mathrm{d}\theta, \tag{5.17a}$$

$$F = \frac{1}{2} c \int_0^{2\pi} \int_0^L \left(\dot{u}^2 + \dot{v}^2 + \dot{w}^2 \right) \mathrm{d}x \, R \, \mathrm{d}\theta, \tag{5.17b}$$

where in this formulation of the virtual work W due to the pressure load is assumed to be displacement independent, which is a good approximation for moderate deflections of thin shells as is the case here. However, for large deformations, it is essential to model the pressure as a displacement dependent load [3].

The resulting equations of motion for the coupled system can be written in matrix form as

$$(\mathbf{M_S} + \mathbf{M_F})\ddot{\mathbf{q}} + \left(\mathbf{C} + \mathbf{C_F} \right) \dot{\mathbf{q}} + \left[\mathbf{K_S} + \mathbf{K_F} + \mathbf{N_2}(\mathbf{q}) + \mathbf{N_3}(\mathbf{q},\mathbf{q}) \right] \mathbf{q} = \mathbf{Q}, \tag{5.18}$$

where $\mathbf{M_S}$ and $\mathbf{M_F}$ are the mass matrices of the shell and the fluid, respectively, $\mathbf{C_F}$ is the gyroscopic matrix due to the flow, $\mathbf{K_F}$ is the stiffness matrix due to the flow and $\mathbf{C}$ the damping matrix that simulates dissipation. Moreover, $\mathbf{K_S}$ is the linear stiffness matrix of the vessel, $\mathbf{N_2}$ and $\mathbf{N_3}$ give the quadratic and cubic nonlinear stiffness terms of the shell, respectively; $\mathbf{Q}$ is the vector representing the external loads including viscous and pulsatile effects. In order to obtain the equations of motion in a suitable form for numerical implementation, the system Eq. (5.18) is multiplied by the inverse of the mass matrix and is then written in state-space form as follows

$$\begin{cases} \dot{\mathbf{q}} = \mathbf{y} \\ \dot{\mathbf{y}} = -\mathbf{M}^{-1}\left(\mathbf{C}+\mathbf{C}_{\mathbf{F}}\right)\dot{\mathbf{q}} - \left[\mathbf{M}^{-1}\left(\mathbf{K}_{\mathbf{S}}+\mathbf{K}_{\mathbf{F}}\right)+\mathbf{M}^{-1}\mathbf{N}_2(\mathbf{q})+\mathbf{M}^{-1}\mathbf{N}_3(\mathbf{q},\mathbf{q})\right]\mathbf{q}+\mathbf{M}^{-1}\mathbf{Q}, \end{cases} \tag{5.19}$$

where $\mathbf{M}$ is the total mass matrix $\mathbf{M} = \mathbf{M}_{\mathbf{S}} + \mathbf{M}_{\mathbf{F}}$ and $\mathbf{y}$ is the vector of the generalized velocities; the dissipation term $\mathbf{M}^{-1}\mathbf{C}$ is given by

$$\mathbf{M}^{-1}\,\mathbf{C} = \begin{bmatrix} 2\omega_1\varsigma_1 & \cdots & 0 \\ 0 & \ddots & 0 \\ 0 & \cdots & 2\omega_{N_T}\varsigma_{N_T} \end{bmatrix}, \tag{5.20}$$

and it is related to the modal damping ratio ς_j and the natural frequency ω_j (rad/s) of each generalized coordinate q_j. Matrix (5.20) is assumed to be diagonal in order to use modal damping. Modal damping ratios, which can only be defined experimentally via modal analysis, control the vibration amplitude at the corresponding resonance peaks. However, away from the peaks of the frequency-response curve, the mass and stiffness of the system control the vibration amplitude.

In linear viscoelasticity, a measure of “internal friction” is given by the loss tangent defined as the tangent of the angle $\delta(\Omega)$ by which the strain is delayed with respect to the stress; this function depends on the vibration frequency Ω. The loss tangent is the parameter that characterizes dissipation in viscoelastic materials and it can be linked at resonance to the modal damping as follows:

$$2\zeta_j(\Omega) = \frac{\omega_j}{\Omega}\tan\delta_j(\Omega) \quad \text{for } j = 1,.., N_T, \tag{5.21}$$

where the subscript j refers to the j-th generalized coordinate, which has a specific mode shape and ω_j are the N_T natural frequencies of the system. At resonance, the ratio ω_j/Ω on the right hand side of Eq. (5.21) becomes equal to one. Since damping plays a major role only in the frequency neighbourhood of the resonances, being the vibration amplitude controlled by the mass and stiffness of the system away from them, it is possible to replace Eq. (5.21) with

$$2\zeta_j(\Omega) = \tan\delta_j(\Omega) \quad \text{for } j = 1,.., N_T. \tag{5.22}$$

In multi-degree-of-freedom systems, the use of modal damping with respect to viscoelastic dissipation presents the advantage of choosing different damping values for different degrees of freedom. Indeed, preliminary experimental modal analysis results (still ongoing) confirm that the asymmetric and axisymmetric modes of vibration do not have the same value of modal damping. In case of viscoelastic dissipation, the damping value depends on the vibration frequency but it is the same for any vibration mode shape. Moreover, the modal damping takes into account dissipation phenomena of different sources not only due to the material but also to fluid-structure interaction and boundary conditions.

In this study, the modal damping is assumed to be constant for all the generalized coordinates. The value considered is $\zeta = 0.04$ that has been obtained by preliminary modal analysis experiments (presently ongoing) on a *Maquet Hemashiled* woven Dacron graft.

5.3 Numerical results

The Lagrange equations of motion have been obtained using the software *Mathematica* [133] able to perform analytical surface integrals of trigonometric functions. For computational convenience, vibration amplitudes have been non-dimensionalized with respect to the shell thickness h, as well as normalized with respect to the principal vibration period. A home-developed continuation code performing direct integration of the Lagrange equations of motion by means of IMSL DIVPAG Fortran routine has been employed to solve the set of nonlinear ordinary differential equations Eq. (5.19). In this direct integration method, which uses the Adams Gear integration scheme, at any increment of the bifurcation parameter (i.e. excitation frequency) the solution is restarted by adding a small perturbation to the solution at the previous point used as the initial condition. Poincaré maps and the related bifurcation diagrams obtained thanks to this method allow the study of very complex nonlinear dynamics.

The mechanical properties of the Dacron graft investigated here are: L =0.18 m, h=0.361 mm, R=0.015 m, $\nu_{\theta x}$ =0.3, E_θ=12 MPa, E_x=0.87 MPa, ρ_S=1247 kg/m^3, ρ_F=1050 kg/m^3, k_a=10^3 N/m^2, k_r=10^2 N/rad. These material and geometric properties have been selected based on previous studies [150, 187, 188] conducted on Dacron prostheses. The choice of the Young's modulus values has already been discussed in Section 5.2.

The physiological waveforms of pressure and velocity [186] in the thoracic aorta are applied to the Dacron graft and they are expanded in terms of Fourier series. The first eight harmonics (N=8) of the Fourier expansion are considered to describe accurately enough the pulsatile pressure and flow [186] at rest, as shown in Fig. 5.2. During exercise the flow velocity curve (Fig. 5.2) displays the maximum velocity peak around 2.31 m/s, as provided in the literature as limit value in healthy conditions [225].

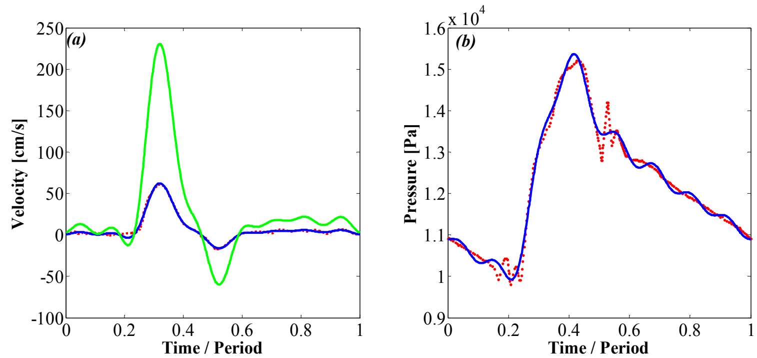

Fig. 5.2. *(a)* Flow velocity at rest (blue line) and during exercise (green line); *(b)* transmural pressure values in the aortic segment; dotted line: physiological data [186], continuous line: Fourier series with N=8.

The small dip displayed in the graph of the aortic pressure (Fig. 5.2(b)) represents the dicrotic notch which coincides with the aortic valve closure. Before gradual decline, it is immediately followed by a brief rise (i.e. dicrotic wave) caused by the arterial elasticity that should be seen in all young individuals. This slight and sudden increase in aortic pressure introduces a high frequency contribution not reproduced in the Fourier expansion with N=8 considered here. However, the absence of the notch in the waveform is considered as the indicator of arterial stiffness, since it depends on physical characteristics of the arterial system such as impedance, compliance, and peripheral resistance. Thus, it is assumed here that the well-known increase in aortic stiffness due to the insertion of a low compliant vessel such as the Dacron implant reduces the amplitude of the dicrotic wave.

The potential effect of the alteration of the physiological waveform of velocity and pressure due to the interposition of a synthetic vessel is neglected. This represents a very interesting research topic that because of its complexity has not been deeply investigated in the literature. Both material and geometrical mismatch of the vascular prosthesis with respect to the host aorta play an important role in this regard. To the authors' knowledge, some studies [189, 190] addressing this subject found that the main effect of the insertion of a thoracic aortic implant slightly affects the shape of the velocity and pressure waveform without any alteration of the general trend (main peaks of the function and mean flow values). The pulse wave velocity $c_0 = 11.72$ m/s obtained through the Moens-Korteweg formula (Eq. 5.10) has been considered for the Dacron implant studied here.

5.3.1 Time responses and FFT to physiological waveforms of pressure and velocity

The time responses of the Dacron graft subjected to the physiological waveforms of pressure and velocity for two different heart rates, $HR = 60$ bpm and $HR = 180$ bpm are presented in Fig. 5.3(a) and Fig. 5.3(b), respectively. The prosthesis radial displacement w, non-dimensionalized with respect to the shell thickness h, is shown versus time at three different axial locations $x = L/4$, $L/2$, $3L/4$ considering the angular coordinate θ=0. The vessel transverse sections are circular at any point since only axisymmetric modes are activated. In Fig. 5.3(a-b), the shell radial displacement for $x = 3L/4$ is delayed with respect to the one for $x = L/4$ because of the pulse-wave propagation phenomenon.

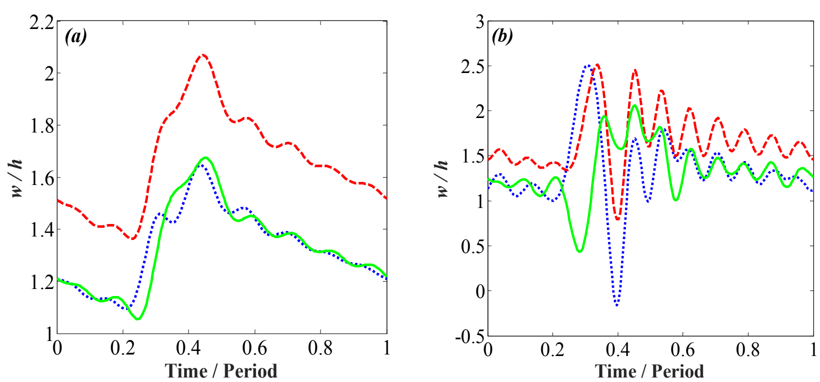

Fig. 5.3. Time response of the nondimensionalized radial displacement w/h under physiological pulsatile pressure and velocity, *(a)* at rest ($HR = 60$ bpm) and *(b)* during exercise ($HR = 180$ bpm); dotted line: $x = L/4$, dashed line: $x = L/2$, continuous line: $x = 3L/4$. Modal damping ratio $\zeta = 0.04$.

It can be noticed that, the time response during exercise (HR = 180 bpm) presents large contributions of higher harmonics while the response at rest (HR = 60 bpm) reproduces the pressure behavior.

Moreover, in Fig. 5.3(b) the vibration is large enough to even reach negative values (i.e. below the original undeformed configuration before pressurization) at $x = L/4$ in correspondence of the systolic pressure peak for $t \approx 0.4\ T$, where T is the time period. This inward axisymmetric contraction is of significant amplitude and reduces the aortic lumen for a short time. This remarkable vibration amplitude highlights potential severe dynamic problems of the prosthesis under exercise conditions. This effect could also be associated to the relatively low damping of the structure that does not allow enough dissipation at high frequencies. Experimental results are needed to validate this interesting and promising finding.

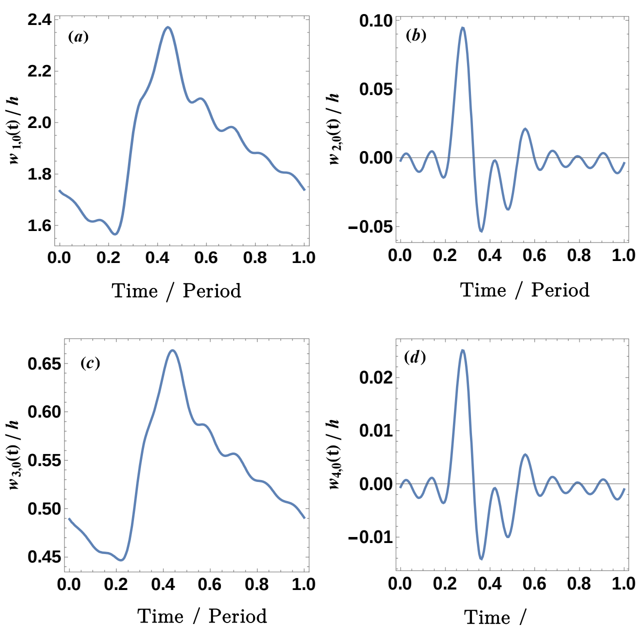

Fig. 5.4. Computed time response of the Dacron prosthesis subjected to physiological pulsatile flow and pressure at rest conditions, $HR = 60$ bpm; *(a)* $w_{1,0}(t)$, *(b)* $w_{2,0}(t)$, *(c)* $w_{3,0}(t)$, *(d)* $w_{4,0}(t)$. Modal damping ratio $\zeta = 0.04$.

The most significant generalized coordinates $w_{1,0}$, $w_{2,0}$, $w_{3,0}$, and $w_{4,0}$ (i.e. those with larger amplitude) are shown in Fig. 5.4(a-d) and Fig. 5.5(a-d) for two different heart rates associated to rest (HR = 60 bmp) and exercise (HR = 180 bpm) conditions, respectively.

The corresponding frequency spectra are represented in Fig. 5.6(a-d) and Fig. 5.7(a-d). The generalized coordinates with an even number of longitudinal half waves are directly excited by the velocity, while the pressure wave acts mainly on the modes with an odd number of longitudinal half waves.

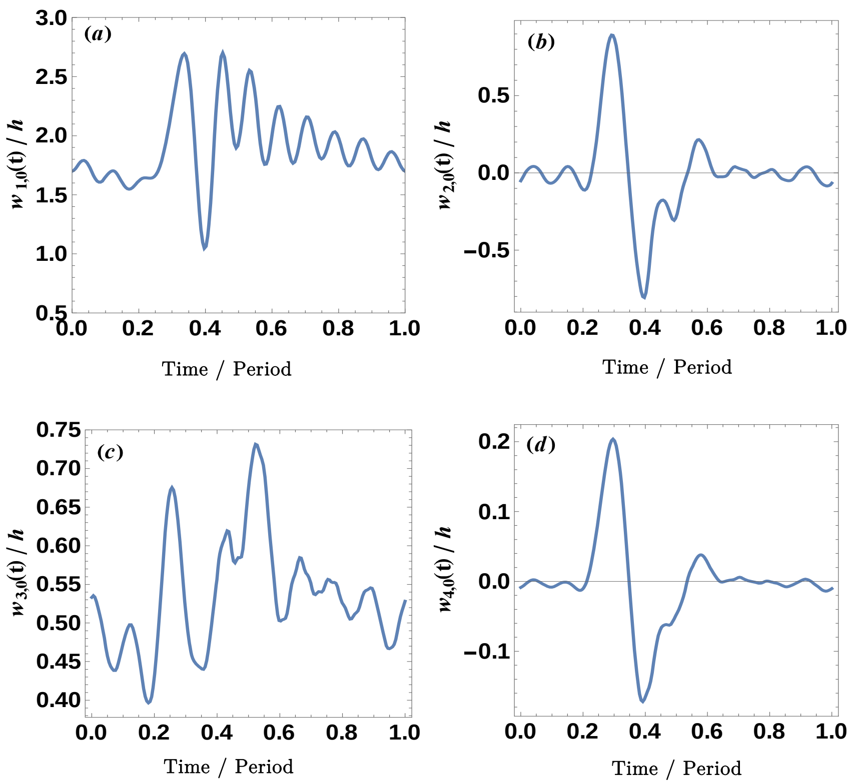

Fig. 5.5. Computed time response of the Dacron prosthesis subjected to physiological pulsatile flow and pressure during exercise, $HR = 180$ bpm; *(a)* $w_{1,0}(t)$, *(b)* $w_{2,0}(t)$, *(c)* $w_{3,0}(t)$, *(d)* $w_{4,0}(t)$. Modal damping ratio $\zeta = 0.04$.

The negative amplitude peak of the vibration for $t \approx 0.4\,T$ for HR = 180 bpm is mainly due to modes $w_{2,0}$ and $w_{4,0}$ as shown in Fig. 5.5(b) and Fig. 5.5(d), respectively. The frequency spectra show high harmonic contributions in the response during exercise (HR = 180 bpm), in particular for the generalized coordinate $w_{1,0}$ (Fig. 5.7(a)).

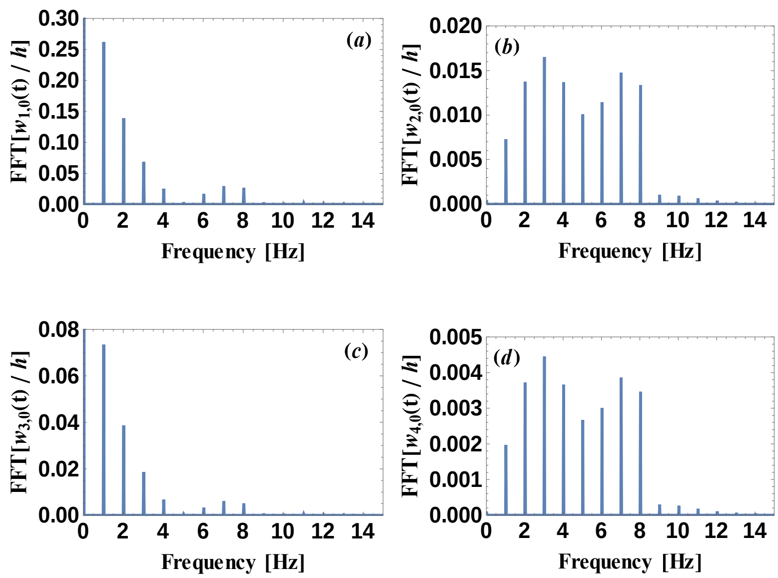

Fig. 5.6. Frequency spectrum of the response of the Dacron prosthesis to physiological pulsatile pressure and velocity at rest conditions, HR = 60 bpm; *(a)* $w_{1,0}(t)$, *(b)* $w_{2,0}(t)$, *(c)* $w_{3,0}(t)$, *(d)* $w_{4,0}(t)$. Modal damping ratio $\zeta = 0.04$.

5.3.2 Frequency-amplitude response for different damping values

Numerical simulations of the vibration amplitude versus heart rate are reported in this section for different values of modal damping ζ in order to investigate the dynamic behavior of the Dacron prosthesis subjected to the physiological conditions of pulsatile flow and pressure during exercise. The values of damping ratio ζ here considered vary between 1% and 5% and they have been selected in agreement with the preliminary experimental results. Fig. 5.8(a-d) presents the maximum amplitude of the response versus the heart rate for the most significant axisymmetric modes $w_{1,0}/h$, $w_{2,0}/h$, $w_{3,0}/h$

and $w_{4,0}/h$ (non-dimensionalized with respect to the thickness h of the shell) obtained by increasing the pulsating frequency.

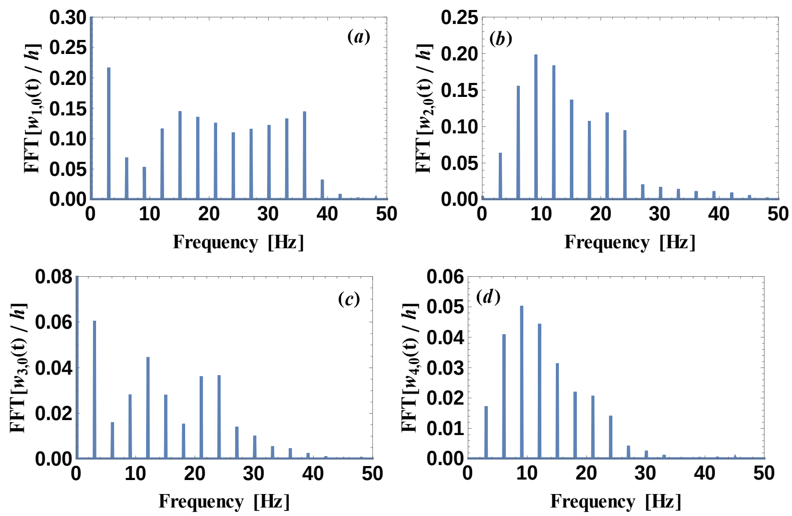

Fig. 5.7. Frequency spectrum of the response of the Dacron prosthesis to physiological pulsatile pressure and velocity during exercise, HR = 180 bpm; *(a)* $w_{1,0}(t)$, *(b)* $w_{2,0}(t)$, *(c)* $w_{3,0}(t)$, *(d)* $w_{4,0}(t)$. Modal damping ratio $\zeta = 0.04$.

As shown in Fig. 5.8, in the range of heart rates between 50 bpm and 130 bpm, all the curves with different modal damping ζ are overlapped and all the vibration amplitudes grow monotonically with the increase of the rate of the heartbeat. This means that in this frequency range, the damping ratio ζ does not affect the response of the system. However, between 130 bpm and 200 bpm, multiple peaks appear in the vibration amplitudes and their magnitudes notably increase by reducing the damping ratio ζ as shown in the zoomed figures Fig. 5.9. When the vessel is pressurized with the steady transmural pressure $\bar{p}_m = 12253$ Pa, which is the mean value obtained in Fig. 5.2(b), the fundamental mode is the first axisymmetric mode whose frequency is $\omega_{1,0} = 35.75$ Hz. Resonance peaks shown in Fig. 9 correspond to the superharmonics of the excitation (i.e. pulsatile flow velocity) with frequency $\Omega = \omega_{1,0} / k$ where $k = 2, 3,.., 2N$. Indeed, the physiological pulsatile flow and pressure are here represented with eight harmonics (N=8), but higher harmonics up to 2N exist in the excitation due to the squared velocity term that appears in the potential flow energy V_F (Eq. 5.11b), the pressure drop $\Delta P_{0,L}$ (Eq. 5.13), and the pulsatile axial friction traction force per unit area τ_x (Eq. 5.14).

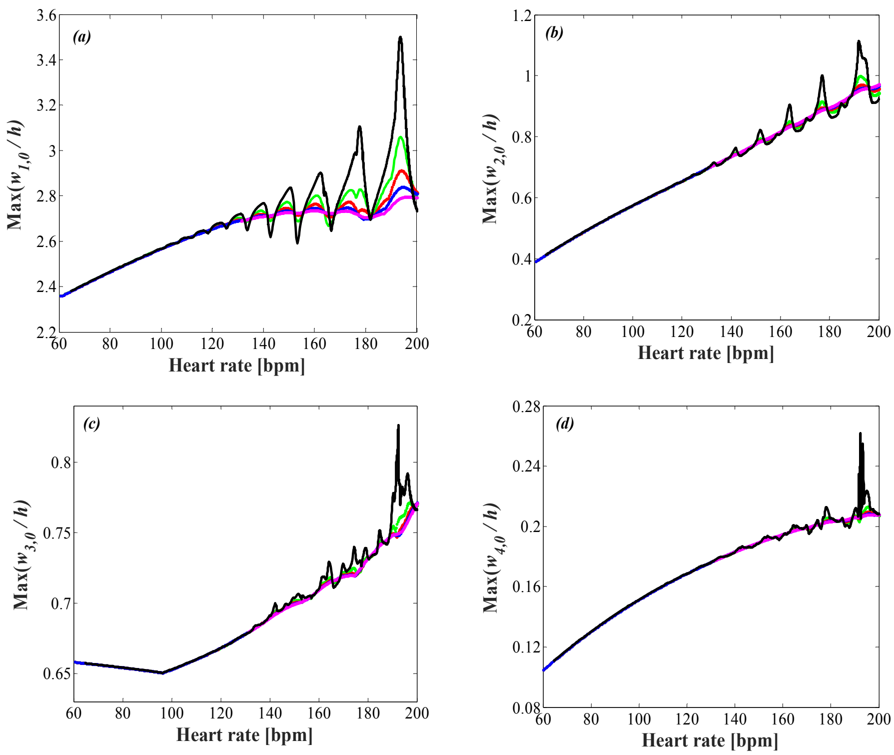

Fig. 5.8. Frequency response curves of the axisymmetric modes: *(a)* $w_{1,0}$, (b) $w_{2,0}$, *(c)* $w_{3,0}$, and *(d)* $w_{4,0}$ obtained by varying the heart rate (HR); ζ = 0.01 (black line), ζ = 0.02 (green line), ζ = 0.03 (red line), ζ = 0.04 (blue line), ζ = 0.05 (magenta line).

Resonant peaks for different values of damping ζ correspond to a circumferential oscillating dilation of the prosthesis that can compromise its long term functioning. It is well known that graft dilation is one of the main reasons of graft failure, since it can induce yarn breakages and eventually tears. The oscillations of the value of the cross-section diameter for different heart rates represented by the resonant peaks may also provoke fluctuations in the flow shear stress and disturbed blood flow. Moreover, as shown in Fig. 5.10, for the limit case of damping $\zeta = 0.01$, which is a bit smaller than what seems to be a realistic dissipation value, and high heart rates around $HR = 190$ bpm, the prosthesis presents asymmetric vibration with deformation of the cross-section, compromising its proper functioning. A period-doubling bifurcation appears giving dynamic instability for a heart rate of 191.4 bpm. The mode shape of the vibrating Dacron prosthesis displays deformation with circumferential wave number n=2 [89] and it introduces bending of the wall, generating much higher stress in the inner wall. The response is periodic with the excitation period T for 191.4 bpm $< HR <$ 192.8 bpm and with two times the excitation period (2T) for 193.1 bpm $< HR <$ 194.1 bpm.

Figs. 5.11(a,b) are Poincaré maps obtained from direct time integration used to study the system in the spectral neighborhood associated to the asymmetric modes activation. The periodic response with two times the excitation period (2T) is detected by the two spots on the Poincaré maps for $HR =$ 193.31 bpm (Fig. 5.11). The system recovers its stability at $HR = 194.2$ bpm associated to the zero amplitude vibration of the asymmetric modes.

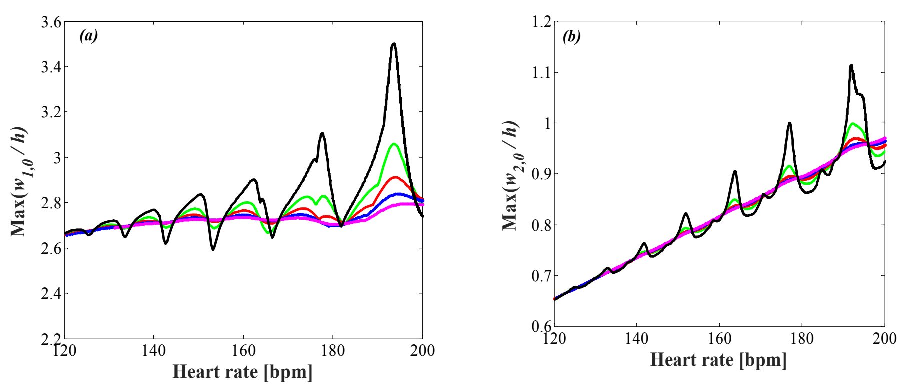

Fig. 5.9. Zoom in the sueperharmonic resonant peaks zone of the frequency response curves of the axisymmetric modes: *(a)* $w_{1,0}$, *(b)* $w_{2,0}$, *(c)* $w_{3,0}$, and *(d)* $w_{4,0}$ obtained by varying the heart rate (HR); ζ = 0.01 (black line), ζ = 0.02 (green line), ζ = 0.03 (red line), ζ = 0.04 (blue line), ζ = 0.05 (magenta line).

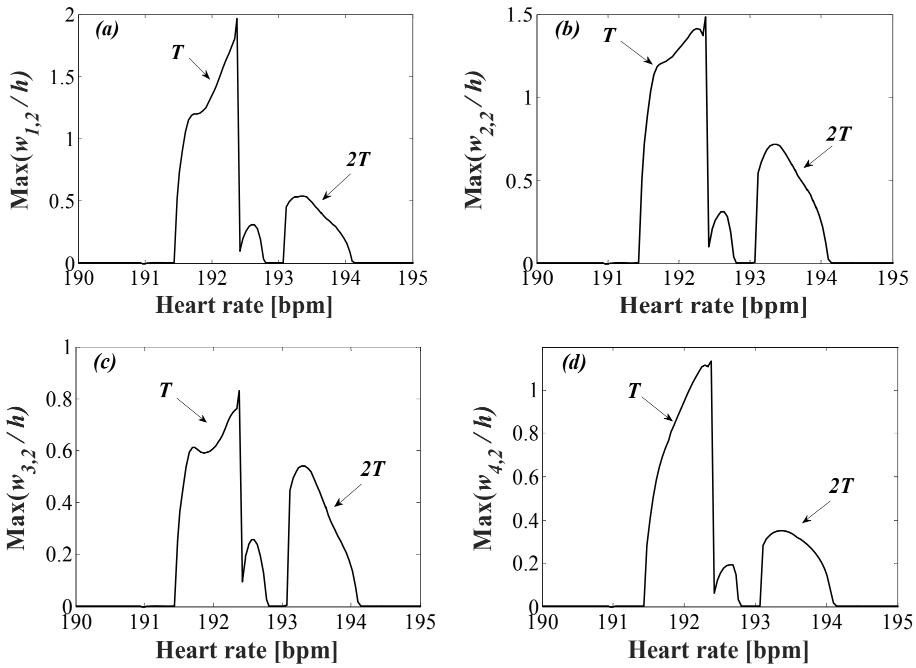

Fig. 5.10. Bifurcation diagrams for the asymmetric modes (a) $w_{1,2}$, (b) $w_{2,2}$, (c) $w_{3,2}$, (d) $w_{4,2}$; T and 2T stand for periodic response with the excitation period and twice the excitation period, respectively. Modal damping ratio $\zeta = 0.01$.

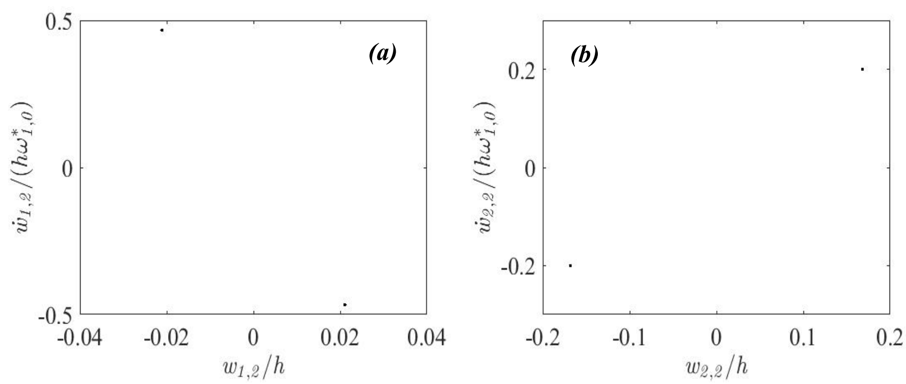

Fig. 5.11. Poincaré maps of the generalized coordinates (a) $w_{1,2}$ and (b) $w_{2,2}$ for HR = 193.32 bpm. Modal damping ratio $\zeta = 0.01$.

5.4 Conclusions

This study provides a deep insight in the dynamic behavior of textile structures used nowadays as vascular prosthetic grafts. Nonlinear vibrations of an artificial vessel excited by physiological pulsatile pressure and flow are here studied with time responses and frequency-amplitude responses by varying the heart rate.

Modal damping values estimated by preliminary experimental modal analysis are relatively small (between $\zeta \approx 0.01$ and $\zeta \approx 0.04$), especially if compared to the damping values of biological soft tissues.

Time responses of the vessel radial displacement for different values of the axial coordinate are considered for two physiological conditions: at rest (60 bpm) and during exercise (180 bpm). They both show the wave motion propagation downstream inside the vessel. Frequency contributions associated with higher harmonics are observed in the time responses at 180 bpm, while the response at 60 bpm reproduces the behavior of the pulsatile pressure.

The effect of different modal damping ratios on the frequency response of the system is also investigated. Vibration amplitudes for heart rates between 60 bpm and 130 bpm are shown to not be affected by the damping values. Frequency-responses show resonance peaks for heart rates between 130 bpm and 200 bpm due to the superharmonics of the pulsatile flow excitation; their amplitudes are strongly affected by the value of the modal damping ratio. These resonant peaks can facilitate the graft dilative characteristic and disturb the flow. Different damping values ζ are considered based on the preliminary experimental characterization of this parameter. For the limit case of $\zeta = 0.01$, flow-induced asymmetric vibration of the aortic prosthesis is possible. A period-doubling bifurcation appears at $HR = 191.4$ bpm giving a dynamic instability characterized by a periodic response with two times the excitation period (2T). This vibration can cause high stress concentration which, combined with the fatigue cycles of the heart beats, could contribute to material deterioration. We are currently developing a more accurate structural model that includes the imperfections of the vessel wall. Our experimental activities aim to characterize the viscous and viscoelastic parameters extracted in nonlinear dynamic regime.

Interesting future research studies include simulating more realistic connections with the host artery by releasing boundary conditions in the radial direction, which would lower the natural frequencies of the system and make the vibration even more significant. Moreover, the effect of surface waves due to the crimped structure of the graft in the longitudinal direction can be included in the model. A more accurate experimental characterization of the material properties of Dacron implants currently used in clinical practice can be introduced in the analysis. The completion of the ongoing experimental activity aiming to obtain realistic damping values of such prostheses will provide a deeper insight in the dynamic behavior of these artificial vessels.

Making surgeons aware of the effects in the differences between dynamical behavior of prostheses with respect to the human arteries can aid in surgical decision making and eventually inspire the design of new materials or techniques for the fabrication of a next generation prostheses that may be strong enough to resist dilatation and compliant enough to permit arterial pulsatile flow.

Acknowledgements

The authors would like to thank NSERC Discovery Grant program, Qatar Foundation grant NPRP 7-032-2-016 and the Canada Research Chair program for their financial support. The first author received a scholarship from the Fonds de recherche du Québec – Nature et technologies (FRQNT).

Chapter 6

Quasi-linear viscoelasticity applied to an aortic woven Dacron graft

An accurate experimental characterization of the material properties of woven Dacron implants is presented in this chapter. An innovative formulation of quasi-linear viscoelastic theory has been used to experimentally investigate the direction-dependent relaxation of an aortic graft made of woven Dacron by using a bi-dimensional material model. The manuscript "Application of three-dimensional quasi-linear viscoelasticity to relaxation of an aortic woven Dacron Graft" presented in this chapter has been recently submitted in a peer-reviewed international journal.

APPLICATION OF THREE-DIMENSIONAL QUASI-LINEAR VISCOELASTICITY TO RELAXATION OF AN AORTIC WOVEN DACRON GRAFT

Marco Amabili, Giovanni Ferrari, Prabakaran Balasubramanian, Eleonora Tubaldi

Department of Mechanical Engineering, McGill University

Abstract

An original, exact (within the limits of validity of the quasi-linear viscoelasticity) and simple formulation of the three-dimensional quasi-linear viscoelasticity is directly obtained manipulating the original Fung equation. The model allows a relevant simplification in case of direction-dependent viscoelasticity. The present formulation is applied to fit original experimental data of relaxation in axial and circumferential directions of an aortic graft made of woven Dacron. A significant difference between the reduced relaxation in circumferential and axial directions has been identified. The loss tangent, which is relevant in dynamic modelling, has been evaluated from the relaxation data and shows a large dependence on the direction.

6.1 Introduction

The quasi-linear viscoelasticity (QLV) was introduced in biomechanics by Fung [1, 2], even if it was known before for rubber materials.

The theory of linear viscoelasticity applies for small deformations. In case of finite deformations, like the ones reached in arteries due to the pressure and flow pulsation, it is required the use of nonlinear (hyperelastic) stress-strain relationships. In order to address this problem, Fung introduced the QLV. The superposition principle is assumed to hold true in the QLV. The superposition is a characteristic of linear systems; in the

QLV it is applied to nonlinear elasticity and named nonlinear superposition. This is the reason for labelling the theory as quasi-linear: it extends the linear viscoelasticity to hyperelastic materials. The QLV presents the simplification that the reduced relaxation function is independent of the strain level.

The QLV theory is still very popular, as proved by its wide use in biomechanics literature. Here just a short review is reported.

Dortmans *et al*. [3] obtained the exact formulation for the reduced creep function in the case of continuous spectrum of relaxation within the framework of the QLV. Puso and Weiss [4] formulated a finite element implementation of anisotropic QLV using a discrete spectrum approximation and a single relaxation function. An implementation of three-dimensional QLV has been developed by Bischoff [5] and Giles *et al*. [6], also by using a single relaxation function for stresses in different directions. Giles *et al*. [6] also obtained interesting results by using a different nonlinear viscoelastic model based on the study conducted by Holzapfel *et al*. [7].

Sarver *et al*. [8] derived stress normalization methods for QLV modeling of soft tissue. Gimbel *et al*. [9] studied the effect of overshoot on estimated QLV parameters. Abramovitch and Woo [10] developed an improved technique for fitting experimental relaxation experiments to the QLV relaxation function for continuous spectrum. Troyer *et al*. [11] introduced a correction method for stress relaxation experiments, applicable also to QLV. Even in recent experiments on relaxation, data are fitted by using the reduced relaxation function obtained by Fung with the QLV (Castile *et al*. [12]). Babaei *et al*. [13, 14] introduced a discrete spectral analysis for determining QLV properties of biological materials.

In the present study, an original, exact (within the limits of validity of the QLV) and simple formulation of the three-dimensional QLV is obtained manipulating the original

Fung [2] equation. The model allows for a relevant simplification in case of direction-dependent viscoelasticity. The present formulation is applied to fit original experimental data of uniaxial relaxation tests of strips taken in axial and circumferential directions from an aortic graft made of woven Dacron (*Hemashield Platinum* by *Maquet*). No previous studies on relaxation of woven Dacron (PET: polyethylene terephthalate), except the one by Lee and Wilson [15] at low strain rates, are known to the authors, while the static mechanical properties have been well investigated (e.g. Hasegawa and Azuma [16]; How [17]; Yeoman *et al*. [18]).

6.2 Three-Dimensional QLV Theory

The three-dimensional QLV was introduced by Fung in Section 7.13 of his monograph [2] by using the equation (here a different notation is used)

$$\sigma_{ij}(t)=\sum_{k=1}^{3}\sum_{l=1}^{3}\left\{\tilde{\sigma}_{kl}\left[\mathbf{E}(0+)\right]G_{ijkl}(t)+\int_{0}^{t}G_{ijkl}(t-\tau)\frac{\partial\tilde{\sigma}_{kl}\left[\mathbf{E}(\tau)\right]}{\partial\tau}\mathrm{d}\tau\right\}, \tag{6.1}$$

where σ_{ij} are the components of the second Piola-Kirchhoff stress tensor $\boldsymbol{\sigma}(t)$, $\mathbf{E}$ is the Green's strain tensor, $\tilde{\sigma}_{kl}$ are the components of the instantaneous second Piola-Kirchhoff stress tensor $\tilde{\boldsymbol{\sigma}}$ corresponding to the static strain tensor $\mathbf{E}$, and G_{ijkl} are the components of the fourth-order tensor of the reduced relaxation functions. Many of the components of G_{ijkl} are not independent. In case of isotropic material, only two independent functions can be used.

If the derivatives of both G_{ijkl} and $\tilde{\sigma}_{kl}$ are continuous functions, equation (6.1) can be integrated by parts

$$\begin{aligned}\sigma_{ij}(t) &= \sum_{k=1}^{3}\sum_{l=1}^{3}\left\{G_{ijkl}(t=0)\,\tilde{\sigma}_{kl}\left[\mathbf{E}(t)\right]+\int_0^t \tilde{\sigma}_{kl}\left[\mathbf{E}(t-\tau)\right]\frac{\partial G_{ijkl}(\tau)}{\partial\tau}\,\mathrm{d}\,\tau\right\}\\ &= \sum_{k=1}^{3}\sum_{l=1}^{3}\left\{G_{ijkl}(t=0)\,\tilde{\sigma}_{kl}\left[\mathbf{E}(t)\right]+\int_0^t \tilde{\sigma}_{kl}\left[\mathbf{E}(\tau)\right]\frac{\partial G_{ijkl}(t-\tau)}{\partial(t-\tau)}\,\mathrm{d}\,\tau\right\},\end{aligned} \tag{6.2}$$

where the last passage has been obtained by using the variable change $\xi = t-\tau$ and then changing back the variable symbol ξ to τ in the resulting expression. Equations (6.1) and (6.2) are equivalent. Equation (6.2) must be valid also for t = 0, for which $\sigma_{ij}(t=0)=\tilde{\sigma}_{ij}[\mathbf{E}(0)]$; this gives

$$G_{ijkl}(t=0)=\delta_{ik}\delta_{jl}\,, \tag{6.3}$$

where δ indicates the Kronecker delta. Equation (6.3) shows that many of the functions $G_{ijkl}(t)$ are zero at t = 0; these $G_{ijkl}(t)$ decrease with time and are positive-valued functions, so they must be zero at any time if their initial value is zero. Therefore, the relationship $G_{ijkl}(t)$ = 0 holds true if $i \neq k$ and $j \neq l$. This property can be used to rewrite equations (6.1) and (6.2) in a simplified way

$$\sigma_{ij}(t) = \tilde{\sigma}_{ij}\left[\mathbf{E}(0+)\right]G_{ij}(t)+\int_0^t G_{ij}(t-\tau)\frac{\partial\tilde{\sigma}_{ij}\left[\mathbf{E}(\tau)\right]}{\partial\tau}\,\mathrm{d}\,\tau\,, \tag{6.4}$$

$$\sigma_{ij}(t) = \tilde{\sigma}_{ij}\left[\mathbf{E}(t)\right]+\int_0^t \tilde{\sigma}_{ij}\left[\mathbf{E}(\tau)\right]\frac{\partial G_{ij}(t-\tau)}{\partial(t-\tau)}\,\mathrm{d}\,\tau\,. \tag{6.5}$$

Equations (6.4) and (6.5), with respect to equation (6.2), do not contain summations anymore, so each stress has its own reduced relaxation function, which is much simpler and more intuitive. In addition, the fourth-order tensor of the reduced relaxation functions has been substituted with a second-order tensor $\mathrm{G}(t)$ of components $G_{ij}(t)$. This simplification is a consequence of considering the instantaneous elastic stress $\tilde{\sigma}$ instead of the strain in the QLV theory. Therefore, the same simplification cannot be achieved for the three-dimensional linear viscoelasticity. The number of independent reduced relaxation functions in the three-dimensional QLV theory is 6, even in the most general anisotropic case. Even more important, there is no cross-link between relaxation in different directions. The reduced relaxation functions $G_{ij}(t)$ can be identified by three uniaxial and three shear relaxation tests.

The instantaneous elastic stresses $\tilde{\sigma}_{kl}\left[\mathbf{E}(t)\right]$ due to the Green's strain tensor $\mathbf{E}(t)$ can be obtained from the hyperelastic model of the material [19]

$$\tilde{\boldsymbol{\sigma}} = \frac{\partial W[\mathbf{E}(t)]}{\partial \mathbf{E}(t)}, \tag{6.6}$$

which can be rewritten in terms of components

$$\tilde{\sigma}_{kl} = \frac{\partial W[\varepsilon_{11}(t), \varepsilon_{12}(t), \varepsilon_{13}(t), ...]}{\partial \varepsilon_{kl}(t)}. \tag{6.7}$$

In equations (6.6) and (6.7) W is the strain energy density function of the material, obtained from one of the many hyperelastic models available in the literature for anisotropic materials.

The following expression, obtained by Fung [2] using the continuous spectrum of relaxation, can be applied for each one of the six independent functions $G_{ij}(t)$, so that they differ from each other only for the three material coefficients a_{ij}, $\tau_{1_{ij}}$ and $\tau_{2_{ij}}$

$$G_{ij}(t) = \left\{1 + a_{ij}\left[g\left(\frac{t}{\tau_{2_{ij}}}\right) - g\left(\frac{t}{\tau_{1_{ij}}}\right)\right]\right\}\left[1 + a_{ij}\ln\left(\frac{\tau_{2_{ij}}}{\tau_{1_{ij}}}\right)\right]^{-1}, \tag{6.8}$$

where $g(t)$ is the exponential integral function defined by

$$g(t) = \int_t^{\infty} \frac{e^{-x}}{x}\,\mathrm{d}x, \qquad \text{for } t \geq 0. \tag{6.9}$$

For $t \to \infty$, the function $g(t)$ tends to zero and $G_{ij}(t)$ takes the limit value

$$G_{ij}(\infty) = \left[1 + a_{ij}\ln\left(\frac{\tau_{2_{ij}}}{\tau_{1_{ij}}}\right)\right]^{-1}. \tag{6.10}$$

The reduced relaxation function $G(t)$ given in equation (6.8) is plotted in Figure 6.1 versus time for $\tau_1 = 0.01$ s, $\tau_2 = 100$ s and three different values of the coefficient *a*: 0.05, 0.1, 0.25.

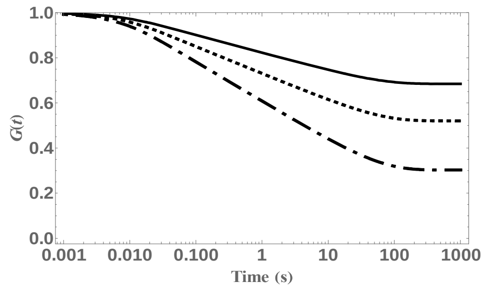

Fig. 6.1. Reduced relaxation function $G(t)$ versus time for $\tau_1 = 0.01$ s, $\tau_2 = 100$ s; curves for three different values of *a* are plotted: continuous line, $a = 0.05$; dashed line, $a = 0.1$; dot-dashed line, $a = 0.25$.

In most cases, the viscoelastic material characterization is not available in different directions. Then, it is common practice to use a single function $G(t)$ obtained by uniaxial tests (Puso and Weiss [4]; Bischoff [5]; Giles *et al.* [6]). Under this simplification, it is possible to write (in tensor notation)

$$\boldsymbol{\sigma}(t) = \tilde{\boldsymbol{\sigma}}\left[\mathbf{E}(0+)\right]G(t) + \int_0^t G(t-\tau)\frac{\partial\tilde{\boldsymbol{\sigma}}\left[\mathbf{E}(\tau)\right]}{\partial\tau}\mathrm{d}\tau\,, \tag{6.11}$$

$$\boldsymbol{\sigma}(t) = \tilde{\boldsymbol{\sigma}}\left[\mathbf{E}(t)\right] + \int_0^t \tilde{\boldsymbol{\sigma}}\left[\mathbf{E}(\tau)\right]\frac{\partial G(t-\tau)}{\partial(t-\tau)}\mathrm{d}\tau\,. \tag{6.12}$$

6.3 Stress relaxation of a woven Dacron graft

Strips of dimension 33.6 × 15 mm taken in axial and circumferential directions have been cut from an aortic woven Dacron graft (diameter 30 mm, thickness 0.35 mm, *Maquet 175428P Hemashield Platinum Woven Double Velour*). The grafts and the strips present waves of height 0.25 mm and wavelength 2.26 mm in the axial direction that are designed in order to reduce the axial stiffness. Uniaxial traction tests have been performed on a test machine (*Admet MicroEP* with *MTEST Quattro* controller and load cell *Honeywell 34*) at room temperature, as shown in Figure 6.2. Both extension (at different strain rates) and relaxation tests have been carried out on both strips after some preconditioning cycles. A few samples from the same graft were tested and several tests were repeated. A similar outcome was obtained from different samples and repeated experiments.

The results of uniaxial extension tests are presented in Figures 6.3(a,b) and show an hyperelastic behaviour with very different stiffness in the two directions. The effect of the strain rate is also significant. Previous results available in the literature for woven Dacron were for static tests (Hasegawa and Azuma [16]; Yeoman *et al*. [18]) or tests at low strain rates (Lee and Wilson [15]).

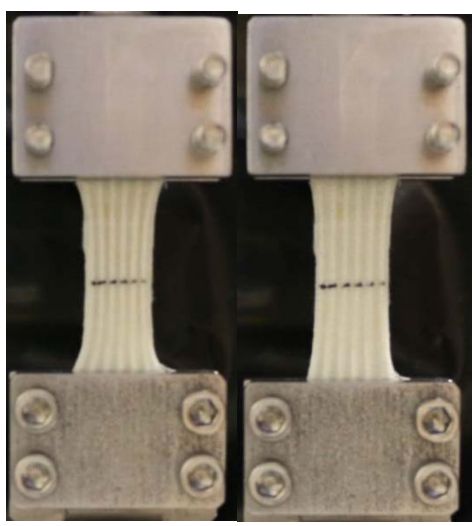

Fig. 6.2. Photos of the extension experiment on the circumferential strip. On the left it is presented the strip before loading and on the right it is at the end of the extension test, showing a significant widening in the orthogonal direction. The “waves” in the axial direction of the specimen are clearly visible in both photos.

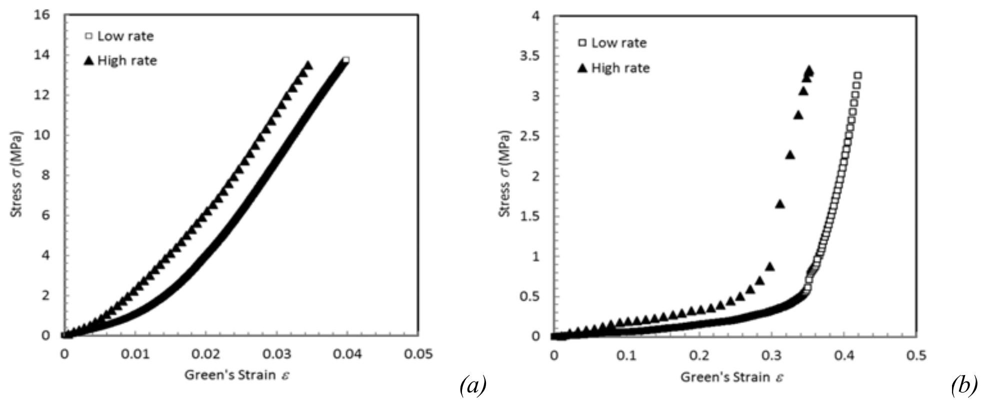

Fig. 6.3. Uniaxial extension tests on strips from a woven Dacron aortic graft (Hemashield Platinum by Macquet) at "low" and "high" strain rates; 2nd Piola-Kirchhoff stresses. *(a)* Circumferential strip, strain rates $\gamma_{\theta\theta} = 0.01869$ s^{-1} and $\gamma_{\theta\theta} = 0.0001246$ s^{-1}; *(b)* axial strip, strain rates $\gamma_{xx} = 0.06187$ s^{-1} and $\gamma_{xx} = 0.0001547$ s^{-1}.

6.3.1 Model fitting of experimental results to hyperelastic law

In case of simple deformation (plane stress and no shear), the anisotropic strain energy density function W can be written in the following form (Yeoman *et al.* [18]), which considers higher-order terms with respect to Fung *et al.* [20]

$$W = C\left\{\exp(c_1\varepsilon_{\theta\theta}^2 + c_{12}\varepsilon_{xx}\varepsilon_{\theta\theta} + c_2\varepsilon_{xx}^2 + c_3\varepsilon_{\theta\theta}^3 + c_{34}\varepsilon_{xx}^2\varepsilon_{\theta\theta} + c_{43}\varepsilon_{xx}\varepsilon_{\theta\theta}^2 + c_4\varepsilon_{xx}^3) - 1\right\}, \qquad (6.13)$$

where $C > 0$ is a stress-like material parameter and c_i are non-dimensional material parameters, all independent; however, they must guarantee the convexity of W [21]. The fitting of the experimental data of the aortic graft material has shown that the model can be simplified, without losing accuracy, assuming $c_2 = c_3 = c_{34} = c_{43} = 0$. The convexity of W is guaranteed if $c_1 > 0$, $c_4 > 0$ and $c_{12} < 0$.

By using the expression of W formulated in equations (6.13), the second Piola-Kirchhoff principal stresses take the following expressions

$$\tilde{\sigma}_{xx} = \frac{\partial W}{\partial \varepsilon_{xx}} = C(c_{12}\varepsilon_{\theta\theta} + 3c_4\varepsilon_{xx}^2)\exp(c_1\varepsilon_{\theta\theta}^2 + c_{12}\varepsilon_{xx}\varepsilon_{\theta\theta} + c_4\varepsilon_{xx}^3), \qquad (6.14a)$$

$$\tilde{\sigma}_{\theta\theta} = \frac{\partial W}{\partial \varepsilon_{\theta\theta}} = C\,(2c_1\varepsilon_{\theta\theta} + c_{12}\varepsilon_{xx})\exp(c_1\varepsilon_{\theta\theta}^2 + c_{12}\varepsilon_{xx}\varepsilon_{\theta\theta} + c_4\varepsilon_{xx}^3)\,. \tag{6.14b}$$

In case of uniaxial extension in axial direction x, equation (6.14a) is used to fit the data and (6.14b) is used to obtain $\varepsilon_{\theta\theta}$ as a function of ε_{xx}, which is then substituted back into equation (6.14a), by setting equation (6.14b) equal to zero. In fact, in case of uniaxial extension in axial direction x, $\tilde{\sigma}_{\theta\theta}$=0. This gives

$$\varepsilon_{\theta\theta} = -\frac{c_{12}}{2c_1}\varepsilon_{xx}\,. \tag{6.15}$$

Similarly, the curve for uniaxial extension in circumferential direction θ is obtained from equation (6.14b) by setting (6.14a) equal to zero; the latter gives

$$\varepsilon_{xx} = \frac{\sqrt{-3c_{12}c_4\,\varepsilon_{\theta\theta}}}{3c_4}\,. \tag{6.16}$$

Each one of equations (6.14a,b) fits the corresponding experimental data set, in order to obtain the unknown material parameters C, c_1, c_{12}, c_4. In particular, the material parameters that guarantee the best fit of the experimental data are obtained by minimizing the following nonlinear stress based function

$$f_s = \sum_{i=1}^{N}\left\{\left(\left.\frac{\partial W}{\partial \varepsilon_{xx}}\right|_i - \sigma_{xx}^{(i)}\right)^2_{(axial)} + \left(\left.\frac{\partial W}{\partial \varepsilon_{\theta\theta}}\right|_i - \sigma_{\theta\theta}^{(i)}\right)^2_{(circ)}\right\}, \tag{6.17}$$

where i indicates the i-th experimental data and the subscripts "*axial*" and "*circ*" indicate if the tested strip of the graft is taken in axial or circumferential direction, respectively.

The experimental data for "low strain rate" and the fitting material model are presented in Figures 6.4(a,b) for the aortic graft in circumferential and axial directions, respectively.

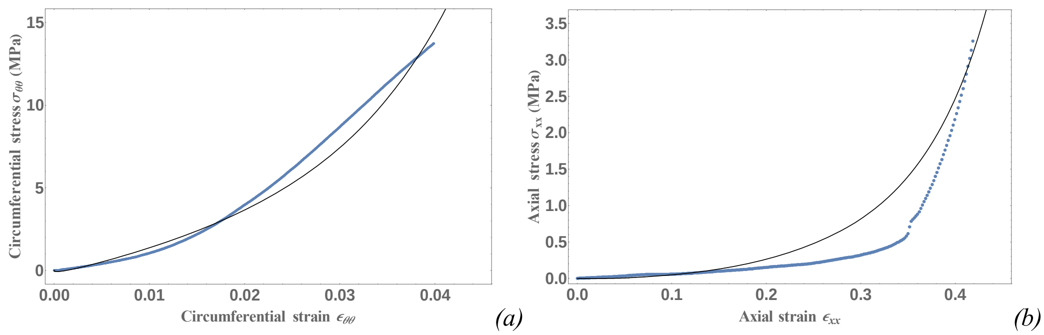

Fig. 6.4. Fitting of the data from the “low strain rate” uniaxial extension tests to hyperelastic law. •, experimental data; —, material model. *(a)* Circumferential direction; *(b)* axial direction.

The identified hyperelastic material parameters are given in Table 6.1. It is interesting to note that $c_{12} < 0$, which justifies the expansion in the direction orthogonal to the applied uniaxial tension observed in Figure 6.2. A significant deviation of the hyperelastic model with respect to the experimental data is observed in Figure 6.4(b) in the mid-range strains, where the curve presents a quick slope change. An improved curve-fitting is possible only choosing a different expression for the strain energy density function W.

Table 6.1. Hyperelastic material model of the aortic graft in woven Dacron (Hemashield Platinum) obtained from “low strain rate” extension tests.

C (MPa)	c_1	c_{12}	c_2	c_4
0.1641	630	-45.0	0	15.0

6.3.2 Model fitting of experimental results for relaxation

Uniaxial relaxation tests have been performed on axial and circumferential strips of an aortic Dacron graft. Relaxation experimental tests cannot be performed applying a step strain. Actual tests have a short ramp of strain growth, possibly linear and with high strain rate, followed by a hold at constant strain to allow relaxation. In order to fit actual experiments with the reduced relaxation function given in equation (6.8), the following procedure is applied [10]. The instantaneous hyperelastic stresses in axial and circumferential directions are given by equations (6.14a,b), respectively (where (6.15) and (6.16) must be used). In the time interval $0 < t < t_{0_{xx}}$, i.e. during the ramp for the axial strip, the strain versus time is given by

$$\varepsilon_{xx}(\tau) = \gamma_{xx}\,\tau\,, \tag{6.18}$$

where γ_{xx} is the constant strain rate. The time derivative of equation (14a) in the interval $0 < t < t_{0_{xx}}$, making use of (6.15), is

$$\begin{aligned}\frac{\partial \tilde{\sigma}_{xx}}{\partial \tau} &= C\; e^{\frac{-\gamma_{xx}^2 \tau^2 \left(c_{12}^2 - 4 c_1 c_4 \gamma_{xx} \tau\right)}{4 c_1}} \\ &\times \frac{\gamma_{xx}\left(c_{12}^4 \gamma_{xx}^2 \tau^2 + 12 c_1^2 c_4 \gamma_{xx} \tau \left(2 + 3 c_4 \gamma_{xx}^3 \tau^3\right) - 2 c_1 c_{12}^2 \left(1 + 6 c_4 \gamma_{xx}^3 \tau^3\right)\right)}{4 c_1^2}.\end{aligned} \tag{6.19}$$

Inserting equation (6.19) into (6.4), the following expression is obtained

$$\sigma_{xx}(t) = \int_0^t \frac{\partial \tilde{\sigma}_{xx} / \partial \tau}{1 + a_{xx} \ln\left(\dfrac{\tau_{2_{xx}}}{\tau_{1_{xx}}}\right)} \left\{1 + a_{xx}\left[g\left(\frac{t-\tau}{\tau_{2_{xx}}}\right) - g\left(\frac{t-\tau}{\tau_{1_{xx}}}\right)\right]\right\} \mathrm{d}\,\tau, \qquad 0 < t < t_{0_{xx}}. \tag{6.20}$$

In the time interval $t > t_{0_{xx}}$, *i.e.* at constant strain $\varepsilon_{xx}(\tau) = \gamma_{xx}\, t_{0_{xx}}$, the stress is given by

$$\sigma_{xx}(t) = \int_0^{t_{0_{xx}}} \frac{\partial \tilde{\sigma}_{xx} / \partial \tau}{1 + a_{xx} \ln\left(\dfrac{\tau_{2_{xx}}}{\tau_{1_{xx}}}\right)} \left\{1 + a_{xx}\left[g\left(\frac{t-\tau}{\tau_{2_{xx}}}\right) - g\left(\frac{t-\tau}{\tau_{1_{xx}}}\right)\right]\right\} \mathrm{d}\,\tau, \qquad t > t_{0_{xx}}, \tag{6.21}$$

since after $t = t_{0_{xx}}$ the derivative of equation (6.14a) with respect to time is zero. Experiments give the values of the measured stresses R_i at discrete times t_i. Equation (6.20) or (6.21), where the choice between the two expressions is made according to the value of t_i, is evaluated at those specific times, giving $\sigma_i = \sigma(t)\big|_{t=t_i}$. Then, the following least square objective function f_{xx}, function of the material parameters, is built

$$f_{xx}(C, c_1, c_{12}, c_4, a_{xx}, \tau_{1_{xx}}, \tau_{2_{xx}}) = \sum_{i=1}^{N} \left[R_i - \sigma_i \right]^2 , \tag{6.22}$$

where N is the number of experimental stresses measured. A similar objective function is built for the circumferential stress. The expression replacing equation (6.19) for tests in circumferential direction is

$$\begin{aligned} \frac{\partial \tilde{\sigma}_{\theta\theta}}{\partial \tau} &= C\, e^{\frac{\gamma_{\theta\theta}\tau\left(9 c_1 c_4 \gamma_{\theta\theta}\tau + 2\sqrt{3} c_{12} \sqrt{-c_{12} c_4 \gamma_{\theta\theta}\tau}\right)}{9 c_4}} \\ &\times \frac{\left(-2 c_{12}^3 \gamma_{\theta\theta}^2 \tau^2 + 24 c_1^2 c_4 \gamma_{\theta\theta}^3 \tau^3 + \sqrt{3} c_{12} \sqrt{-c_{12} c_4 \gamma_{\theta\theta}\tau} + 4 c_1 \gamma_{\theta\theta}\tau \left(3 c_4 + 2\sqrt{3} c_{12} \gamma_{\theta\theta}\tau \sqrt{-c_{12} c_4 \gamma_{\theta\theta}\tau}\right)\right)}{6 c_4 \tau}. \end{aligned} \tag{6.23}$$

The hyperelastic and relaxation parameters that best fit the experiments are obtained by minimizing both objective functions simultaneously. However, while the hyperelastic parameters are strongly coupled, the coupling of the relaxation parameters is weak: *i.e.* their variation influences only slightly the hyperelastic parameters. Once the hyperelastic parameters of the material are known, the relaxation parameters are obtained individually minimizing the two objective functions independently.

Since minimizing the two objective functions simultaneously to obtain the 7 parameters indicated in equation (6.22) is cumbersome, a different procedure has been implemented in the present study. Initially, the hyperelastic parameters C, c_1, c_{12}, c_4 have been identified by using the two stress-strain curves corresponding to the two ramps (just the raising part) at constant strain rate, obtained for the axial and circumferential strips, minimizing equation (6.17). These results are different than those obtained in Table 6.1 and Figures 6.4(a,b) since the strain rate is higher. Then, a multiplication coefficient has been applied to the 3 parameters c_1, c_{12}, c_4 (while C has been kept constant). This multiplication coefficient and the three reduced relaxation parameters $a_{xx}, \tau_{1_{xx}}, \tau_{2_{xx}}$, have been identified by minimizing a single least square objective function built for a single strip (axial or circumferential). This operation is relatively straightforward; it simply requires verifying that the identified multiplication coefficient is the same obtained from the minimization of the two objective functions in different directions; otherwise it is necessary to iterate. In the present case, it was found the value 1.082 for the coefficient without any iteration. The method introduced by Babaei *et al*. [13, 14] could also be applied to identify the reduced relaxation parameters independently.

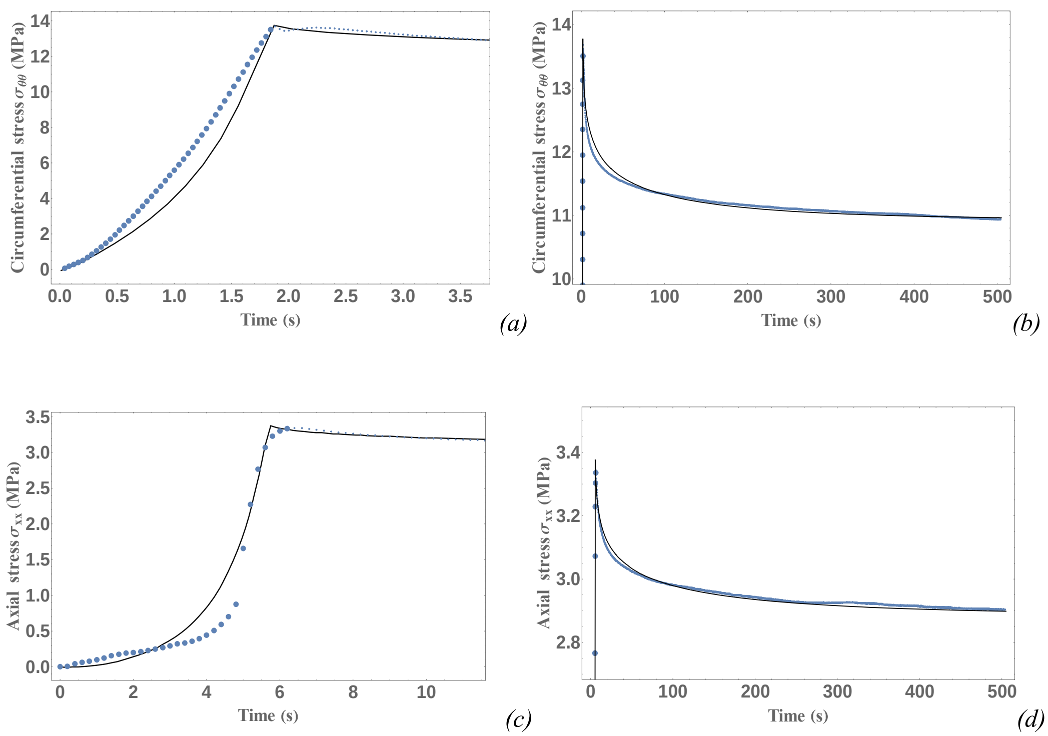

Fig. 6.5. Fitting of relaxation experiments to QLV model. •, experimental data (large dots for points on the ramp and small dots for points at constant strain); —, material model. *(a)* Circumferential direction, $t_{0_{\theta\theta}} = 1.841$ s, $\gamma_{\theta\theta} = 0.01869$ s^{-1}; close-up of the ramp and beginning of the relaxation curve for circumferential strip; *(b)* relaxation curve for circumferential strip; *(c)* axial direction, $t_{0_{xx}} = 5.688$ s, $\gamma_{xx} = 0.06187$ s^{-1}; close-up of the ramp and beginning of the relaxation curve for axial strip; *(d)* relaxation curve for axial strip.

The experimental results and the stress obtained by the material model versus time are compared in Figure 6.5(a-d). Differences in the relaxation time history (*i.e.* after the ramp) are very small, except at the very beginning when the test machine cannot stop the ramp instantaneously, but it has a short deceleration phase. This is more visible in the test of the axial strip since a significantly larger strain rate has been used with respect to the circumferential strip. Instead, some differences are observed in the ramps and are related to the accuracy of the hyperelastic law, previously discussed. The identified material parameters for instantaneous hyperelastic response are given in Table 6.2; the values of c_i are larger than those obtained in Table 6.1, while C is identical in this case. The coefficients of the two reduced relaxation functions are given in Table 6.3. Considering these values in equation (6.10), it gives the reduced relaxations for $t \to \infty$, which are 0.675 and 0.752 in circumferential and axial direction, respectively, with a significant difference.

Table 6.2. Hyperelastic material model of the instantaneous elastic response of the aortic graft obtained from the relaxation tests according to the QLV theory.

C (MPa)	c_1	c_{12}	c_2	c_4
0.1641	799.2	-54.15	0	25.21

Table 6.3. Reduced relaxation parameters of the aortic graft according to the QLV theory.

Direction	τ_1 (s)	τ_2 (s)	a
Circumferential	0.005	300	0.0437
Axial	0.007	400	0.0301

6.4 Damping and storage modulus

The reduced relaxation parameters are linked to the loss tangent by [2]

$$\tan\delta = \frac{a\left[\tan^{-1}(\omega\tau_2) - \tan^{-1}(\omega\tau_1)\right]}{1 + \frac{a}{2}\left[\ln\left(1+\omega^2\tau_2^2\right) - \ln\left(1+\omega^2\tau_1^2\right)\right]}, \tag{6.24}$$

where ω is the vibration circular frequency (rad/s). This is interesting for the dynamic modelling of aortic grafts under pulsatile blood pressure and flow, where structural dissipation must be included. The real part of the reduced dynamic modulus to be used in this type of model is given by

$$\mathrm{Re}\left(\tilde{E}^*(\omega)\right) = \frac{1 + \frac{a}{2}\left[\ln\left(1+\omega^2\tau_2^2\right) - \ln\left(1+\omega^2\tau_1^2\right)\right]}{1 + a\ln\left(\frac{\tau_2}{\tau_1}\right)} \quad . \tag{6.25}$$

Figures 6.6 and 6.7 show the frequency dependence of the loss tangent and the real part of the reduced dynamic modulus, respectively, in circumferential and axial directions for the woven Dacron graft. The physiological frequency range is 6.28 ÷ 18.8 rad/s. For ω = 10 rad/s, $\tan\delta = 0.049$ and 0.036 in circumferential and axial direction, respectively; the damping difference between the two directions is larger than 26 % with respect to the circumferential direction and 36 % with respect to the axial direction. It seems that this is the first time that direction-dependent damping values are reported for vascular grafts.

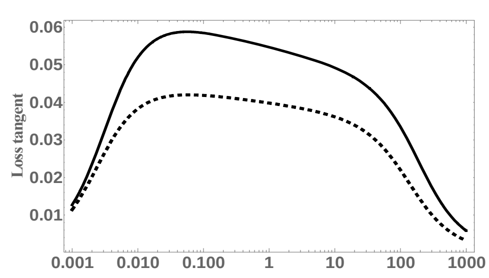

Fig. 6.6. Frequency dependence (rad/s) of the loss tangent. Continuous line, circumferential direction; dashed line, axial direction.

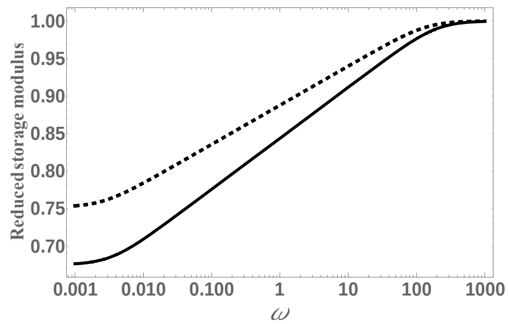

Fig. 6.7. Frequency dependence (rad/s) of the real part of the reduced dynamic modulus (also named storage modulus). Continuous line, circumferential direction; dashed line, axial direction

6.5 Conclusions

Equations (6.4) and (6.5) seem that have been obtained in the present study for the first time; they allow a relevant simplification in case of direction-dependent viscoelasticity. These equations are exact, within the limits of validity of the QLV theory. The present formulation has been used to experimentally investigate, for the first time, the direction-dependent relaxation of an aortic graft made of woven Dacron by using a bi-dimensional material model. A 11 % difference of the reduced relaxations for $t \to \infty$ between axial and circumferential directions has been observed for the woven Dacron, while the difference in the reduced relaxation parameters and damping is even larger. This indicates that investigation of direction-dependent viscoelasticity is worth the effort, and the present simplified formulation of the three-dimensional QLV facilitates the application of the theory.

Acknowledgments

The authors acknowledge the financial support of the NSERC Discovery Grant, the Canada Research Chair program and the Qatar grant NPRP 7-032-2-016.

Chapter 7

Vibration tests of a woven Dacron prosthesis with internal fluid pressure

7.1 Experiments

Experimental activities on the vibrations of Dacron prosthesis have been undertaken in the Laboratory of Mechanical Vibrations and Fluid-Structure Interaction at McGill University.

The experimental setup is composed by the tested Dacron prosthesis (***Maquet 175428P Hemashield Platinum Woven Double Velour Vascular Graft***) with its supporting metal frame Fig. 7.1(a-b), and the transducers and data acquisition system used to perform forced vibration testing. The sample dimensions are 28 mm diameter and 140 mm length in the pre-stretch configuration. A realistic value of axial stretch of the 30% of the original length has been imposed to the prosthesis installed onto a modular and adjustable frame designed for the experiment. Fixed boundary conditions were realized gluing the prosthesis at both ends to the support with a cyanoacrylic glue. In order to apply constant internal pressure, a pipe filled in with fluid has been connected to upper end of the Dacron graft. In the intent to simulate the physiological average pressure in the thoracic aorta, a constant internal pressure of 100 mmHg has been imposed through the fluid column of 1.36 m.

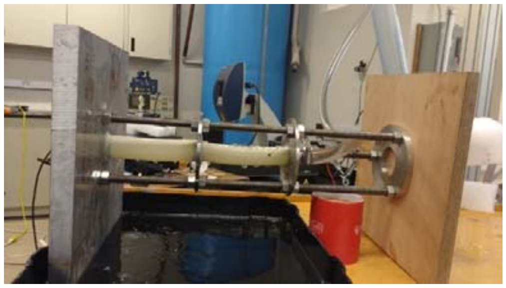

(a)

(b)

Fig. 7.1. (*a*) Experimental testing of Dacron prosthesis with internal fluid pressure; (*b*) Zoomed image of the tested prosthesis.

Fig. 7.1(a) show the two segments of Dacron prosthesis used in the experimental setup. The tested sample is the one the right while the left one has been introduced to accommodate the volume change due to the axisymmetric modes with an odd number of half-waves. This configuration avoids the movement of the fluid in the water column and the related change in damping and potential energy. The horizontal configuration has been preferred with respect to the vertical one in order to not introduce a gradient of potential energy in the tested sample.

The fluid used is a solution of glycerol (30%) and water (70%) that simultaneously matches the kinematic viscosity and density of the blood [226] as shown in Table 7.1.

Table 7.1. Properties of the glycerin mix compared with the blood properties.

Properties	Blood	Glycerin mix
Density (kg/m^3)	1060	1077.8
Viscosity (Ns/m^2)	0.003-0.004	0.0030031

A Brüel & Kjær 8203 miniaturized force transducer has been used to measure the value of the excitation force. The transducer is connected by a stinger to the vibration electrodynamic exciter (shaker), a Brüel & Kjær 4810 powered by a Brüel & Kjær 2718 power amplifier. The shape of natural modes of vibration has been obtained by means of scanning laser Doppler vibrometer (PolytecPSV-400).This technique allows the non-contact measurement of a multitude of points on the surface of the circular cylindrical graft, disposed on a fine grid. Non-contact measurement systems are favored also because they do not introduce unwanted added masses. Modal analysis made use of a dedicated Polytec OFV-5000 data acquisition system. The data have been transferred and processed by the LMSTest.Lab – modal analysis module software. A low amplitude pseudo-random excitation has been used to perform an experimental modal analysis of the shell. The LMS Test. Lab system records the signals from vibration and force sensors both in time and frequency domain.

The pressurized Dacron graft has been subjected to an experimental modal analysis, in order to characterize it. The experimental set-up has been used to perform a modal analysis on the fluid-filled shell, extracting the lowest natural frequencies and the corresponding normal modes and damping ratios. A burst-random signal has been generated by the electrodynamic exciter and the resulting applied force and the velocity response have been recorded and processed at a fine grid of points on the shell surface by using the laser Doppler scanning vibrometer [227]. The vibration velocity of a set of points on the surface of the artificial vessel has been measured and processed by the LMS PolyMax algorithm [228]. As a result, the sum of the Frequency Response Functions has been obtained and it is represented in Fig. 7.2; the corresponding mode shape is indicated at each resonance peak.

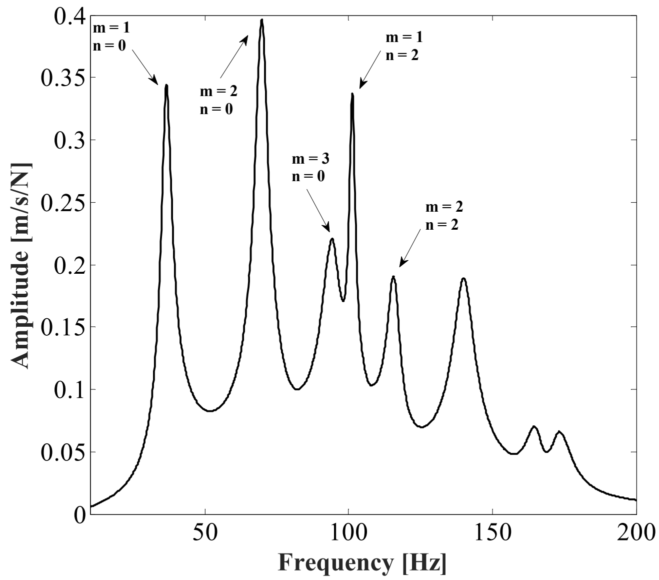

Fig. 7.2. Sum of the frequency response functions (FRFs) of the clamped Dacron prosthesis.

The natural modes are classified by the number of half-waves *m* and *n* in the axial and circumferential direction, respectively. The experimental natural frequencies of the first five modes are given in Table 7.2, which also includes the modal damping ratios, calculated by the algorithm PolyMax.

Table 7.2. Experimental modal analysis results of the clamped Dacron prosthesis. Natural frequencies and corresponding damping ratios.

Mode Shape		Experimental Results	
m	*n*	*Freq.* [*Hz*]	*Damping,* %
1	0	36.48	4.79
2	0	69.74	3.24
3	0	94.35	3.82
1	2	101.22	0.92
2	2	115.79	1.82

It has to be noted that, reduced changes in the internal pressure in a range between 90 mmHg and 110 mmHg do not affect significantly the sequence of the first three modes. As reported, the experimentally identified damping ratios vary between 0.92% and 4.79%. To the knowledge of the authors, these damping values represent the first experimental characterization of such parameter for Dacron thoracic aortic implants. Their range between 1% and 5 % is considerably smaller than the corresponding one of biological soft tissues that is commonly considered between 10% and 15% [217]. This discrepancy proves once again that the mechanical properties of Dacron implants significantly differ from the ones of the host arteries. Low values of modal damping, which indicate low energy dissipation, makes the study of the system's dynamic behavior in response to the pulsatile flow more significant for its important clinical application and possible physiopathological effects.

The modal damping values estimated by these experimental modal analysis tests have inspired the choice of the damping ratios considered in Chapter 5.

7.2 Numerical simulations and comparisons with experimental results

The structural model of the orthotropic circular cylindrical shell described in Chapter 5 has been improved by including the surface waves due to the crimped structure of the graft in the longitudinal direction (Fig. 7.1(b)).

The surface waves have been modeled as initial geometric imperfections of the circular cylindrical shell associated with zero initial stress. These surface imperfections are denoted by radial displacement w_0 while in-plane initial imperfections are neglected. The middle surface strain-displacement relationships, changes in the curvature and torsion obtained for the Novozhilov nonlinear shell theory of circular cylindrical shells with imperfections can be found in Appendix D.

In order to determine the amplitude and the wavelength of the surface wave imperfections of the tested sample, pictures with high resolution camera have been taken and post-processed to determine the pixel location along the diameter and along the length of the shell as shown in Fig. 7.3(a). The extrapolated amplitude of a single wave imperfection is displayed in Fig. 7.3(b).

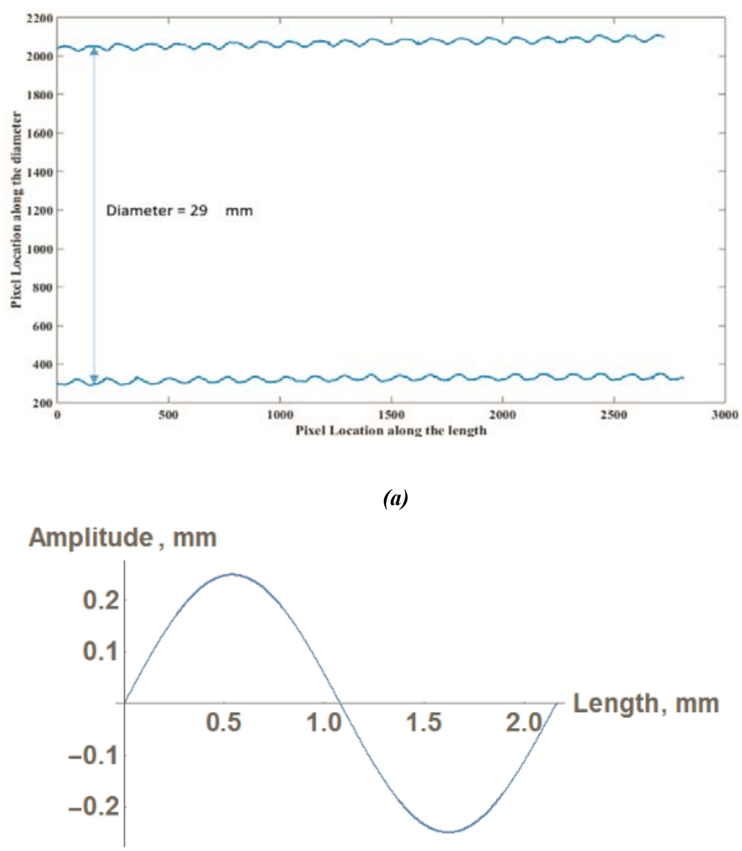

(a)

(b)

Fig. 7.3. *(a)* Location of the pixel along the length vs diameter of the prosthesis; *(b)* extrapolated dimensions of the surface wave on the longitudinal direction of the prosthesis wall.

The total number of waves in the longitudinal direction of the tested Dacron prosthesis is equal to 62. The correspondent semi-amplitude in the radial direction is given by 0.2515mm. The geometric imperfections w_0 modelling the surface waves have been represented as follows:

$$w_0 = A_0 \sin\left(\frac{124\,\pi}{L}\right), \tag{7.1}$$

where the semi-amplitude A_0 is equal to 0.2515 mm and the numbers of half-waves in the longitudinal direction is given by 124.

The energy approach, described in Chapter 5 - Section 5.2.1, has been applied to obtain the Lagrange equations of motion. The flexible boundary conditions, represented by the distributed axial and rotational springs, have been replaced by immovable edges to simulate the experimental setup. Consequently, the potential energy due to the springs U_{spring} is equal to zero in this case. The kinetic T_S and elastic strain U_{shell} energies of the shell are given by Eq. (5.2) and Eq. (5.4), respectively. The added mass effect due to the internal fluid is represented by the kinetic energy of the fluid T_F given by Eq. (5.11a). Since the fluid is quiescent (flow velocity U = 0) the contribution of the gyroscopic E_G and potential V_F energy of the fluid is equal to zero.

The effect of the initial pre-stress of the Dacron sample has been considered as additional strain energy of the shell. This additional strain energy due to an initial axial static pre-load can be written as follows:

$$\begin{aligned} U_{preload} &= \frac{1}{2}\int_{-h/2}^{h/2}\int_{0}^{L}\int_{0}^{2\pi} \sigma_x^s \varepsilon_x (1 + z/R) R \,\mathrm{d}z\,\mathrm{d}x\,\mathrm{d}\theta \\ &= \frac{1}{2}\int_{-h/2}^{h/2}\int_{0}^{L}\int_{0}^{2\pi} \sigma_x^s \left(\varepsilon_{x,0} + z\,k_x\right)(1 + z/R) R \,\mathrm{d}z\,\mathrm{d}x\,\mathrm{d}\theta \\ &= \frac{1}{2}\int_{0}^{L}\int_{0}^{2\pi} N_x^s \left[\varepsilon_{x,0} R + \frac{h^2}{12} k_x\right] \mathrm{d}x\,\mathrm{d}\theta, \end{aligned} \tag{7.2}$$

where σ^S is the stress contribution of the static pre-load assumed to be uniform through the thickness and N_x^s is the initial axial pre-load per unit length in x direction, measured in N/m. The value of N_x^s=59.6 N/m considered here, has been obtained experimentally through a tensile test performed on the Dacron sample.

The Lagrange equations of motion can be written as

$$\frac{d}{dt}\left[\frac{\partial\left(T_S+T_F\right)}{\partial \dot{q}_j}\right]+\frac{\partial\left(U_S+U_{preload}\right)}{\partial q_j}=Q_j, \quad j=1 \ldots N_T \,, \tag{7.3}$$

where the generalized external forces Q_j are given by

$$Q_j=\frac{\partial W}{\partial q_j}-\frac{\partial F}{\partial \dot{q}_j}. \tag{7.4}$$

The energy F is associated to the viscous damping (Eq. (5.17b)) and the virtual work W is due to the pressure load

$$W=\int_0^{2\pi}\int_0^L p_m w \,\mathrm{d}\,x\, R\, \mathrm{d}\,\theta, \tag{7.5}$$

where the internal pressure p_m = 100 mmHg reproduces the experimental conditions.

The approximate trigonometric functions used to describe the middle surface displacements u and w are the same as the ones considered in Eq. (5.6a,c). The circumferential displacement v is neglected since in case of quiescent fluid the torsional mode is decoupled with respect to the axial and radial modes. Only the axisymmetric modes are considered here with the addition of the modes $w_{124,0}$, $u_{124,0}$, $w_{372,0}$, and $u_{372,0}$ associated to the imperfections. The total number of degrees of freedom is N_T = 22 and it is given by: $w_{1,0}$, $w_{2,0}$, $w_{3,0}$, $w_{4,0}$, $w_{5,0}$, $w_{6,0}$, $w_{7,0}$, $w_{9,0}$, $w_{11,0}$, $w_{124,0}$, $w_{372,0}$, $u_{1,0}$, $u_{2,0}$, $u_{3,0}$, $u_{4,0}$, $u_{5,0}$, $u_{6,0}$, $u_{7,0}$, $u_{9,0}$, $u_{11,0}$, $u_{124,0}$, $u_{372,0}$.

The software Mathematica [133] has been used to perform the surface integrals and to obtain the 2× N_T first-order ordinary differential equations (ODEs) written in state space form (Eq. (5.19)). These nonlinear ODEs are solved by using the bifurcation analysis software AUTO [106].

The geometrical and mechanical properties of the shell considered here are given by: L = 0.14 m, h = 0.35 mm, R = 0.0145 m, $\nu_{\theta x}$ = 0.3, E_θ = 7.15 MPa, E_x = 0.53 MPa, ρ_S = 1247 kg/m^3, ρ_F = 1066.7 kg/m^3. The pressurized natural frequencies obtained via the continuation analysis have been compared to the experimental ones in Table 7.3.

Table 7.3. Natural frequencies comparisons between numerical and experimental results.

Mode	Numerical frequencies [Hz]	Experimental frequencies [Hz]	Error %
1,0	35.12	36.48	3.72
2,0	68.90	69.74	1.2
3,0	100.01	94.35	5.99

As shown in Table 7.3, the numerical and experimental natural frequencies present a good agreement with an error lower than the 6%. This experimental validation proves that the structural model considered is appropriate for representing the dynamic behavior of woven Dacron prostheses currently used in thoracic surgery.

Chapter 8

Conclusions

8.1 Implications of the study

This thesis has dealt with the topic of the interaction of a flexible body with a pulsatile fluid that is a widespread phenomenon in nature, occurring in several applied disciplines and at different scales. This challenging problem has been addressed from a theoretical perspective focusing the attention on the development of coupled fluid-structure Lagrange equations of motion able to reproduce the nonlinear dynamic behavior of plates and shells in axial pulsatile flow.

The main contribution of this research to the knowledge of plates in axial flow can be summarized in two relevant findings. First, the pitchfork bifurcation (divergence) that flat plates exhibit when subjected to uniform flow is destroyed by the presence of positive transmural uniform pressure and small pulsation frequency. Secondly, the frequency-amplitude responses that display a hardening type behavior in case of zero uniform transmural pressure become softening in the presence of uniform transmural pressure. Typical phenomena of internal resonances in the response of the fundamental mode with other modes are observed for certain frequency ranges.

Modeling of shell structures conveying pulsatile flow represents the most significant research outcome of the present study due to its meaningful implications in biomechanics.

The pulse-wave propagation phenomenon manifested in pressure and flow traveling waves propagating throughout the flexible medium has been included in the mathematical formulation presented. Vibrations and stability of woven Dacron grafts used in clinical settings for replacements of damaged thoracic aorta have been deeply studied for the first time in the literature. The pulse wave velocity, considered an index of the stiffness of the vessel, has been found to also play a key role in the dynamical behavior of the vascular graft. Decreasing the pulse wave velocity, by reaching close values to the mean aortic pulse wave velocity, stabilizes the system. Severe vibration phenomena of the graft wall have been detected in the physiological range under exercise conditions (i.e. high heart rates and pulsatile flow velocity) where several superharmonic resonance peaks have been detected. This behavior can cause high stress concentration which, combined with the fatigue cycles of the heart beats, could contribute to material deterioration. These findings highlight how urgent is to develop a new design of textile vascular implants able to mimic the mechanical and biological properties of the native aorta.

Material properties of a woven Dacron prosthesis have been investigated with an original formulation of the three-dimensional quasi-linear viscoelasticity. This formulation has been used to experimentally study, for the first time, the direction-dependent relaxation of an aortic graft made of woven Dacron by applying a bi-dimensional material model.

Experimenatal results of the modal analysis of woven Dacron prosthesis pressurized with internal fluid at the mean physiological pressure have been presented. Experimental modal damping values have been reported showing a good agreement with the numerical damping values considered throughout the thesis. The numerical and experimental natural frequencies have been compared presenting a good agreement with an error lower than the 6%. This experimental validation proves that the structural model considered is appropriate for representing the dynamic behavior of woven Dacron prostheses currently used in thoracic surgery.

8.2 Ongoing research

Interesting ongoing research developments include the simulation of more realistic connections with the native aorta by releasing boundary conditions in the radial direction, which has shown experimentally to lower the natural frequencies of the system. Under these conditions, the vibration issue becomes even more widespread in the physiological range.

8.3 Future developments

The fluid-structure interaction model presented in this study can be validated experimentally. In this regard, measurements of radial displacements of a woven Dacron prosthesis excited by a pulsatile pump that reproduces the pumping heart should be undertaken.

The model can be also applied to investigate the dynamic behavior of the human thoracic aortic segment. With this purpose, an accurate description of the viscoelastic and hyperelastic behavior of the aortic tissue should be included in the structural model. The experimental tests described in Section 6.2 could be performed on a segment of thoracic aorta in order to characterize it dynamically. Comparing the dynamic response to pulsatile flow of Dacron implants with the native aorta could unveil important directions in design optimisation research of vascular implants. Moreover, in case of vibration phenomena or instability of the aorta in the physiological frequency range, the proper functioning of the vessel that ensures blood flow would be compromised. High stress concentration regions would appear on the aortic wall representing a possible reason behind the initiation of aortic dissection. This potential outcome would bring a huge contribution to the understanding of the underlying mechanism of aortic dissection that currently does not have a biomechanical explanation.

Appendix A. Lagrange equations for a non material volume

Irshik and Holl [183] derived the Lagrange equations for a non-material (control) volume (used also by Ghayesh *et al.* [230]) as follows

$$\frac{\mathrm{d}}{\mathrm{d}t}\left(\frac{\partial T}{\partial \dot{q}_j}\right)-\frac{\partial T}{\partial q_j}+\int_S \frac{\partial T^{'}}{\partial \dot{q}_j}(\tilde{\mathbf{v}}-\tilde{\mathbf{w}})\cdot\mathbf{n}\,\mathrm{d}\,s-\int_S T^{'}\left(\frac{\partial \tilde{\mathbf{v}}}{\partial \dot{q}_j}-\frac{\partial \tilde{\mathbf{w}}}{\partial \dot{q}_j}\right)\cdot\mathbf{n}\,\mathrm{d}s+\frac{\partial\left(U_p+V_f\right)}{\partial q_j}=Q_j\,, \quad \text{(A.1)}$$

where T denotes the total kinetic energy contained in the control volume (i.e. the structure and the flowing fluid), $\tilde{\mathbf{v}}$ is the velocity vector of the fluid, $\tilde{\mathbf{w}}$ is the velocity vector of the structure, Q_j denotes the generalized forces. $T^{'}=\frac{1}{2}J^{-1}\rho_f\left(\tilde{\mathbf{v}}\cdot\tilde{\mathbf{v}}\right)$ denotes the density of the kinetic energy transported by the fluid where J is the Jacobian determinant of the deformation gradient tensor (i.e. $J=1$ for incompressible fluid). The surface integrals are evaluated at the boundary surface of the control volume $S=S_{in}+S_{out}+S_{plate}+S_{wall}$ and $\mathbf{n}$ denotes the outer normal unit vector at that surface. The total kinetic energy T of the system is given by

$$T=T_f+T_p+E_g\,. \quad \text{(A.2)}$$

Compared to the classical formulation for a material volume, a correction term containing the flux of kinetic energy appearing to be transported through the surface of the control volume is introduced in the equations of Lagrange written for a non-material volume.

For the geometry under consideration, the natural domain of integration due to the shape functions in Eqs. (2.4a-c) and Eq. (2.13) is $2a$ and $2b$ in x and y-direction, respectively.

The two integrals of Eq. (A.1) calculated on the plate $S_{plate}\,(z=0)$ have the following expression

$$\int_0^{2a}\int_0^{2b}\frac{\partial T'}{\partial \dot{q}_j}\left(\frac{\partial \Phi}{\partial z}-\dot{w}\right)dx\,dy-\int_0^{2a}\int_0^{2b}T'\left(\frac{\partial^2 \Phi}{\partial \dot{q}_j\partial z}-\frac{\partial \dot{w}}{\partial \dot{q}_j}\right)dx\,dy. \tag{A.3}$$

For the anti-symmetry of the plate deflection at the periodic supports, these two terms vanish.

At the entry S_{in} and exit S_{out} surfaces, the velocity vector of the plate $\tilde{\boldsymbol{w}}$ is zero (i.e. immovable edges) and the two integrals of Eq. (A.1) would vanish since the system conditions are the same and they cancel each other. Finally for the boundary condition Eq. (2.12b), the two integrals of Eq. (A.1) calculated at the wall surface S_{wall} give zero contribution. Hence, the Lagrange equations of motion for the plate coupled to flowing fluid, knowing that $\partial T_p/\partial q_j = \partial T_f/\partial q_j = 0$, are

$$\frac{d}{dt}\left[\frac{\partial\left(T_p+T_f+E_g\right)}{\partial \dot{q}_j}\right]-\frac{\partial E_g}{\partial q_j}+\frac{\partial\left(U_p+V_f\right)}{\partial q_j}=Q_j, \quad j=1...dof\ , \tag{A.4}$$

where $dof = R\cdot S + M\cdot N + C\cdot D$ is the number of degrees of freedom and $\boldsymbol{q} = \left[q_1,...,q_{dof}\right]^T = \left[u_{rs}, v_{c,2d}, w_{mn}\right]^T$, for $r=1..R$, $s=1..S$, $m=1..M$, $n=1..N$, $c=1..C$, $d=1..D$.

Appendix B. Fluid-structure interaction by Bernoulli's theorem

An alternative approach to discuss the fluid-structure interaction between the plate and the fluid flow is to apply the Bernoulli's theorem to describe the relationship between the perturbation pressure p^* and perturbation potential Φ. In the case of inviscid and irrotational flow, Euler's equations simplify to the well-known unsteady Bernoulli without body forces,

$$\frac{\partial \Psi}{\partial t} + \frac{1}{2}V^2 + \frac{p}{\rho_f} = \frac{p_{stag}}{\rho_f}, \tag{B.1}$$

where p_{stag} is the stagnation pressure. The pressure p is defined by

$$p = p_0 + p^*, \tag{B.2}$$

where p_0 corresponds to the steady potential flow and p^* is the perturbation component. It is assumed that the disturbances causing the deformations of the plate are sufficiently small for their squares and higher-order terms to be ignored. The perturbation pressure p^*, exerted by the fluid on the plate is given by the linearized form of Eq. (B.1) and it may be shown that it has the following expression

$$p^* = -\rho_f\left(\frac{\partial \Psi}{\partial t} + U\frac{\partial \Phi}{\partial x}\right). \tag{B.3}$$

Using the definition of the flow potential Ψ (Eq. (2.10)), Eq. (B.3) becomes

$$p^* = -\rho_f\left(\dot{U}x + \frac{\partial \Phi}{\partial t} + U\frac{\partial \Phi}{\partial x}\right). \tag{B.4}$$

The virtual work W_{pre} done by the perturbation pressure p^* on the plate is given by

$$W_{pre} = -\int_0^a\int_0^b p^* w \,\mathrm{d}x\,\mathrm{d}y = \rho_f U\int_0^a\int_0^b \frac{\partial \Phi}{\partial x} w \,\mathrm{d}x\,\mathrm{d}y + \rho_f\int_0^a\int_0^b \frac{\partial \Phi}{\partial t} w \,\mathrm{d}x\,\mathrm{d}y + \dot{U}\rho_f\int_0^a\int_0^b x\, w \,\mathrm{d}x\,\mathrm{d}y\,. \tag{B.5}$$

According to this approach, the Lagrange equations of motion can be written as follows

$$\frac{\mathrm{d}}{\mathrm{d}t}\left[\frac{\partial T_p}{\partial \dot{q}_j}\right]+\frac{\partial U_p}{\partial q_j}=\tilde{Q}_j, \quad j=1...dof, \tag{B.6}$$

where the generalized forces $\tilde{Q}_j$ can be obtained

$$\tilde{Q}_j=\frac{\partial W_{pre}}{\partial q_j}=\frac{\partial W_{p1}}{\partial q_j}+\frac{\partial W_{p2}}{\partial q_j}+\frac{\partial W_{p3}}{\partial q_j}, \tag{B.7}$$

where $W_{p1}=\rho_f U\int_0^a\int_0^b \frac{\partial \Phi}{\partial x}\, w \,\mathrm{d}x\,\mathrm{d}y$, $W_{p2}=\rho_f \int_0^a\int_0^b \frac{\partial \Phi}{\partial t}\, w \,\mathrm{d}x\,\mathrm{d}y$ and $W_{p3}=\dot{U}\rho_f \int_0^a\int_0^b x\, w \,\mathrm{d}x\,\mathrm{d}y$. Analogies can be found between the right-hand terms of Eq. (B.5) and the energy approach used in paragraph (2.3). The first term W_{p1}, using Eq. (2.4c) and Eq. (2.13) can be rewritten as

$$W_{p1}=\rho_f U\int_0^a\int_0^b \frac{\partial \Phi}{\partial x}\, w \,\mathrm{d}x\,\mathrm{d}y=\rho_f\,\frac{Ub\pi}{2}\sum_{m=1}^{M}\sum_{n=1}^{N}\sum_{r=1}^{R} m_{rn}(0)k_{rn}\beta_{rm} r\; w_{mn}, \tag{B.8}$$

where $m_{rn}(0)$, k_{rn} and β_{rm} have been defined in Eq. (2.16a), Eq. (2.14) and Eq. (2.15), respectively. Applying Eq. (2.14) to Eq. (B.8) and knowing that $\beta_{mr}m=-\beta_{rm}r$, we obtain

$$W_{p1}=W_{p1A}+W_{p1B}=\rho_f\,\frac{Ub\pi}{2}\sum_{m=1}^{M}\sum_{n=1}^{N}\sum_{r=1}^{M}\dot{w}_{rn}m_{rn}(0)\beta_{rm}\; r\; w_{mn}+\rho_f\,\frac{bU^2\pi^2}{a}\sum_{m=1}^{M}\sum_{n=1}^{N}\sum_{r=1}^{M}\sum_{p=1}^{M} w_{pn}\;\beta_{pr}\;\; p\; m_{rn}(0)\beta_{rm}\; r\; w_{mn}. \tag{B.9}$$

The following analogy with Eq. (2.22c) has been found

$$2V_f=-W_{p1B}=\mathbf{w}^{\mathbf{T}}\mathbf{K_f}\mathbf{w}. \tag{B.10}$$

The second term W_{p2} of Eq. (B.5), using Eq. (2.4c) and Eq. (2.13) can be rewritten as

$$W_{p2}=\rho_f \int_0^a\int_0^b \frac{\partial \Phi}{\partial t}\, w \,\mathrm{d}x\,\mathrm{d}y=\rho_f\,\frac{ab}{4}\sum_{m=1}^{M}\sum_{n=1}^{N} w_{mn}\, m_{mn}(0)\,\dot{k}_{mn}, \tag{B.11}$$

where

$$\dot{k}_{mn} = \ddot{w}_{mn} + \frac{2U\pi}{a}\sum_{p=1}^{M}\beta_{pm}\; p\; \dot{w}_{pn} + \frac{2\dot{U}\pi}{a}\sum_{p=1}^{M}\beta_{pm}\; p\; w_{pn}, \tag{B.12}$$

is obtained by substituting the expression of the coefficient k_{mn} (Eq. (2.14)). Hence, the virtual work W_{p2} can be seen as a sum of three terms

$$W_{p2} = W_{p2A} + W_{p2B} + W_{p2C}, \tag{B.13}$$

where it has been defined

$$W_{p2A} = \rho_f \frac{ab}{4}\sum_{m=1}^{M}\sum_{n=1}^{N} w_{mn}\, m_{mn}(0)\, \ddot{w}_{mn}, \tag{B.14a}$$

$$W_{p2B} = \rho_f \frac{bU\pi}{2}\sum_{m=1}^{M}\sum_{n=1}^{N}\sum_{p=1}^{M} w_{mn}\, m_{mn}(0)\, \beta_{pm}\; p\; \dot{w}_{pn}, \tag{B.14b}$$

$$W_{p2C} = \rho_f \frac{\dot{U}b\pi}{2}\sum_{m=1}^{M}\sum_{p=1}^{M}\sum_{n=1}^{N} w_{mn}\, m_{mn}(0)\, \beta_{pm}\; p\; w_{pn}. \tag{B.14c}$$

The following analogy with Eq. (2.22a) has been found

$$2T_f = \dot{\mathbf{w}}^{\mathbf{T}}\mathbf{M_f}\dot{\mathbf{w}} \quad \text{corresponds to} \quad W_{p2A} = -\ddot{\mathbf{w}}\,\mathbf{M_f}\mathbf{w}, \tag{B.15}$$

giving the same fluid inertial term in the Lagrange equations. In analogy, for the gyroscopic term we obtain

$$2E_g = W_{p2B} + W_{p1A} = \dot{\mathbf{w}}^{\mathbf{T}}\mathbf{C_f}\mathbf{w}. \tag{B.16}$$

Moreover, according to the energy approach under the hypothesis of unsteady flow, the term $-\dfrac{b\dot{U}\pi\rho_f}{4}\displaystyle\sum_{p=1}^{M} w_{pn}\left(m_{pn}(0) + m_{mn}(0)\right) p\beta_{pm}$ appeared in the gyroscopic term $\dfrac{\mathrm{d}}{\mathrm{d}t}\left[\dfrac{\partial E_g}{\partial \dot{w}_{mn}}\right]$ of the Lagrange equations (Eq. (2.32)) for $m = 1 \ldots M$, $n = 1 \ldots N$. Applying the Bernoulli's theorem, the following analogy has been found

$$2\tilde{E}_g = \dot{\mathbf{w}}^{\mathbf{T}}\tilde{\mathbf{C}}_{\mathbf{f}}\mathbf{w} \quad \text{corresponds to} \quad W_{p2C} = -\mathbf{w}^{\mathbf{T}}\tilde{\mathbf{C}}_{\mathbf{f}}\mathbf{w}, \tag{B.17}$$

where

$$\tilde{E}_g = -\frac{b\dot{U}\pi\rho_f}{4}\sum_{m=1}^{M}\sum_{n=1}^{N}\sum_{p=1}^{M} w_{pn}\dot{w}_{mn}\left(m_{pn}(0)+m_{mn}(0)\right)p\beta_{pm}, \tag{B.18}$$

$$\tilde{C}_f((p-1)N+n, n+(m-1)N) = -\frac{b\rho_f\dot{U}\pi}{2}(m_{mn}(0)+m_{pn}(0))p\beta_{pm}. \tag{B.19}$$

Furthermore, the third term W_{p3} of Eq. (B.5), corresponds to the term W_{II} (Eq. (2.35b)). In case of channel pressurization, the virtual work W_I (Eq. (2.35a)) done by the related external force must be added to these terms.

Finally, substituting Eq. (B.9), Eq. (B.14a-c) and Eq. (2.35b) in the expression of the generalized coordinates $\tilde{Q}_j$ (Eq. (B.7)), the Lagrange equations of motion expressed in Eq. (B.6) will coincide with the Lagrange equations (Eq. (2.32)) found following the energy approach.

Appendix C. Convergence analysis

By using a different number of terms in the expansions of the displacements *u, v*, and *w* it is possible to study the convergence and the accuracy of the solution. The bifurcation diagrams of the fundamental mode w_{11} with the flow velocity U as the bifurcation parameter based on 13, 29 and 37 *dof* models are shown in Fig. C1. The results from all models are in close agreement. In particular, the bifurcation point coincides for all the models under consideration. This indicates a quick convergence of the solution which presents a very slightly smaller amplitude of the stable branches of the deformed configuration for the model with 13 *dof*. On the other hand, the curves corresponding to 29 and 37 dof models coincide perfectly. The model with 13 *dof* has the following terms $w_{11}, w_{21}, w_{31}, u_{21}, u_{41}, u_{61}, u_{81}, v_{12}, v_{14}, v_{16}, v_{18}, v_{22}, v_{34}$ and the 37 *dof* has the following terms in Eqs. (4):

$w_{11}, w_{12}, w_{13}, w_{21}, w_{22}, w_{23}, w_{31}, w_{32}, w_{33}, u_{21}, u_{22}, u_{23}, u_{24}, u_{41}, u_{42}, u_{43}, u_{44}, u_{61}, u_{62}, u_{63}, u_{64}, u_{81}, u_{83}, v_{12}, v_{14}, v_{16}, v_{18}, v_{22}, v_{24}, v_{26}, v_{28}, v_{32}, v_{34}, v_{36}, v_{42}, v_{44}, v_{46}$.

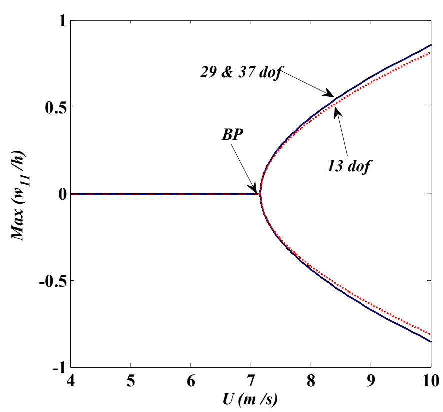

Fig. C1. Amplitude of the static solutions of the fundamental mode w_{11} versus the flow velocity for the plate obtained using different numerical models; BP denotes pitchfork bifurcation. Only stable solutions are plotted (see Tubaldi *et al.* [116]).

Appendix D. Novozhilov Nonlinear Shell Theory: strain-displacement relationships

According to the Novozhilov [231] nonlinear shell theory, the middle surface strain-displacement relationships, changes in curvature and torsion, are given by

$$\varepsilon_{x,0} = \frac{\partial u}{\partial x} + \frac{1}{2}\left[\left(\frac{\partial u}{\partial x}\right)^2 + \left(\frac{\partial v}{\partial x}\right)^2 + \left(\frac{\partial w}{\partial x}\right)^2\right] + \frac{\partial w}{\partial x}\frac{\partial w_0}{\partial x}, \tag{D.1}$$

$$\varepsilon_{\theta,0} = \frac{\partial v}{R\partial\theta} + \frac{w}{R} + \frac{1}{2R^2}\left[\left(\frac{\partial u}{\partial\theta}\right)^2 + \left(\frac{\partial v}{\partial\theta} + w\right)^2 + \left(\frac{\partial w}{\partial\theta} - v\right)^2\right] + \frac{1}{R^2}\left[\frac{\partial w_0}{\partial\theta}\left(\frac{\partial w}{\partial\theta} - v\right) + w_0\left(w + \frac{\partial v}{\partial\theta}\right)\right], \tag{D.2}$$

$$\gamma_{x\theta,0} = \frac{\partial v}{\partial x} + \frac{\partial u}{R\partial\theta} + \frac{1}{R}\left[\frac{\partial u}{\partial x}\frac{\partial u}{\partial\theta} + \frac{\partial v}{\partial x}\left(\frac{\partial v}{\partial\theta} + w\right) + \frac{\partial w}{\partial x}\left(\frac{\partial w}{\partial\theta} - v\right) + \frac{\partial w_0}{\partial x}\left(\frac{\partial w}{\partial\theta} - v\right) + \frac{\partial w}{\partial x}\frac{\partial w_0}{\partial\theta} + \frac{\partial v}{\partial x}w_0\right], \tag{D.3}$$

$$k_x = -\frac{\partial^2 w}{\partial x^2}, \tag{D.4}$$

$$k_\theta = -\frac{\partial^2 w}{R^2\partial\theta^2} + \frac{\partial u}{R\partial x} + \frac{\partial v}{R^2\partial\theta}, \tag{D.5}$$

$$k_{x\theta} = -2\frac{\partial^2 w}{R\partial\theta\,\partial x} - \frac{\partial u}{R^2\partial\theta} + \frac{\partial v}{R\partial x}, \tag{D.6}$$

where w_0 represents the initial radial geometric imperfections of circular cylindrical shells associated with zero initial stress.

Appendix E. Elastic strain energy of circular cylindrical shells made of isotropic and linearly elastic materials

The elastic strain energy U_{shell} (Eq. 3.4) of a circular cylindrical shell made of isotropic and linearly elastic material, under Kirchhoff-Love hypotheses, meaning that stresses in the direction normal to the shell middle surface are negligible and strains vary linearly within the thickness, is given by

$$U_{shell} = \frac{1}{2}\rho_S \int_0^L \int_0^{2\pi} \int_0^h \left(\sigma_x \varepsilon_x + \sigma_\theta \varepsilon_\theta + \tau_{x\theta}\gamma_{x\theta}\right)\left(1 + z/R\right) \mathrm{d}x\, R\, \mathrm{d}\theta\, \mathrm{d}z, \tag{E.1}$$

where σ_x, σ_θ and $\tau_{x\theta}$ represent the Kirchhoff stresses for a homogeneous and isotropic material ($\sigma_r = 0$, case of plane stress) and are given by

$$\sigma_x = \frac{E}{1-\upsilon^2}\left(\varepsilon_x + \upsilon\varepsilon_\theta\right), \quad \sigma_\theta = \frac{E}{1-\upsilon^2}\left(\varepsilon_\theta + \upsilon\varepsilon_x\right), \; \tau_{x\theta} = \frac{E}{2\left(1+\upsilon\right)}\gamma_{x\theta}, \tag{E.2a-c}$$

with E being the Young's modulus and υ the Poisson ratio.

The strains $\varepsilon_x, \varepsilon_\theta$ and $\gamma_{x\theta}$ of an arbitrary point of the shell are the Green's strains represented by

$$\varepsilon_x = \varepsilon_{x,0} + zk_x, \quad \varepsilon_\theta = \varepsilon_{\theta,0} + zk_\theta, \quad \gamma_{x\theta} = \gamma_{x\theta,0} + zk_{x\theta}, \tag{E.3a-c}$$

where z is the distance of the arbitrary point from the middle surface of the shell. Finally, the strains $\varepsilon_{x,0}, \varepsilon_{\theta,0}$ and $\gamma_{x\theta,0}$ are the middle surface strains and k_x, k_θ and $k_{x\theta}$ are the changes in the curvature and torsion of the middle surface as represented in Eq. (D.1-6).

Appendix F. Darcy Friction Factor

Energy losses in circular shells conveying flow are influenced by the flow resistance associated to the type of flow. The Darcy friction factor for a fully developed laminar flow ($\mathrm{Re} < 2300$) in a circular channel can be expressed as follows

$$f = \frac{64}{\mathrm{Re}}, \tag{F.1}$$

where $\mathrm{Re} = \frac{2RU}{\nu}$ represents Reynolds number, U is the mean velocity of the fluid and ν is the kinematic viscosity of the fluid. As shown in Eq. (F.1), in the laminar case the friction factor is independent of the roughness of the circular channel.

However, in case of turbulent flow ($\mathrm{Re} > 3000$), the roughness of the tube surface influences the friction factor. In particular, in case of a smooth pipe with turbulent flow, an approximation formula due to Colebrook and White is

$$\frac{1}{\sqrt{f}} = -2\log\left(\frac{2.51}{\mathrm{Re}\sqrt{f}}\right). \tag{F.2}$$

The relative wall roughness is defined as

$$\varepsilon_{REL} = \frac{\delta}{2R}, \tag{F.3}$$

where δ is the average height of surface roughness of the shell surface. Eq. (F.2) is applicable when $\varepsilon_{REL} < 10^{-6}$ (hydraulic smooth regime). Due to its implicit nature, Eq. (F.2) cannot be solved with respect to *f*. As a consequence, it is necessary to use an interpolation technique or another approximation formula, such as the empirical formula given by Blasius [75]

$$f = \frac{0.3164}{\sqrt[4]{\mathrm{Re}}}. \tag{F.4}$$

Both approximation formulas Eq. (F.2) and Eq. (F.4), with the relative discussion of turbulence, are based on steady mean flow. However, pulsatile flow makes the phenomenon of laminar-turbulence transition much more complex [232]. In this study, the following procedure has been used in order to obtain an approximation of the Darcy friction factor f in case of pulsatile flow. The average velocity $\bar{U}$ calculated via Fourier series of the physiological waveform of velocity during the heart beating period [154] is equal to $\bar{U} = 0.07387\, m/s$. Assuming the blood kinematic viscosity $\nu = 3.6 \cdot 10^{-6}\, m^2/s$, the Reynolds number calculated using $\bar{U}$ and the dimensions of the cylindrical shell under consideration ($R = 0.01575\, m$), is equal to $\mathrm{Re} = 646.36$ (laminar flow regime). Hence, using Eq. (F.1), it is found the Darcy friction factor $f_{avg} = 0.099$.

The maximum flow velocity $U_{\max}$ of the physiological waveform of velocity during the heart beating period [154] is equal to $U_{\max} = 0.61\, m/s$ which corresponds to the Reynold number $\mathrm{Re} = 5337.5$ (turbulent flow regime). Indeed, in the descending aorta, turbulence is generally tolerated during the deceleration of systolic flow [232]. In addition, assuming $\delta = 2.1 \cdot 10^{-9}\, m$ as the average height of surface roughness of Dacron aortic prostheses [233], the condition $\varepsilon_{REL} < 10^{-6}$ is verified. Applying Eq. (F.4), it is found the Darcy friction factor $f_{\max} = 0.037$.

In order to obtain an approximation of the Darcy friction factor in case of the pulsatile physiological blood flow, an average between the two aforementioned values f_{avg} and $f_{\max}$ has been considered obtaining $f = 0.068$.

Appendix G. Axial wave propagation in an elastic shell

The pulsatile flow discussed here is ideal since it is assumed that for a given time instant, the pulsatile pressure and flow velocity are the same for all points of the control volume. In particular, it is assumed that the oscillatory pressure changes occur simultaneously at every point of shell to the effect that the fluid oscillates in bulk. Under this hypothesis, the flow velocity does not depend on the axial coordinate x but it depends only on the time variable t and the radial component of the transportation velocity is neglected. Hence, the wave motion of local movements of the fluid caused by pressure changes in a deformable shell is not taken into account. Since the wave speed (i.e. the speed with which the wave propagates axially down the shell) increases by reducing the elasticity of the shell, this approximation is adequate when the shell presents a low elasticity allowing the wave speed to be much higher than the maximum flow velocity. If the wall thickness is small compared with the shell radius and if the effects of viscosity can be neglected, the wave speed c_0 is given approximately by the so called Moens-Korteweg formula [74, 234]

$$c_0 = \sqrt{\frac{E\,h}{2\,\rho_F\,R}}\,, \tag{G.1}$$

where E is the Young modulus of the shell, h and R are the thickness and the radius of the shell respectively and ρ_F is the constant fluid density.

In first approximation, the woven Dacron graft can be considered transversely isotropic and its stress-strain relation can be modeled with a linear model both in longitudinal and circumferential directions [188] with the following average value for the circumferential Young's Modulus $E_\theta = 12$ MPa. Hence, the wave speed c_0 for the case studied here $(R = 0.01575\ m, \rho_F = 1050\,Kg/m^3\,, h = 0.000361\ m)$ assumes the approximate value of $c_0 = 11.44$ m/s. Since the length of the prosthesis under consideration is $L = 0.126$ m, the time delay Δt due to the wave speed c_0 between outlet ($x = L$) and the inlet ($x = 0$) surfaces can be calculated

$$\Delta t = L / c_0 = 0.011\,\mathrm{s}, \tag{G.2}$$

where it is assumed that all the harmonics of the pulsatile pressure and velocity travel at the same speed and that there are no effects of wave reflection. In the physiological range, the heart beating period T varies between $T_{min} = 0.3$ s (around 200 beats/minute) and $T_{max} = 1.1$ s (around 55 beats/minute), hence the time delay Δt in Eq. (G.2) represents the 1% T_{max} and the 3.7% T_{min}.

Appendix H. Lagrange equations for a non-material volume

Irschik and Holl [183] derived the Lagrange equations for a non-material volume that represents an arbitrarily moving control volume in the terminology of fluid mechanics. The extension of the Lagrange equations to a control volume was obtained by using the method of fictitious particles. Within a continuum mechanics based framework, it is assumed that the instantaneous positions of both, the original particles included in the material volume, and the fictitious particles included in the control volume, are given as functions of their positions in the respective reference configurations, of a set of time-dependent generalized coordinates, and of time. Imagining that the fictitious particles do transport the density of kinetic energy of the original particles, the partial derivatives of the total kinetic energy included in the material volume with respect to generalized coordinates and velocities are related to the respective partial derivatives of the total kinetic energy contained in the control volume. Within this concept, the total kinetic energy T of the original body instantaneously enclosed in the material volume V coincides with the total kinetic energy of the original particles enclosed in the fictitious non-material volume V_w (which instantaneously is coinciding with V):

$$T = \int_{V_w} T^{'} dV_w = \int_{V} T^{'} dV, \tag{H.1}$$

where the variable $T^{'}$ denotes the density of the kinetic energy transported by the fluid and it has the following expression

$$T^{'} = \frac{1}{2} J^{-1} \rho_F \left(\mathbf{v_F} \cdot \mathbf{v_F} \right), \tag{H.2}$$

and J is the Jacobian determinant of the deformation gradient tensor (i.e. $J = 1$ for incompressible fluid).

The version of the Lagrange equations found by Irschik and Holl [183] extended with respect to a non-material volume has the following expression:

$$\frac{\mathrm{d}}{\mathrm{d}t}\left(\frac{\partial T}{\partial \dot{q}_j}\right)-\frac{\partial T}{\partial q_j}+\int_S \frac{\partial T'}{\partial \dot{q}_j}\left(\mathbf{v_F}-\mathbf{v_S}\right)\cdot\mathbf{n}\,\mathrm{d}s-\int_S T'\left(\frac{\partial \mathbf{v_F}}{\partial \dot{q}_j}-\frac{\partial \mathbf{v_S}}{\partial \dot{q}_j}\right)\cdot\mathbf{n}\,\mathrm{d}s+\frac{\partial\left(U_S+V_F\right)}{\partial q_j}=Q_j\,, \tag{H.3}$$

where T denotes the total kinetic energy contained in the control volume (i.e. the structure and the flowing fluid), $\mathbf{v_F}$ and $\mathbf{v_S}$ are the velocity vector of the fluid and of the structure, respectively; Q_j denotes the generalized forces without the terms associated to the potential energy of the fluid V_F and of the structure U_S (both considered in the left side of the equation). The surface integrals are evaluated at the boundary surface S and $\mathbf{n}$ denotes the outer normal unit vector at that surface. The scalar product $\left(\mathbf{v_F}\cdot\mathbf{v_F}\right)$ can be rewritten as

$$\left(\mathbf{v_F}\cdot\mathbf{v_F}\right)=\left(U+\nabla\Phi\right)\cdot\left(U+\nabla\Phi\right)=U^2+2U\frac{\partial\Phi}{\partial x}+\nabla\Phi\cdot\nabla\Phi\,, \tag{H.4}$$

where U is the undisturbed (pulsatile) blood flow velocity, which is time dependent, and Φ is the unsteady perturbation potential (Eq. (3.9)). For low frequency ranges $\left(U>>\nabla\Phi\right)$, the term $\nabla\Phi\cdot\nabla\Phi$ (second-order perturbation term) can be neglected in Eq. (H.4) with respect to the other two terms (zero and first-order perturbation term).

The total kinetic energy T of the system is given by

$$T=T_F+T_S+E_G\,. \tag{H.5}$$

Compared to the classical formulation for a material volume, a correction term containing the flux of kinetic energy appearing to be transported through the surface of the control volume is introduced in the equations of Lagrange written for a non-material volume. For the geometry under consideration, the natural domain of integration due to the shape functions in Eqs. (3.6a-c) is $2L$ in axial direction x. Indeed, since the distance between the periodical supports is L, the shell radial displacement w (Eq. (3.6c)) is assumed to be a periodic function of main period $2L$, and the same is verified for the velocity potential (Eq. (3.9)) and the perturbation pressure (Eq. (3.10)).

The boundary surface S is composed by three terms

$$S = S_{in} + S_{out} + S_{shell} \;, \tag{H.6}$$

where S_{in} and S_{out} represent the inlet ($x = 0$) and outlet ($x = 2L$) surfaces, respectively and S_{shell} is the shell lateral surface. The two integrals in Eq. (H.3) evaluated at the inlet surface S_{in} only have the following expression

$$\int_{S_{in}} \frac{\partial T'}{\partial \dot{q}_j}\left[-U(t) - \left.\frac{\partial \Phi}{\partial x}\right|_{x=0} + \left.\frac{\partial u}{\partial t}\right|_{x=0}\right] dS_{in} - \int_{S_{in}} T'\left[-\frac{\partial}{\partial \dot{q}_j}\left(\left.\frac{\partial \Phi}{\partial x}\right|_{x=0}\right) + \frac{\partial}{\partial \dot{q}_j}\left(\left.\frac{\partial u}{\partial t}\right|_{x=0}\right)\right] \mathrm{d}S_{in} \;, \tag{H.7}$$

where $\dfrac{\partial T'}{\partial \dot{q}_j} = \rho_F\, U \dfrac{\partial}{\partial \dot{q}_j}\left[\dfrac{\partial \Phi}{\partial x}\right]$, u is axial displacement of the shell as expressed in Eq. (3.6a) and $\left.\dfrac{\partial u}{\partial t}\right|_{x=0} = -\mathbf{v_S} \cdot \mathbf{n}$ represents the axial velocity of the shell at the inlet surface; for $x =$ 0, both fluid and shell velocities are discordant with the outer normal unit vector $\mathbf{n}$ of the inlet surface.

In the same way, the two integrals in Eq. (H.3) evaluated at the outlet surface S_{out} only have the following expression

$$\int_{S_{out}} \frac{\partial T'}{\partial \dot{q}_j}\left[U(t) + \left.\frac{\partial \Phi}{\partial x}\right|_{x=2L} - \left.\frac{\partial u}{\partial t}\right|_{x=2L}\right] dS_{out} - \int_{S_{out}} T'\left[\frac{\partial}{\partial \dot{q}_j}\left(\left.\frac{\partial \Phi}{\partial x}\right|_{x=2L}\right) - \frac{\partial}{\partial \dot{q}_j}\left(\left.\frac{\partial u}{\partial t}\right|_{x=2L}\right)\right] \mathrm{d}S_{out} \,. \tag{H.8}$$

In this case, for $x = 2L$, both fluid and shell velocities are concordant with the outer normal unit vector $\mathbf{n}$ of the outlet surface. Indeed, since the axial displacement u is symmetrical at the periodic supports, it is verified that $\left.\dfrac{\partial u}{\partial t}\right|_{x=0} = \left.\dfrac{\partial u}{\partial t}\right|_{x=2L}$. Finally, the two integrals in Eq. (H.3) evaluated at the shell surface S_{shell} only have the following expression

$$\int_{S_{shell}} \frac{\partial T^{'}}{\partial \dot{q}_j}\left[\left.\frac{\partial \Phi}{\partial r}\right|_{r=R} - \frac{\partial w}{\partial t}\right] dS_{shell} - \int_{S_{shell}} T^{'}\left[\frac{\partial}{\partial \dot{q}_j}\left(\left.\frac{\partial \Phi}{\partial r}\right|_{r=R}\right) - \frac{\partial}{\partial \dot{q}_j}\left(\frac{\partial w}{\partial t}\right)\right] \mathrm{d}S_{shell}\ . \qquad \text{(H.9)}$$

By substituting Eq. (3.8) into Eq. (H.9) and developing mathematical calculations, Eq. (H.9) may be rewritten as follows

$$\rho_F U^2 \int_{S_{shell}} \frac{\partial}{\partial \dot{q}_j}\left[\left.\frac{\partial \Phi}{\partial x}\right|_{r=R}\right] \frac{\partial w}{\partial x}\, \mathrm{d}S_{shell}. \qquad \text{(H.10)}$$

By substituting Eq. (H.7), Eq. (H.8) and Eq. (H.10) into Eq. (H.3), it can be observed that the contributions at the inlet and outlet surfaces cancel each other since the system conditions at the entry and exit surfaces are the same expect for a discordant sign due to the scalar product with the outer normal at the respective boundary surface. Finally, because of the anti-symmetry of the shell deflection w at the periodic supports, Eq. (H.10) becomes

$$\rho_F U^2 \int_0^{2\pi}\int_0^{L} \frac{\partial}{\partial \dot{q}_j}\left[\left.\frac{\partial \Phi}{\partial x}\right|_{r=R}\right] \frac{\partial w}{\partial x}\ r\, \mathrm{d}\theta\, \mathrm{d}x - \rho_F U^2 \int_0^{2\pi}\int_L^{2L} \frac{\partial}{\partial \dot{q}_j}\left[\left.\frac{\partial \Phi}{\partial x}\right|_{r=R}\right] \frac{\partial w}{\partial x}\, r\, \mathrm{d}\theta\, \mathrm{d}x\,, \qquad \text{(H.11)}$$

where the two terms cancel each other. Hence, the Lagrange equations of motion for the shell coupled to flowing fluid, knowing that $\partial T_S / \partial q_j = \partial T_F / \partial q_j = 0$, are

$$\frac{d}{dt}\left[\frac{\partial\left(T_S + T_F + E_G\right)}{\partial \dot{q}_j}\right] - \frac{\partial E_G}{\partial q_j} + \frac{\partial\left(U_S + V_F\right)}{\partial q_j} = Q_j, \quad j = 1 \ldots N_T. \qquad \text{(H.12)}$$

Appendix I. Conservation of mass in a deformable control volume

The flow velocity vector $\mathbf{v_F}$ is expressed by Eq. (4.8). Considering a portion of the compliant vessel conveying pulsatile flow as a control volume, because of the wave propagation phenomenon within vessel, the net inflow of mass through the boundaries of the control volume is different from zero at any given time. Hence, in order to satisfy mass conservation, the time rate of change of mass must be equal to the net inflow of mass through the boundaries of the vessel. Therefore,

$$\frac{\partial}{\partial t}\int_0^L \rho_F\, \pi \left(R+w\right)^2 \mathrm{d}\,x = -\rho_F\, \pi\, U(x,t)\left(R+w\right)^2\Big|_{x=0}^{x=L}. \tag{I.1}$$

holds true [235]. In equation (I.1) only axisymmetric w is considered since asymmetric w gives no volume and no area changes at the entrance and exit surfaces. Applying the boundary condition Eq. (4.1b), the right-hand side of Eq. (I.1) becomes

$$-\rho_F\, \pi\, U(x,t)\left(R+w\right)^2\Big|_{x=0}^{x=L} = -\rho_F\, \pi\, R^2\left(U(L,t)-U(0,t)\right). \tag{I.2}$$

Writing

$$\frac{\partial}{\partial t}\left(R+w\right)^2 = \frac{\partial}{\partial t}\left(R^2+2Rw+w^2\right) = 2\dot{w}\left(R+w\right), \tag{I.3}$$

Eq. (I.1) can be rewritten as follows,

$$\frac{\partial U}{\partial x} = -\frac{2\dot{w}}{R^2}(R+w). \tag{I.4}$$

The inhomogeneous equation of mass conservation in case of incompressible flow, considering the effect of a mass source term m, is given by

$$\rho_F\, \nabla\cdot\mathbf{v_F} = m, \tag{I.5}$$

where the source m consists of mass of the incompressible fluid density ρ_F of volume fraction $\chi = \chi(x,t)$ injected at a rate of

$$m = \rho_F \frac{\partial \chi}{\partial t}. \tag{I.6}$$

Under the hypothesis of constant length L (i.e. $u\big|_{x=0} << L$ and $u\big|_{x=L} << L$), substituting Eq. (4.8) into Eq. (I.5), it is found that

$$\frac{\partial U}{\partial x} + \nabla^2 \Phi = -\frac{\partial}{\partial t}\left(\frac{\pi\left(R+w\right)^2 L - \pi R^2 L}{\pi R^2 L}\right), \tag{I.7}$$

where the right-hand side of the equation represents the variation of the control volume related to the accumulation ($\partial U/\partial x < 0$) or the subtraction ($\partial U/\partial x > 0$) of the mass of the fluid caused by the wave propagation phenomenon. With a sequence of calculations, it is found

$$-\frac{\partial}{\partial t}\left(\frac{\pi\left(R+w\right)^2 L - \pi R^2 L}{\pi R^2 L}\right) = -\frac{\partial}{\partial t}\left(\frac{w^2 + 2Rw}{R^2}\right) = -\frac{2\dot{w}}{R^2}\left(w+R\right). \tag{I.8}$$

Substituting Eq. (I.4) and Eq. (I.8) into Eq. (I.7), we obtain the Laplace equation

$$\nabla^2 \Phi = 0. \tag{I.9}$$

The appearance of travelling pressure waves is interesting both in the mathematical formulation and in the numerical modelling. From a mathematical viewpoint, even if the flow is governed by an elliptic equation (Laplace equation), the general behaviour of the fluid-structure interaction system is in many ways similar to that of a hyperbolic problem (wave equation). Indeed, as demonstrated here, an additional complexity comes from the correct representation of the accumulation/subtraction of mass in the deformable control volume in order to properly describe the traveling wave phenomenon.

Appendix J. Expression of the modified gyroscopic energy $\bar{E}_G$

The modified gyroscopic energy $\bar{E}_G$ calculated not only on the shell wall, Eq.(4.18c), but also on the inlet and outlet surfaces, can be written in the following vectorial notation:

$$\bar{E}_G = E_{G\,shell} + E_{G\,In\&Out} = \frac{1}{2}\tilde{\mathbf{q}}^{\mathbf{T}}\,\mathbf{G}\;\dot{\tilde{\mathbf{q}}} + \frac{1}{2}\tilde{\mathbf{q}}^{\mathbf{T}}\,\mathbf{G}_{In\&Out}\;\dot{\tilde{\mathbf{q}}}, \tag{J.1}$$

where the vector $\tilde{\mathbf{q}} = \{\tilde{\mathbf{q}}_{ASYM}, \tilde{\mathbf{q}}_{AXISYM}\} = \{w_{1,2},..,w_{m,2},..,w_{M,2},w_{1,0},..,w_{l,0},..,w_{\bar{M},0}\}$ represents the generalized asymmetric $\tilde{\mathbf{q}}_{ASYM}$ and axisymmetric $\tilde{\mathbf{q}}_{AXISYM}$ coordinates of the radial displacement w only. For simplicity, here only the first harmonic is considered in the pulsatile component of the flow velocity ($a_{1v} = U_P$ and $b_{1v} = 0$ in Eq. (4.12a)). The matrix $\mathbf{G}$ is not a gyroscopic matrix but it can be expressed in the following form

$$\mathbf{G} = \bar{U}\cdot\mathbf{G}_{\mathbf{GYRO}} + U_P\cos(\Omega t)\cdot(\mathbf{G_1}+\mathbf{G_2}) + U_P\cos\left(\frac{L\Omega}{c_0} - \Omega t\right)\cdot(\mathbf{G_3}+\mathbf{G_4}), \tag{J.2}$$

where $\mathbf{G}_{\mathbf{GYRO}}$ is the gyroscopic matrix associated to the pulsatile mean flow velocity $\bar{U}$ in the following antisymmetric form with zeros on the diagonal,

$$\mathbf{G}_{\mathbf{GYRO}} = \begin{bmatrix} 0 & & \mathbf{B} \\ & \ddots & \\ \mathbf{-B^T} & & 0 \end{bmatrix}, \tag{J.3}$$

where $\mathbf{B}$ is a triangular submatrix. This matrix corresponds exactly to the gyroscopic matrix associated to the gyroscopic energy E_G in the case of shells conveying steady flow [4]. However, in the case of shells conveying pulsatile flow, the presence of travelling waves inside the shell due to pulse wave propagation, causes the appearance of the four matrices, $\mathbf{G_1}, \mathbf{G_2}, \mathbf{G_3}$ and $\mathbf{G_4}$, associated with the pulsatile component U_P of the velocity.

In particular, matrices $\mathbf{G_1}$ and $\mathbf{G_3}$ are block diagonal matrices. $\mathbf{G_1}$ can be expressed in the following form:

$$\mathbf{G_1} = \begin{bmatrix} \mathbf{F} & \mathbf{0} \\ \mathbf{0} & \mathbf{H} \end{bmatrix}. \tag{J.4}$$

The submatrix $\mathbf{F}$ has the following form:

$$\mathbf{F} = \begin{bmatrix} 0 & -\frac{1}{2}\eta_{1,2} & -\frac{1}{j}\eta_{1,j} & -\frac{1}{M}\eta_{1,M} \\ \eta_{1,2} & 0 & -\frac{i}{j}\eta_{i,j} & -\frac{i}{M}\eta_{i,M} \\ \eta_{1,j} & \eta_{i,j} & 0 & -\frac{M-1}{M}\eta_{(M-1),M} \\ \eta_{1,M} & \eta_{i,M} & \eta_{(M-1),M} & 0 \end{bmatrix}, \tag{J.5}$$

where the subscripts i and j represent the number of longitudinal half-waves in the i-th generalized coordinate of the vector $\dot{\tilde{\mathbf{q}}}_{ASYM}$ and of the j-th generalized coordinate of the vector $\tilde{\mathbf{q}}_{ASYM}$, respectively. The submatrix $\mathbf{H}$ can be expressed as follows:

$$\mathbf{H} = \begin{bmatrix} 0 & -\frac{1}{2}\bar{\eta}_{1,2} & -\frac{1}{j}\bar{\eta}_{1,j} & -\frac{1}{\bar{M}}\bar{\eta}_{1,\bar{M}} \\ \bar{\eta}_{1,2} & 0 & -\frac{i}{j}\bar{\eta}_{i,j} & -\frac{i}{\bar{M}}\bar{\eta}_{1,\bar{M}} \\ \bar{\eta}_{1,j} & \bar{\eta}_{i,j} & 0 & -\frac{\bar{M}-1}{\bar{M}}\bar{\eta}_{(\bar{M}-1),\bar{M}} \\ \bar{\eta}_{1,\bar{M}} & \bar{\eta}_{i,\bar{M}} & \bar{\eta}_{(\bar{M}-1),\bar{M}} & 0 \end{bmatrix}, \tag{J.6}$$

where the subscripts i and j represent the number of longitudinal half-waves of the i-th generalized coordinate of the vector $\dot{\tilde{\mathbf{q}}}_{AXISYM}$ and of the j-th generalized coordinate of the vector $\tilde{\mathbf{q}}_{AXISYM}$, respectively. Matrix $\mathbf{G_3}$ has the same structure as matrix $\mathbf{G_1}$. In particular, $\mathbf{G_3}$ is given by

$$\mathbf{G_3} = \begin{bmatrix} \hat{\mathbf{F}} & \mathbf{0} \\ \mathbf{0} & \hat{\mathbf{H}} \end{bmatrix}. \tag{J.7}$$

The submatrix $\hat{\mathbf{F}}$ has the following form:

$$\hat{\mathbf{F}} = \begin{bmatrix} 0 & -\frac{1}{2}\hat{\eta}_{1,2} & -\frac{1}{j}\hat{\eta}_{1,j} & -\frac{1}{M}\hat{\eta}_{1,M} \\ \hat{\eta}_{1,2} & 0 & -\frac{i}{j}\hat{\eta}_{i,j} & -\frac{i}{M}\hat{\eta}_{i,M} \\ \hat{\eta}_{1,j} & \hat{\eta}_{i,j} & 0 & -\frac{M-1}{M}\hat{\eta}_{(M-1),M} \\ \hat{\eta}_{1,M} & \hat{\eta}_{i,M} & \hat{\eta}_{(M-1),M} & 0 \end{bmatrix}. \tag{J.8}$$

Moreover, the following relation among the coefficients holds true:

$$\hat{\eta}_{i,j} = \begin{cases} \eta_{i,j} & if \ \ (i+j) = odd, \\ -\eta_{i,j} & if \ (i+j) = even. \end{cases} \tag{J.9}$$

Submatrix $\hat{\mathbf{H}}$ can be expressed as follows:

$$\hat{\mathbf{H}} = \begin{bmatrix} 0 & -\frac{1}{2}\hat{\bar{\eta}}_{1,2} & -\frac{1}{j}\hat{\bar{\eta}}_{1,j} & -\frac{1}{\bar{M}}\hat{\bar{\eta}}_{1,\bar{M}} \\ \hat{\bar{\eta}}_{1,2} & 0 & -\frac{i}{j}\hat{\bar{\eta}}_{i,j} & -\frac{i}{\bar{M}}\hat{\bar{\eta}}_{1,\bar{M}} \\ \hat{\bar{\eta}}_{1,j} & \hat{\bar{\eta}}_{i,j} & 0 & -\frac{\bar{M}-1}{\bar{M}}\hat{\bar{\eta}}_{(\bar{M}-1),\bar{M}} \\ \hat{\bar{\eta}}_{1,\bar{M}} & \hat{\bar{\eta}}_{i,\bar{M}} & \hat{\bar{\eta}}_{(\bar{M}-1),\bar{M}} & 0 \end{bmatrix}, \tag{J.10}$$

and the following relation among the coefficients holds true

$$\hat{\bar{\eta}}_{i,j} = \begin{cases} \bar{\eta}_{i,j} & if \ \ (i+j) = odd, \\ -\bar{\eta}_{i,j} & if \ (i+j) = even. \end{cases} \tag{J.11}$$

Matrices $\mathbf{G_2}$ and $\mathbf{G_4}$ in Eq. (J.2) are also block diagonal matrices. $\mathbf{G_2}$ can be expressed as follows:

$$\mathbf{G_2} = \begin{bmatrix} \mathbf{N} & \mathbf{0} \\ \mathbf{0} & \mathbf{P} \end{bmatrix}. \tag{J.12}$$

Submatrix $\mathbf{N}$ has the following form:

$$\mathbf{N}=\begin{bmatrix} \gamma_{1,1} & \frac{1}{2}\widehat{\eta}_{1,2} & \frac{1}{j}\widehat{\eta}_{1,j} & \frac{1}{M}\widehat{\eta}_{1,M} \\ \widehat{\eta}_{1,2} & \gamma_{2,2} & \frac{i}{j}\widehat{\eta}_{i,j} & \frac{i}{M}\widehat{\eta}_{i,M} \\ \widehat{\eta}_{1,j} & \widehat{\eta}_{i,j} & \gamma_{j,j} & \frac{M-1}{M}\widehat{\eta}_{(M-1),M} \\ \widehat{\eta}_{1,M} & \widehat{\eta}_{i,M} & \widehat{\eta}_{(M-1),M} & \gamma_{M,M} \end{bmatrix}, \tag{J.13}$$

and submatrix $\mathbf{P}$ can be expressed as follows:

$$\mathbf{P}=\begin{bmatrix} \breve{\gamma}_{1,1} & \frac{1}{2}\breve{\eta}_{1,2} & \frac{1}{j}\breve{\eta}_{1,j} & \frac{1}{\bar{M}}\breve{\eta}_{1,\bar{M}} \\ \breve{\eta}_{1,2} & \breve{\gamma}_{2,2} & \frac{i}{j}\breve{\eta}_{i,j} & \frac{i}{\bar{M}}\breve{\eta}_{1,\bar{M}} \\ \breve{\eta}_{1,j} & \breve{\eta}_{i,j} & \breve{\gamma}_{j,j} & \frac{\bar{M}-1}{\bar{M}}\breve{\eta}_{(\bar{M}-1),\bar{M}} \\ \breve{\eta}_{1,\bar{M}} & \breve{\eta}_{i,\bar{M}} & \breve{\eta}_{(\bar{M}-1),\bar{M}} & \breve{\gamma}_{\bar{M},\bar{M}} \end{bmatrix}. \tag{J.14}$$

The coefficients of matrices $\mathbf{G_4}$ and matrix $\mathbf{G_2}$ display the same relationship between as that observed for matrices $\mathbf{G_3}$ and $\mathbf{G_1}$. The matrix $\mathbf{G}_{In\&Out}$, associated to the gyroscopic energy due to the inlet and outlet surfaces $E_{G\,In\&Out}$ in Eq . (J.1) is a symmetric matrix and it can be written as follows:

$$\mathbf{G}_{In\&Out}=U_P\,\mathbf{R}\left(\cos(\Omega t)-\cos(\Omega(t-2L/c_0))\right), \tag{J.15}$$

where $\mathbf{R}$ is a block diagonal matrix that can be written as,

$$\mathbf{R}=\begin{bmatrix} \mathbf{S} & \mathbf{0} \\ \mathbf{0} & \mathbf{T} \end{bmatrix}, \tag{J.16}$$

where $\mathbf{S}$ and $\mathbf{T}$ are symmetric submatrices that couple the asymmetric and the axisymmetric modes, respectively. As shown in Eq. (4.23), in the Lagrange equations of motion the terms associated to the modified gyroscopic energy $\bar{E}_G$ are given by $\frac{d}{dt}\left[\frac{\partial \bar{E}_G}{\partial \dot{q}_j}\right]-\frac{\partial \bar{E}_G}{\partial q_j}$. Assuming

$$\frac{\partial}{\partial \dot{q}_j}\dot{\mathbf{q}} = \begin{pmatrix} 0 \\ \vdots \\ 1 \\ \vdots \\ 0 \end{pmatrix} = \mathbf{J}, \tag{J.17}$$

where $\mathbf{J}$ is the unit vector that has only the j–th unit term different from zero, it is possible to write

$$\frac{d}{dt}\left[\frac{\partial \bar{E}_G}{\partial \dot{q}_j}\right] = \frac{d}{dt}\left[\frac{1}{2}\tilde{\mathbf{q}}^{\mathbf{T}}\,\mathbf{G}\;\;\mathbf{J} + \frac{1}{2}\tilde{\mathbf{q}}^{\mathbf{T}}\,\mathbf{G}_{In\&Out}\;\mathbf{J}\right] = \frac{1}{2}\left(\dot{\tilde{\mathbf{q}}}^{\mathbf{T}}\,\mathbf{G}\;\;\mathbf{J} + \tilde{\mathbf{q}}^{\mathbf{T}}\,\dot{\mathbf{G}}\;\;\mathbf{J} + \dot{\tilde{\mathbf{q}}}^{\mathbf{T}}\,\mathbf{G}_{In\&Out}\;\mathbf{J} + \tilde{\mathbf{q}}^{\mathbf{T}}\,\dot{\mathbf{G}}_{In\&Out}\;\mathbf{J}\right), \tag{J.18}$$

where

$$\dot{\mathbf{G}} = -\,\Omega\,U_P \sin\left(\Omega t\right)\cdot\left(\mathbf{G_1}+\mathbf{G_2}\right) + U_P \sin\left(\frac{L\Omega}{c_0} - \Omega t\right)\cdot\left(\mathbf{G_3}+\mathbf{G_4}\right), \tag{J.19a}$$

$$\dot{\mathbf{G}}_{In\&Out} = U_P\;\Omega\,\mathbf{R}\left(-\sin(\Omega t) + \sin(\Omega(t - 2L/c_0))\right). \tag{J.19b}$$

Similarly, the following expression is obtained

$$-\frac{\partial \bar{E}_G}{\partial q_j} = -\frac{1}{2}\left(\mathbf{J}^{\mathbf{T}}\,\mathbf{G}\;\;\dot{\tilde{\mathbf{q}}} + \mathbf{J}^{\mathbf{T}}\,\mathbf{G}_{In\&Out}\;\dot{\tilde{\mathbf{q}}}\right) = -\frac{1}{2}\left(\;\dot{\tilde{\mathbf{q}}}^{\mathbf{T}}\mathbf{G}^{\mathbf{T}}\mathbf{J} + \dot{\tilde{\mathbf{q}}}^{\mathbf{T}}\mathbf{G}^{\mathbf{T}}_{In\&Out}\;\mathbf{J}\;\right). \tag{J.20}$$

Hence, the terms of the Lagrange equations of motion associated to the modified gyroscopic energy $\bar{E}_G$ can be rewritten as follows:

$$\frac{d}{dt}\left[\frac{\partial \bar{E}_G}{\partial \dot{q}_j}\right] - \frac{\partial \bar{E}_G}{\partial q_j} = \frac{1}{2}\left(\dot{\tilde{\mathbf{q}}}^{\mathbf{T}}\left(\mathbf{G}-\mathbf{G}^{\mathbf{T}}\right)\mathbf{J} + \tilde{\mathbf{q}}^{\mathbf{T}}\,\dot{\mathbf{G}}\;\;\mathbf{J} + \dot{\tilde{\mathbf{q}}}^{\mathbf{T}}\left(\mathbf{G}_{In\&Out} - \mathbf{G}^{\mathbf{T}}_{In\&Out}\right)\mathbf{J} + \tilde{\mathbf{q}}^{\mathbf{T}}\,\dot{\mathbf{G}}_{In\&Out}\;\mathbf{J}\right), \tag{J.21}$$

where both matrices $\frac{1}{2}\left(\mathbf{G}-\mathbf{G}^{\mathbf{T}}\right)$ and $\frac{1}{2}\left(\mathbf{G}_{In\&Out} - \mathbf{G}^{\mathbf{T}}_{In\&Out}\right)$ are clearly antisymmetric (gyroscopic). Consequently, there is no dissipation in the system due to the fluid model. Moreover, since both matrices $\mathbf{G}_{In\&Out}$ and $\mathbf{G}$ are time-dependent, substituting Eq. (J.19a) and Eq. (J.19b) in Eq. (J.21), new time dependent (variable positive/ negative) stiffness terms will appear in the Lagrange equation of motion because of the wave propagation phenomenon. In particular, the contribution of the symmetric matrix

$\mathbf{G}_{In\&Out}$ in the Lagrange equations of motion, associated with the asymmetric modes $\tilde{\mathbf{q}}_{ASYM}$, is a stiffness term (proportional to the displacement generalized coordinates) that couples the equations. Consequently, the same coupling in the stiffness due to $\mathbf{G}_{In\&Out}$ (Eq. (J.15)) is verified for the equations of motion associated with the axisymmetric modes $\tilde{\mathbf{q}}_{AXISYM}$. The effect of the matrix $\mathbf{G}$ into the equations of motion of the generalized coordinates $\tilde{\mathbf{q}}_{ASYM}$ can be summed up as follows:

(i) in the equation of the generalized coordinate q_j, the damping terms due to $\dot{q}_i$ (with $i \neq j$) have the same coefficients with opposite sign as the corresponding damping terms due to $\dot{q}_j$ in the equation of the generalized coordinate q_i , giving a pure gyroscopic effect;

(ii) in the equation of the generalized coordinate q_j, stiffness terms appear due to q_i (with $i \neq j$) with coefficients that respect the relations shown for matrices $\mathbf{F}$ and $\mathbf{N}$, with respect to the corresponding stiffness terms due to q_j in the equation of the generalized coordinate q_i .

(iii) in the equation of the generalized coordinate q_j , there are stiffness terms associated to q_j.

Same three contributions of the matrix $\mathbf{G}$ are found into the equations of motion of the generalized coordinates $\tilde{\mathbf{q}}_{AXISYM}$, where in the second point instead of submatrices $\mathbf{F}$ and $\mathbf{N}$ we refer to $\mathbf{H}$ and $\mathbf{P}$.

Appendix K. Displacement dependent pressure load for finite deflection of thick circular cylindrical shells

The expression of the displacement dependent pressure load for circular cylindrical shells is given by [236]

$$
\begin{aligned}
W = \int_0^L \int_0^{2\pi} p \Bigg\{ & w\left[\left(1+\frac{\partial u}{\partial x}\right)\left(1+\frac{\partial v}{R\partial\theta}+\frac{w}{R}\right)-\frac{\partial v}{\partial x}\frac{\partial u}{R\partial\theta}\right]+u\left[-\left(1+\frac{\partial v}{R\partial\theta}+\frac{w}{R}\right)\frac{\partial w}{\partial x}-\frac{\partial v}{\partial x}\left(-\frac{\partial w}{R\partial\theta}+\frac{v}{R}\right)\right] \\
& +v\left[\left(1+\frac{\partial u}{\partial x}\right)\left(-\frac{\partial w}{R\partial\theta}+\frac{v}{R}\right)+\frac{\partial w}{\partial x}\frac{\partial u}{R\partial\theta}\right]\Bigg\} \mathrm{d}x\, R\,\mathrm{d}\theta,
\end{aligned}
\tag{K.1}
$$

where the higher-order terms are significant, compared to the linear term *pw,* in case of large deformations. However, for thin shells, their influence is smaller since the amplitude of the deformation *w/R* is smaller for the same order of normalized displacement *w/h*. Fig. 4.20 shows the comparison between the radial deformation of the shell under the static pressure load $\bar{p}_m$ evaluated by the exact displacement dependent Eq. (K1) and by the approximated displacement independent pressure $\bar{p}_m$. The curves are perfectly overlapped showing that the nonlinear terms of Eq. (K.1) are negligible for the case investigated here. However, the exact formulation of the virtual work done by the displacement dependent pressure must be used for large deformations. This formulation is of particular interest for soft biological tissue which can be described with different types of hyperelastic constitutive relationships and usually present large strains and deformations [237].

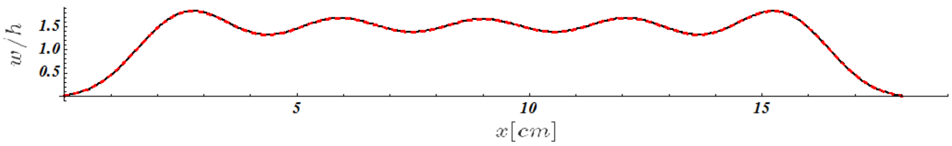

Fig. 4.20. Longitudinal section. Normalized amplitude with respect to shell thickness h; load by pressure $\overline{p}_m$ evaluated by the exact displacement dependent Eq. (K.1) (red dashed line), load by displacement independent pressure $\overline{p}_m$ (black line); $\zeta = 0.1$.

Bibliography

[1] E. Tubaldi, M. Amabili, F. Alijani, Nonlinear vibrations of plates in axial pulsating flow, Journal of Fluids and Structures, 56 (2015) 33-55.

[2] E. Tubaldi, M. Amabili, M.P. Païdoussis, Fluid–structure interaction for nonlinear response of shells conveying pulsatile flow, Journal of Sound and Vibration, 371 (2016) 252-276.

[3] E. Tubaldi, M. Amabili, M.P. Païdoussis, Nonlinear dynamics of shells conveying pulsatile flow with pulse-wave propagation. Theory and numerical results for a single harmonic pulsation, Journal of Sound and Vibration, 369 (2017) 217-245.

[4] M. Amabili, Nonlinear Vibrations and Stability of Shells and Plates, Cambridge University Press Cambridge, 2008.

[5] M.P. Païdoussis, Fluid-Structure Interactions: Slender Structures and Axial Flow. Volume 2, Academic Press, 2003.

[6] M. Amabili, M.P. Païdoussis, Review of studies on geometrically nonlinear vibrations and dynamics of circular cylindrical shells and panels, with and without fluid-structure interaction, Applied Mechanics Reviews, 56 (2003) 349-356.

[7] F. Alijani, M. Amabili, Non-linear vibrations of shells: A literature review from 2003 to 2013, International Journal of Non-Linear Mechanics, 58 (2014) 233-257.

[8] H. Lamb, On the vibrations of an elastic plate in contact with water, Proceedings of the Royal Society of London. Series A, 98 (1920) 205-216.

[9] M. Kwak, K. Kim, Axisymmetric vibration of circular plates in contact with fluid, Journal of Sound and Vibration, 146 (1991) 381-389.

[10] M.K. Kwak, Hydroelastic vibration of rectangular plates, Journal of Applied Mechanics, Transactions ASME, 63 (1996) 110-115.

[11] Y. Fu, W.G. Price, Interactions between a partially or totally immersed vibrating cantilever plate and the surrounding fluid, Journal of Sound and Vibration, 118 (1987) 495-513.

[12] M. Amabili, M.K. Kwak, Free vibrations of circular plates coupled with liquids: Revising the lamb problem, Journal of Fluids and Structures, 10 (1996) 743-761.

[13] M. Chiba, Nonlinear hydroelastic vibration of a cylindrical tank with an elastic bottom, containing liquid. Part I: Experiment, Journal of Fluids and Structures, 6 (1992) 181-206.

[14] C. Guo, M. Païdoussis, Stability of rectangular plates with free side-edges in two-dimensional inviscid channel flow, Journal of Applied Mechanics, 67 (2000) 171-176.
[15] Y. Kerboua, A.A. Lakis, M. Thomas, L. Marcouiller, Vibration analysis of rectangular plates coupled with fluid, Applied Mathematical Modelling, 32 (2008) 2570-2586.
[16] E. Dowell, C. Ventres, Flutter of low aspect ratio plates, AIAA Journal, 8 (1970) 1162-1164.
[17] E. Dowell, Flutter of multibay panels at high supersonic speeds, AIAA Journal, 2 (1964) 1805-1814.
[18] E.H. Dowell, Aeroelasticity of plates and shells, Springer, 1974.
[19] E.H. Dowell, Nonlinear oscillations of a fluttering plate, AIAA Journal, 4 (1966) 1267-1275.
[20] E.H. Dowell, Nonlinear oscillations of a fluttering plate. II, AIAA Journal, 5 (1967) 1856-1862.
[21] C. Ellen, The non-linear stability of panels in incompressible flow, Journal of Sound and Vibration, 54 (1977) 117-121.
[22] A.D. Lucey, G.J. Cafolla, P.W. Carpenter, M. Yang, The nonlinear hydroelastic behaviour of flexible walls, Journal of Fluids and Structures, 11 (1997) 717-744.
[23] M.P. Païdoussis, J.P. Denise, Flutter of thin cylindrical shells conveying fluid, Journal of Sound and Vibration, 20 (1972) 9-26.
[24] D. Weaver, T. Unny, On the dynamic stability of fluid-conveying pipes, Journal of Applied Mechanics, 40 (1973) 48-52.
[25] M.P. Païdoussis, S.P. Chan, A.K. Misra, Dynamics and stability of coaxial cylindrical shells containing flowing fluid, Journal of Sound and Vibration, 97 (1984) 201-235.
[26] M.P. Païdoussis, A.K. Misra, S.P. Chan, Dynamics and stability of coaxial cylindrical shells conveying viscous fluid, Journal of Applied Mechanics, Transactions ASME, 52 (1985) 389-396.
[27] S.S. Chen, Flow-induced vibration of circular cylindrical structures, 1985.
[28] Y. Matsuzaki, Y.C. Fung, Unsteady fluid dynamic forces on a simply-supported circular cylinder of finite length conveying a flow, with applications to stability analysis, Journal of Sound and Vibration, 54 (1977) 317-330.
[29] A. Lakis, P. Van Dyke, H. Ouriche, Dynamic analysis of anisotropic fluid-filled conical shells, Journal of Fluids and Structures, 6 (1992) 135-162.
[30] A. Selmane, A.A. Lakis, Vibration analysis of anisotropic open cylindrical shells subjected to a flowing fluid, Journal of Fluids and Structures, 11 (1997) 111-134.

[31] Y.L. Zhang, D.G. Gorman, J.M. Reese, Vibration of prestressed thin cylindrical shells conveying fluid, Thin-Walled Structures, 41 (2003) 1103-1127.
[32] P.S. Koval'chuk, Nonlinear vibrations of a cylindrical shell containing a flowing fluid, International Applied Mechanics, 41 (2005) 405-412.
[33] K.N. Karagiozis, M.P. Païdoussis, A.K. Misra, E. Grinevich, An experimental study of the nonlinear dynamics of cylindrical shells with clamped ends subjected to axial flow, Journal of Fluids and Structures, 20 (2005) 801-816.
[34] K.N. Karagiozis, M.P. Païdoussis, A.K. Misra, E. Grinevich, Addendum to "An experimental study of the nonlinear dynamics of cylindrical shells with clamped ends subjected to axial flow", Journal of Fluids and Structures, 22 (2006) 595-596.
[35] K.N. Karagiozis, M.P. Païdoussis, A.K. Misra, Transmural pressure effects on the stability of clamped cylindrical shells subjected to internal fluid flow: Theory and experiments, International Journal of Non-Linear Mechanics, 42 (2007) 13-23.
[36] K.N. Karagiozis, M.P. Païdoussis, M. Amabili, A.K. Misra, Nonlinear stability of cylindrical shells subjected to axial flow: Theory and experiments, Journal of Sound and Vibration, 309 (2008) 637-676.
[37] M. Amabili, K. Karagiozis, M.P. Païdoussis, Effect of geometric imperfections on non-linear stability of circular cylindrical shells conveying fluid, International Journal of Non-Linear Mechanics, 44 (2009) 276-289.
[38] Z. del Prado, P.B. Gonçalves, M.P. Païdoussis, Nonlinear vibrations and imperfection sensitivity of a cylindrical shell containing axial fluid flow, Journal of Sound and Vibration, 327 (2009) 211-230.
[39] S. Uchida, The pulsating viscous flow superposed on the steady laminar motion of incompressible fluid in a circular pipe, Journal of Applied Mathematics and Physics (ZAMP), 7 (1956) 403-422.
[40] J. Gerrard, M. Hughes, The flow due to an oscillating piston in a cylindrical tube: a comparison between experiment and a simple entrance flow theory, Journal of Fluid Mechanics, 50 (1971) 97-106.
[41] M. Hino, M. Sauramoto, S. Takasu, Experiments on transition to turbulence in an oscillatory pipe flow, Journal of Fluid Mechanics, 75 (1976).
[42] T. Muto, K. Nakane, Unsteady flow in circular tube/Velocity distribution of pulsating flow, JSME International Journal Series B, 23 (1980) 1990-1996.
[43] L. Shemer, I. Wygnanski, E. Kit, Pulsating flow in a pipe, Journal of Fluid Mechanics, 153 (1985) 313-337.
[44] S. Chen, Dynamic stability of tube conveying fluid, Journal of Engineering Mechanics, (1971).

[45] M.P. Païdoussis, N.T. Issid, Dynamic stability of pipes conveying fluid, Journal of Sound and Vibration, 33 (1974) 267-294.
[46] J.H. Ginsberg, The dynamic stability of a pipe conveying a pulsatile flow, International Journal of Engineering Science, 11 (1973) 1013-1024.
[47] M. Païdoussis, Stability of flexible slender cylinders in pulsatile axial flow, Journal of Sound and Vibration, 42 (1975) 1-11.
[48] M. Bohn, G. Herrmann, The dynamic behavior of articulated pipes conveying fluid with periodic flow rate, Journal of Applied Mechanics, 41 (1974) 55-62.
[49] S. Ariaratnam, N.S. Namachchivaya, Dynamic stability of pipes conveying pulsating fluid, Journal of Sound and Vibration, 107 (1986) 215-230.
[50] U. Lee, C. Pak, S. Hong, The dynamics of a piping system with internal unsteady flow, Journal of Sound and Vibration, 180 (1995) 297-311.
[51] D. Gorman, J. Reese, Y. Zhang, Vibration of a flexible pipe conveying viscous pulsating fluid flow, Journal of Sound and Vibration, 230 (2000) 379-392.
[52] L.D. Landau, E.M. Lifshits, Fluid Mechanics: Transl. from the Russian by JB Sykes and WH Reid, Addison-Wesley, 1959.
[53] C. Fan, B.T. Chao, Unsteady, laminar, incompressible flow through rectangular ducts, Journal of Applied Mathematics and Physics (ZAMP), 16 (1965) 351-360.
[54] E. Richardson, E. Tyler, The transverse velocity gradient near the mouths of pipes in which an alternating or continuous flow of air is established, Proceedings of the Physical Society, 42 (1929).
[55] T. Sexl, Über den von EG Richardson entdeckten "Annulareffekt", Zeitschrift für Physik, 61 (1930) 349-362.
[56] R. Kadoli, N. Ganesan, Parametric resonance of a composite cylindrical shell containing pulsatile flow of hot fluid, Composite structures, 65 (2004) 391-404.
[57] V.D. Kubenko, P.S. Koval'Chuk, L.A. Kruk, Application of asymptotic methods to the investigation of one-frequency nonlinear oscillations of cylindrical shells interacting with moving fluid, Ukrainian Mathematical Journal, 59 (2007) 533-545.
[58] P.S. Koval'chuk, L.A. Kruk, Forced nonlinear oscillations of cylindrical shells interacting with fluid flow, International Applied Mechanics, 42 (2006) 447-454.
[59] P. Koval'chuk, L. Kruk, Nonlinear parametric vibrations of orthotropic cylindrical shells interacting with a pulsating fluid flow, International Applied Mechanics, 45 (2009) 1007-1015.
[60] V.D. Kubenko, P.S. Koval'chuk, N.P. Podchasov, Analysis of nonstationary processes in cylindrical shells interacting with a fluid flow, International Applied Mechanics, 46 (2011) 1119-1131.

[61] G. Morgan, J. Kiely, Wave propagation in a viscous liquid contained in a flexible tube, The Journal of the Acoustical Society of America, 26 (1954) 323-328.
[62] J.R. Womersley, Oscillatory motion of a viscous liquid in a thin-walled elastic tube-I: The linear approximation for long waves, Philosophical Magazine, 46 (1955) 199-221.
[63] H. Atabek, H. Lew, Wave propagation through a viscous incompressible fluid contained in an initially stressed elastic tube, Biophysical Journal, 6 (1966) 481-503.
[64] R.H. Cox, Comparison of linearized wave propagation models for arterial blood flow analysis, Journal of Biomechanics, 2 (1969) 251-265.
[65] S. Ling, H. Atabek, A nonlinear analysis of pulsatile flow in arteries, Journal of Fluid Mechanics, 55 (1972) 493-511.
[66] J.R. Womersley, Method for the calculation of velocity, rate of flow and viscous drag in arteries when the pressure gradient is known, The Journal of Physiology, 127 (1955) 553-563.
[67] J. Womersley, The mathematical analysis of the arterial circulation in a state of oscillatory motion, Wright Air Development Center Technical Report WADC-TR-56-614, (1957).
[68] D.A. McDonald, Blood flow in arteries, 1960.
[69] D. Bergel, Cardiovascular Fluid Dynamics, Academic Press, London & New York, 1972.
[70] D.A. McDonald, Blood Flow in Arteries, 2nd edn. London: Edward Arnold (1974).
[71] W. Nichols, M. O'Rourke, C. Vlachopoulos, McDonald's Blood Flow in Arteries: Theoretical, Experimental and Clinical Principles, CRC press, 2011.
[72] T.J. Pedley, The Fluid Mechanics of Large Blood Vessels, Cambridge University Press Cambridge, 1980.
[73] Y.C. Fung, Biodynamics: Circulation, Springer Verlag, 1984.
[74] D.J. Korteweg, Über die Fortpflanzungsgeschwindigkeit des Schalles in Elastischen Röhren, Annalen der Physik 241 (12): 525–542, (1878).
[75] Y.C. Fung, Biomechanics: Circulation, Springer Science & Business Media, 1997.
[76] M. Taylor, An approach to an analysis of the arterial pulse wave II. Fluid oscillations in an elastic pipe, Physics in Medicine and Biology, 1 (1957) 321.
[77] D. McDonald, Regional pulse-wave velocity in the arterial tree, Journal of Applied Physiology, 24 (1968) 73-78.
[78] W. Nichols, D. McDonald, Wave-velocity in the proximal aorta, Medical and Biological Engineering, 10 (1972) 327-335.
[79] M. Zamir, Hemo-dynamics, Springer, 2016.
[80] A. Shapiro, Physiologic and medical aspects of flow in collapsible tubes, in: Proc. Sixth Canadian Congress of Applied Mechanics, 1977, pp. 883-906.

[81] A.H. Shapiro, Steady Flow in in Collapsible Tubes, ASME Journal of Biomechanical Engineering, 99 (1977) 126-147.

[82] R.D. Kamm, T.J. Pedley, Flow in collapsible tubes: A brief review, Journal of Biomechanical Engineering, 111 (1989) 177-179.

[83] W.A. Conrad, Pressure-flow relationships in collapsible tubes, IEEE Transactions on Biomedical Engineering, (1969) 284-295.

[84] A.I. Katz, Y. Chen, A.H. Moreno, Flow through a collapsible tube: experimental analysis and mathematical model, Biophysical Journal, 9 (1969) 1261-1279.

[85] Y. Matsuzaki, K. Seike, Numerical analysis of flow in a collapsible vessel based on unsteady and quasi-steady flow theories, in: Computational Biomechanics, Springer, 1996, pp. 185-198.

[86] Y. Matsuzaki, Self-excited oscillation of a collapsible tube conveying fluid, in: Frontiers in Biomechanics, Springer, 1986, pp. 342-350.

[87] R.D. Kamm, A.H. Shapiro, Unsteady flow in a collapsible tube subjected to external pressure or body forces, Journal of Fluid Mechanics, 95 (1979) 1-78.

[88] H.-C. Han, J.K. Chesnutt, J.R. Garcia, Q. Liu, Q. Wen, Artery buckling: new phenotypes, models, and applications, Annals of Biomedical Engineering, 41 (2013) 1399-1410.

[89] M. Amabili, K. Karazis, R. Mongrain, M.P. Païdoussis, R. Cartier, A three-layer model for buckling of a human aortic segment under specific flow-pressure conditions, International Journal for Numerical Methods in Biomedical Engineering, 28 (2012) 495-512.

[90] W.C. Roberts, Aortic dissection: anatomy, consequences, and causes, American heart journal, 101 (1981) 195-214.

[91] S.A. LeMaire, L. Russell, Epidemiology of thoracic aortic dissection, Nature Reviews Cardiology, 8 (2011) 103-113.

[92] S. Bhat, Cardiovascular Implants and Extracorporeal Devices, in: Biomaterials, Springer Netherlands, 2002, pp. 130-162.

[93] T. Franz, Cardiovascular and Cardiac Therapeutic Devices, Springer, 2014.

[94] F. Silver, Biomaterials, Medical Devices and Tissue Engineering: An Integrated Approach, Springer Science & Business Media, 1994.

[95] L. Sauvage, Dacron arterial grafts, in: A.K. HE Kambic, P Sung (Ed.) Vascular Graft Update: Safety and Performance, ASTM Publication, Williamsburg, 1986, pp. 16-24.

[96] F. Hess, History of (MICRO) vascular surgery and the development of small-caliber blood vessel prostheses (with some notes on patency rates and re-endothelialization), Microsurgery, 6 (1985) 59-69.

[97] R. Deterling Jr, S. Bhonslay, An evaluation of synthetic materials and fabrics suitable for blood vessel replacement, Surgery, 38 (1955) 71.
[98] W.M. Abbott, A. Callow, W. Moore, R. Rutherford, F. Veith, S. Weinberg, Evaluation and performance standards for arterial prostheses, Journal of vascular surgery, 17 (1993) 746-756.
[99] F. Miyawaki, T. How, D. Annis, Effect of compliance mismatch on flow disturbances in a model of an arterial graft replacement, Medical and Biological Engineering and Computing, 28 (1990) 457-464.
[100] C. Singh, C.S. Wong, X. Wang, Medical textiles as vascular implants and their success to mimic natural arteries, Journal of Functional Biomaterials, 6 (2015) 500-525.
[101] W.M. Abbott, J. Megerman, J.E. Hasson, G. L'Italien, D.F. Warnock, Effect of compliance mismatch on vascular graft patency, Journal of Vascular Surgery, 5 (1987) 376-382.
[102] A. Nayfeh, D. Mook, Nonlinear Oscillations, Wiley, New York.
[103] G. Duffing, Erzwungene Schwingungen bei veränderlicher Eigenfrequenz und ihre technische Bedeutung, R, Vieweg & Sohn, 1918.
[104] W.H. Press, S.A. Teukolsky, W.T. Vetterling, B.P. Flannery, Numerical recipes in FORTRAN, in, Cambridge Univ. Press, 1992.
[105] R. Seydel, From equilibrium to chaos, Elsevier, 1988.
[106] E.J. Doedel, A.R. Champneys, T.F. Fairgrieve, Y.A. Kuznetsov, B. Sandstede, X. Wang, Auto97, Continuation and bifurcation software for ordinary differential equations, (1998).
[107] G. Schmidt, A. Tondl, Non-linear vibration, Cambridge University Press, 1986.
[108] J. Argyris, H. Maria, G. Faust, An exploration of chaos, North-Holland, 1994.
[109] R. Grimshaw, Nonlinear ordinary differential equations, CRC Press, 1991.
[110] A.H. Nayfeh, B. Balachandran, Applied nonlinear dynamics: analytical, comptational and experimental methods, in: Wiley Series in Nonlinear Sciences, John Wiley & Sons, Inc New York, 1995.
[111] F.C. Moon, Chaotic and fractal dynamics, John Wiley & Sons, 1992.
[112] A.H. Nayfeh, B. Balachandran, Applied nonlinear dynamics: analytical, computational and experimental methods, John Wiley & Sons, 2008.
[113] M. Chiba, Nonlinear hydroelastic vibration of a cylindrical tank with an elastic bottom, containing liquid. Part II: linear axisymmetric vibration analysis, Journal of Fluids and Structures, 7 (1993) 57-73.
[114] M. Chiba, Non-linear hydroelastic vibration of a cylindrical tank with an elastic bottom containing liquid-III. Non-linear analysis with Ritz averaging method, International Journal of Non-Linear Mechanics, 31 (1996) 155-165.

[115] E. Tubaldi, M. Amabili, Vibrations and stability of a periodically supported rectangular plate immersed in axial flow, Journal of Fluids and Structures, 39 (2013) 391-407.

[116] E. Tubaldi, F. Alijani, M. Amabili, Non-linear vibrations and stability of a periodically supported rectangular plate in axial flow, International Journal of Non-Linear Mechanics, 66 (2014) 54-65.

[117] M.T. Landahl, On the stability of a laminar incompressible boundary layer over a flexible surface, Journal of Fluid Mechanics, 13 (1962) 609-632.

[118] T.B. Benjamin, Effects of a flexible boundary on hydrodynamic stability, Journal of Fluid Mechanics, 9 (1960) 513-532.

[119] T.B. Benjamin, The threefold classification of unstable disturbances in flexible surfaces bounding inviscid flows, Journal of Fluid Mechanics, 16 (1963) 436-450.

[120] N. Peake, Nonlinear stability of a fluid-loaded elastic plate with mean flow, Journal of Fluid Mechanics, 434 (2001) 101-118.

[121] C. Von Kerczek, S.H. Davis, Linear stability theory of oscillatory stokes layers, Journal of Fluid Mechanics, 62 (1974).

[122] D.J. Schneck, S. Ostrack, Pulsatile blood flow in a channel of small exponential divergence. The linear approximation for low mean Reynolds number, Journal of Fluids Engineering, 97 (1974) 353-360.

[123] D. Elad, A. Shochat, R.J. Shiner, Computational model of oscillatory airflow in a bronchial bifurcation, Respiration Physiology, 112 (1998) 95-111.

[124] M. Zamir, The physics of pulsatile flow, Springer, 2000.

[125] R. Akhavan, R.D. Kamm, A.H. Shapiro, Investigation of transition to turbulence in bounded oscillatory Stokes flows Part 2. Numerical simulations, Journal of Fluid Mechanics, 225 (1991) 423-444.

[126] R. Akhavan, R.D. Kamm, A.H. Shapiro, Investigation of transition to turbulence in bounded oscillatory Stokes flows Part 1. Experiments, Journal of Fluid Mechanics, 225 (1991) 395-422.

[127] D.M. Eckmann, J.B. Grotberg, Experiments on transition to turbulence in oscillatory pipe flow, Journal of Fluid Mechanics, 222 (1991) 329-350.

[128] M. Ohmi, M. Iguchi, K. Kakehashi, T. Masuda, Transition to turbulence and velocity distribution in an oscillating pipe flow, Bulletin of the JSME, 25 (1982) 365-371.

[129] L. Fishler, R. Brodkey, Transition, turbulence and oscillating flow in a pipe a visual study, Experiments in fluids, 11 (1991) 388-398.

[130] R. Berguer, J.L. Bull, K. Khanafer, Refinements in mathematical models to predict aneurysm growth and rupture, Annals of the New York Academy of Sciences, 1085 (2006) 110-116.
[131] K.M. Khanafer, J.L. Bull, G.R. Upchurch Jr, R. Berguer, Turbulence significantly increases pressure and fluid shear stress in an aortic aneurysm model under resting and exercise flow conditions, Annals of Vascular Surgery, 21 (2007) 67-74.
[132] K.M. Khanafer, J.L. Bull, R. Berguer, Fluid–structure interaction of turbulent pulsatile flow within a flexible wall axisymmetric aortic aneurysm model, European Journal of Mechanics-B/Fluids, 28 (2009) 88-102.
[133] S. Wolfram, The MATHEMATICA® Book, Version 4, Cambridge University Press, 1999.
[134] N. Yamaki, M. Chiba, Nonlinear Vibrations of a Clamped Rectangular Plate with Initial Deflection and Initial Edge Displacement -Part I : Theory Thin-Walled Structures, Vol.1 (1983) pp. 3-29
[135] N. Yamaki, K. Otomo, M. Chiba, Nonlinear Vibrations of a Clamped Rectangular Plate with Initial Deflection and Initial Edge Displacement -Part II : Experiment Thin-Walled Structures, Vol. 1 (1983) pp. 101-119
[136] M. Amabili, C. Touzé, Reduced-order models for nonlinear vibrations of fluid-filled circular cylindrical shells: Comparison of POD and asymptotic nonlinear normal modes methods, Journal of Fluids and Structures, 23 (2007) pp. 885-903.
[137] M. Amabili, F. Pellicano, M. Païdoussis, Non-linear dynamics and stability of circular cylindrical shells containing flowing fluid. Part I: stability, Journal of Sound and Vibration, 225 (1999) 655-699.
[138] M. Amabili, F. Pellicano, M. Païdoussis, Non-linear dynamics and stability of circular cylindrical shells containing flowing fluid, Part II: large-amplitude vibrations without flow, Journal of Sound and Vibration, 228 (1999) 1103-1124.
[139] M. Amabili, F. Pellicano, M. Païdoussis, Non-linear dynamics and stability of circular cylindrical shells containing flowing fluid. Part III: truncation effect without flow and experiments, Journal of Sound and Vibration, 237 (2000) 617-640.
[140] M. Amabili, F. Pellicano, M. Païdoussis, Non-linear dynamics and stability of circular cylindrical shells containing flowing fluid. Part IV: large-amplitude vibrations with flow, Journal of Sound and vibration, 237 (2000) 641-666.
[141] M. Amabili, K. Karagiozis, M. Païdoussis, Effect of geometric imperfections on non-linear stability of circular cylindrical shells conveying fluid, International Journal of Non-Linear Mechanics, 44 (2009) 276-289.

[142] K. Karagiozis, M. Amabili, M.P. Païdoussis, Nonlinear dynamics of harmonically excited circular cylindrical shells containing fluid flow, Journal of Sound and Vibration, 329 (2010) 3813-3834.

[143] M. Paak, M.P. Païdoussis, A.K. Misra, Nonlinear dynamics and stability of cantilevered circular cylindrical shells conveying fluid, Journal of Sound and Vibration, 332 (2013) 3474-3498.

[144] I. Chueshov, I. Ryzhkova, Unsteady interaction of a viscous fluid with an elastic shell modeled by full von Karman equations, Journal of Differential Equations, 254 (2013) 1833-1862.

[145] R.W. Ogden, Non-linear elastic deformations, Courier Dover Publications, 1997.

[146] G.A. Holzapfel, Nonlinear solid mechanics, Wiley Chichester, 2000.

[147] G.A. Holzapfel, T.C. Gasser, R.W. Ogden, A new constitutive framework for arterial wall mechanics and a comparative study of material models, Journal of Elasticity, 61 (2000) 1-48.

[148] G.A. Holzapfel, T.C. Gasser, R.W. Ogden, Comparison of a Multi-Layer Structural Model for Arterial Walls with a Fung-Type Model, and Issues of Material Stability, Journal of Biomechanical Engineering, 126 (2004) 264-275.

[149] G.A. Holzapfel, R.W. Ogden, Constitutive modelling of arteries, Proceedings of the Royal Society A: Mathematical, Physical and Engineering Science, 466 (2010) 1551-1597.

[150] D. Tremblay, T. Zigras, R. Cartier, L. Leduc, J. Butany, R. Mongrain, R.L. Leask, A comparison of mechanical properties of materials used in aortic arch reconstruction, The Annals of Thoracic Surgery, 88 (2009) 1484-1491.

[151] C.A. Taylor, J. Humphrey, Open problems in computational vascular biomechanics: hemodynamics and arterial wall mechanics, Computer Methods in Applied Mechanics and Engineering, 198 (2009) 3514-3523.

[152] B.J. Daly, Pulsatile flow through a tube containing rigid and distensible sections, in: Proceedings of the Fifth International Conference on Numerical Methods in Fluid Dynamics June 28–July 2, 1976 Twente University, Enschede, Springer, 1976, pp. 153-158.

[153] M.M. T Karino , HL. Goldsmith Flow patterns in model and natural vessels., in: S.l.e. al. (Ed.) Biologic and synthetic vascular prostheses, Grune and Stratton, New York, 1982, pp. pp 153-178.

[154] K. Khanafer, R. Berguer, Fluid–structure interaction analysis of turbulent pulsatile flow within a layered aortic wall as related to aortic dissection, Journal of biomechanics, 42 (2009) 2642-2648.

[155] J. Hale, D. McDonald, J. Womersley, Velocity profiles of oscillating arterial flow, with some calculations of viscous drag and the Reynolds number, The Journal of Physiology, 128 (1955) 629-640.
[156] M. Hasegawa, T. Azuma, Mechanical properties of synthetic arterial grafts, Journal of Biomechanics, 12 (1979) 509-517.
[157] L. Weltert, R. De Paulis, R. Scaffa, D. Maselli, A. Bellisario, S. D'Alessandro, Re-creation of a sinuslike graft expansion in Bentall procedure reduces stress at the coronary button anastomoses: A finite element study, The Journal of Thoracic and Cardiovascular Surgery, 137 (2009) 1082-1087.
[158] H. Lamb, On the velocity of sound in a tube, as affected by the elasticity of the walls, Manchester Memoirs, 42 (1898) 116.
[159] R. Skalak, An extension of the theory of water hammer, in, DTIC Document, 1955.
[160] T. Lin, G. Morgan, Wave propagation through fluid contained in a cylindrical, elastic shell, The Journal of the Acoustical Society of America, 28 (1956) 1165-1176.
[161] M. Junger, The effect of a surrounding fluid on pressure waves in a fluid-filled elastic tube, Journal Applied Mechanics, 22 (1955) 227-231.
[162] C.A. Taylor, T.J. Hughes, C.K. Zarins, Finite element modeling of blood flow in arteries, Computer Methods in Applied Mechanics and Engineering, 158 (1998) 155-196.
[163] M. Oshima, R. Torii, T. Kobayashi, N. Taniguchi, K. Takagi, Finite element simulation of blood flow in the cerebral artery, Computer Methods in Applied Mechanics and Engineering, 191 (2001) 661-671.
[164] K. Perktold, G. Rappitsch, Computer simulation of local blood flow and vessel mechanics in a compliant carotid artery bifurcation model, Journal of Biomechanics, 28 (1995) 845-856.
[165] C.A. Figueroa, I.E. Vignon-Clementel, K.E. Jansen, T.J. Hughes, C.A. Taylor, A coupled momentum method for modeling blood flow in three-dimensional deformable arteries, Computer Methods in Applied Mechanics and Engineering, 195 (2006) 5685-5706.
[166] L. Formaggia, J.-F. Gerbeau, F. Nobile, A. Quarteroni, On the coupling of 3D and 1D Navier–Stokes equations for flow problems in compliant vessels, Computer Methods in Applied Mechanics and Engineering, 191 (2001) 561-582.
[167] T.J. Hughes, W.K. Liu, T.K. Zimmermann, Lagrangian-Eulerian finite element formulation for incompressible viscous flows, Computer Methods in Applied Mechanics and Engineering, 29 (1981) 329-349.
[168] J. Womersley, Oscillatory flow in arteries. II: The reflection of the pulse wave at junctions and rigid inserts in the arterial system, Physics in Medicine and Biology, 2 (1958) 313.

[169] C. Bertram, The dynamics of collapsible tubes, in: Symposia of the Society for Experimental Biology, 1994, pp. 253-264.
[170] M. Heil, The stability of cylindrical shells conveying viscous flow, Journal of Fluids and Structures, 10 (1996) 173-196.
[171] T. Pedley, X. Luo, Modelling flow and oscillations in collapsible tubes, Theoretical and Computational Fluid Dynamics, 10 (1998) 277-294.
[172] J. Humphrey, Continuum biomechanics of soft biological tissures, Proceedings of the Royal Society of London. Series A, Mathematical and Physical Sciences, 459 (2002) 1-44.
[173] J.F. Rodríguez, C. Ruiz, M. Doblaré, G.A. Holzapfel, Mechanical stresses in abdominal aortic aneurysms: influence of diameter, asymmetry, and material anisotropy, Journal of Biomechanical Engineering, 130 (2008) 021023.
[174] G. Holzapfel, R. Ogden, Modelling the layer-specific three-dimensional residual stresses in arteries, with an application to the human aorta, Journal of the Royal Society Interface, 7 (2010) 787-799.
[175] J. Humphrey, S. Na, Elastodynamics and arterial wall stress, Annals of Biomedical Engineering, 30 (2002) 509-523.
[176] I. Kidson, The effect of wall mechanical properties on patency of arterial grafts, Annals of the Royal College of Surgeons of England, 65 (1983) 24.
[177] A. Nicolaides, Haemodynamic aspects of vascular grafting, Acta Chirurgica Scandinavica. Supplementum, 529 (1984) 7-16.
[178] A. Setchi, A.J. Mestel, J.H. Siggers, K.H. Parker, M.W. Tan, K. Wong, Mathematical model of flow through the patent ductus arteriosus, Journal of Mathematical Biology, 67 (2013) 1487-1506.
[179] D.N. Ku, Blood flow in arteries, Annual Review of Fluid Mechanics, 29 (1997) 399-434.
[180] A. Frydrychowicz, A. Berger, A.M. Del Rio, M.F. Russe, J. Bock, A. Harloff, M. Markl, Interdependencies of aortic arch secondary flow patterns, geometry, and age analysed by 4-dimensional phase contrast magnetic resonance imaging at 3 Tesla, European radiology, 22 (2012) 1122-1130.
[181] C.S. Park, S. Payne, Nonlinear and viscous effects on wave propagation in an elastic axisymmetric vessel, Journal of Fluids and Structures, 27 (2011) 134-144.
[182] D.L. Fry, Acute vascular endothelial changes associated with increased blood velocity gradients, Circulation Research, 22 (1968) 165-197.
[183] H. Irschik, H. Holl, The equations of Lagrange written for a non-material volume, Acta Mechanica, 153 (2002) 231-248.

[184] F. Alijani, M. Amabili, P. Balasubramanian, S. Carra, G. Ferrari, R. Garziera, Damping for large-amplitude vibrations of plates and curved panels, part 1: Modeling and experiments, International Journal of Non-Linear Mechanics, (2016).

[185] M. Amabili, F. Alijani, J. Delannoy, Damping for large-amplitude vibrations of plates and curved panels, part 2: Identification and comparisons, International Journal of Non-Linear Mechanics, (2016).

[186] C. Mills, I. Gabe, J. Gault, D. Mason, J. Ross, E. Braunwald, J. Shillingford, Pressure-flow relationships and vascular impedance in man, Cardiovascular Research, (1970) 405-417.

[187] L. Rocha, A. Sepulveda, A. Pontes, J. Viana, I.C. Santos, J.M.R. Tavares, Study of pressure sensors placement using an abdominal aortic aneurysm (AAA) Model, Technology and Medical Sciences, (2011) 261.

[188] J.M. Lee, G.J. Wilson, Anisotropic tensile viscoelastic properties of vascular graft materials tested at low strain rates, Biomaterials, 7 (1986) 423-431.

[189] O. Vardoulis, E. Coppens, B. Martin, P. Reymond, P. Tozzi, N. Stergiopulos, Impact of aortic grafts on arterial pressure: a computational fluid dynamics study, European Journal of Vascular and Endovascular Surgery, 42 (2011) 704-710.

[190] J. Chung, J.P. Matonick, J.-J. Li, Synthetic arterial graft design on the influence of pulse wave propagation within the aorta, in: Bioengineering Conference, 2002. Proceedings of the IEEE 28th Annual Northeast, IEEE, 2002, pp. 17-18.

[191] I. Voges, M. Jerosch-Herold, J. Hedderich, E. Pardun, C. Hart, D.D. Gabbert, J.H. Hansen, C. Petko, H.-H. Kramer, C. Rickers, Normal values of aortic dimensions, distensibility, and pulse wave velocity in children and young adults: a cross-sectional study, Journal of Cardiovascular Magnetic Resonance, 14 (2012) 1.

[192] K. Sutton-Tyrrell, S.S. Najjar, R.M. Boudreau, L. Venkitachalam, V. Kupelian, E.M. Simonsick, R. Havlik, E.G. Lakatta, H. Spurgeon, S. Kritchevsky, Elevated aortic pulse wave velocity, a marker of arterial stiffness, predicts cardiovascular events in well-functioning older adults, Circulation, 111 (2005) 3384-3390.

[193] R. Walden, J. Gilbert, J. Megerman, W.M. Abbott, Matched elastic properties and successful arterial grafting, Archives of Surgery, 115 (1980) 1166-1169.

[194] J.L. Cronenwett, K.W. Johnston, Rutherford's vascular surgery, Elsevier Health Sciences, 2014.

[195] J.D. Bronzino, Biomedical engineering handbook, CRC press, 1999.

[196] R.F. Appleyard, L.R. Sauvage, Haemodynamic consequences of arterial replacement with a synthetic graft, Cardiovascular research, 20 (1986) 26-35.

[197] T. Mitsui, H. Maeta, I. Fukuda, H. Ijima, K. Okamura, A. Sakai, J. Sakurai, M. Hori, Left ventricular hypertrophy due to aortic bypass grafting with a long prosthesis, The Journal of Cardiovascular Surgery, 27 (1985) 201-206.
[198] H. Maeta, M. Hori, Effects of a lack of aortic" Windkessel" properties on the left ventricle, Japanese Circulation Journal, 49 (1985) 232-237.
[199] S.Y. Kim, T.J. Hinkamp, W.R. Jacobs, R.C. Lichtenberg, H. Posniak, R. Pifarré, Effect of an inelastic aortic synthetic vascular graft on exercise hemodynamics, The Annals of Thoracic Surgery, 59 (1995) 981-989.
[200] N. Westerhof, J.-W. Lankhaar, B.E. Westerhof, The arterial windkessel, Medical & Biological Engineering & Computing, 47 (2009) 131-141.
[201] D. Mehigan, B. Fitzpatrick, H. Browne, D. Bouchier-Hayes, Is compliance mismatch the major cause of anastomotic arterial aneurysms? Analysis of 42 cases, The Journal of Cardiovascular Surgery, 26 (1984) 147-150.
[202] F. Knowlton, E. Starling, The influence of variations in temperature and blood-pressure on the performance of the isolated mammalian heart, The Journal of Physiology, 44 (1912) 206-219.
[203] J. Womersley, Oscillatory motion of a viscous liquid in a thin-walled elastic tube. I:The linear approximation for long waves, Philos. Mag, 46 (1955) 199.
[204] T. Moodie, R. Tait, J. Haddow, Waves in compliant tubes, Wave propagation in viscoelastic media (Mainardi, F., ed.), (1982) 124-168.
[205] C. Bertram, Fluid flow in distensible vessels, Clinical and Experimental Pharmacology and Physiology, 36 (2009) 206-216.
[206] A.M. Malek, S.L. Alper, S. Izumo, Hemodynamic shear stress and its role in atherosclerosis, JAMA, 282 (1999) 2035-2042.
[207] S. Laurent, P. Boutouyrie, R. Asmar, I. Gautier, B. Laloux, L. Guize, P. Ducimetiere, A. Benetos, Aortic stiffness is an independent predictor of all-cause and cardiovascular mortality in hypertensive patients, Hypertension, 37 (2001) 1236-1241.
[208] T.J. Hughes, A study of the one-dimensional theory of arterial pulse propagation, Structural Engineering Laboratory, University of California, 1974.
[209] J. Alastruey, K.H. Parker, S.J. Sherwin, Arterial pulse wave haemodynamics, in: 11th International Conference on Pressure Surges, Virtual PiE Led t/a BHR Group: Lisbon, Portugal, 2012, pp. 401-442.
[210] F.N. van de Vosse, N. Stergiopulos, Pulse wave propagation in the arterial tree, Annual Review of Fluid Mechanics, 43 (2011) 467-499.
[211] M. Heil, A.L. Hazel, Fluid-structure interaction in internal physiological flows, Annual Review of Fluid Mechanics, 43 (2011) 141-162.

[212] C.A. Taylor, C. Figueroa, Patient-specific modeling of cardiovascular mechanics, Annual Review of Biomedical Engineering, 11 (2009) 109-134.
[213] A. Quarteroni, A. Veneziani, Analysis of a geometrical multiscale model based on the coupling of ODE and PDE for blood flow simulations, Multiscale Modeling & Simulation, 1 (2003) 173-195.
[214] M.Á. Fernández, M. Moubachir, A Newton method using exact Jacobians for solving fluid–structure coupling, Computers & Structures, 83 (2005) 127-142.
[215] M.S. Olufsen, C.S. Peskin, W.Y. Kim, E.M. Pedersen, A. Nadim, J. Larsen, Numerical simulation and experimental validation of blood flow in arteries with structured-tree outflow conditions, Annals of Biomedical Engineering, 28 (2000) 1281-1299.
[216] T.J. Hughes, J. Lubliner, On the one-dimensional theory of blood flow in the larger vessels, Mathematical Biosciences, 18 (1973) 161-170.
[217] Y.C. Fung, Biomechanics: Mechanical Properties of Living Tissues, Springer Science & Business Media, 1993.
[218] J.D. Humphrey, Cardiovascular solid mechanics: cells, tissues, and organs, Springer Science & Business Media, 2013.
[219] D. Tang, C. Yang, S. Kobayashi, D.N. Ku, Steady flow and wall compression in stenotic arteries: a three-dimensional thick-wall model with fluid-wall interactions, ASME Journal of Biomechanical Engineering, 123 (2001) 548-557.
[220] R.M. Nerem, Role of mechanics in vascular tissue engineering, Biorheology, 40 (2003) 281-287.
[221] G.C. Cheng, H.M. Loree, R.D. Kamm, M.C. Fishbein, R.T. Lee, Distribution of circumferential stress in ruptured and stable atherosclerotic lesions. A structural analysis with histopathological correlation, Circulation, 87 (1993) 1179-1187.
[222] D. Tang, C. Yang, S. Kobayashi, J. Zheng, P.K. Woodard, Z. Teng, K. Billiar, R. Bach, D.N. Ku, 3D MRI-based anisotropic FSI models with cyclic bending for human coronary atherosclerotic plaque mechanical analysis, Journal of Biomechanical Engineering, 131 (2009) 061010.
[223] N. Smith, A. Pullan, P.J. Hunter, An anatomically based model of transient coronary blood flow in the heart, SIAM Journal on Applied mathematics, 62 (2002) 990-1018.
[224] E. De Langre, Ondes variqueuses absolument instables dans un canal élastique, Comptes Rendus de l'Académie des Sciences-Series IIB-Mechanics-Physics-Astronomy, 328 (2000) 61-65.

[225] T.W. Rowland, M. Garrard, S. Marwood, M.E. Guerra, D. Roche, V.B. Unnithan, Myocardial performance during progressive exercise in athletic adolescent males, Medicine and Science in Sports and Exercise, 41 (2009) 1721-1728.
[226] Y.C. Fung, Biorheology of soft tissues, Biorheology, 10 (1973) 139-155.
[227] L. Dortmans, A. van de Ven, A. Sauren, A note on the reduced creep function corresponding to the quasi-linear visco-elastic model proposed by Fung, Journal of Biomechanical Engineering, 116 (1994) 373-375.
[228] M. Puso, J. Weiss, Finite Element Implementation of Anisotropic Quasi-linear Viscoelasticty using a Discrete Spectrum Approximation, Journal of Biomechanical Engineering, 120 (1998) 62-70.
[229] J.E. Bischoff, Reduced parameter formulation for incorporating fiber level viscoelasticity into tissue level biomechanical models, Annals of Biomedical Engineering, 34 (2006) 1164-1172.
[230] J.M. Giles, A.E. Black, J.E. Bischoff, Anomalous rate dependence of the preconditioned response of soft tissue during load controlled deformation, Journal of Biomechanics, 40 (2007) 777-785.
[231] G.A. Holzapfel, T.C. Gasser, M. Stadler, A structural model for the viscoelastic behavior of arterial walls: continuum formulation and finite element analysis, European Journal of Mechanics-A/Solids, 21 (2002) 441-463.
[232] J.J. Sarver, P.S. Robinson, D.M. Elliott, Methods for quasi-linear viscoelastic modeling of soft tissue: application to incremental stress-relaxation experiments, Journal of Biomechanical Engineering, 125 (2003) 754–758.
[233] J.A. Gimbel, J.J. Sarver, L.J. Soslowsky, The effect of overshooting the target strain on estimating viscoelastic properties from stress relaxation experiments, Journal of Biomechanical Engineering, 126 (2004) 844-848.
[234] S.D. Abramowitch, S.L.Y. Woo, An Improved Method to Analyze the Stress Relaxation of Ligaments Following a Finite Ramp Time Based on the Quasi-Linear Viscoelastic Theory, Journal of Biomechanical Engineering, 126 (2004) 92-97.
[235] K.L. Troyer, D.J. Estep, C.M. Puttlitz, Viscoelastic effects during loading play an integral role in soft tissue mechanics, Acta Biomaterialia, 8 (2012) 234-243.
[236] R.M. Castile, N.W. Skelley, B. Babaei, R.H. Brophy, S.P. Lake, Microstructural properties and mechanics vary between bundles of the human anterior cruciate ligament during stress-relaxation, Journal of Biomechanics, 49 (2016) 87-93.
[237] B. Babaei, S.D. Abramowitch, E.L. Elson, S. Thomopoulos, G.M. Genin, A discrete spectral analysis for determining quasi-linear viscoelastic properties of biological materials, Journal of The Royal Society Interface, 12 (2015) 20150707.

[238] B. Babaei, A.J. Velasquez-Mao, S. Thomopoulos, E.L. Elson, S.D. Abramowitch, G.M. Genin, Discrete quasi-linear viscoelastic damping analysis of connective tissues, and the biomechanics of stretching, Journal of the Mechanical Behavior of Biomedical Materials, 69 (2017) 193-202.
[239] T. How, Mechanical properties of arteries and arterial grafts, in: Cardiovascular biomaterials, Springer, 1992, pp. 1-35.
[240] M.S. Yeoman, D. Reddy, H.C. Bowles, D. Bezuidenhout, P. Zilla, T. Franz, A constitutive model for the warp-weft coupled non-linear behavior of knitted biomedical textiles, Biomaterials, 31 (2010) 8484-8493.
[241] G.A. Holzapfel, Nonlinear Solid Mechanics, Wiley Chichester, 2006.
[242] Y.C. Fung, K. Fronek, P. Patitucci, Pseudoelasticity of arteries and the choice of its mathematical expression, American Journal of Physiology-Heart and Circulatory Physiology, 237 (1979) H620-H631.
[243] G.A. Holzapfel, Determination of material models for arterial walls from uniaxial extension tests and histological structure, Journal of Theoretical Biology, 238 (2006) 290-302.
[244] T. Nguyen, Y. Biadillah, R. Mongrain, J. Brunette, J. Tardif, O. Bertrand, A method for matching the refractive index and kinematic viscosity of a blood analog for flow visualization in hydraulic cardiovascular models, Journal of Biomechanical Engineering(Transactions of the ASME), 126 (2004) 529-535.
[245] M. Amabili, P. Balasubramanian, G. Ferrari, Travelling wave and non-stationary response in nonlinear vibrations of water-filled circular cylindrical shells: Experiments and simulations, Journal of Sound and Vibration, 381 (2016) 220-245.
[246] B. Peeters, H. Van der Auweraer, P. Guillaume, J. Leuridan, The PolyMAX frequency-domain method: a new standard for modal parameter estimation?, Shock and Vibration, 11 (2004) 395-409.
[247] M.H. Ghayesh, M.P. Païdoussis, M. Amabili, Nonlinear dynamics of cantilevered extensible pipes conveying fluid, Journal of Sound and Vibration, 332 (2013) 6405-6418.
[248] V.V. Novozhilov, Foundations of the Nonlinear Theory of Elasticity, Graylock Press, Rochester, NY, USA 1953.
[249] R. Nerem, W. Seed, An in vivo study of aortic flow disturbances, Cardiovascular Research, 6 (1972) 1-14.
[250] S. François, N. Chakfé, B. Durand, G. Laroche, Effect of polyester prosthesis micro-texture on endothelial cell adhesion and proliferation, Trends Biomater. Artif. Organs, 22 (2008) 89-99.
[251] A.I. Moens, Die Pulskurve, Leiden, The Netherlands: E.J. Brill, (1878).

[252] J. Kevorkian, Partial differential equations: Analytical Solution Techniques, Springer Science & Business Media, 1999.
[253] M. Amabili, I.D. Breslavsky, Displacement dependent pressure load for finite deflection of doubly-curved thick shells and plates, International Journal of Non-Linear Mechanics, 77 (2015) 265-273.
[254] T.C. Gasser, R.W. Ogden, G.A. Holzapfel, Hyperelastic modelling of arterial layers with distributed collagen fibre orientations, Journal of the Royal Society Interface, 3 (2006) 15-35.